International Committee for Future Accelerators

Sponsored by the Particles and Fields Commission of IUPAP

Beam Dynamics Newsletter

No. 57

Issue Editor:
Y. Cai

Editor in Chief:
W. Chou

April 2012

Contents

1 Foreword

1.1 From the Chair

Weiren Chou, Fermilab
Mail to: chou@fnal.gov

The International Committee for Future Accelerators (ICFA) met on February 2-3, 2012 at Oxford University, UK. Pier Oddone, Fermilab Director and the new ICFA Chair chaired the meeting. This meeting was preceded by an ILC Steering Committee (ILCSC) meeting earlier on February 2 in the same place.

An important subject discussed was a report from Jonathan Bagger, Chair of ILCSC, about the post-2012 plan of his committee. By the end of 2012, the ILC GDE will complete its mission after the publication of two milestone documents: the *Technical Design Report* (TDR) for the ILC accelerators and the *Detailed Baseline Design* (DBD) for the ILC detectors. The GDE will then cease to exist in mid-2013, and a successor organization will be needed to continue the necessary R&D. Bagger's proposed plan is to form a Linear Collider Board (LCB) as a panel of ICFA replacing the present ILCSC. Its mission will be to promote the construction of an electron-positron collider and its detectors as a worldwide collaborative effort. The LCB will establish a Directorate. The LC Director will be appointed by ICFA and be the overall leader for the linear collider effort. He or she will represent this effort to the worldwide science community and funding agencies. Reporting to this LC Director will be three associate directors: one for ILC, one for CLIC, and one for physics and detectors. Depending on LHC discoveries, the LC organization will evolve towards a single proposal for the appropriate linear collider. At this time, a search committee headed by Oddone for the first LC Director has been formed and is welcoming recommendations.

The meeting heard a report from a *US DOE Intensity Frontier Workshop*. Its goal was to look at a coherent program at this frontier, to gauge community support and to discuss strategy and opportunities. More than 500 people attended this workshop. There was also a report on the *International Design Study for the Neutrino Factory*. This topic was brought to ICFA several years ago and ICFA had then declined to become involved. However, there is much more information available now. ICFA could help by forming a new panel to provide coordination among several different proposals.

Five ICFA panels (Beam Dynamics, Advanced and Novel Accelerators, Instrumentation, Data Preservation and Interregional Connectivity) presented reports at the meeting.

In 2011, the Beam Dynamics (BD) Panel organized one Advanced Beam Dynamics Workshop (50th ABDW on *Energy Recovery Linacs ERL2011*, October 16-21 at KEK, Japan) and two mini-workshops (*Low Emittance Rings*, October 3-5 at Crete, Greece, and *Dielectric Laser Acceleration DLA2011*, September 15-16 at SLAC, USA). In 2012, the BD panel will organize two ABDWs (the 51st on *Future Light Sources FLS2012*, March 5-9 at Jlab, USA, and the 52nd on *High Intensity High Brightness Hadron Beams HB2012*, September 17-21 in Beijing, China) as well as two mini-workshops (*Breakdown Science and High Gradient Technology*, April 18-20 at KEK, Japan, and *Deflecting/Crab Cavity Applications in Accelerators*, July 11-13 in Lanzhou, China). The BD panel also published three issues of the *ICFA Beam Dynamics Newsletter* in 2011: No. 54 edited by J. Gao (IHEP, China), No. 55 by M. Palmer (Cornell/Fermilab) and No. 56 by W. Leemans (LBNL), W. Chou (Fermilab) and M. Uesaka (Tokyo U.). This last issue included a White Paper from the *ICFA-ICUIL Joint Task Force*. ICFA received a briefing about this paper. This ICFA-ICUIL collaboration has already produced several useful results, including that laser beams developed for the Livermore LIFE fusion project could find direct application in a $\gamma\gamma$ collider.

The BD panel received a request from the *Organization for Economic Co-operation and Development* (OECD) *Global Science Forum* (GSF) for input on changes over the past 25 years in the numbers and locations of energy-frontier HEP accelerators. The panel compiled a HEP Collider Table (1984-2011) and sent it to the GSF. The readers can find the table in Section 4.1.

The Seventh International Accelerator School for Linear Colliders will be held from November 27 – December 8, 2012 at the Raja Ramanna Center for Advanced Technology (RRCAT) at Indore, India. RRCAT will be the host. Please see Section 2.1 for the details. The school web site is http://www.linearcollider.org/school/2012/.

Susumu Kamada, who was responsible for the distribution and printing of this newsletter in the Asia and Pacific region since 1988, is retired from KEK. The baton was passed to Toshiyuki Okugi. Susumu's 24-year voluntary work is a great example of community service, the foundation of all ICFA activities. On behalf of the panel, I want to express our sincere thanks to him.

The editor of this issue is Dr. Yunhai Cai, a panel member and a senior staff scientist at SLAC, USA. Yunhai collected 14 excellent articles in the theme section "*Low Emittance Rings*." These articles give a comprehensive review of this field. In this issue there are also one workshop report (*FLS2012*) and five workshop announcements (*HB2012*, *Deflecting/Crab Cavity*, *ICAP2012*, *BIW2012* and *FEL2012*). I thank Yunhai for editing and producing a newsletter of great value to our community.

1.2 From the Editor

Yunhai Cai, SLAC National Accelerator Laboratory
Mail to: yunhai@slac.stanford.edu

Electron storage rings are widely used for high luminosity colliders, damping rings in high-energy linear colliders, and in synchrotron light sources. They have become essential facilities in high-energy physics research, material science, and structure biology. To further increase the luminosity of colliders or the brightness of synchrotron light sources, the beam emittance is being continually reduced, recently into the nanometer region. In the next decade, several orders of magnitude in further reduction are expected. This requirement of ultra-low emittance presents many challenges both in beam dynamics and accelerator technologies. Accelerator physics in ultra-low emittance storage rings has been selected as the theme of this issue of the beam dynamics newsletter.

On this research topic, two successful workshops LER2010 [1], in Geneva and LER2011 [2] in Crete were held at which the great progress in the field was presented along with many in depth discussions. To share these exciting developments with other colleagues in the accelerator community, I chose most of the articles from those presentations. I would like to thank Yannis Papaphilippou and Hermann Schmickler who successfully organized the workshops. Other articles were selected from recent talks at IPAC 2011 in San Sebastian, and from the workshops on Future Light Sources in 2010 at SLAC and 2012 at JLab.

The first part of the newsletter focuses on the design of the extremely low emittance rings. It begins with an overview by Riccardo Bartolini, continues with various designs, and ends with the CLIC damping ring by Yannis. The second part of the newsletter contains four articles which review the methods and tools available for the design and operation of these storage rings. The third part is devoted to collective effects with emphasis on coherent synchrotron radiation. The last article is about R&D for future storage rings by Robert Hettel.

I am very grateful for this opportunity to share these recent exciting developments in storage ring design. Finally, I would like thank all the authors for their important contributions to our accelerator community.

References:

1. LER2010 Workshop, http://ler2010.web.cern.ch/ler2010
2. LER2011 Workshop, http://lowering2011.web.cern.ch/lowering2011

2 International Linear Collider (ILC)

2.1 Seventh International Accelerator School for Linear Colliders

Barry Barish (Caltech), Weiren Chou (Fermilab) and P. D. Gupta (RRCAT)
Mail to: chou@fnal.gov

We are pleased to announce the *Seventh International Accelerator School for Linear Colliders*. This school is a continuation of the series of schools which began six years ago. The first school was held in 2006 at Sokendai, Hayama, Japan, the second in 2007 at Erice, Sicily, Italy, the third in 2008 at Oakbrook Hills, Illinois, USA, the fourth in 2009 at Huairou, Beijing, China, the fifth in 2010 at Villars-sur-Ollon, Switzerland, and the sixth in 2011 at Pacific Grove, California, USA. The school is organized by the International Linear Collider (ILC) Global Design Effort (GDE), the Compact Linear Collider (CLIC) and the International Committee for Future Accelerators (ICFA) Beam Dynamics Panel.

The school this year will take place at the Raja Ramanna Center for Advanced Technology (RRCAT) at Indore, India from November 27 to December 8, 2012. It is hosted by RRCAT and sponsored by a number of funding agencies and institutions around the world including the U.S. Department of Energy (DOE), the U.S. National Science Foundation (NSF), Fermilab, SLAC, CERN, DESY, INFN, IN2P3, CEA, CPAN, KEK, IHEP, RRCAT and India Department of Atomic Energy (DAE).

The 11-day program includes 8-1/2 days of lectures, an excursion, a site visit and an examination. The first three days will be an introductory course with an overview of proposed future lepton colliders (ILC, CLIC and the muon collider) as well as introductions to linac basics and beam instrumentation. This will be followed by two elective courses, one on accelerator physics and the other on RF technology to run in parallel for 6 days. Each student is required to take the introductory course and one of the two electives. A complete description of the program can be found on the school web site (www.linearcollider.org/school/2012/). There will be homework assignments and a final examination but no university credits.

We encourage young physicists (graduate students, post doctoral fellows, junior researchers) to apply. In particular we welcome those physicists who are considering changing to a career in accelerator physics. This school is adopting an in-depth approach. Therefore, former students are welcome to apply if they have a compelling reason to do so. The school will accept a maximum of 70 students from around the world. Students will receive financial aid covering their expenses for attending including travel (full or partial). There will be no registration fee. Each applicant should complete the online registration form (which can be found on the school web site) and submit a curriculum vita as well as a letter of recommendation from his/her supervisor (in electronic form, either PDF or MS WORD). The application deadline is July 20, 2012. For more information, please contact: Dr. Satish C. Joshi, Raja Ramanna Centre for Advanced Technology, Indore, M. P. – 452013, India, telephone: + 91-731-2442244, fax: + 91-731-2442200, email: lcs2012@rrcat.gov.in

Organizing Committee

Barry Barish (GDE/Caltech, Chair)
Alex Chao (SLAC)
Hesheng Chen (IHEP)
Weiren Chou (ICFA BD Panel/Fermilab)
Paul Grannis (Stony Brook Univ.)
P. D. Gupta (RRCAT)
In Soo Ko (PAL)
Shin-ichi Kurokawa (KEK)
Hermann Schmickler (CERN)
Nick Walker (DESY)
Kaoru Yokoya (KEK)

Curriculum Committee

Weiren Chou (Fermilab, Chair)
William Barletta (USPAS)
Alex Chao (SLAC)
Jie Gao (IHEP)
Srinivas Krishnagopal (BARC)
Carlo Pagani (INFN/Milano)
Joerg Rossbach (DESY)
Hermann Schmickler (CERN)
Nobuhiro Terunuma (KEK)
Kaoru Yokoya (KEK)

Local Committee

P. D. Gupta (RRCAT, Chair)
P. R. Hannurkar (RRCAT)
S. C. Joshi (RRCAT)
S. K. Shukla (RRCAT)

3 Low Emittance Rings

3.1 Review of Lattice Design for Low Emittance Rings

R. Bartolini
Diamond Light Source, Harwell Science and Innovation Campus, Chilton, Didcot,
OX11 0DE and John Adams Inst., U. of Oxford, Keble Road, OX1 3HR, Oxford, UK
Mail to: riccardo.bartolini@diamond.ac.uk

3.1.1 Introduction

The research on low emittance ring design has strongly revamped in the last few years involving a large community of accelerator physicists and projects, spanning HEP colliders, damping rings and light sources. Indeed the performance of these three types of ring is strongly influenced by the design emittance. The main quality factor for a collider, the luminosity L, is inversely proportional to the beam emittance. Likewise, the brilliance B of a light source is also inversely proportional to the beam emittance, at least far from the diffraction limit. Furthermore, damping rings are also required to generate low emittance beams for the downstream colliders.

In more detail, the luminosity of a collider is given by

$$L = \frac{n_b f_{rev} N_1 N_2}{4\pi\varepsilon_x k \beta^*} S \tag{1}$$

where n_b is the number of bunches in the train, f_{rev} is the revolution frequency, N_1 and N_2 the number of particles per bunch, ε_x the horizontal emittance, k the emittance coupling, β^* is the beta function at the interaction point and S is a geometric factor. In order to achieve ~10^{36} $cm^{-2}s^{-1}$ luminosity in upcoming B-factories low emittance ring designs have been adopted: 2 nm for SuperB High Energy Ring (HER) at 6.7 GeV [1] and 2.4 nm for superKEKB HER at 7 GeV [2].

The brilliance B of a light source, is given by

$$B = \frac{\Phi}{4\pi \Sigma_x \Sigma_{x'} \Sigma_y \Sigma_{y'}} \tag{2}$$

where Φ is the total flux and the Σs are quantities which depend on the quadratic convolution of the rms beam size and divergence and the natural photon rms beam size and divergence, assuming Gaussian electrons and photons beam. To reach diffraction limited operation of a light source, the electron beam emittance should satisfy the relation

$$\varepsilon_{x,y} < \frac{\lambda}{4\pi} \tag{3}$$

which implies an emittance of less than 10 pm in both plans for diffraction limited operation at λ = 1 Angstrom. Present day light sources operate with emittances of 1nm or larger, however, all new projects are targeting emittance well below 1 nm, aiming at reaching the diffraction limit at least in the soft X-rays. Damping rings for linear colliders also demand emittances below 1 nm, e.g. 500 pm horizontal and 2 pm in vertical emittance for ILC damping ring at 5 GeV [3] and 100 pm horizontal and 1 pm for the CLIC damping rings (2.4 GeV) [4].

The quest for low emittance ring design and the development of the associated technology has gathered the communities of light sources, colliders and damping rings in a series of very successful workshops LER2010 [5] in Geneva and LER2011 [6] in Crete, aimed specifically at sharing experience, information and techniques among such diverse communities. In this paper we review the present status with the development and low emittance rings, discuss the main design issues, solutions and the operational experience with the most advanced low emittance lattices presently in operation.

3.1.2 **Low Emittance Ring Design**

Low emittance lattices were initially developed for third generation light sources on the basis of Double Bend Achromat (DBA) and Triple Bend Achromat (TBA) designs. These lattices allowed sufficiently long straight sections to accommodate long insertion devices and, at the same time, they allowed reasonable dynamic aperture for injection and momentum aperture for a good Touschek lifetime.

The horizontal emittance of a lattice is given by the formula [7]

$$\varepsilon_{\mathrm{x}} = \mathrm{C_q}\frac{\gamma^2}{\mathrm{J_x}}\frac{\oint \mathrm{H(s)}/\rho^3(\mathrm{s})\mathrm{ds}}{\oint 1/\rho^2(\mathrm{s})\mathrm{ds}} \tag{4}$$

where $\mathrm{C_q} = 3.84\cdot 10^{-13}$ m, the integrals are taken along the ring circumference, $\mathrm{J_x}$ is the horizontal damping partition number, ρ is the reference orbit radius, H is the dispersion invariant

$$\mathrm{H} = \frac{1}{\beta_{\mathrm{x}}}\left[\mathrm{D}_{\mathrm{x}}^2 + (\alpha_{\mathrm{x}}\mathrm{D}_{\mathrm{x}} + \beta_{\mathrm{x}}\mathrm{D'}_{\mathrm{x}})^2\right] = \gamma_{\mathrm{x}}^2\mathrm{D}_{\mathrm{x}}^2 + 2\alpha_{\mathrm{x}}\mathrm{D}_{\mathrm{x}}\mathrm{D'}_{\mathrm{x}} + \beta_{\mathrm{x}}^2\mathrm{D'}_{\mathrm{x}}^2 \tag{5}$$

α_x, β_x and γ_x are the optics functions, D_x and D'_x are the horizontal dispersion and its derivative. Formula (4-5) provide the basic guidelines for designing a low emittance lattice, namely by reducing the dispersion invariant in the bending magnets and by increasing the damping partition number J_x. It can be proven that the minimum emittance for a given achromat lattice type scales as

$$\varepsilon_{\mathrm{x}} = \mathrm{C_q}\mathrm{F}\gamma^2\theta^3 \propto \frac{1}{\mathrm{N_d^3}} \tag{6}$$

where θ is the bending angle of the dipoles in the cell, F is a proportionality factor that depends on the details of the cell design and N_d is the number of bends per cell. Minimum theoretical values for F exists for various type of lattices

$$F_{ME-DBA} = \frac{4}{\sqrt{15}} \qquad F_{ME-TBA} = \frac{7}{9} F_{ME-DBA} \tag{7}$$

However, it is well know that such extreme designs pose tough challenges in the optimisation of the nonlinear beam dynamics, therefore a commonly adopted strategy is to back off from the minimum theoretical limits in order to gain a better control of dynamic and momentum apertures. Initially, many light sources opted for a modified DBA or TBA lattice where the achromatic condition was broken to allow a better control of the dispersion in the dipoles. This approach was eventually adopted as the baseline design in modern storage ring light sources such as Diamond and SOLEIL, which operate with distributed dispersion, achieving emittances of 2.7 nm at 3 GeV and 3.7 nm at 2.75 GeV respectively.

It was also noted that formula (6) clearly favours the lattice design with many dipoles in the unit cell and indeed the most challenging designs make use of so-called multiple bend achromat (MBA) lattices. MBAs were first proposed by Einfeld [8] for a diffraction limited synchrotron light source and later selected for the baseline design of MAX-IV by Eriksson and co-workers [9], based on a 7BA which delivers 330pm in the baseline design. Fig. 1 shows the optics function of MAX-IV unit cell.

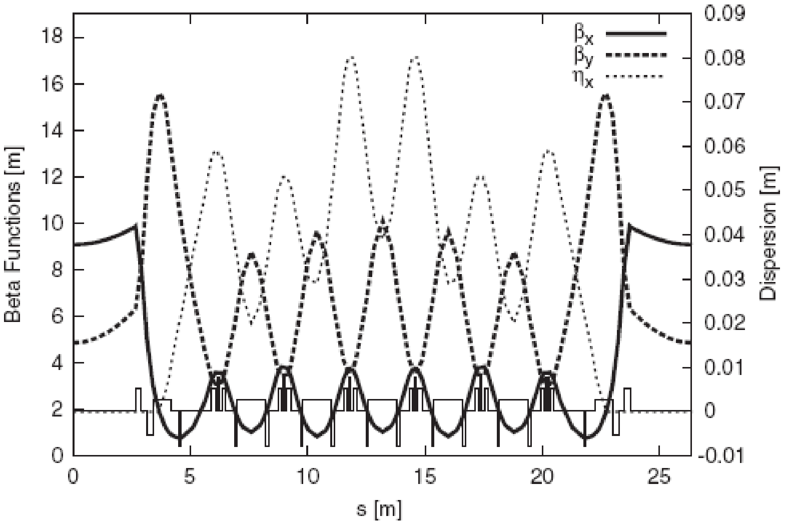

Figure 1: Optics functions for the MAX-IV 3 GeV ring 7BA unit cell [15]

Noticeable progress has been achieved also by the SPring-8 group which proposed the design of a low emittance ring, based on a 10BA [10] and later on a 6BA [11] for the SPring-8 upgrade. More recently, these efforts have been pointing toward the so called Ultimate Storage Ring (USR) [12], i.e. a storage ring which is diffraction limited in the hard X-rays. The most advanced designs have been proposed using the PEP-II tunnel in the PEP-X storage ring [13] which reached 30 pm in the baseline design and most recently using the a Tevatron-sized tunnel with the TeVUSR design that has produced a lattice with a baseline emittance of 3pm [14].

A rather different approach is followed in the design of low emittance damping rings where the low emittance is generally achieved by using strong damping wigglers rather than through fine tailoring the optics in the arcs [16]. These two approaches are now combined in the most aggressive design of low emittance rings, whereby further emittance reduction is achieved with damping wiggler added to low emittance lattice. In this way the design of MAX-IV reaches 220pm horizontal emittance. Including damping wigglers in the lattice design of PEP-X achieves 11 pm horizontal emittance [17] while the TeVUSR reduces the emittance to the present record of 1.6 pm [14].

Fig. 2 presents the emittance values in both planes of the main rings in operation and the upcoming projects. It is interesting to observe that several light sources have already proven experimentally the operation with very low vertical emittance 2pm and below.

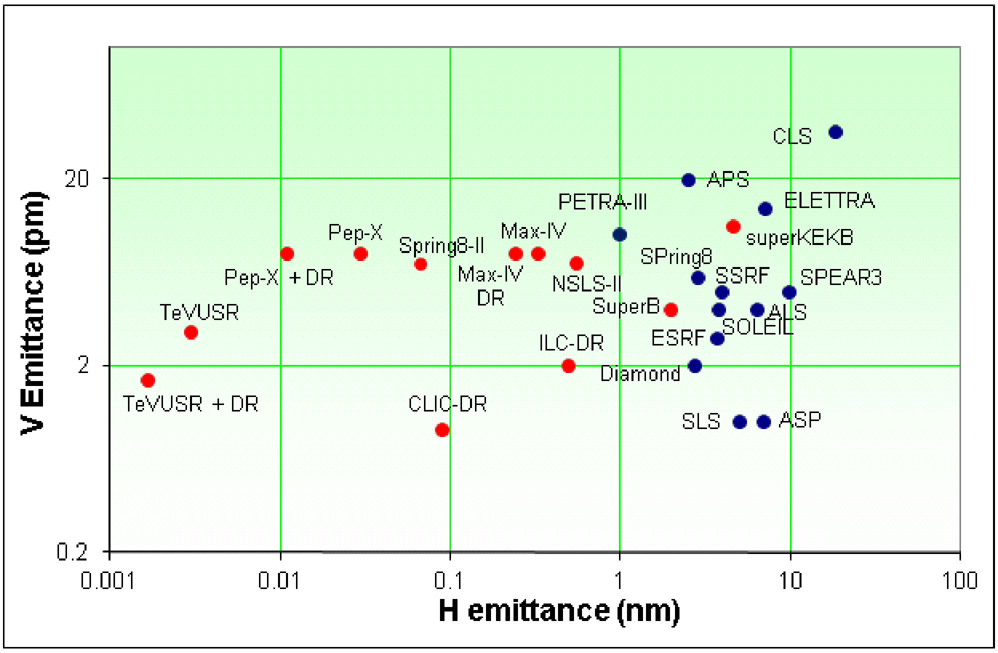

Figure 2: Horizontal and minimum achieved vertical emittances of the major low emittance rings: blue dots are the operational facilities and red dots are the upcoming projects.

It is worth mentioning that also existing rings are considering options for lowering further the emittance. In particular, the SOLEIL team has revitalised the idea of using Robinson Wigglers to control the damping partition number in (4) and hence reduce the emittance [18]. On a similar line the NSLS team has proposed the control of the damping partition number with orbit bumps in the achromats [19]. Both schemes can achieve a significant reduction of the horizontal emittance, up to a factor 2 for the Robinson wiggler and more for the orbit bumps scheme. However the benefits for a light source have to be gauged with the corresponding increase of the energy spread of such modified lattices.

3.1.3 Low Emittance Ring Optimisation

One of the main challenges in the design and optimisation of low emittance rings is related to the correction of the large natural chromaticity that the MBA lattices tend to generate. Usually the dispersion is small in the arcs and therefore strong chromatic sextupoles are needed to correct the chromaticity to zero or slightly positive values. The chromatic sextupoles generate higher order aberrations which limit the dynamic aperture available for injection and the momentum aperture, reducing the Touschek lifetime. Therefore additional sextupoles are used to compensate the detrimental effects of the chromatic sextupoles.

Usually, the correction of the nonlinearities is based on the analysis and correction of the nonlinear resonance driving terms excited in the ring [20]. Recently, however, significant progress has been made with the use of Multi-objective Genetic Algorithms (MOGA) in the optimisation of the beam dynamics. MOGA have been used to refine the linear lattice and to enlarge the dynamic aperture and momentum aperture directly from tracking. These approaches are computationally intensive and require good-size computer clusters, however they are able to efficiently explore a large portion of the machine parameters set, usually providing satisfactory solution. The typical problem consists in the definition of one or more objectives, e.g. the dynamic aperture and the momentum aperture, which need to be optimised as a function of a set of parameters, e.g. the sextupole families. Brute force tracking can be used to compute the apertures and in principle the search can include multipolar or random errors and misalignments, directly in the optimisation. Examples of successful use of this technique can be found in the optimisation of the NSLS-II and SPEAR-III dynamic aperture [21-22]. Fig. 3 shows the results of the simultaneously optimisation of dynamic aperture and Touschek lifetime directly from tracking in SPEAR-III, with MOGA.

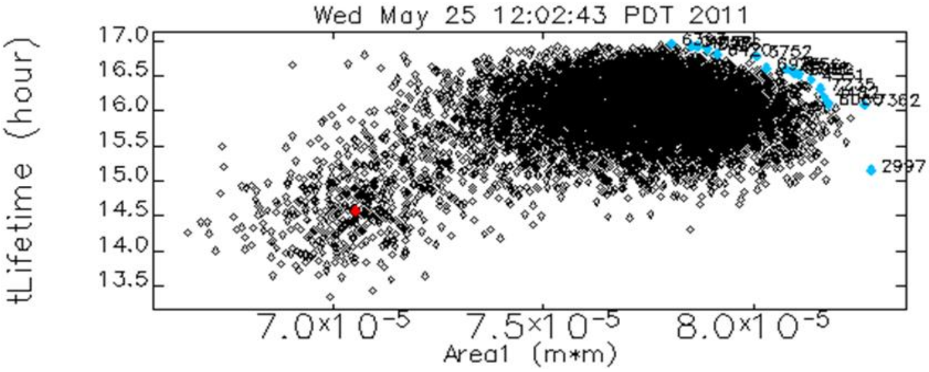

Figure 3: SPEAR-III Dynamic aperture and Touschek lifetime optimisation with MOGA. The blue dots correspond to the Pareto-Optimal front [22].

Traditional schemes based on the analysis of nonlinear resonance have also proven very successful in dealing with the optimisation of low emittance lattices. Resonance driving terms compensation was used in NLSL-II [23]; Frequency Map Analysis guided the optimisation of MAX-IV [24]. In this last case the benefit of weak octupoles in the dynamics optimisation were highlighted. The successful correction of nonlinear resonance driving term has been instrumental in achieving a good dynamic aperture in the design of PEP-X [25]. Fig. 4 shows the correction of a fourth order resonance ($2Q_x - 2Q_y$) which appeared to be a limiting factor for the dynamic aperture.

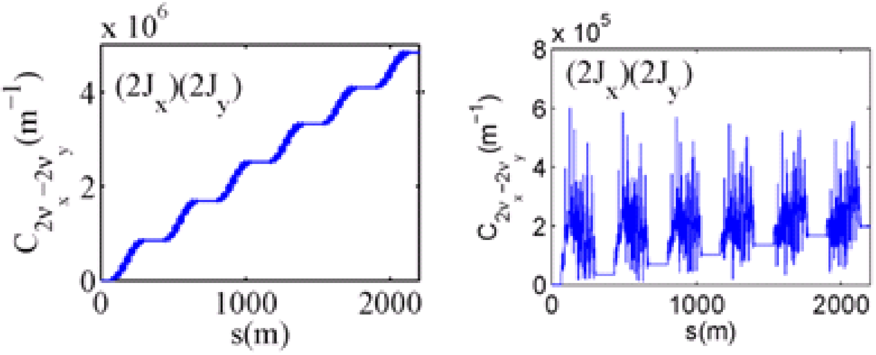

Figure 4: Control of fourth order resonances for PEP-X: left no harmonic sextupoles, (right) with harmonic sextupoles

Damping wigglers are used to reduce further emittance in light sources like NSLS-II and in all the USR type of design. The contribution of a wiggler to the synchrotron radiation integrals I_k is described by

$$I_k = I_{ka} + I_{kw} \tag{8}$$

and introducing the ratio

$$F_w = \frac{I_{2a}}{I_{2w}} \tag{9}$$

the ring emittance with wigglers can be written as [26]

$$\varepsilon_x = \varepsilon_{xa} \frac{J_{x0}}{J_{x0} + F_w} + \varepsilon_{xw} \frac{F_w}{J_{x0} + F_w} \tag{10}$$

where ε_{xa} and J_{x0} are the emittance and the damping partition number produced by the arcs in the absence of wigglers, respectively; ε_{xw} is the emittance generated by the wigglers in the limit of $F_w \to \infty$. The effect of damping wigglers on the emittance for the PEP-X design is reported in Fig. 5. Choosing a wiggler period λ_w = 5cm with a peak magnetic field B_w = 1.5T and a length of 89.7 m the ring emittance was reduced to 11 pm.

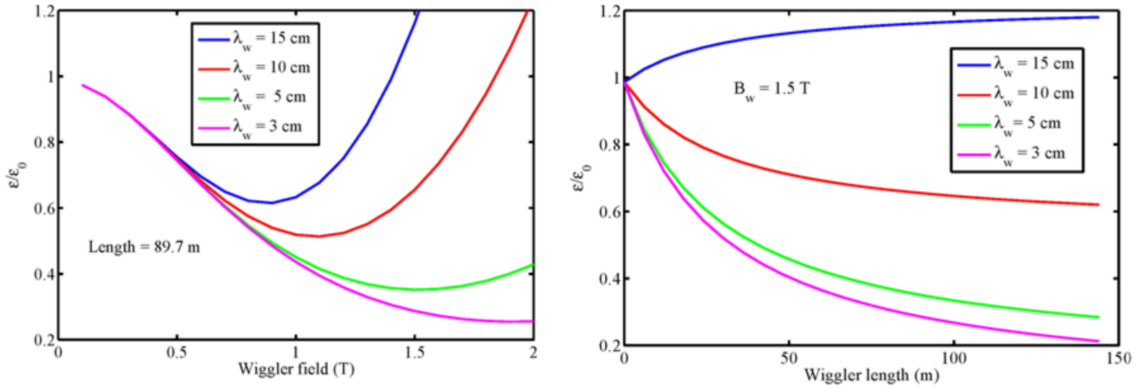

Figure 5: Emittance dependence for damping wiggler period λ_w and peak magnetic field B_w for PEP-X.

Finally, wigglers play a major role in damping ring design to the extent that significantly different arc designs turn out to be equivalently acceptable in terms of emittance and damping times. Both ILC and CLIC damping ring designs share a similar racetrack structure with long straight sections for damping wigglers as shown in Fig. 6.

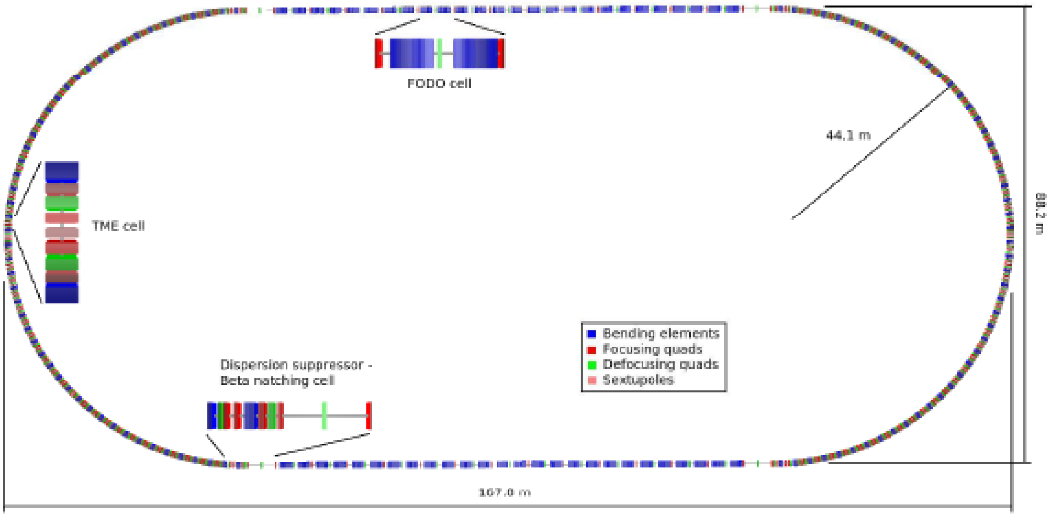

Figure 6: CLIC damping ring layout with racetrack structure and TME based arcs

The ILC team has evaluated different arc designs based on FODO, TME and SuperB-type of arcs [27]. The CLIC damping ring arcs are based on a modified TME cell [28]. Table 1 reports the main parameters of the ILC and CLIC damping ring design.

Table 1: ILC and CLIC damping ring main design parameters

	ILC-DCO4	**ILC-DTC01**	**CLIC**
Arc lattice	Modified FODO	TME-style	Modified TME
Energy	5	5	2.86
Circumference (m)	6476	3239	493
Horizontal Emittance (nm)	0.45	0.45	0.079
Damping time τ_x (ms)	21	24	2.4
Energy spread	0.13	0.11	0.1
Energy loss/turn U_0 (MeV)	10.2	4.5	3.9
$F_w = U_{arc}/U_{wiggler}$	10.7	4.6	6.9
Wiggler field (T)	1.6	1.5	2.5
Total wiggler length (m)	216	104	152

As for the light sources, the main issue remains the optimisation of the nonlinear beam dynamics. The tools for the optimisation are based on the analysis of arc cell phase advance, global tunes and by deploying sophisticated sextupole patterns. Nonlinear resonance driving terms, frequency maps and Genetic Algorithms are proficiently used and, in most advanced designs, the lattice optimisation is tied to the control of collective effects.

3.1.4 **Low Emittance Ring Operation**

A careful implementation of both the linear and the nonlinear optics of the machine is essential to guarantee the nominal performance of a low emittance ring. In recent years light sources have clearly lead the way, proving that low emittance rings can be successfully operated and reaching in many cases excellent agreement between the design and the actual performance of the low emittance rings.

3.1.4.1 ***Linear Optics***

A key technique for the correct implementation of the linear optics is given by the analysis of the orbit response matrix, in the so called LOCO programme [29]. LOCO uses the closed orbit response matrix to detect any deviation of the linear optics from the nominal model and provides a set of quadrupole corrections that restore the nominal optics functions. LOCO-type approaches were used in most of modern light sources with excellent results and in most cases, the residual β-beating is corrected to less than 1% peak to peak as shown in Table 2. Correspondingly, most light sources reported a very good agreement between the measured emittance and energy spread and the nominal values.

Alternative tools have been developed for the correction of the linear optics based on the excitation of betatron oscillations by means of pinger magnets or resonantly driven by stripline kickers. By acquiring turn-by-turn data at all BPMs in the ring, we can obtain information about the optics function of the ring. In fact the amplitude of the spectral line corresponding to the betatron frequencies is proportional to $(\beta_x)^{1/2}$ in the horizontal plane and $(\beta_y)^{1/2}$ in the vertical plane and can be used to monitor or correct the optics. Experimental studies at the SLS [30] have shown that LOCO and the frequency analysis of turn-by-turn provide very similar results and are both very effective in controlling the residual beta-beating. It is therefore expected that such techniques can be used successfully in the characterisation of a low emittance USR.

3.1.4.2 *Vertical Emittance Control*

The control and the minimization of the vertical emittance has been the subject of a strong research activity mainly among light sources in the last four years. This effort has benefited significantly from the development of advanced diagnostics for the measurement of such small electron beam vertical emittance. After the initial studies at ATF which achieved 4pm vertical emittance in 2004 [31], SLS reached 3.2 pm emittance in 2008 [32], Diamond 2.2 pm in 2009 [33] and APS reported 1 pm in 2010 [34]. These values are remarkably close to the quantum limit achievable for the vertical emittance in these machines (e.g 0.55 pm for Diamond). Presently the SLS has also reached 1 pm 2011 [35] while Diamond is moving towards offering reduced coupling at 0.3% (8 pm) for users' operation. It is worth mentioning also the remarkable effort undertaken by the ESRF which reached a minimum of 2.8 pm vertical emittance and has built a coupling feedback system which maintains the ultra low vertical emittance (down to 3-4pm) even in presence of ID movement [36-37]. A summary of the present status of coupling correcting at the major synchrotron light sources is reported in Table 2.

Such powerful coupling corrections have been achieved with different algorithms at different machines. The most widely used approach is based on the analysis of the off-diagonal block of the orbit response matrix (like LOCO [29] or similar) to provide skew quadrupole corrections. This has proven very successful at SLS, Diamond and ASP. ESRF adopted a technique based on the minimization of the resonant driving terms responsible for the excitation of the coupling resonances ($Q_x \pm Q_y$). In all cases additional control of the vertical dispersion is required and a complex analysis of the spurious coupling effect introduced by the Beam Position Monitors is required.

Alternative techniques for low emittance tuning were also recently proposed on the basis of dispersion and coupling free steering [38]. Such techniques make use of the orbit in the arcs to generate additional quadrupole and skew quadrupoles terms by feed-down due to the off-axis orbit in the arc sextupoles. Although these techniques are well suited to colliders and damping rings, their application to light sources appears difficult in so far it requires orbit adjustment which might conflict with beamline alignment. It was shown however that these algorithms generate a fast coupling correction which in the case of Diamond exceeded the performance of LOCO, generating a vertical emittance of 1.7 pm with a simultaneous good correction of the nominal optics.

At the same time advanced diagnostics have been developed to measure such low emittances: SLS used a system based on the measurement of the vertical polarisation of the emission of synchrotron radiation from a bending magnet. Diamond used a pinhole camera with an advanced estimation of the point spread function. Finally the ASP used an indirect emittance measurement based on the Touschek lifetime dependence with coupling.

Table 2: Summary of linear optics measurement at various light sources. The measured horizontal emittance agrees very well in all cases with the nominal emittance.

	Measured H emittance (nm)	β-beating (rms)	best coupling ($\varepsilon_y/\varepsilon_x$)	Vertical emittance (pm)
ALS	6.7	0.5 %	0.1%	4-7
APS	2.5	1 %	0.8%	20
ASP	10	1 %	0.01%	1-2
CLS	17-19	4.2%	0.2%	36
Diamond	2.7-2.8	0.4 %	0.07%	2.0
ELETTRA	7	2%	0.5%	5.6
ESRF	4	1%	0.07%	2.8
SLS	5.4-7	1%	0.02%	1.0
SOLEIL	3.70-3.75	0.3 %	0.1%	4
SPEAR3	9.8	< 1%	0.05%	5
SPring8	3.2-3.6	1.5%	0.2%	6.4
SSRF	3.8-4.0	<1%	0.13%	5 pm

3.1.4.1 *Nonlinear Optics*

Once the linear optics is corrected and understood, the ultimate performance of a low emittance lattice still requires a careful understanding of the nonlinear dynamics. Several light sources made extensive campaigns of measurements to understand and correct the nonlinear beam dynamics. The most promising of these investigations are based on the analysis of the turn-by-turn data of excited betatron oscillations to extract Frequency Maps and resonant driving terms. These measurements can be compared with the same information obtained from tracking data in the computer model of the storage ring and thus provide a method to compare the nonlinear beam dynamics on the real accelerator with the model. The discrepancies can be corrected by fitting algorithms which use the sextupole gradients as fit parameters. In this way the nonlinear machine model can be correctly implemented in the real accelerator. Fig. 7 reports the excellent agreement achieved at SOLEIL in the modelisation of the Frequency Map for off momentum deviation up to ±4% [39] showing a very good understanding of the nonlinear optics. Similar results were obtained at the Diamond Light Source [40].

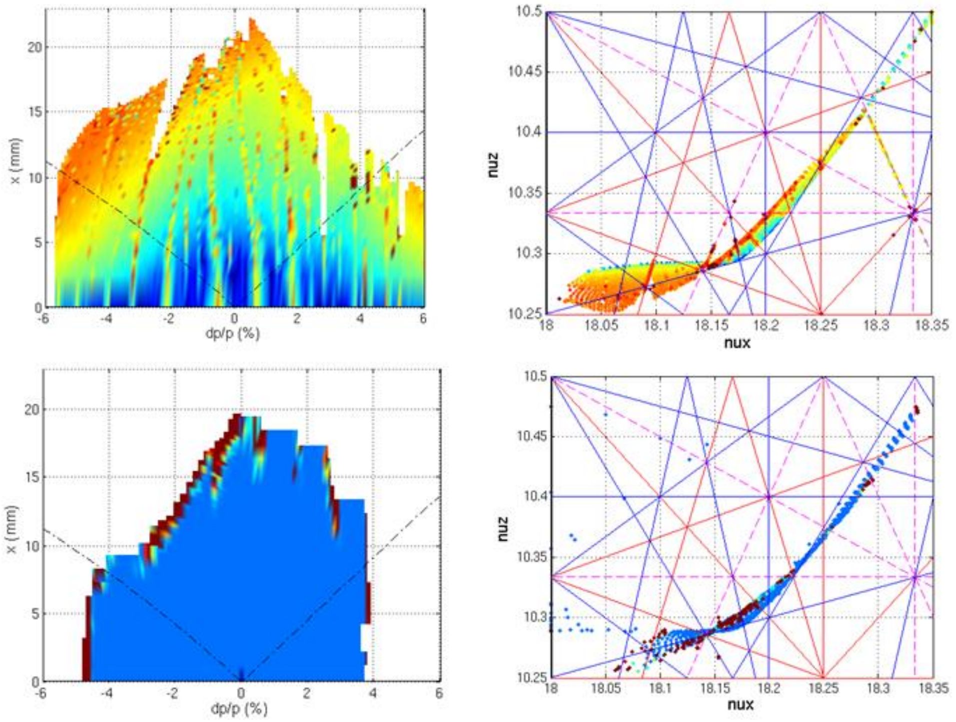

Figure 7: Comparison of dynamic aperture and frequency maps in the (x, dp/p) planes. Simulation (top graphs) measurements (bottom graphs).

3.1.5 Conclusion

We have presented an overview of the research activity on low emittance rings describing the main theoretical and experimental approaches. Other aspects related to the analysis of collective effects and to the required technological developments will be covered in other papers in this newsletter. It is worth however to observe that the progress with low emittance lattice design and operation in the last year has been remarkable. Although some technological development deserves further investment, especially in the impedance design of a USR or the injection schemes required to inject the beam in a small dynamic aperture, none of them appear to pose major difficulties in the construction of an ultimate storage ring, a collider or damping ring with very low emittance.

3.1.6 References

1. SuperB Progress Report: The Collider, http://arxiv.org/abs/1009.6178v3, (2010).
2. S. Masuzawa, Next Generation B factories, Proceedings of the IPAC10, 4764, (2010).
3. International Linear Collider Reference Design Report, August 2007, ILC-REPORT-2007-001.
4. Y. Papaphilippou et al., Design optimisation of the CLIC Damping Rings, Proceedings of the IPAC 10, 3554, (2010).
5. LER2010 Workshop, http://ler2010.web.cern.ch/ler2010/
6. LER2011 Workshop, http://lowering2011.web.cern.ch/lowering2011/
7. M. Sands, The Physics of Electron Storage Rings, SLAC R-121, (1971).
8. D. Einfeld et al., Design of a diffraction limited light source, Proceedings of the PAC1995, 177, (1996).

9. H. Tarawneh et al., MAX-IV lattice, dynamics properties and magnet system, Nucl. Inst. and Math, **A508**, 480, (2003).
10. K. Tsumaki et al., Very low emittance light source storage ring, Nucl. Inst. and Math, **A565**, 394, (2006).
11. Y. Shimosaki et al., Lattice design for a very low emittance storage ring for Spring-8-II, Proceedings of the IPAC11, 942, (2011).
12. M. Bei et al., The Potential of an Ultimate Storage Ring for Future Light Sources, Nucl. Inst and Meth. **A622**, 518, (2009).
13. R. Hettel et al., Ideas for a future Pep-X bright source, Proceedings of the EPAC08, 2031, (2008).
14. M. Borland, slides presented at the Future Light Source Workshop, Jefferson Labs, March 2012.
15. S. Leemann et al., Beam dynamics and expected performance of Sweden's new storage ring light sources: MAX-IV, PRSTAB **12**, 120701, (2009)
16. S. Guiducci, Damping rings towards ultra low emitances, Proceedings of the EPAC06, 1857, (2006).
17. Y. Nosockhov et al., Lattice Design for Pep-X Ultimate Storage ring, Proceedings of the IPAC11, 3068, (2011).
18. L. Nadolski, slides presented at the Low Emittance Ring Worksop 2011, Crete, (2011)
19. W. Guo, slides presented at the Low Emittance Ring Worksop 2011, Crete, (2011)
20. G. Guignard, A general treatment of resonances in accelerators, CERN 78-11, (1978).
21. L. Yang, Multiobjective Optimisation of Dynamic Aperture, PRSTAB, **14**, 054001, (2011).
22. J. Safranek, slides presented at the Future Light Source Workshop, Jefferson Labs, March 2012.
23. J. Bengtsson, NLSL-II: control of Dynamic Aperture, BNL-81770-2008-IR, (2008)
24. S. Leemann et al., Perspectives for future light source incorporating yet uncommon magnets, PRSTAB **14**, 030701, (2010)
25. Y. Cai, Single Particle Dynamics in Electron Storage Rings with Extremely Low Emittance, Nucl. Inst. and Meth. A645, 168, (2011).
26. P. Emma et al., Systematic Approach to Damping Ring Design, PRSTAB **4**, 021001, (2001).
27. S. Guiducci et al., Update to the ILC damping ring baseline design, Proceedings of the IPAC 11, (2011).
28. Y. Papaphilippou et al., Design Optimisation of the CLIC Damping Ring, Proceedings of the IPAC10, 3554, (2010).
29. J. Safranek, "Experimental determination of storage ring optics using orbit response measurements", Nucl. Instrum. Methods Phys. Res. A **388**, 27 (1997)
30. M. Aiba et al., Comparison of Linear Optics correction Means at SLS, Proceedings of the IPAC11, 3032, (2011).
31. Y. Honda et al., Achievement of ultra low emittance beam in the Accelerator Test Facility damping ring, Phys. Rev. Lett. **92**, 054802, (2004).
32. A. Andersson et al., Determination of a small vertical electron beam profile and emittance at the Swiss Light Source, Nucl. Inst. and Meth. **A591**, 437, (2008).
33. C. Thomas et al., Xray pinhole camera and emittance measurements, PRSTAB, **13**, 022805, (2010).
34. R. Dowd et al., Achievement of ultra low emittance coupling in the Australian Synchrotron storage ring, PRSTAB **14**, 012804, (2011).
35. L. Rivkin, private communication.
36. A. Franchi et al., Vertical emittance reduction and preservation in electron storage rings via resonant driving terms correction, PRSTAB **14**, 034002, (2011).
37. A. Franchi, slides presented at the Future Light Source Workshop 2012, Jefferson Laboratory, USA, (2012).

38. S. Liuzzo et al. Test of Low emittance tuning at Diamond, Proceedings of the IPAC11, 2031, (2011).
39. L. Nadolski, Methods and tools to simulate and analyse nonlinear beam dynamics in electron storage rings, slides presented at the IPAC11, (2011).
40. R. Bartolini et al., Calibration of the nonlinear ring model at the Diamond Light Source, PRSTAB 14, 054003, (2011).

3.2 The MAX IV 3 GeV Storage Ring

Simon C. Leemann
MAX-lab, Lund University, SE-22100 Lund, Sweden
Mail to: simon.leemann@maxlab.lu.se

3.2.1 Introduction

The MAX IV facility [1], which is presently under construction in southern Sweden, will become fully operational in 2015. Once complete, it will provide users with synchrotron radiation covering a spectral range from infrared to hard X-rays and time structures from ~ 30 fs to ~ 200 ns. In addition to spontaneous radiation, spatially and temporally coherent radiation will eventually also be produced. Early on in the design process, it was established that not all of the user requirements of an advanced synchrotron radiation source can be equally fulfilled by a single machine. Instead, a global optimization of the facility based on the wide range of user demands was performed, resulting in a solution using two separate storage rings (3 GeV and 1.5 GeV) [2-4] and a linac-driven short-pulse facility (SPF) [5,6] which will be upgraded to a FEL in a second phase. This 3.5 GeV linac also serves as a full-energy injector to both storage rings therefore enabling top-up operation at a constant 500 mA in both rings.

The 1.5 GeV storage ring is a fairly conventional DBA design with 96 m circumference, 10 user straights, and 6 nm rad equilibrium emittance. It is essentially an upgraded version of the existing MAX II storage ring using the fully integrated magnet design demonstrated in MAX III. This ring will replace the old MAX II and MAX III storage rings as the source for IR and UV radiation at MAX-lab and a few present-day beamlines will move to this new storage ring. This ring will be built twice: once in Lund for the MAX IV facility and once in Krakow, Poland for the Solaris Project [7].

The 3 GeV storage ring on the other hand, is a entirely novel design based on a 20-fold multibend achromat lattice offering 19 user straights with an equilibrium emittance below 300 pm rad. Moderate coupling will ensure vertical beam sizes in the insertion devices (ID's) below the 1 Å diffraction limit. With a constant stored current of 500 mA, the MAX IV 3 GeV storage ring is expected to become the brightest storage ring-based light source worldwide when it goes into operation in 2015. Not only does this storage ring deliver unprecedented ultralow emittance, it makes use of several less conventional technologies. The rest of this article will focus on the design and expected performance of this storage ring.

3.2.2 Lattice and Optics

The 3 GeV storage ring will serve as the main radiation source of the MAX IV facility. In order to generate high-brightness hard X-rays with state-of-the-art ID's an ultralow-emittance design was targeted [8,9]. One simple and robust method to achieve ultralow emittance is the use of a multibend achromat (MBA) lattice [10-12]. The MBA exploits the inverse cubic dependence of emittance on the number of bending magnets. By choosing a very small bending angle per dipole and introducing a vertically focusing gradient in the dipoles (the emittance scales inversely with the horizontal damping partition J_x), the emittance can be dramatically reduced while the dispersion is limited to small values. This in turn allows the use of narrow vacuum chambers and compact magnets with strong gradients. Finally, by adding properly balanced sextupoles and octupoles, the nonlinear optics can be tuned for large momentum acceptance and dynamic aperture rendering long Touschek lifetime and high injection efficiency despite the very low emittance [13].

3.2.2.1 *Linear Optics*

The MAX IV 3 GeV storage ring consists of twenty 7-bend achromats separated by 4.6 m long straight sections for ID's. An overview of one MAX IV achromat is shown in Fig.1. Each of the achromats consists of 5 unit cells and 2 matching cells. The unit cells have a 3° bending magnet, while the matching cells at the ends of the achromat have a 1.5° soft-end bending magnet. In these soft-end dipoles, the magnetic field drop-off towards the long straight reduces the amount of radiation hitting a downstream ID therefore facilitating the design of superconducting IDs. All dipoles contain a vertically focusing gradient. The matching cells contain dedicated quadrupole doublets in order to match the achromat optics to the ID in the long straight. Each achromat also contains two 1.3 m short straights that separate the matching cells from the unit cells. These short straights can be used for RF cavities and diagnostics so that all long straights but the injection straight are available for installation of IDs.

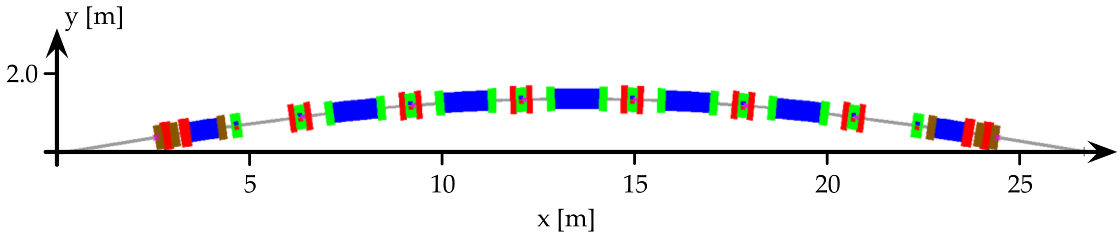

Figure 1: Schematic of one of the 20 achromats of the MAX IV 3 GeV storage ring. Magnets indicated are gradient dipoles (blue), focusing quadrupoles (red), sextupoles (green), and octupoles (brown).

Since the vertical focusing is performed by the gradient dipoles, dedicated quadrupoles are, apart from ID matching, only required for horizontal focusing. Horizontally focusing quadrupoles are installed between the cells of the achromat in pairs of two where the two quadrupoles are installed on either side of a sextupole magnet. There are two families of focusing quadrupoles, one in the unit cells and one in the matching cells. Adjustment of the vertical focusing is performed by exciting a current in the pole-face strips (PFS's) that are installed in all dipoles. This results in a very compact optics with strong focusing, low beta functions, and very small peak dispersion. The optics for one achromat are displayed in Fig.2 and ring parameters are given in Table 1.

The working point was chosen away from systematic resonances and so that both fractional tunes are just above the integer and away from the most dangerous resonances. With the working point held constant during operation, the nonlinear optics can be set to minimize the chromatic and amplitude-dependent tune shifts therefore keeping the tunes of most stored beam particles clear of dangerous resonances. This shall be explained in the next section.

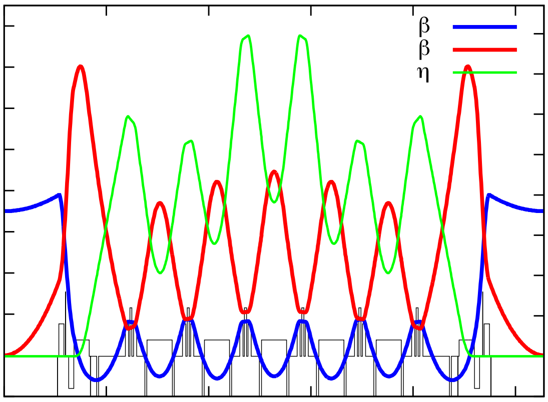

Figure 2: Beta functions and dispersion for one achromat of the MAX IV 3 GeV storage ring. Magnet positions are indicated at the bottom.

Table 1: Parameters for the MAX IV 3 GeV storage ring.

Parameter	***Unit***	***Value***
Energy	GeV	3.0
Main radio frequency	MHz	99.931
Circulating current	mA	500
Circumference	m	528
Number of achromats	…	20
Number of long straights available for IDs	…	19
Betatron tunes (H/V)	…	42.20 / 16.28
Natural chromaticities (H/V)	…	-50.0 / -50.2
Corrected chromaticities (H/V)	…	+1.0 / +1.0
Momentum compaction factor	…	3.07×10^{-4}
Horizontal damping partition	…	1.85
Horizontal emittance (bare lattice)	nm·rad	0.326
Radiation losses per turn (bare lattice)	keV	360.0
Natural energy spread	…	0.077%
Required momentum acceptance	…	4.5%

3.2.2.2 *Nonlinear Optics*

Despite comparably relaxed linear optics, the nonlinear optics of such a MBA lattice are demanding. The strong focusing gives rise to large negative natural chromaticities that need to be corrected to prevent head-tail instability. This can be performed with chromatic sextupoles. Because of the low dispersion in the MBA these sextupoles tend to become very strong. Although this is not a concern for the magnet design (the 25 mm nominal magnet bore allows strong gradients), it presents an optics design challenge as such strong sextupoles give rise to pronounced nonlinear, amplitude-dependent behavior, which can limit both dynamic aperture and momentum acceptance. The most common approach is to install several additional families of sextupoles separated by appropriate phase advances in an attempt to cancel resonance driving terms and limit chromatic tune shifts [14].

The MAX IV 3 GeV storage ring contains five sextupole families, three focusing and two defocusing. The focusing sextupoles are installed between the focusing quadrupoles in the unit cells. This puts these sextupoles at locations with comparably large horizontal beta function and dispersion. The defocusing sextupoles are installed as close as possible to the maximum of the product of dispersion and vertical beta: unit cell dipoles are flanked on either side by a defocusing sextupole of one family while the defocusing sextupoles in the matching cells are installed in the short straights right next to the matching cell soft-end dipole. In this way, sextupoles compensate chromaticity where it's created thus limiting chromatic beta beating. Because of the large number of installed sextupoles and the small magnet gap, the sextupoles can be kept short.

Sextupole optimization was performed with the codes OPA [15] and Tracy-3 [16]. The linear chromaticities were corrected to +1.0 in both planes and the first-order resonance driving terms along with second and third-order chromaticity were minimized as detailed in [14]. However, amplitude-dependent tune shifts (ADTS's) are only corrected as a second-order effect in sextupoles therefore requiring a lot of sextupole gradient strength and in turn driving resonances and chromatic tune shifts. This can necessitate extra sextupoles and/or increased sextupole gradients in order to keep first-order terms in check. Apart from leading to a potential run-away problem, this is a delicate balance that is easily disturbed by ID's, alignment errors, and higher-order multipoles — all of which exist in a real machine. In an attempt to solve this fundamental challenge of nonlinear optimization in a MBA lattice, three achromatic octupole families were introduced into the matching cells of the 3 GeV achromat in locations with appropriate beta function ratios [2,13]. These octupoles correct the three terms for ADTS *to first order*. Analogous to the linear system, which is solved to find sextupole strengths that give a certain chromaticity, a linear system can be set up to describe the ADTS's that result from an octupole in the lattice. This system can be inverted to calculate octupole strengths that give the desired ADTS's. Rather than setting the linear ADTS to zero, the octupoles in the MAX IV MBA were adjusted so the resulting overall ADTS is minimized throughout the physical acceptance (cf. Fig.3).

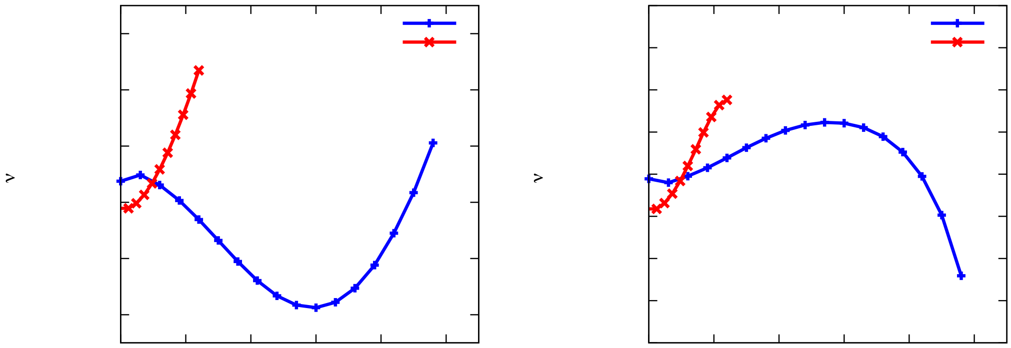

Figure 3: Amplitude-dependent tune shift in the MAX IV 3 GeV storage ring with octupoles at design strength.

Because the ADTS is corrected with the octupoles, the sextupoles are freed up for first-order corrections (linear chromaticity, resonance driving terms). Some extra weight was added to minimize second and third-order chromaticity in an attempt to limit the chromatic tune footprint (cf. Fig.4).

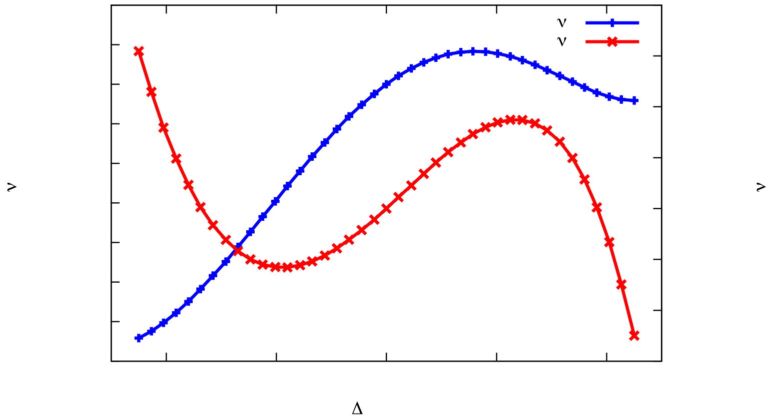

Figure 4: Chromaticity in the MAX IV 3 GeV storage ring with octupoles at design strength.

The result of this nonlinear optimization is a very limited tune footprint for particles with a range of amplitudes covering the physically accessible aperture (roughly 9 mm / 2 mm [H/V] at the center of the ID's) and energies covering the required ±4.5% acceptance. This results in large dynamic aperture and momentum acceptance (cf. Fig.5 and Section 3.2.3.3), which ensure high injection efficiency and good Touschek lifetime. Frequency map analysis confirmed the "wrap-up" of tune shifts around the working point which results in this compact tune footprint. This holds also for a realistic machine, i.e. a storage ring with errors, misalignments, and IDs. This shall be discussed in the next section.

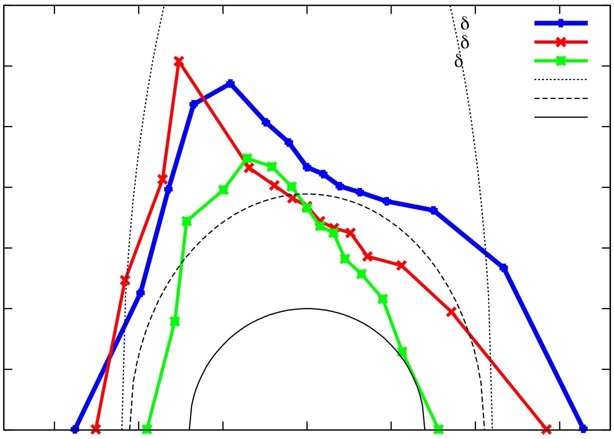

Figure 5: Dynamic aperture at the center of the long straight section in the MAX IV 3 GeV storage ring (bare lattice). Tracking was performed with Tracy-3 in 6D for half a synchrotron period. For comparison, the vacuum chamber and physical aperture (projection of vacuum chamber to the track point) are also indicated in the plot.

3.2.2.3 *Matching and Correction*

With the quadrupole doublets in the matching cells the beta functions in the long straights can be tuned over a fairly wide range. This allows matching of the linear optics to the ID. The ID matching is performed both locally (beta functions are matched to prevent beta beats) and globally (phase advances are corrected to restore the design working point). For the global correction the PFS's in the dipoles are used to adjust the vertical focusing. Because this matching results in restoring the design linear optics within the achromat, the nonlinear optics optimization is left almost undisturbed. If the multipolar content of the IDs is limited to specified values [17], neither sextupoles nor octupoles have to be adjusted with ID gap movement. Tracking studies (with Tracy-3 using kick maps) reveal that, in the storage ring equipped with many strong in-vacuum undulators, the dynamic aperture is not substantially reduced if the ID matching is properly performed.

All octupoles and sextupoles are equipped with extra windings that can be powered in different ways. This allows adding dispersive and non-dispersive skew quadrupoles for coupling control and removal of spurious vertical dispersion as well as auxiliary sextupoles in order to restore the design symmetry of the nonlinear optics [14]. These windings can also be powered as upright quadrupoles, which will be used to calibrate BPMs to the magnetic centers of the adjacent sextupoles.

Finally, each achromat also contains 10 horizontal and 9 vertical dipole correctors as well as 10 BPMs that will be included in a slow orbit feedback. Because of the vertical beam size in the user straights reaching values as low as 2 μm rms, beam stability is crucial. There are 4 dedicated fast correctors installed around each user straight which, together with the BPM system, will allow operation of a fast orbit feedback in order to cancel beam motion effectively up to roughly 100 Hz [18]. Tracking studies have revealed that adequate dynamic aperture remains when expected misalignments are added to the lattice and the orbit is corrected using the dipole correctors [20]. This also holds if multipole errors are added to all magnets.

3.2.3 Technology

The MBA gives a very low emittance, but it requires strong magnets and compact optics, which leave little space for a conventional vacuum. Therefore, several less conventional technology choices have been made for the MAX IV 3 GeV storage ring. These shall be presented briefly in this section.

3.2.3.1 *Magnets*

The magnets for the 3 GeV storage ring are designed using a technology already successfully demonstrated at MAX III [20]. The dipoles and quadrupoles for each cell are machined out of just two solid blocks of iron. The sextupoles, octupoles, and dipole correctors are installed into precision-machined grooves in these blocks. Each achromat cell is then built up of a lower and upper block that are brought together around the vacuum chamber. Figure 6 shows this magnet design using the matching cell as an example. This magnet technology integrates girder and magnet design, which results in reduced cost and higher alignment accuracy. Furthermore, misalignments of magnets tend to be correlated and can be minimized using beam-based realignment of the blocks as demonstrated at MAX III. The blocks are installed on massive concrete supports at low height, which pushes vibrational eigenfrequencies of the assembly beyond 100 Hz thus improving beam stability.

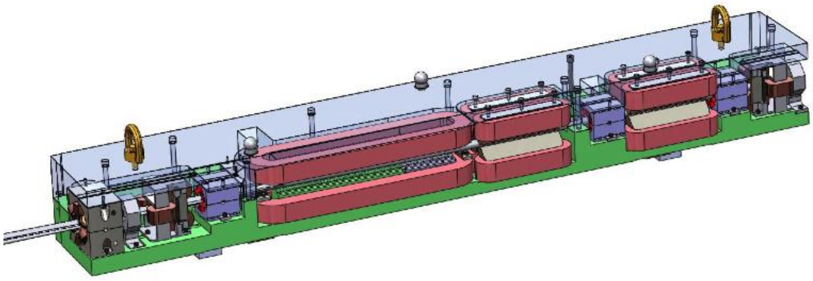

Figure 6: Drawing of a matching cell magnet block with soft-end gradient dipole, quadrupole doublet, defocusing sextupole (far left), three octupoles (blue), and two dipole corrector pairs.

3.2.3.2 *Vacuum System*

The small magnets of the MAX IV 3 GeV storage ring require a narrow vacuum chamber. Such systems are often plagued by poor vacuum conductance. In addition, because of the very compact optics of the storage ring, there is no space for lumped absorbers or distributed pumping. Instead, the 3 GeV storage ring makes use of a 22/24 mm (ID/OD) circular copper tube which is uniformly NEG-coated around the entire machine (as demonstrated [21] in two sectors of MAX II) [22]. Lumped absorbers can be avoided as synchrotron radiation is distributed along long sections of the chamber. A cooling channel is brazed to the outside of the vacuum chamber. The magnet block design foresees simple removal of the chamber for activation bake-outs in the tunnel. Few small discrete pumps will be installed in straight sections. Narrow-gap chambers and in-vacuum IDs (5 mm full vertical aperture) are foreseen in user straights. Short tapers make the transition from the circular standard vacuum chamber to the ID chambers. Bellows and valves are RF-shielded. Bellows and BPM bodies (which are rigidly fastened to the magnet blocks) are manufactured from stainless steel. These bellows are also used for mounting of the fast orbit correctors, as the copper chamber is unsuited because of strong Eddy currents.

3.2.3.3 *RF System*

Since users are provided with short pulses from the dedicated MAX IV short-pulse facility, the MAX IV storage rings can be operated with long bunches. Without increasing the chromaticity to large values (possibly limiting the energy acceptance), this alleviates instability issues that often arise when using narrow vacuum chambers. The MAX IV storage rings will therefore use a warm 100 MHz main RF system and Landau cavities at the third harmonic for additional bunch lengthening [23]. The six main cavities are an improved version of the present-day MAX II and III cavities. They are of capacity-loaded type and are HOM-damped. RF power is delivered by six stations with two 60 kW tetrode amplifiers each. This is considered a modular and cost-effective approach. The main cavities offer a maximum total gap voltage of 1.8 MV, which corresponds to an RF acceptance of between 4.5% and 7% depending on number and type of operated IDs. Figure 7 shows the RF and lattice acceptances in the achromat. The lattice momentum acceptance exceeds the RF acceptance except when a bare lattice is combined with maximum cavity voltage.

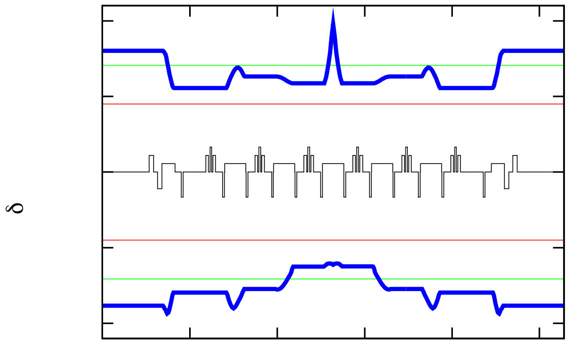

Figure 7: Momentum acceptance for one achromat of the MAX IV 3 GeV storage ring. A bare lattice and cavities at maximum voltage 1.8 MV have been assumed (green line, corresponds to 7% MA). For comparison, the red line shows 1.02 MV which corresponds to 4.5% MA in this configuration. The blue line shows overall MA, calculated from tracking with Tracy-3 for half a synchrotron period.

The Landau cavities are a new in-house development based on the main cavities' capacity-loaded design. Three warm and passive Landau cavities deliver roughly 500 kV gap voltage, which is expected to stretch bunches by a factor 5-6. Not only do these long bunches increase Touschek lifetime (cf. Section 3.2.4.2) and reduce IBS-related emittance growth (cf. Section 3.2.4.1), they also make the ring more tolerant against coupled-bunch instabilities.

3.2.3.4 *Injection*

Injection via a vertical transfer line from the linac is performed with a DC Lambertson septum in the storage ring. Originally it was foreseen to use a closed four-kicker injection bump, but subsequent studies have shown that injection with very high efficiency can be performed with a single pulsed multipole magnet [24]. Only a single dipole kicker remains in the storage ring to provide a simple and robust injection during early commissioning and later, for use as a horizontal pinger magnet. Pulsed multipole injection not only facilitates alignment and synchronization, it also reduces residual perturbations of the stored beam during injection. It is therefore an ideal injection method for top-up injection into an ultralow-emittance storage ring with very tight beam stability tolerance.

3.2.4 **Expected Performance**

3.2.4.1 *Emittance and Intrabeam Scattering*

The ultralow emittance of the 3 GeV storage ring depends on the number and type of installed ID's and is limited by intrabeam scattering (IBS). The bare lattice has an equilibrium emittance of 326 pm rad, but at the shortest bunch length (i.e. at maximum cavity voltage and without Landau cavities) of 9 mm, IBS blows up the emittance by 46% (calculated with ZAP and Tracy-3). Once the Landau cavities are tuned in and the bunches lengthened to 54 mm, the IBS blow-up results in an emittance of 370 pm rad, i.e. 13% above the lattice emittance [19]. For a moderately ID-equipped ring with cavities running at maximum voltage (giving an RF acceptance of 6%), the emittance including the effect of IBS and Landau cavities is expected to lie at about 270 pm rad. This figure can be lowered further by reducing the RF cavity voltage. The IBS calculations are performed assuming an even filling to 500 mA (5 nC / bunch) as well as coupling adjusted for a vertical emittance of 8 pm rad corresponding to the 1 Å diffraction limit. Since this is a very generous coupling and skew quadrupoles are available for coupling adjustment, the vertical emittance can be reduced to around 2 pm rad if required by users. Damping wigglers were also considered in order to reduce the emittance even further and to increase the energy spread, thus mitigating emittance blow-up from IBS.

3.2.4.2 *Lifetime*

Gas scattering lifetimes in the 3 GeV ring including in-vacuum IDs have been estimated at roughly 25 hours (elastic) and 56 hours (inelastic) where the latter has been calculated assuming a momentum acceptance of only 4.5%. The Touschek lifetime of the moderately ID-equipped ring at 270 pm rad is 21 hours at natural bunch length and 114 hours with Landau cavities tuned in (6D tracking in Tracy-3) [19]. If the vertical emittance is reduced to 2 pm rad (0.7% coupling), the Touschek lifetime with Landau cavities is still above 50 hours. This results in a total lifetime of about 13 hours, which equates to one top-up injection every four minutes (0.5% top-up deadband).

Despite the ultralow emittance of the MAX IV 3 GeV storage ring, the lifetime is very good. This is the result of large momentum acceptance achieved with the nonlinear optics optimization, but also of a peculiarity of Touschek lifetime at ultralow emittance. At ultralow emittance, there are only few particles in the bunch with sufficient transverse momentum to generate Touschek losses; most of the scattering events are

IBS, which blows up the emittance, but does not lead to particle loss from the RF bucket. A nice example for this behavior is the observation that, as ID's are added to the 3 GeV storage ring, the emittance (including IBS) decreases, but Touschek lifetime actually improves. Studies have indicated that the change of Touschek lifetime behavior with emittance occurs around 0.7 nm rad for the MAX IV 3 GeV lattice [2]. Since all operation conditions foresee emittances below this value, an emittance reduction should always lead to a Touschek lifetime improvement in the 3 GeV ring. The consequence is that having as many strong ID's (and possibly damping wigglers) in the storage ring not only leads to lowest emittance, but also to best lifetime.

3.2.4.3 *Insertion Device Radiation*

To conclude this article, a performance outlook shall be given for the synchrotron radiation generated by a typical ID in the MAX IV 3 GeV storage ring. Figure 8 shows spectral brightness as calculated by SPECTRA [25] for a 3.3 m in-vacuum undulator of hybrid type (18 mm period, 4 mm gap, B_{eff} = 1.15 T) installed in the storage ring where the vertical emittance has been set to 8 pm rad [2 pm rad]. After matching the achromat optics to this ID, the rms beam size at the ID center is 49 μm / 4 μm [2 μm] (H/V).

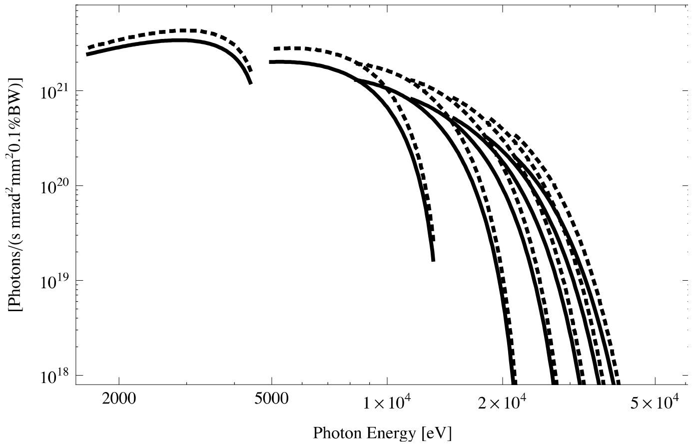

Figure 8: Spectral brightness at peak energy of a typical in-vacuum undulator installed in the MAX IV 3 GeV storage ring with 500 mA stored current and vertical emittance set to 8 pm rad (solid line) and 2 pm rad (dashed line) [26].

3.2.5 **References**

1. The MAX IV Detailed Design Report, http://www.maxlab.lu.se/maxlab/max4/DDR_public
2. S.C. Leemann et al., "Beam dynamics and expected performance of Sweden's new storage-ring light source: MAX IV", Phys. Rev. ST Accel. Beams **12**, 120701 (2009).
3. S.C. Leemann et al., "Status of the MAX IV Storage Rings", Proceedings of IPAC'10, Kyoto, Japan, p.2618.
4. S.C. Leemann, "Recent Improvements to the Lattices for the MAX IV Storage Rings", Proceedings of IPAC'11, San Sebastián, Spain, p.3029.
5. S. Werin et al., "Short pulse facility for MAX-lab", Nucl. Instr. and Meth. A **601**, 98 (2009).
6. S. Thorin et al., "Design of the MAX IV Ring Injector and SPF/FEL Driver", Proceedings of PAC'11, New York, USA, p.2447.
7. C.J. Bocchetta et al., "Project Status of the Polish Synchrotron Radiation Facility

Solaris", Proceedings of IPAC'11, San Sebastián, Spain, p.3014.
8. H. Tarawneh, et al., "MAX-IV lattice, dynamic properties and magnet system", Nucl. Instr. and Meth. A **508** (2003) 480.
9. M. Eriksson, et al., "Some small-emittance light-source lattices with multi-bend achromats", Nucl. Instr. and Meth. A **587** (2008) 221.
10. W. Joho, et al., "Design of a Swiss Light Source (SLS)", Proceedings of EPAC 1994, London, England, p.627.
11. D. Einfeld, J. Schaper, M. Plesko, "Design of a Diffraction Limited Light Source (DIFL)", Proceedings of PAC 1995, Dallas TX, USA, p.177.
12. D. Kaltchev, et al., "Lattice Studies for a High-brightness Light Source", Proceedings of PAC 1995, Dallas TX, USA, p.2823.
13. S.C. Leemann, A. Streun, "Perspectives for future light source lattices incorporating yet uncommon magnets", Phys. Rev. ST Accel. Beams **14**, 030701 (2011).
14. A. Streun, "A standard method of nonlinear lattice optimization and application to the Swiss Light Source storage ring", this newsletter.
15. OPA lattice design code, http://people.web.psi.ch/streun/opa
16. J. Bengtsson, Tracy-2 User's Manual (unpublished).
17. E. Wallén, S.C. Leemann, "Strategy for Neutralizing the Impact of Insertion Devices on the MAX IV 3 GeV Ring", Proceedings of PAC'11, New York, USA, p.1262.
18. M. Sjöström et al., "Orbit Feedback System for the MAX IV 3 GeV Storage Ring", Proceedings of IPAC'11, San Sebastián, Spain, p.499.
19. S.C. Leemann, "Updates to the MAX IV 3 GeV Storage Ring Lattice", MAX-lab internal note 20110117, http://www.maxlab.lu.se/maxlab/max4/max_iv_reports_public
20. M. Sjöström et al., "The MAX III storage ring", Nucl. Instr. and Meth. A **601**, 229 (2009).
21. A. Hansson, M. Berglund, E. Wallén, "Orbit Feedback System for the MAX IV 3 GeV Storage Ring", Proceedings of EPAC 2008, Genoa, Italy, p.3693.
22. E. Al-dmour et al., "Vacuum System Design for the MAX IV 3 GeV Ring", Proceedings of IPAC'11, San Sebastián, Spain, p.1554.
23. Å. Andersson et al., "The 100 MHz RF System for the MAX IV Storage Rings", Proceedings of IPAC'11, San Sebastián, Spain, p.193.
24. S.C. Leemann et al., "Pulsed Multipole Injection for the MAX IV Storage Rings", Proceedings of PAC'11, New York, USA, p.2522.
25. T. Tanaka, H. Kitamura, "SPECTRA: a synchrotron radiation calculation code", J. Synchrotron Rad. (2001). **8**, 1221-1228.
26. E. Wallén, private communication.

3.3 Lattice Design of a Very Low Emittance Storage Ring for the SPring-8 Upgrade Plan

Y. Shimosaki, K. Soutome, JASRI / SPring-8, Hyogo, Japan
On behalf of SPring-8 Upgrade Working Group
Mail to: shimosaki@spring8.or.jp

3.3.1 Introduction

The SPring-8 storage ring is a third generation synchrotron light source with the electron energy of 8 GeV and the circumference of 1436 m located in Hyogo, Japan (see Fig. 1). The ring stores a nominal current of 100 mA and has provided brilliant hard X-rays of the order of 10^{20} (photons/sec/mm^2/mrad^2/0.1%B.W.) to users since

1997 [1]. The super-period of the ring is 4, and one super-period consists of 9 unit cells, 2 matching cells and a long straight section (see Fig. 2). The natural emittance of 3.4 nm.rad is achieved by the double bend lattice implemented in the unit cell, where the dispersion function is leaked at the straight section for suppressing the natural emittance.

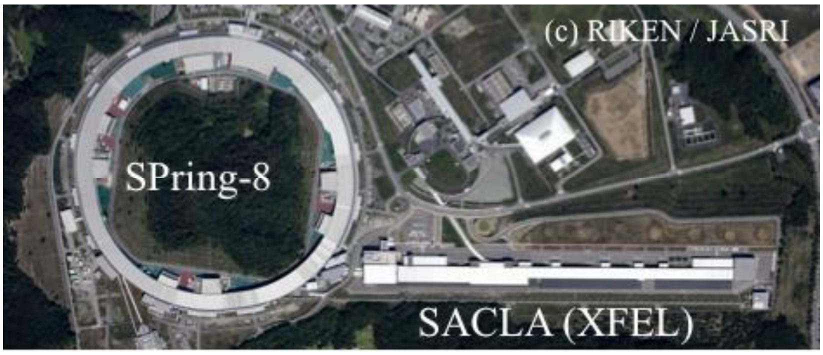

Figure 1: SPring-8 site.

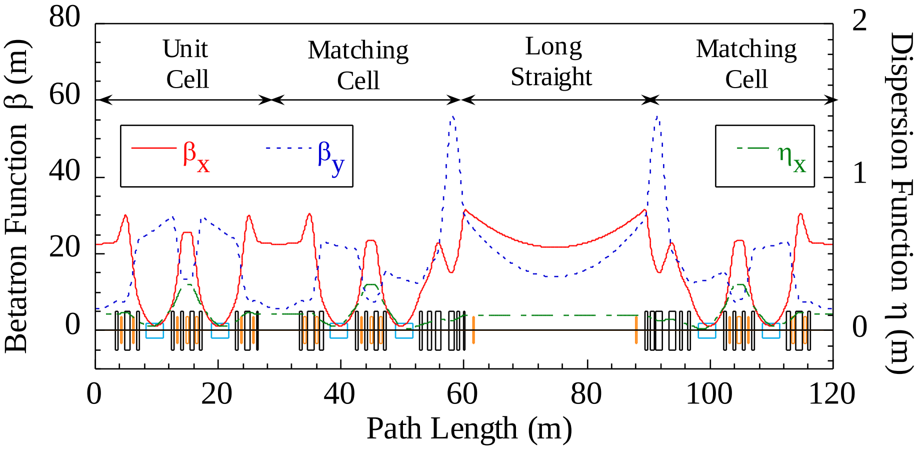

Figure 2: Present lattice of the SPring-8 storage ring.

In order to advance promising science and to support industrial innovations, an upgrade plan of the SPring-8, the SPring-8 II, has been proposed [2]. In this plan the emittance of a stored beam is drastically reduced aiming at an "ultimate" value of 10 pm.rad, corresponding to the diffraction limit for 10 keV photons. The photon science will be changed by a significant improvement in brilliance and coherence and by synergy with the X-ray Free Electron Laser (XFEL), SACLA. An estimation of the brilliance as a function of the natural emittance predicted by SPECTRA [3] is shown in Fig. 3, where we assumed the electron energy of 6 GeV, the stored current of 100 mA, the coupling factor of 2 %, the beta functions of 1 m at the light source point in both horizontal and vertical directions, and the undulator with the period of 18 mm, the length of 3 m and the maximum K-value of 2. It is seen that as the natural emittance becomes smaller the brilliance starts to saturate at around 10 pm.rad. This is why we set an ultimate target of machine upgrading to a diffraction limited light source.

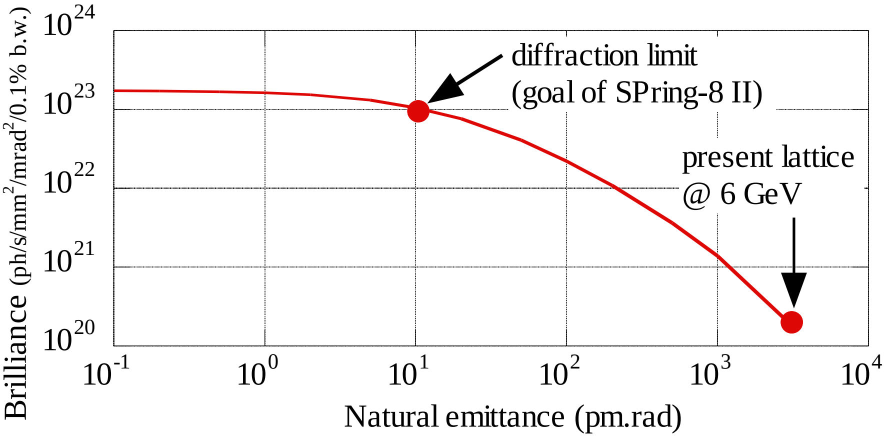

Figure 3: Brilliance vs. natural emittance (by T. Watanabe).

3.3.2 A Way of Upgrading

From a viewpoint of the cost efficiency, the SPring-8 II is planned to reuse the existing tunnel and the beamline of the insertion devices, which means that the length of the unit cell for the SPring-8 II should not be changed largely from that of the present. In addition, the shutdown time is planned about a year. The design study for the SPring-8 II is in progress with these constraints. A baseline design of an upgraded lattice is presented below, which is still under consideration and may change according to the future progress.

The theoretical minimum of the natural emittance without the constraint of the achromat condition is given by

$$\varepsilon_{\min} = \frac{1}{12\sqrt{15}} \frac{C_q \gamma^2 \theta^3}{J_x}, \tag{1}$$

where $C_q = 3.84\times10^{-13}$ m, γ is the Lorentz factor of electrons, θ is the bending angle and J_x is the damping partition number in the horizontal direction [4]. Equation 1 suggests that the natural emittance can generally be reduced by (1) lowering the beam energy, which also suppresses the heating of machine components by the synchrotron radiation, (2) increasing the number of bending magnets in a unit cell (multi-bend lattice), and (3) controlling the damping partition number with a combined bending magnet. In addition, the horizontal emittance can also be reduced by (4) introducing a damping wiggler and (5) controlling x-y coupling. Generation of hard X-rays is realized by adopting short-period in-vacuum undulators with a narrow gap.

At the SPring-8 II, a lower energy operation of 6 GeV has been selected [2], and we have been designing the multi-bend lattices, step by step (see Figs. 4).

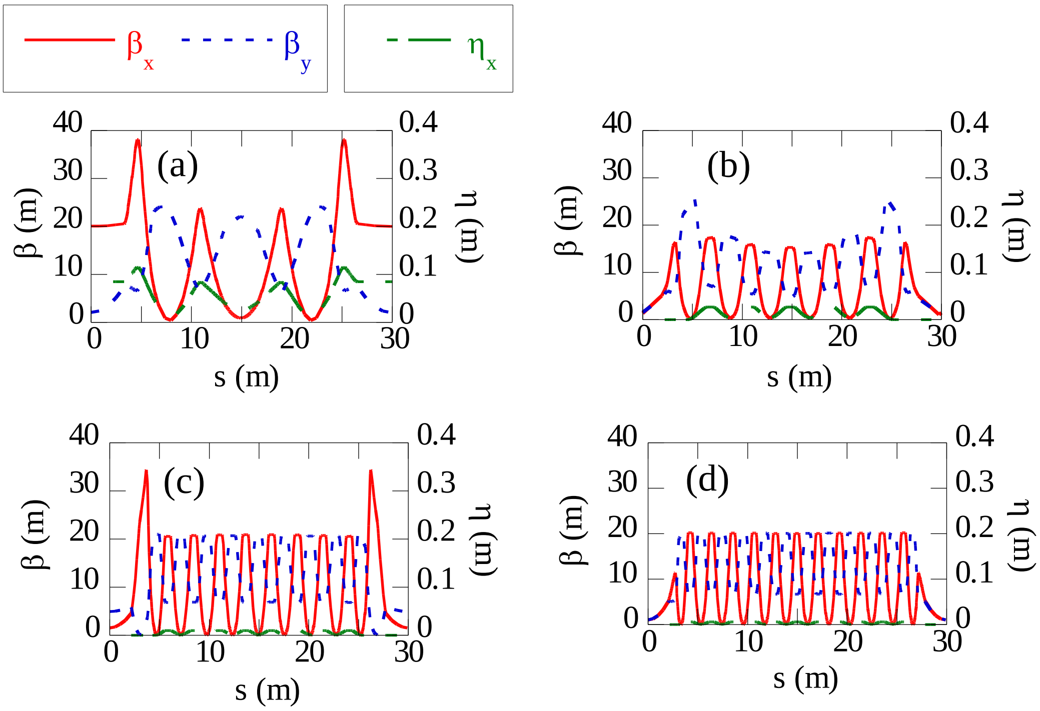

Figure 4: Examples of lattice function of a unit cell: (a) triple-bend lattice, (b) sextuple-bend achromatic lattice, (c) 9-bend achromatic lattice, and (d) 12-bend achromatic lattice.

The evaluated natural emittance, the maximum quadrupole magnetic field (QM), the maximum dispersion function and the natural chromaticity for these multi-bend lattices are presented in Figs. 5. In general, the dynamic aperture becomes narrower as the natural emittance becomes lower. The reason is that (1) stronger QMs are generally required to strongly focus an electron beam at a given interval for achieving a lower natural emittance (see Fig. 5(b)), (2) these stronger QMs cause a lower dispersion function (Fig. 5(c)) and larger chromaticity (Fig. 5(d)). Therefore, stronger sextupole magnetic fields (SXs) are required for the chromatic correction and they excite more serious nonlinear resonances. Then, the electron's motion is affected and the dynamic aperture becomes narrower.

We have been examining the way of dynamic aperture enlargement by correcting the nonlinear resonances induced by SXs for the double bend lattice (2B), the triple-bend lattice (3B), the quadruple-bend lattice (4B) and the sextuple-bend achromatic lattice (6B) [5-7]. The enlarged dynamic apertures at the injection point are shown in Figs. 6, together with those normalized by $\beta_x^{1/2}$ and by the equilibrium beam size σ_x. In these calculations the on-momentum particles in the ideal lattice are assumed. As seen from Figs. 6, while the dynamic apertures normalized by σ_x are enlarged to 100 in each lattice by correcting the nonlinear resonances, the unnormalized one (in the x-y coordinate) becomes narrower as the natural emittance becomes smaller.

For the stable user operation at the SPring-8 II, the off-axis injection is indispensable not only for the normal injection but also for the top-up operation. The bucket-by-bucket off-axis injection scheme by the fast kicker has been proposed for a lattice with a small dynamic aperture [2]. With this injection scheme, the dynamic aperture of ±2 mm is acceptable. From the results shown in Figs. 5 and 6, we see that the 6B lattice will be a critical case where we can secure the dynamic aperture of ±2 mm when machine errors are taken into account. From this point of view, the 6B lattice has been chosen as the first candidate for the SPring-8 II.

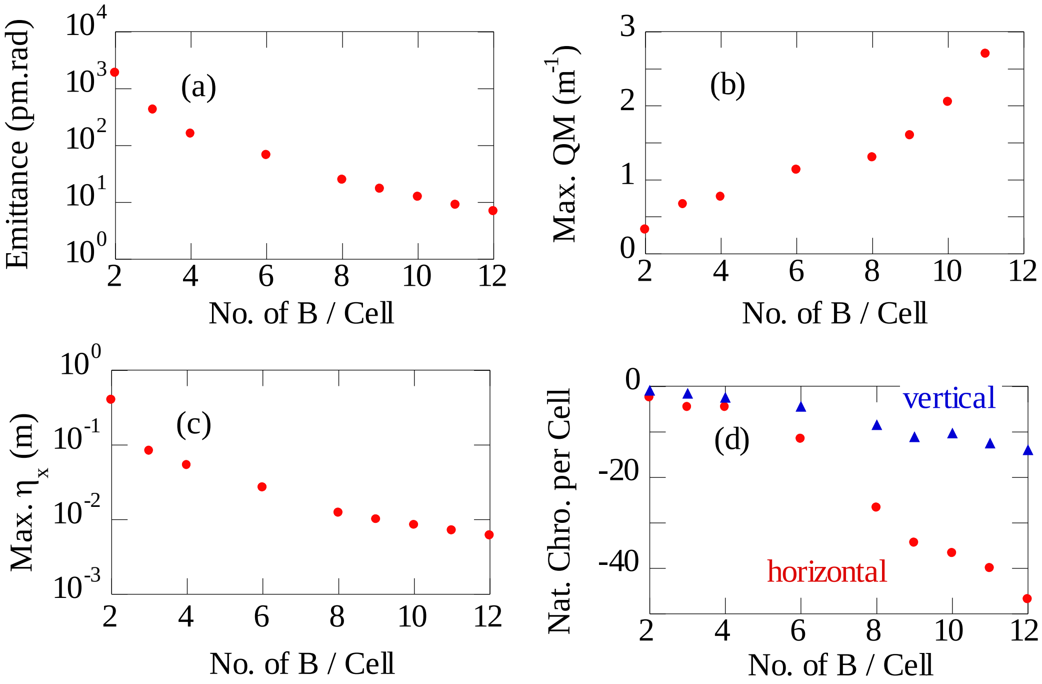

Figure 5: (a) Natural emittance, (b) maximum QM, (c) maximum dispersion function and (d) natural chromaticity for designed multi-bend lattice.

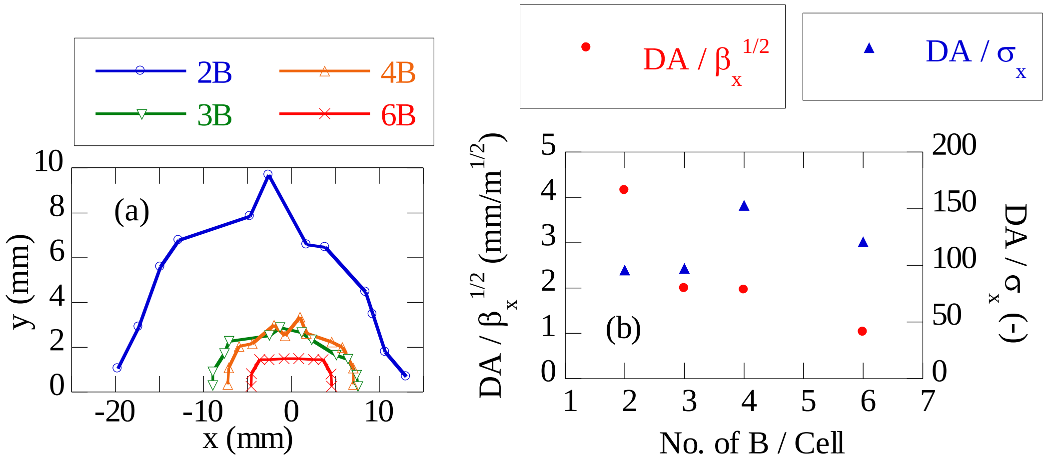

Figure 6: (a) Dynamic apertures at the injection point; (b) horizontal dynamic apertures normalized by $\beta_x^{1/2}$ and by σ_x.

3.3.3 Strategy of Lattice Design

One of the most important issues in the upgrade plan is a superior increment in the brilliance, and in designing the lattice this must be considered in addition to the dynamic aperture correction. Then, not only the emittance reduction down to the diffraction limit level but also the optimization of the beta function at the light source point of insertion devices is indispensable. We hence took three steps in the lattice optimization: "design of linear optics", "tune selection" and "design of nonlinear optics".

3.3.3.1 *Design of Linear Optics*

In designing the linear optics, we have set the first priority to obtain the lattice which has as low natural chromaticity as possible. Since the strength of the SXs needed for the chromaticity correction becomes smaller as the natural chromaticity is lower, the harmful effect of nonlinear forces due to these SXs becomes small. The position and strength of the bending magnetic field and QMs have been determined in accordance with this concept.

The lattice function of the 6B lattice including a tentative design of the long straight is shown in Fig. 7. In the case of the upgraded SPring-8 II storage ring, one super-period consists of 11 unit cells and one long straight with a FODO structure. In order to maximize the brilliance, the betatron function at the normal straight was set to 1 m in both horizontal and vertical directions for matching the emittance of electrons to the diffraction-limited emittance [8]. Since the dynamic aperture observed at the normal straight having a low-beta value becomes small in proportion to $\beta^{1/2}$, the horizontally high-beta (25 m) section is set at the long straight for beam injection. The damping wigglers are considered to be installed at the low-beta sections of the long straight.

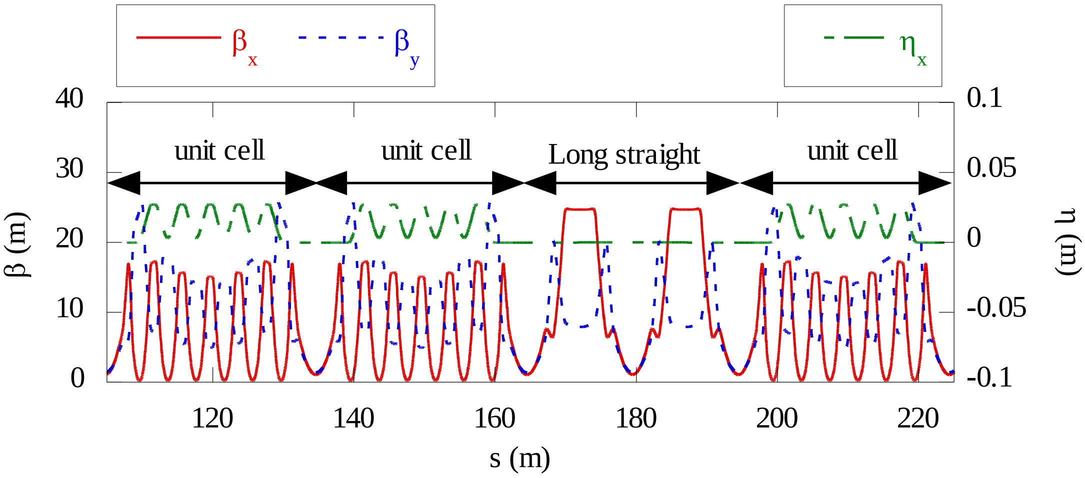

Figure 7: Lattice function of 6B lattice including a tentative design of the long straight.

3.3.3.2 *Tune Selection*

The tune has been selected not only to avoid the strong resonances but also to adjust the betatron phase advance to provide nearly *-I* transformation between SXs in order to suppress the higher order resonances for on-momentum particles [8]. A schematic view of this (non-)interleaved SXs is illustrated in Fig. 8. The non-interleaved SXs configuration is locally set inside the unit cell in the horizontal direction (dashed lines in the figure). Concerning the interleaved SXs, the phase advance is adjusted every 4 cells in the horizontal and every 2 cells in the vertical direction (solid lines in the figure). In this process of betatron phase adjustment we paid attention to the natural chromaticity and emittance so that they are not deteriorated and their values stay within a tolerance.

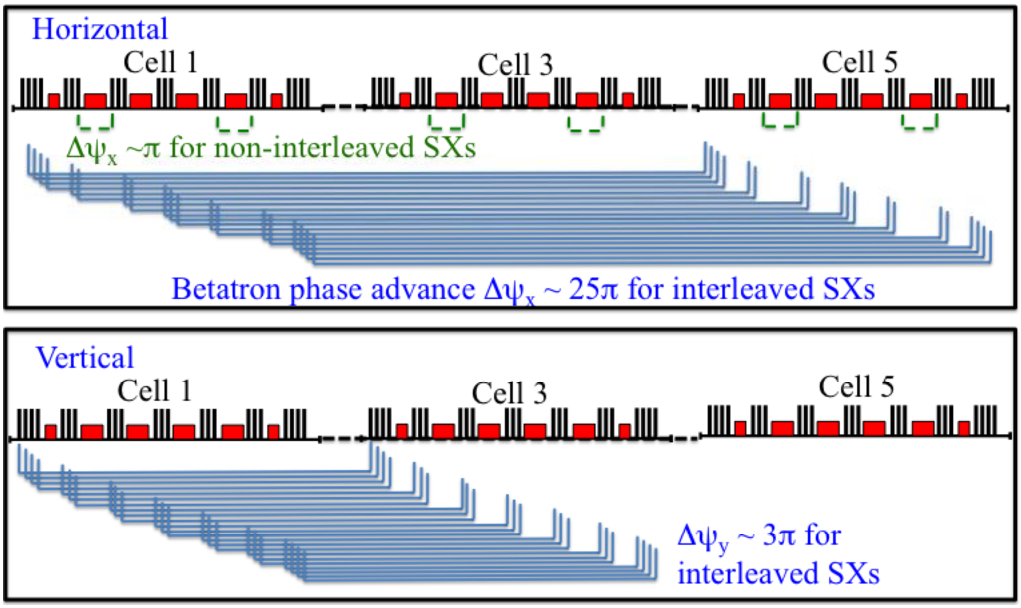

Figure 8: Configuration of (non-)interleaved SXs.

3.3.3.3 *Design of Nonlinear Optics*

The nonlinear optics for the SPring-8 II storage ring has been optimized by iterating five processes as explained below. Since the method of the (non-)interleaved SXs determines the phase advance between a pair of SXs for –*I* transformation but does not fully constrain the strength of SXs, there remain some degrees of freedom in determining the optimum values of their strengths. This can be done by solving the simultaneous equations derived by the following processes of 1) - 4):

1) The correction of the linear chromaticity (2 degrees of freedom are required).
2) The correction of nonlinear resonances induced by the SXs independent of the momentum deviation (Q_x ~ int., 3 Q_x ~ int. and $Q_x \pm 2 Q_y$ ~ int., where Q_x and Q_y are the horizontal and vertical tunes, respectively). The dominant term of the resonant potential in the isolated resonance Hamiltonian [9] is set to zero by optimizing the SXs.
3) The correction of nonlinear resonances induced by the QMs and SXs for off-momentum particles (2 Q_x ~ int. and 2 Q_y ~ int.). The QMs are not variable when the linear optics is fixed. Therefore, QM-induced resonances are cancelled out by superimposing the SX-induced resonances with the harmonic method. At the same time the momentum-dependent tune shift would be suppressed to a certain extent because the off-momentum beta-beat is also suppressed by this scheme [8]. Additional correction of the momentum-dependent tune shift can be carried out by correcting the second-order dispersion function with the harmonic method in the same way as in the COD correction by using a closed form expression [6, 10, 11]. In our recent studies, however, we found that the strength of the SX becomes stronger for correcting the second order dispersion function and this yields a reduction of the dynamic aperture though the momentum dependent tune

shift could be small. We hence excluded the correction of second-order dispersion in optimizing the latest version of lattice.

4) The amplitude-dependent tune shift is corrected by adding the SXs as the tuning knob and numerically searching the expected values.
5) The (non-)interleaved SXs configuration is kept as mentioned above.

It is noted that the SX-alignment error induces the QM error and causes a serious shrinking of the dynamic aperture from the unperturbed one, if the optimization of the nonlinear optics is not sufficient. We then optimized the nonlinear optics by observing the dynamic aperture and the momentum aperture with the errors so as to avoid the serious shrinking.

3.3.4 **Latest Design of 6B Lattice**

The lattice for the SPring-8 II has been designing by iterating the above steps, where 12 SX families in the 6B cell have been optimized with PATRASH [9], and the tracking has been performed by CETRA [12] and ELEGANT [13]. The latest lattice design (as of Sep. 21, 2011) is presented in this section. The main parameters of the latest lattice are listed in Table 1.

Table 1: Main parameters of SPring-8 and SPring-8 II (as of Sep. 21, 2011).

Parameter	***Unit***	***SPring-8***	***SPring-8 II***
Beam energy	GeV	8	6
Stored current	mA	100	300
Lattice type	…	Double bend	Sextuple bend achromatic (6B)
Natural emittance (0 current)	pmrad	3470	67.5
Momentum deviation	%	0.109	0.096
Tunes (Q_x,Q_y)	…	(40.14, 19.35)	(141.865, 36.65)
Natural chromaticities (ξ_x, ξ_y)	…	(-88, -42)	(-475, -191)
Lattice function at source point of ID (β_x, β_y, η_x)	m	(22.6, 5.6, 0.11)	(1.0, 1.4, 0.0)
Bending field	T	0.68	0.70
Max. QM B'L / Bρ	m^{-1}	0.40	1.49
Max. SX B"L / Bρ	m^{-2}	6.20	110

3.3.4.1 ***Emittance and Brilliance of 6B Lattice***

The natural emittance of 67.5 pm.rad has been achieved at zero bunch current. The dependence of the horizontal emittance ε and momentum deviation δ on the radiation damping due to the insertion devices (IDs) are shown in Fig. 9(a), where we assumed that 28 planar undulators of λ_u =18 mm and L_u = 3 m are installed at the nominal straights. Fig. 9 (a) indicates that the residual dispersion $\otimes\eta$ must be suppressed below 1 mm to avoid the emittance growth by the IDs. From the figure we see that the natural emittance of 67.5 pm.rad can be reduced to about 30 pm.rad at the undulator field of 1.6 T. Starting from this emittance value of 30 pm.rad we can further reduce it by using the damping wigglers (DWs). The emittance reduction by the DWs with λ_{DW} =50 mm and

L_{DW} = 4 m is shown in Fig. 9(b) and we see that the emittance below 20 pm.rad can be achieved.

We note that even when the residual dispersion is suppressed below 1mm, the natural emittance strongly depends on the undulator field. This means that the experimental condition for one user is unsettled and can be changed when other users move the gap of their IDs at the user-time. Therefore, the DWs should be utilized not only to achieve the diffraction limit (10 pm.rad for 10 keV photons) but also to keep the emittance at some value during the user-time (like a feedforward system for keeping the emittance).

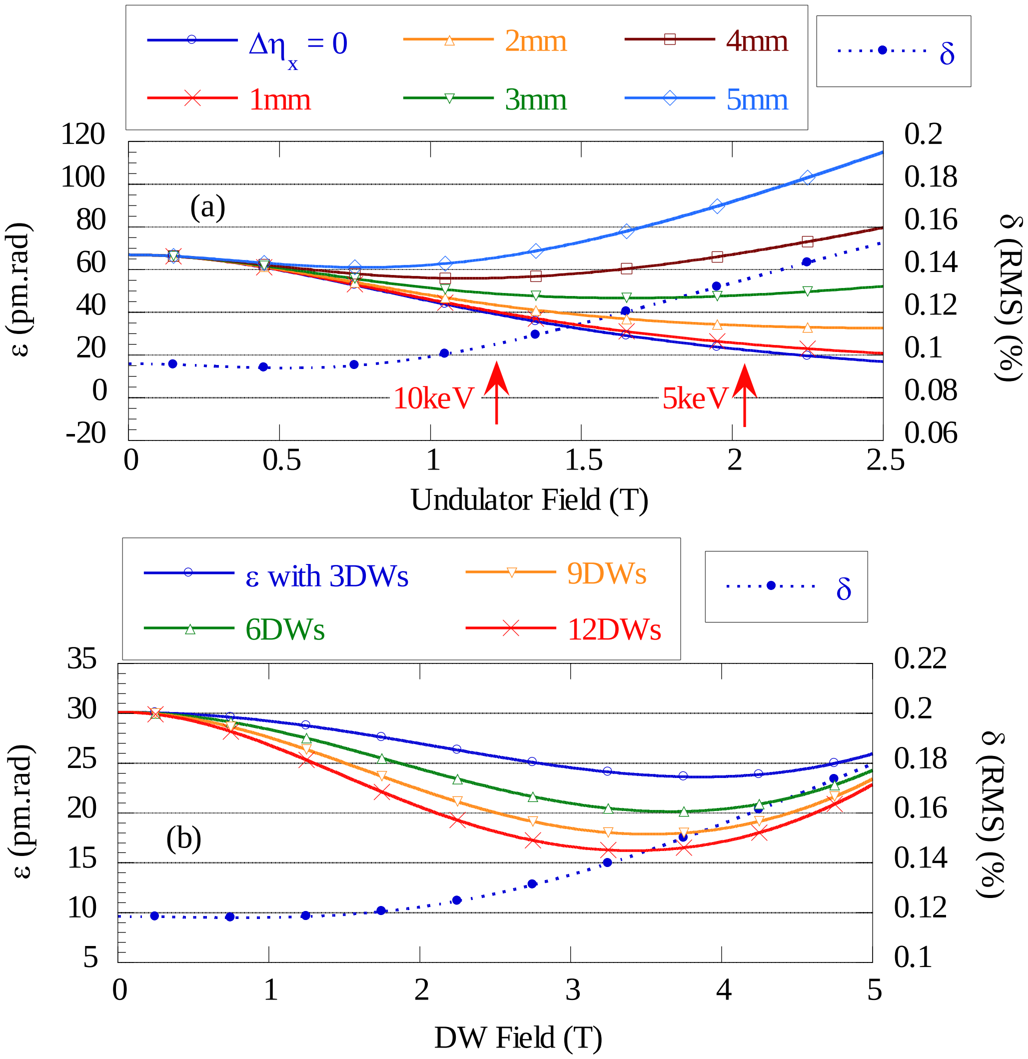

Figure 9: Emittance and momentum deviation as a function of (a) undulator field and (b) damping wiggler field.

The brilliance of the 6B lattice predicted by SPECTRA is shown in Fig. 10 [1, 2], where the horizontal emittance of 35 pm.rad is assumed to be achieved by using the IDs and the DWs at the coupling of 2 %. We see that 10^3 times higher brilliance than the present is expected in this estimation.

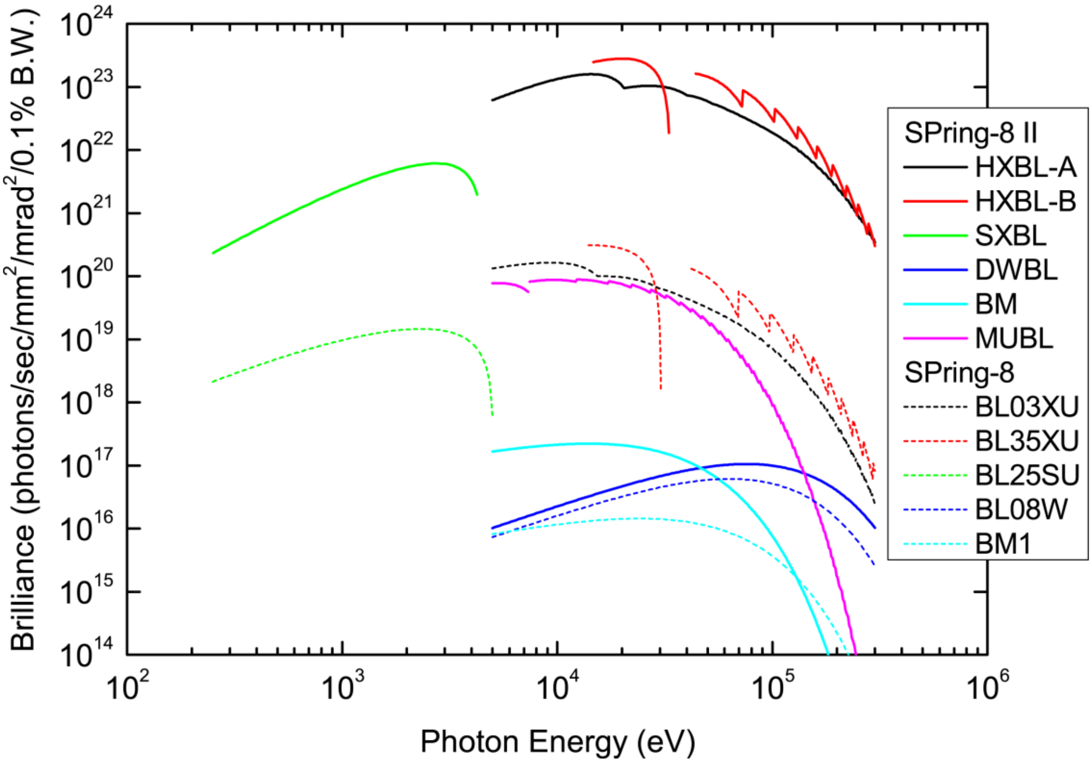

Figure 10: Brilliance of 6B lattice (by T. Tanaka).

3.3.4.2 *Beam Dynamics*

The dynamic aperture for the on-momentum particles at the injection point, where (β_x, β_y, η_0) = (24.2 m, 7.8 m, 0 m), is shown in Figs. 11. In Fig. 11(a) the SX-alignment errors of σ = 10 μm were distributed along the ring according to the Gaussian distribution with the cut-off at 2σ and dynamic aperture calculations were performed by changing the seed for random pattern generation. In addition to the errors we included the effects of synchrotron oscillation with the RF voltage of 4.5 MV and the radiation damping due to bending magnets (with energy loss of 4 MeV). The ID's effects (the nonlinear fields and the radiation damping) are not included in these calculations. The results are shown in Fig. 11(b). In both figures the error-induced COD and beta-beat were not corrected for revealing the effects of the correction of the nonlinear resonances.

The maximum strength of SXs is very large in this lattice: $B''L / B\rho = 110\ \text{m}^{-2}$ (or B'' = 13000 T / m^2), which comes from the constraint that the length of the unit cell for the SPring-8 II storage ring is almost fixed and should not be changed largely from that of the present ring. However, we see that the horizontal dynamic aperture with the error is larger than ±2 mm, the required value from the viewpoint of beam injection. The feasibility study of a very strong multipole magnet and a very precise alignment system is ongoing [2].

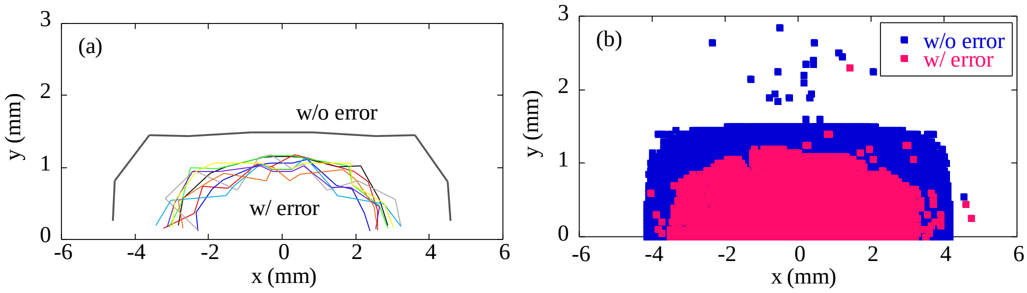

Figure 11: Dynamic aperture at the injection point (a) without and (b) with synchrotron oscillation and radiation damping by bending magnets.

The position dependence of the momentum acceptance is shown in Figs. 12 as the function of the RF voltage, where Fig. 12(a) is the case of the ideal lattice (no errors) and Fig. 12(b) includes the SX-alignment errors of $\sigma = 10$ μm with the cut-off at 2σ. In the case of the ideal lattice, the momentum acceptance is saturated at $\delta = \pm 3$ % over 6.9 MV. This means that the momentum acceptance below 6.9 MV is determined by the synchrotron oscillation and that over 6.9 MV is limited by the transverse motion (the off-momentum dynamic aperture). From Fig. 12(b) we see that though the SX-alignment errors of $\sigma = 10$ μm are distributed and the very strong SX with $B''L \,/\, B\rho = 110$ m^{-2} are utilized, we still have the momentum acceptance of about ± 2 % over 4.5 MV.

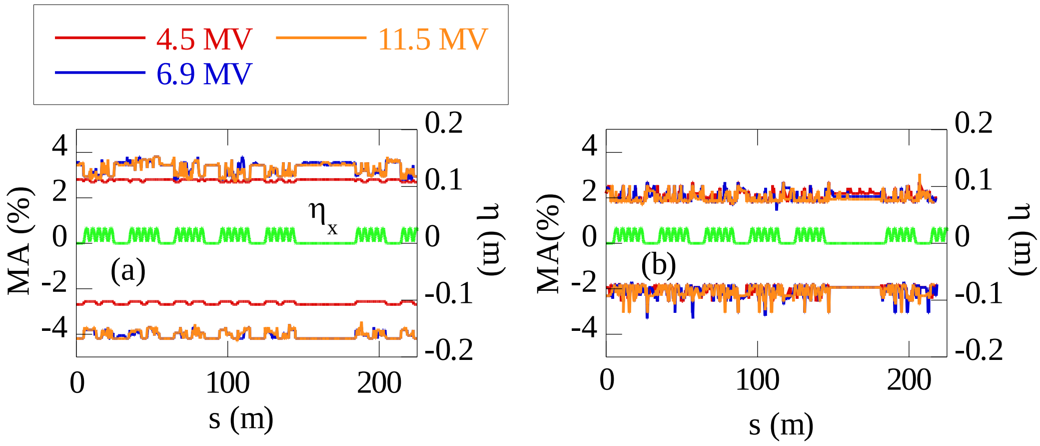

Figure 12: Momentum aperture (a) without and (b) with SX-alignment errors of $\sigma = 10$ μm (with the cut-off at 2σ).

By using the results of Fig. 12(b), the emittance growth due to the intra-beam scattering and the Touschek lifetime were estimated as the function of the coupling factor κ [14, 15]. The emittance growth is shown in Fig. 13(a), and the Touschek lifetime is given in Fig. 13(b), where the results of intra-beam scattering were used to calculate the Touschek lifetime. Since too high RF voltage causes the bunch shortening and results in the serious emittance growth and lifetime shortening, it will be reasonable to choose the RF voltage where the momentum acceptance determined by the synchrotron oscillation is equal to that by the transverse motion. The RF voltage of 4.5 MV was thus chosen in the calculations of Figs. 13.

Fig. 13(a) indicates that the emittance growth with the coupling factor of 2% is less than 20 % in the horizontal and longitudinal directions at the bunch charge of 1 nC / bunch, which corresponds to 0.2 mA / bunch.

The lifetime of more than 0.5 hour is required to store the beam current of 300 mA in the ring and to keep the stored current stability of the order of 0.01 % when the XFEL (SACLA) linac is used as an injector [2]. It seems that, by controlling the coupling factor, the enough lifetime can be achieved at the required level at the bunch current less than 1 nC / bunch. In order to achieve a longer lifetime at a higher bunch current and/or to suppress the emittance growth by the intra-beam scattering, a control of bunch length by a higher harmonics RF cavity has been proposed [2].

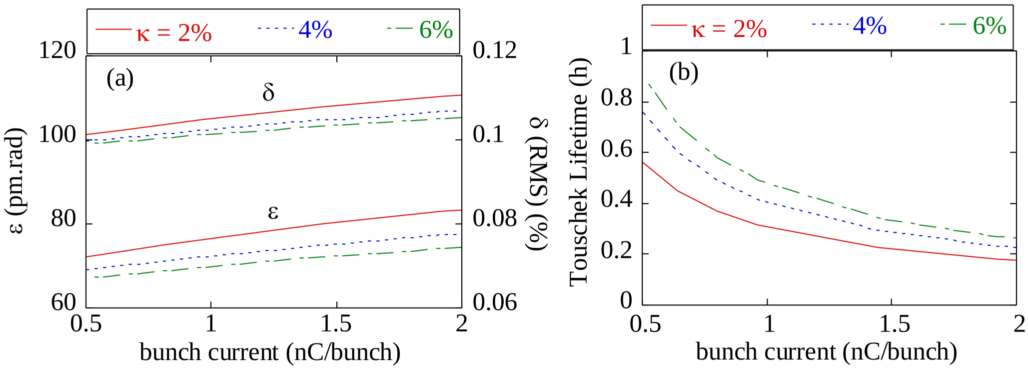

Figure 13: (a) Emittance and momentum deviation with intra-beam scattering effects and (b) Touschek lifetime with SX-alignment errors of σ = 10 μm (with the cut-off at 2σ).

3.3.5 Summary and Future Outlook

The design work of the SPring-8 upgrade plan (SPring-8 II) is in progress [2]. The lattice of the multi-bend type has been examined, step by step, and the sextuple-bend achromatic lattice is currently chosen as the first candidate of the SPring-8 II storage ring from the viewpoint of the emittance, dynamic aperture and momentum acceptance. The natural emittance is 67.5 pm.rad at 6 GeV operation.

In designing the lattice we took three steps: "design of linear optics", "tune selection" and "design of nonlinear optics". Concerning the design of nonlinear optics, the harmonic method with the (non-)interleaved sextupole has been adopted to correct nonlinear resonances for on- and off-momentum particles. Even though the very strong sextupole magnetic field of $B''L$ / $B\rho$ = 110 m^{-2} (B'' = 13000 T / m^2) is required, the dynamic aperture of about ±2 mm in the horizontal direction and the momentum acceptance of about ±2 % are obtained for the ring with the sextupole's alignment errors of σ = 10 μm (Gaussian distribution with the cut-off at 2σ). The feasibility study of a very strong multipole magnet and a very precise alignment system is ongoing. The additional enlargement of the dynamic aperture and the momentum acceptance, effects of IDs, and the correction scheme of errors will also be studied in detail. The genetic algorism has been tested for this purpose. The correction method of the nonlinear resonances will be compared between this algorism and the harmonic method with the (non-)interleaved sextupoles.

The lattice design of the SPring-8 II storage ring aims at the ultimate value of the emittance, and this inevitably requires many technological challenges such as strong multipole magnets, a precise alignment system of magnets, a fast kicker for bucket-by-bucket injection, precise beam position monitors, thinner vacuum chambers suitable for small bore radius of magnets, higher harmonic RF cavities, photon absorbers for high heat load and short-period cryogenic undulators. The R&D of these has been started.

3.3.6 **References**

1. http://www.spring8.or.jp/
2. SPring-8 Upgrade Plan Preliminary Report: http://www.spring8.or.jp/en/about_us/whats_sp8/spring-8_II
3. T. Tanaka and H. Kitamura: SPECRA code ver. 9.02 (2012).
4. S. Y. Lee, "Emittance optimization in three- and multiple-bend achromats", Phys. Rev. E 54, 1940 (1996).
5. K. Soutome, Y. Shimosaki, J. Schimizu, M. Takao and H. Ohkuma, "Design Study of a Very Low-emittance Storage Ring for the Future Upgrade Plan of SPring-8", proceedings of the first International Particle Accelerator Conference, Kyoto, Japan (2010), WEPEA032.
6. Y. Shimosaki, K. Soutome, J. Schimizu, K. Kaneki, M. Takao, T. Nakamura and H. Ohkuma, "Dynamic aperture correction for very low-emittance ring of SPring-8 II", proceedings of the 8th Annual Meeting of Particle Accelerator Society of Japan, Ibaraki, Japan (2011), WELH06.
7. Y. Shimosaki, K. Soutome, J. Schimizu, K. Kaneki, M. Takao, T. Nakamura and H. Ohkuma, "Lattice design of a very low-emittance storage ring for SPring-8 II", proceedings of the second International Particle Accelerator Conference, San Sebastián, Spain (2011), TUOAB01.
8. H. Wiedemann, “Particle Accelerator Physics, 3rd edition”, Springer-Verlag, Berlin Heidelberg New York (2007).
9. Y. Shimosaki and K. Takayama, "Halo formation at early stage of injection in high-intensity hadron rings", Phys. Rev. E 68, 036503 (2003).
10. M. Takao, "Formulation of nonlinear chromaticity in circular accelerators by canonical perturbation method", Phys. Rev. E 72, 046502 (2005).
11. H. Tanaka, M. Takao, K. Soutome, H. Hama, M. Hosaka, "A perturbative formulation of nonlinear dispersion for particle motion in storage rings", Nucl. Instr. Meth. A 431 (1999), 396-408.
12. J. Schimizu, K. Soutome, M. Takao and H. Tanaka, "Development of a tracking and analysis code for beam dynamics in SPring-8", proceedings of 13th Symp. on Accel. Sci. and Tech. Osaka, Japan (2001), pp.80-82.
13. M. Borland, "elegant: A Flexible SDDS-Compliant Code for Accelerator Simulation", APS LS-287, Sept. 2000.
14. K. L. F. Bane, H. Hayano, K. Kubo, T. Naito, T. Okugi, and J. Urakawa, "Intrabeam scattering analysis of measurements at KEK’s Accelerator Test Facility damping ring", Phys. Rev. ST Accel. Beams 5, 084403 (2002).
15. K. Kubo, S. K. Mtingwa and Andrzej Wolski, "Intrabeam scattering formulas for high energy beams", Phys. Rev. ST Accel. Beams 8, 081001 (2005).

3.4 Exploration of a Tevatron-Sized Ultimate Storage Ring*

Michael Borland
Argonne National Laboratory, 9700 South Cass Avenue, Argonne, IL 60439
Mail to: borland@aps.anl.gov

3.4.1 Introduction

Impressive as present capabilities are, there is still room for progress in the performance of storage ring light sources. Notable recent efforts are the PETRA-III ring [1], now in operation at 6 GeV with 1-nm emittance, and the NSLS-II [2] and MAX-IV [3] projects, which are expected to reach below 1 nm at 3 GeV. These developments are significant given that only a few years ago it was widely believed that storage rings had reach the end of their development capability.

A significant challenge is to further improve the emittance and energy spread. One approach is to make the circumference C very large, since the emittance scales like $1/C^3$ for a fixed cell length. With this in mind, the recent permanent shutdown of the Tevatron raises the intriguing possibility of using this large tunnel, which has a 6.28-km circumference, to house a storage ring light source of unprecedented brightness. This paper presents a preliminary exploration of this idea.

3.4.2 Optimization of Emittance

The equilibrium emittance scales as $\gamma^2\theta^3$, where θ is the angle of each bending magnet [4]. Hence, an effective strategy for making smaller emittance is to build a ring with many weak dipoles.

In the simplest approach, one can simply increase the number of cells in a ring with fixed circumference, which increases the number of dipoles and hence decreases θ. Starting with a ring like the Advanced Photon Source (APS), which has 40 cells in a 1.1-km circumference and accommodates 4.8-m-long insertion devices (IDs), one might imagine packing 80 half-length cells in the same circumference. This would nominally reduce the emittance by factor of 8 (from 3.1 nm to 0.4 nm) while leaving room for 80 2.4-m-long IDs. Given that many straight sections at 3rd-generation light sources have two half-length devices with a slight trajectory angle between them, this would probably be a significant improvement for most users. However, it would not be sufficient to remain competitive with the promises of Energy Recover Linacs (ERLs). Going further in this direction, i.e., simply making the cells shorter is impractical because the flux shrinks as the individual IDs shrink in length.

Another alternative that is very straightforward is to simply increase the circumference by adding more cells of the same design (albeit with weaker dipole field). A better approach [5] is to adopt a new cell design with many more dipoles, a so-called Multi-Bend Achromat (MBA). However, before discussing the MBA concept, we will explore straightforward circumference scaling, since it provides a convenient way to understand the challenges of making a very low-emittance ring.

---

* Work supported by the U.S. Department of Energy, Office of Science, Office of Basic Energy Sciences, under Contract No. DE-AC02-06CH11357.

3.4.3 Scaling of DBA Lattice with Circumference

For this exercise, we used **elegant** [6] and worked with the existing APS double-bend cell layout. Although originally configured as an achromat, it is presently operated with dispersion in the straight sections, which reduces the effective emittance significantly [7]. We retained this tuning while gradually increasing the number of cells, starting from the actual value of 40. To ensure reasonably uniform results, we increased the number of cells in steps of ~10%, with each new solution starting from the previous solution. The beta functions in the straight sections were fixed, as were the limits on maximum values of the lattice functions. In addition, the effective emittance was minimized, which results in the tune per cell staying roughly constant.

As Figure 1 shows, the scaling of the emittance with the number of dipoles agrees very well with the expected $1/N_d^3$ dependence, while the energy spread shows the expected $1/N_d^{1/2}$ dependence. Since the dispersion is proportional to the bending angle, we expect (and find) that the average dispersion will scale like $1/N_d$. This is one factor that will drive up the sextupole strengths, since these are proportional to the average dispersion. Given that the tunes and natural chromaticities are also proportional to N_d, we expect the required sextupole strengths to increase like N_d^2. Naively, the dynamic and momentum aperture would be expected to decrease like $1/N_d^2$, which illustrates the difficulty of creating an extremely low-emittance storage ring.

The momentum compaction factor is proportional to $\eta\theta$, giving a $1/N_d^2$ dependence. The energy loss per turn scales like $1/N_d$. Hence, to maintain constant rf bucket height, the rf voltage is required to scale like $1/N_d$, assuming a fixed rf frequency. Under this assumption, the synchrotron tune scales like $1/N_d$, while the bunch length scales like $1/N_d^{1/2}$. This has worrisome implications for collective instabilities.

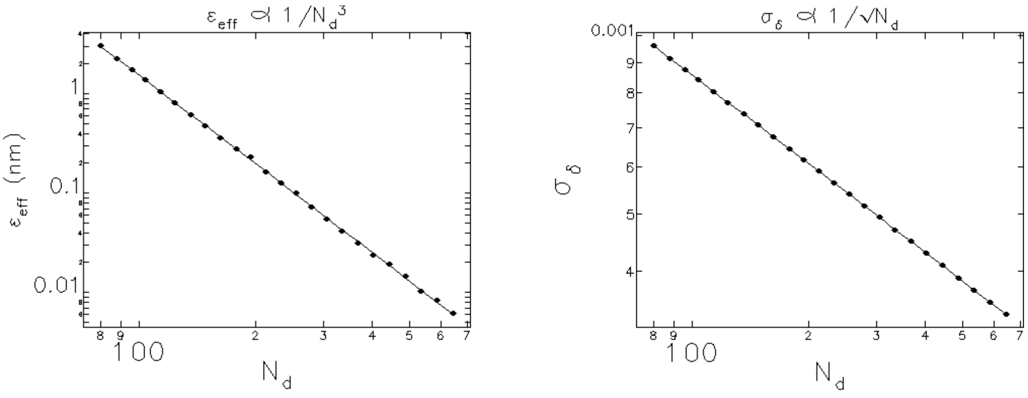

Figure 1: Scaling of the effective emittance and momentum spread with the number of dipoles, for a 7-GeV ring using APS cells.

3.4.4 Scaling of Collective Effects

We can use these results to estimate the scaling of the thresholds of the microwave and fast head-tail instabilities, which are perhaps the two dominant instabilities affecting low-emittance light source rings. The microwave instability threshold is [4] $I = \frac{\sqrt{2\pi}\alpha_c E\sigma_l\sigma_\delta^2}{R(Z_l/n)}$, which scales like $1/N_d^{5.5}$, assuming a fixed rf frequency and bucket height. For the APS, the microwave instability occurs at a bunch current of ~5 mA [8], so for a Tevatron-sized 7 GeV ring we'd estimate the instability at about 0.3 μA, which is very low. Fitting based on simulations vs energy shows that the threshold scales as $E^{3.3}$ (again assuming fixed rf bucket height). Note that the APS and other storage rings run well above this threshold, at the expense of increased energy spread [9]. In the case of APS, we can store beam with five times the threshold, limited by other effects.

The threshold for the fast head-tail instability is [4] $I = \frac{\nu_s E \sigma_l b^2}{(Z_l / n)\langle \beta_b \rangle}$. Assuming a fixed beam pipe radius *b* and that the beta functions scale weakly with N_d, we estimate that this threshold scales like $1/N_d^{3/2}$, assuming fixed rf frequency and bucket height. Hence, the ~2 mA threshold we have in the APS [8] for low chromaticity would scale to ~150 μA assuming fixed beam energy.

Two additional collective effects that are important in low emittance rings are intrabeam scattering (IBS) and Touschek scattering. The functional dependence of the IBS rate was obtained by performing fitting to simulation results, giving $n_b N_d^{5.5} / E^8$, where n_b is the number of particles in a bunch. The scaling for the Touschek scattering rate is less straightforward, but is roughly $n_b N_d^2 / E^4$ for the range covered by the simulation data.

For all of these effects, increasing N_d is detrimental, often dramatically so. However, the scaling results indicate that we can benefit from higher beam energy as we seek to raise N_d. In addition, we can benefit from damping wigglers (to increase the energy spread) and higher-harmonic cavities (to lengthen the bunch). As we'll see below, these results provide only a rough guide for MBA lattices and ignore some important considerations.

3.4.5 **Effect and Choice of Emittance Ratio**

An unstated assumption of the scaling results for IBS and Touschek lifetime is that the emittance ratio κ is fixed. However, it is not helpful to reduce the vertical emittance below approximately λ/(4π), where λ is the photon wavelength. For 10-keV photons, the threshold is about 10 pm. From the scaling study, we expect that the natural emittance for a Tevatron-sized ring will be ~1 pm. It is pointless to keep κ fixed in this case. Instead, we should increase κ in order to reduce the IBS and Touschek rates. When the natural emittance is below about 10 pm, κ≈1 is probably the all-around best choice.

There are several ways to increase κ. One can couple horizontal emittance into the vertical plane by, e.g., introducing skew quadrupole elements or taking advantage of the difference coupling resonance and random skew components due to roll errors of normal quadrupoles. One can introduce vertical dispersion, thus creating effective vertical emittance via the product of energy spread and dispersion. One can also introduce "native" vertical emittance by introducing a vertically deflecting wiggler with a relatively long period. Of these, only the first option reduces the horizontal emittance as the vertical emittance is increased. Hence, this is the preferred method.

However, in storage rings with small vertical apertures for undulators, excessive x-y coupling will result in difficulties with injection, as the residual oscillations from injection will couple into the vertical plane, resulting in beam loss. In particular, if we wish to operate with a highly coupled machine, we must inject on-axis [10] so that there is no significant residual oscillation. (Interestingly, TANTALUS, the first dedicated synchrotron radiation ring, operated this way for similar reasons [11].) This implies using “swap-out” injection, wherein an existing bunch or bunch train is removed from the ring and replaced with a fresh bunch or bunch train. As discussed in [12] and below, the injector requirements for this operation mode are not particularly demanding.

An additional advantage of operating in this mode is that the requirements for dynamic aperture decrease dramatically. Instead of the ~10 mm that is required in rings today, on-axis injection should allow operation with sub-millimeter dynamic apertures. Of course, one must pay attention to issues such as quantum lifetime and gas-scattering lifetime. The former is of little concern given the very small emittances.

We also note that by giving up the requirement of large horizontal dynamic aperture, we introduce the possibility of using insertion devices with small apertures in both planes.

3.4.6 **Design Concept**

The foregoing provides a glimpse of the promise and challenges of a Tevatron-sized light source ring. In this section, we begin to explore more of the details. We made no attempt to match the detailed geometry of the Tevatron in this exploratory stage. Instead, we sought only to approximately match the circumference of 6.28 km and the basic six-fold symmetry. Our design has six arcs and six long straight sections. The design is built up out of optics modules from the PEP-X seven-bend achromat design [13], which in turn is modeled on the MAX-IV design. We found a reasonably close match to the desired circumference (6.21 km vs 6.28 km) using N_c=30 cells per arc. With 30 cells per arc, the total number of dipoles is 1260, compared to 80 in the APS.

Of course, strengths of elements were varied in order to achieve the desired optics. Again, because this is an exploratory design, we relaxed the normal concerns about magnet strengths. Analysis of magnet requirements is somewhat involved because the PEP-X layout assumes combined function magnets, including combined function quadrupoles and sextupoles.

We expect that the choice of tune per cell and the number of cells per arc will be important for nonlinear dynamics [14]. In particular, we want each arc to provide a +I transformation in both planes. For an arc of $\underline{N_c}$ cells, we need tunes $\nu_q = n_q + m_q / N_c$, where q is x or y and n_q and m_q are non-negative integers. As a starting point, we chose N_c=30, n_x=2, n_y=1, and n_q=m_q=5, since this is fairly close to the PEP-X cell tunes. However, this caused difficulties for nonlinear dynamics optimization, due to the required sextupole strengths. Hence, we explored reducing the arc cell tunes while keeping the +I transformation in both planes. Figure 2 shows the sextupole strengths and the natural emittance as a function of the cell tunes, assuming beam energy of 9 GeV (see below). We see that moving to ν_x=1.900, ν_y=0.900 results in a 40 to 50% decrease in sextupole strength, while increasing the natural emittance by 40%. This seems acceptable given that the emittance will still be very small.

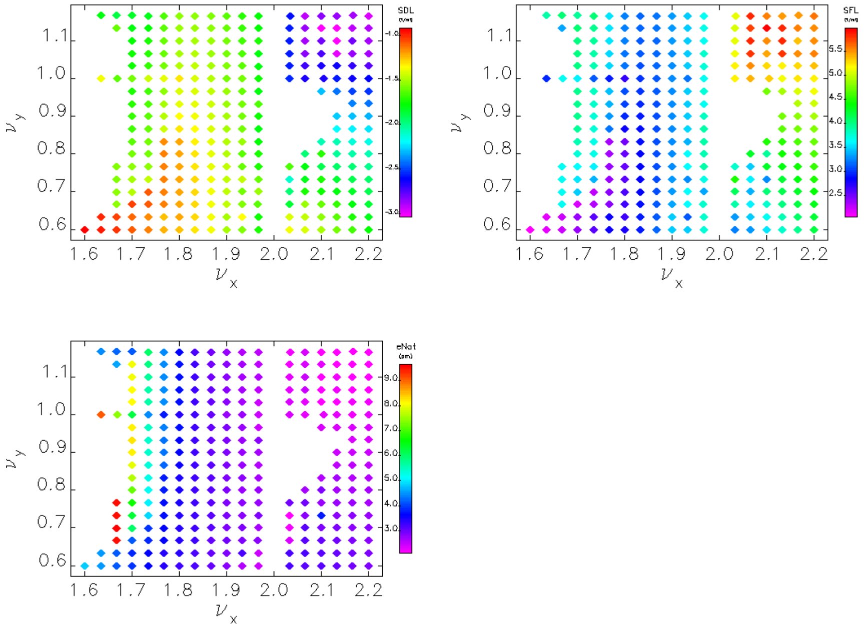

Figure 2: Integrated SD and SF sextupole strengths (top left and right) in 1/m^2 and natural emittance (bottom right) in pm as a function of cell tunes at 9 GeV.

In optimizing the nonlinear dynamics, we elected to keep the cell tunes fixed while varying the overall tunes using the quadrupoles in the matching sections and long straights. Using **elegant**, we explored the range over which the tunes could be varied within the limits of reasonable beta functions and quadrupole strength. We found that the ranges ν_x:[345,360] and ν_y:[167,183] are reasonable in terms of ability to match to desired tunes without beta functions in excess of 200 m. Figure 3 shows typical lattice functions starting from the arc and including half of a long straight. It may be desirable to adopt another design for the straights, e.g., triplet-based focusing, which should allow wider tune variation.

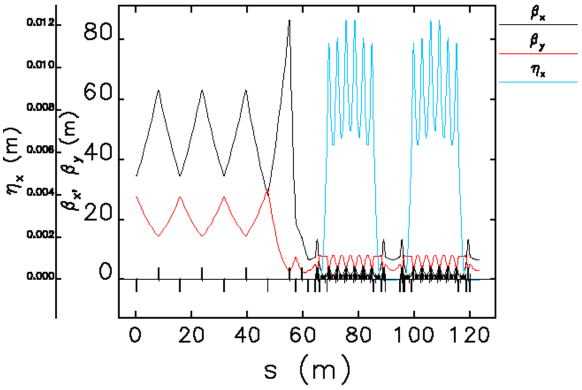

Figure 3: Typical lattice functions, showing half of the long straight section along with two arc cells.

For comparison with the scaling model developed above, we note that the natural emittance at 7 GeV is 1.8 pm, about twice our naive expectation of about 0.8 pm from 1/N_d^3 scaling (Fig. 1). However, the momentum compaction factor, at 6×10^{-6}, is five times larger than the naive 1/N_d^2 scaling indicates, which is welcome news for the microwave instability. The damping times at 7 GeV are very long. In particular, the damping time in the longitudinal plane is 1.5 seconds.

3.4.7 Optimization of Parameters for Increased Microwave Instability Threshold

At 7 GeV the scaling formula leads us to expect a very low microwave instability threshold. Assuming a 352-MHz rf system (as in the APS) and 100-mA stored current with 80% of buckets filled, we would need about 5900 bunches with a bunch current of 17 µA. This is nearly 60 times the estimated threshold. To address this further, we need to make use of more direct analysis rather than simply relying on scaling.

It is also important to recognize that the microwave instability threshold in modern light sources is significantly higher than the naively applied Boussard criterion would indicate. (This is not without theoretical justification. As discussed in section 2.5.6 of [15], the threshold can be very large if the impedance is in the upper part of the complex plane.) For this reason, we look to experimental data for guidance. For APS, we estimate Z/n=0.28 Ohms from measurements of bunch length vs current. Using this with the simple microwave threshold formula and taking into account measured bunch lengthening due to potential well distortion, gives a threshold of 0.9 mA, whereas the observed threshold is 4.9 mA. Given that similar high thresholds are measured in other large light sources [8], we included this five-fold empirical correction in our analysis.

To perform this analysis for our exploratory design, we need values of energy spread and bunch length that include bunch lengthening due to potential well distortion as well as the effects of intrabeam scattering on energy spread and bunch length. Using the APS longitudinal value of Z/n=0.28 Ohms, this is conveniently modeled using the programs **haissinski** [16] and **ibsEmittance** [17]. Using these results, we then computed the microwave instability threshold (with the five-fold empirical adjustment) and the Touschek lifetime.

More specifically, we scanned the beam energy from 6 GeV to 14 GeV for bunch charge values of 0.001 and 0.5 nC, assuming an rf frequency of 500 MHz. We assumed that $\varepsilon_x=\varepsilon_y=\varepsilon_0/2$ at zero current. The results, shown in Figure 4, are surprising. For example, the microwave instability threshold for 0.5 nC bunches generally *decreases* with increasing energy, contrary to expectations of E^3 growth. The reason is that at lower energy, the beam lengthens significantly and also suffers a significant increase in energy spread. These combine to provide a significantly increased microwave instability threshold. Our conclusion is that over a wide range of operating energies, we should be below the microwave threshold if we store 0.5-nC bunches. This provides an operating current of 200 mA if 80% of the 500-MHz buckets are filled.

Figure 4 also shows the Touschek lifetime, which is computed under the assumption of ±2% momentum acceptance and κ=1 using the program **touschekLifetime** [18]. It may be surprising that the lifetime is so long, but this owes much to the high energy and the lack of transverse momentum in the low-emittance beam.

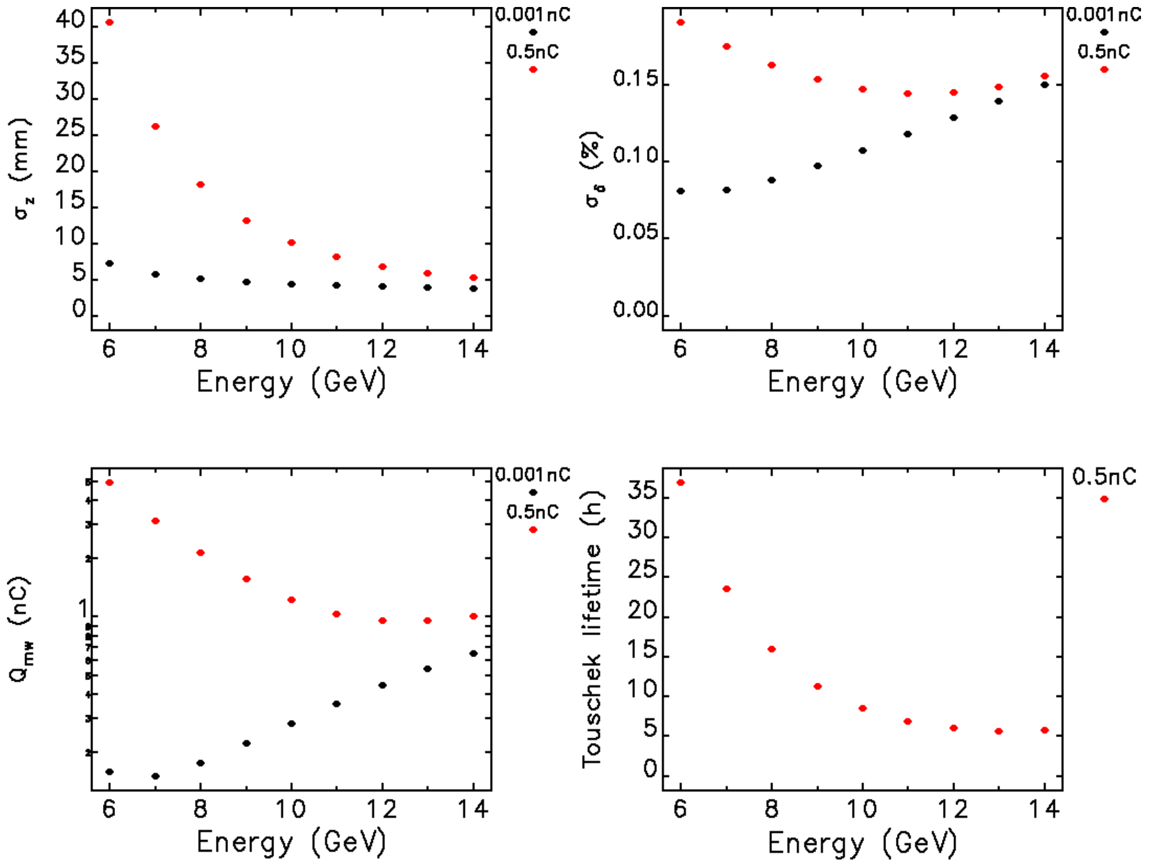

Figure 4: Collective effects as a function of beam energy for two different levels of bunch charge. See text for details.

The emittance is shown in Figure 5, from which we see that it is relatively flat as a function of energy, with a broad minimum around 8 to 10 GeV. Near this energy, IBS roughly doubles the emittance compared to the zero-current value. The three existing high-energy storage ring light sources operate between 6 and 8 GeV. For the remainder of the present study, we'll assume operation at the emittance minimum of 9 GeV.

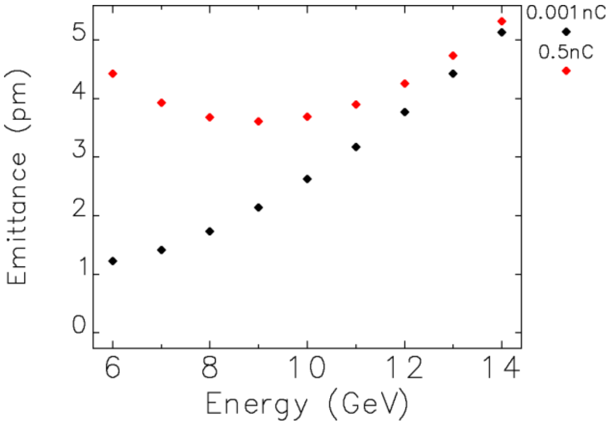

Figure 5: Emittance as a function of beam energy for two values of bunch charge, assuming full coupling.

3.4.8 Nonlinear Dynamics

In the foregoing, we've looked only at the linear optics and made some perhaps plausible assumptions about the achievable momentum acceptance. In this section, we provide a preliminary analysis of nonlinear dynamics optimization. We used a multi-objective genetic algorithm (MOGA) that directly optimizes the dynamic acceptance and the Touschek lifetime [19].

As described above, an initial optimization based on cell tunes close to those used for PEP-X provided poor results, with the momentum acceptance limited to about ±1.5% even in the absence of errors. Hence, we changed the cell tunes to ν_x=1.900 and ν_y=0.900 and revisited the MOGA optimization, now including errors. Errors were set using the methodology of [19] to give approximately 1% beta and dispersion beats and an emittance ratio of 0.2. We also included insertion device apertures with half-gaps of 18 mm (horizontal) and 3 mm (vertical).

The optimizer was allowed to vary the integer and fractional tunes (keeping the cell tunes fixed), as well as the strengths of three SF families, five SD families, and three harmonic sextupole families. The chromaticity was fixed at 1 in both planes. Although the SF and SD magnets were split into several families, the optimization so far has not produced a significant variation in strengths, so that one family of each is apparently sufficient. The harmonic sextupole strengths are 1% or less of the chromatic sextupole strengths, which seems to indicate that they are not in fact needed. Of course, it may be that continued optimization would make use of these knobs to improve results.

Figure 6 shows the best dynamic and momentum acceptances achieved so far. Given that errors are included and that MOGA has explored less than 500 configurations, these are promising. The dynamic aperture is small, but more than adequate for on-axis injection provided the injector emittance is less than about 2 nm (a normalized emittance of 35 μm), which should be no issue. The predicted Touschek lifetime for 0.5-nC bunches is about 8 hours. The estimated gas-scattering lifetime assuming 0.5-nT vacuum pressure is only about 4.5 hours, a result of the small dynamic acceptance. Hence, the total lifetime is about 3 hours.

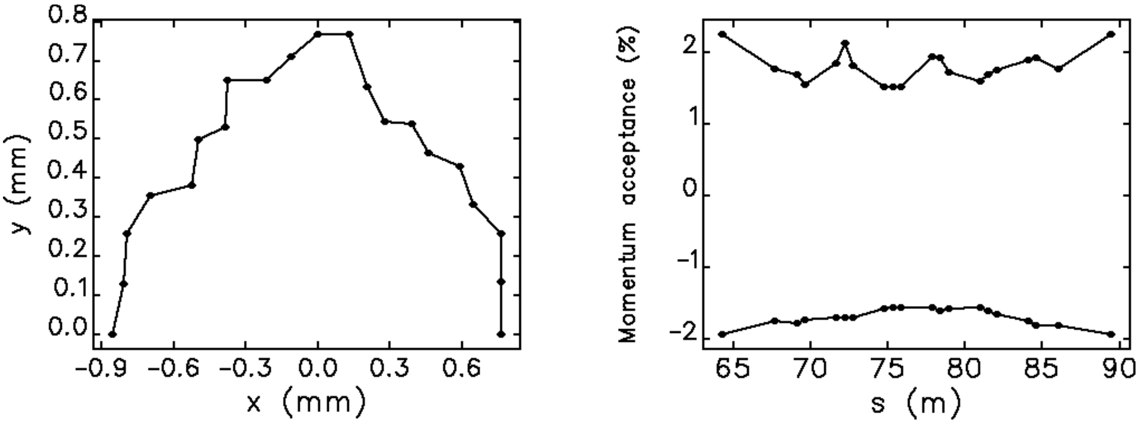

Figure 6: Preliminary MOGA optimization results, showing the dynamic acceptance (left) and the momentum acceptance (right) for one arc cell.

For 200-mA stored beam current, this implies an average injector current of about 0.4 nA, which is not challenging. If we organize the beam into 208 trains of 40 bunches, we'll have to deliver 20 nC per shot every 50 s, with required kicker rise and fall times of 10 ns. Careful collimation design will be needed to ensure that the high loss rate does not damage accelerator components. The fact that the beta functions are largest in the long straights may be useful in this respect.

Figure 7 shows predicted x-ray brightness at 200 mA for several existing APS hybrid-permanent magnet (HPM) undulators. A curve is also shown for the present superconducting undulator prototype parameters (SCU16) [20] and a reasonable extrapolation to a 20mm period [21]. Depending on the photon energy of interest, the brightness is several orders of magnitude above what can presently be achieved with storage ring x-ray sources.

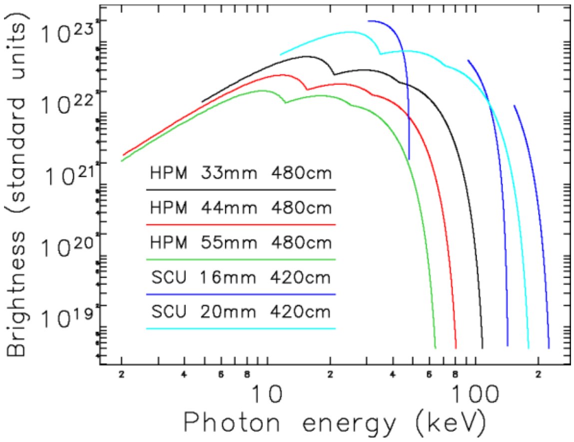

Figure 7: Curves of brightness in photons/s/mm^2/mrad^2/0.1%BW for undulators of various types, period lengths (mm), and total lengths (cm).

3.4.9 Conclusion

We've explored the possibility of a 9-GeV Tevatron-sized storage ring light source with extremely low emittance in both planes. At this point, no serious problems have been found, even though optimization of nonlinear dynamics is in a very early stage. The microwave instability and fast heat-tail instability appear to be under control, largely as a result of natural bunch lengthening due to potential well distortion and intrabeam scattering. Brightness is well above what can be offered today with a storage ring light source and can perhaps be improved further, for example, through the use of damping wigglers. These would also reduce the damping times and presumably reduce issues with some collective effects.

3.4.10 References

1. K. Baleski *et al.*, DESY 2004-035, 2004.
2. J. Ablett *et al.*, NSLS-II CDR, 2006.
3. S. C. Leeman *et al.*, PRST-AB **12**, 120701 (2009).
4. H. Wiedemann, *Particle Accelerator Physics*, Vol. 1, 2nd edition.
5. D. Einfeld *et al.*, Proceedings of PAC1996, 177-179 (1997).
6. M. Borland, Advanced Photon Source Light Source Note LS-287 (2001).
7. L. Farvacque et al., Proceedings of EPAC1994, 612-614 (1995).
8. K. Harkay *et al.*, Proceedings of EPAC2002, 1505-1507 (2002).
9. Y.C. Chae, Proceedings of PAC 2003, 3014-3016 (2003).
10. L. Emery and M. Borland, Proc. of PAC2003, 256-258 (2003).

11. E. M. Rowe and F. E. Mills, Particle Accelerators **4**, 211 (1973).
12. M. Borland, AIP Conf. Proc. **1234**, 911 (2010).
13. Y. Nosochkov *et al.*, Proceedings of IPAC 2011, THPC075, 3068-3070 (2011).
14. Y. Cai, Nucl. Instrum. Methods A **645**, 168 (2011).
15. B. Zotter, *Handbook of Accelerator Physics and Engineering*, A. W. Chao and M. Tigner, eds., World Scientific, 1999.
16. L. Emery et al., unpublished.
17. A. Xiao and M. Borland, Proceedings of PAC 2009, 3821-3823 (2009).
18. A. Xiao and M. Borland, Proceedings of PAC 2007, 3453-3455 (2007).
19. M. Borland *et al*., Advanced Photon Source Light Source Note LS-319, August 2010.
20. I. Ivanyushenkov *et al*., Proceedings of PAC 2009, 313-315 (2009).
21. S. H. Kim, Nucl. Instrum. Methods A **546**, 604 (2005).

3.5 Conceptual design of the CLIC Damping Rings

Yannis Papaphilippou, CERN, Geneva, Switzerland
for the CLIC damping rings design team
Mail to: yannis@cern.ch

3.5.1 Generation of Ultra-Low Emittances

The high luminosity of a linear collider, at the lowest power, depends strongly on the generation of ultra-low emittance high-intensity bunches, with remarkable stability. Conventional electron sources and positron production schemes provide beams with emittances that are several orders of magnitude larger than the ones needed. The natural synchrotron radiation damping of the beam when circulating in rings is the cooling mechanism enabling to reach these small emittances.

Table 1: CLIC versus ILC and NLC parameters driving the DRs design.

Parameter [unit]	***ILC***	***NLC***	***CLIC***
Bunch population [10^9]	20	7.5	4.1
Bunch spacing [ns]	369	1.4	0.5
Number of bunches/train	2625	192	312
Number of trains	1	3	1
Repetition rate [Hz]	5	120	50
Horizontal normalized emittance [nm.rad]	4400	2400	500
Vertical normalized emittance [nm.rad]	20	30	5
Longitudinal normalized emittance [keV.m]	38	11	6

The performance challenges of these damping rings (DRs) are driven by the key parameters of the collider and the requirements of the upstream and downstream systems, and principally the efficiency of the main linac RF. The parameters guiding the design of ILC [1], NLC [2] and CLIC damping rings are presented in Table 1. The technological choice of super-conducting over copper RF cavities for the main linacs, clearly diversifies the design of damping rings, although a number of common design issues and challenges still remain common. In the one flavour of the damping rings as CLIC or NLC, the bunch trains are relatively short with even shorter bunch spacing and with a high repetition rate. The ILC bunch train is much longer necessitating a much longer damping circumference where the train is compressed and uncompressed in a bunch-by-bunch beam transfer scheme. For getting the high luminosity, in the ILC the bunch charge is much higher whereas CLIC targets for much smaller emittances, orders of magnitude lower in all three dimensions (500nm.rad horizontal, 5nm.rad vertical and 6keV.m longitudinal). Although these emittances are unprecedented, modern X-ray storage rings in operation or construction phase are rapidly approaching these regimes. Especially for the vertical emittance, requiring challenging magnet alignment tolerances and stringent control of the optics and orbit, X-ray rings hold the current record, at the level of 1-2pm.rad [3-4] and have recently reached the CLIC DR target [5]. Figure 1 presents the horizontal and vertical normalized emittance in a number of low emittance rings, including test facilities, DRs, B-factories and synchrotron light sources, under operation (red) or in the design phase (blue).

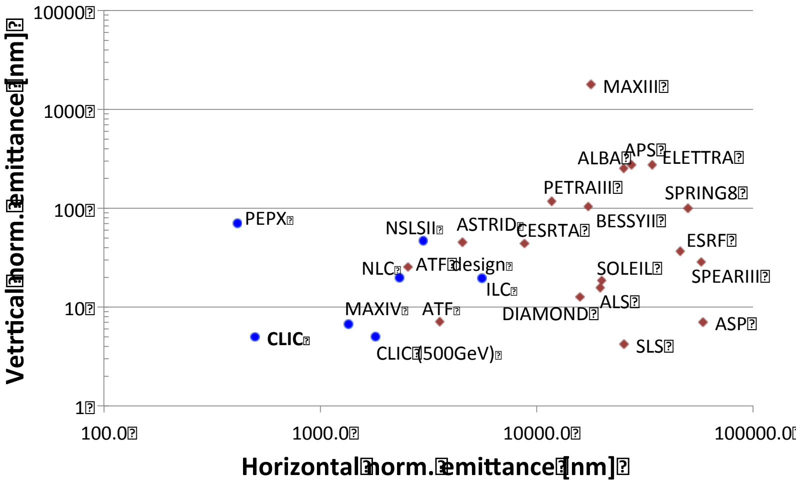

Figure 1: Horizontal versus vertical normalized emittance for low emittance rings in operation (red) and in the design phase (blue).

3.5.2 The CLIC Damping Rings Complex

A schematic layout of the CLIC damping ring complex is shown in Fig. 2 comprising of two pre-damping rings, two damping rings and a delay loop. Two pre-damping rings (PDRs) are needed due to the large input emittance especially coming from the positron source and the high repetition rate of 50Hz.

At every machine cycle, two trains are injected in the damping rings with twice the nominal bunch separation (1 vs 0.5ns), in order to reduce the transient beam loading effects in the RF cavities. The head of each train is separated by half of the damping rings circumference. The two trains are damped simultaneously and then extracted in a single turn from the main damping rings. A delay and recombination loop, downstream of the main rings, is used in order to provide a unique train with the required 2GHz bunch structure.

Standard transport lines transfer the beam between the injector linac, the damping rings, the delay loop and the booster linac. As the train recombination is provided by the same loop for both species, the time delay between the e^+ and e^- trains is recovered in the downstream systems.

3.5.3 Damping Ring Challenges and Parameter Choice

The goals guiding the design of the damping rings are driven by the main parameters of the collider and the requirements of the upstream and downstream systems.

The large energy spread of the positron beam reduces the capture efficiency in the pre-damping rings and explains the much larger bunch population needed at their entrance. Note also that the transverse emittances for the two particle species differ by almost three orders of magnitude. For electrons before and after the pre-damping rings, the bunch population contains roughly a 10% overhead for ring and transfer losses.

Figure 2: The damping ring complex layout including two pre-damping rings, two damping rings and a single delay loop.

For the pre-damping rings, the main challenge is the huge positrons emittance to be captured, necessitating large dynamic transverse and momentum acceptance [6].

The design challenges of the CLIC main DRs are driven from the extremely high bunch density, i.e. the ratio between bunch charge and the 3-dimensional beam volume, and the collective effects associated with it. In this respect, the CLIC DR parameters shown in Table 2 are carefully chosen and optimised in order to mitigate these effects. In addition, these parameters drive the technology of a number of components such as wigglers, RF system, kickers, vacuum, instrumentation and feedback.

After the adaptation of the latest main linac RF systems parameters, which drive the design of most CLIC accelerator systems, the damping rings presented a final emittance with a blow-up of a factor of 5 in the horizontal emittance due to the effect of IBS [7]. The design strategy followed was to raise the ring energy, change the optics, adapt the wiggler parameters and increase slightly the longitudinal emittance in order to mitigate as much as possible the IBS effect, down to a factor of 1.5, with respect to the equilibrium horizontal emittance. In particular, the scaling of the ratio between the steady state and zero current emittances with the energy is shown in the left part of Fig.

3. The IBS effect is reduced for higher energies as expected. The dependence of the steady state emittances to the energy is displayed on the right part of Fig.3. A broad minimum is observed around 2.0 GeV for the horizontal and vertical emittances, where the IBS effect also becomes weaker. Although higher energies may be also interesting for reducing further collective effects, the output emittance is strongly increased due to the domination of quantum excitation. In this respect, the energy of 2.86 GeV was chosen for the CLIC DR, which is close to a steady state emittance minimum but also reduces the IBS impact [7,8].

Table 2: CLIC Damping Rings' design parameters.

DR Parameters [unit]	***Value***
Energy [GeV]	2.86
Circumference [m]	427.5
Energy loss/turn [MeV]	4.0
RF voltage [MV]	5.1
Compaction factor	1.3×10^{-4}
Damping time transverse / longitudinal [ms]	2.0/1.0
Number of arc cells/wigglers	100/52
Dipole/wiggler field [T]	1.0/2.5

The lattice including the number of cells, the bending magnet characteristics, the wiggler field and period are chosen such that the target emittance is reached within the high repetition rate of 50Hz, in a compact ring. In particular, the wigglers have to reach peak fields that only super-conducting materials can provide them. The vertical emittance at "zero current" is dominated more by vertical dispersion and less by coupling, so in order to achieve it, apart from tight alignment tolerances, a very good correction and control of the orbit is necessary. In any case, the geometrical target emittance of less than 1pm.rad is the present achieved record in synchrotron light source storage rings for similar energies and bunch currents [5].

Due to the very small beam size especially in the vertical plane, the space charge tune-shift can be quite important. For reducing it, and apart from the short ring circumference, the bunch length had to be increased to the maximum acceptable level imposed by the RTML, by tuning the TME cell to an increased momentum compaction factor.

The beam loading transients in the RF cavities can be reduced by halving the RF frequency, which indeed imposes injection of two trains with a subsequent recombination in a delay loop. In order to reduce the stationary phase and linearize the bucket, the voltage cannot be raised without shortening the bunch. Instead, the energy loss per turn was increased in a way that it does not affect the fast damping, by reducing the bending field.

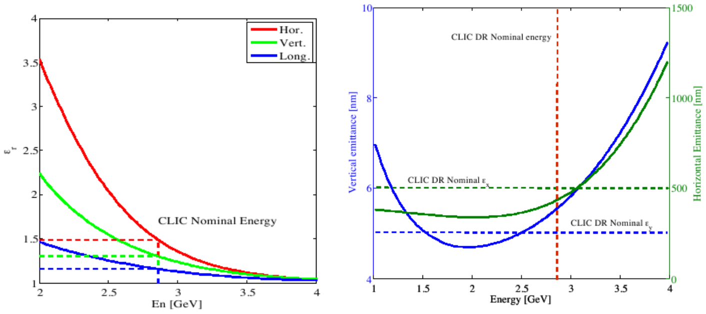

Figure 3: Dependence of the IBS growth factor, i.e. ratio between steady state and equilibrium emittances (left) and steady state emittances (right) with energy.

High bunch density in combination with the short bunch spacing triggers two stream instabilities. In the electron ring, the fast ion instability can be avoided with ultra-low vacuum pressure. This necessitates coating of vacuum chambers with getters like NEG for increasing pumping in addition to vacuum conditioning.

In order for the electron cloud build up to be reduced and the instability not to occur in the positron ring, it is necessary that the vacuum chambers present a low secondary electron and photo-emission yield (SEY and PEY). The low SEY can be achieved with special chamber coatings, whereas the low PEY is already imposed by the required absorption efficiency to reduce the heat deposition in the super-conducting magnets. In addition, the increased bunch spacing with the two trains scheme, indeed relaxes the above requirements.

The stringent beam stability requirement of typically 10% of the beam size, imposes tight jitter tolerances for the damping ring extraction kicker (a few 10^{-4}). An ILC type beam extraction experiment using a proto-type strip-line kicker has been carried out at KEK-ATF [13] with quite encouraging results, approaching the stability requirements of CLIC.

3.5.4 Optics Design

The optics functions for the TME arc cells, long straight sections FODOs, dispersion suppressors and of a quarter of the ring, are shown in Fig. 4. Each arc is filled with 48 TME cells and 2 half cells at either side for the dispersion suppression. The original TME cell was designed as compact as possible but presented several weaknesses with respect to space and magnet strength constraints. A series of optimisation steps was followed in order to rationalise it and, at the same time, to reduce the effect of IBS [9]. The major contribution of IBS is associated to locations where the beam sizes, i.e. beta functions and dispersions, reach their minima. In the TME cell, both horizontal and vertical beam sizes become minimum at the centre of the arc cells and it is exactly at this location where IBS growth rates are maximum. However, the low emittance condition requires only small horizontal betatron function in the bending magnets while the vertical one can be large.

A defocusing gradient in the bending magnet can reduce further the emittance but also reverses the behaviour of the vertical beta at the centre of the dipole (see top left of Fig. 4), hence reducing the IBS growth rate, while the resulting output emittance is almost the same [9].

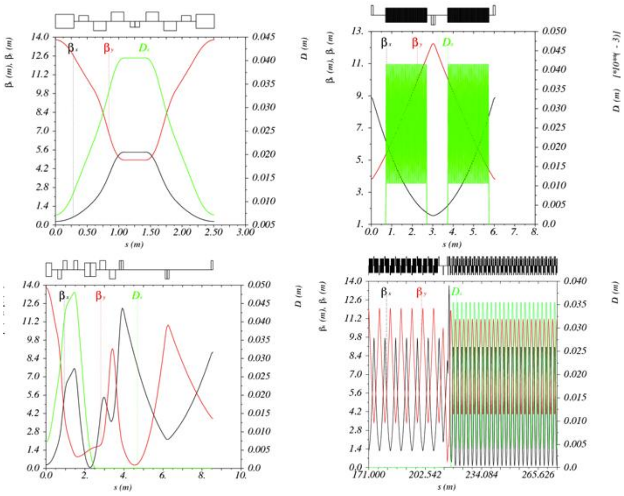

Figure 4: Horizontal (black) vertical (red) beta functions and horizontal dispersion (green) of the TME arc cell (top left), the FODO straight section with wigglers (top right), the dispersion suppressor and matching cell (bottom left) and for a quarter of the CLIC DR (bottom right).

As the final emittance of the ring can be further reduced by the use of damping wigglers in the straight sections, which provide also the fast damping, a detuned TME cell was designed, which is more flexible, easier to achieve and has lower chromaticity. The horizontal and vertical phase advances are $\mu_x = 0.408$ and $\mu_y = 0.005$. The horizontal phase advance allows a higher value of the momentum compaction factor, while keeping the final emittance within the budget. The vertical one is the smallest possible in order to increase the vertical beta functions and reduce IBS kicks while keeping the beam acceptance large enough. The bending radius of the dipole (determining its field of 1 T and length of 0.58 m) was chosen such that the energy loss per turn becomes smaller and the bunch length as large as possible. The optical functions of the resulting TME cell are displayed in the top left part Fig. 4.

The long straight sections (LSS) are filled with FODO cells and accommodate the damping wigglers. There are 13 FODO cells per straight section with two wigglers per cell. Further emittance minimisation can be made by properly choosing the lattice functions in the wiggler [9]. For a FODO cell, the minimum emittance is reached for horizontal phase advance $\mu_x = 0.31$ and for the vertical one tending to zero. The vertical phase advance can then be set as low as possible ($\mu_y = 0.12$) in order for the chromaticity to be minimized. Another possible choice is $\mu_y = 0.25$ corresponding to minimum vertical betas and thus, maximum vertical acceptance. The optics for this option is plotted in top right part of Fig. 4.

The lattice functions between the arcs and the straight sections are matched with the dispersion suppressors and matching sections. The first part is a half TME cell, with different quadrupole strengths. These two quads are used as knobs in order to minimise the length of the suppressor. A dipole is then used for the suppression of the dispersion and four more quads as knobs for matching all the optics functions at the entrance of the LSS. Space is reserved in the dispersion free region for injection/extraction and RF cavities. The optical functions of the dispersion suppressor and matching section are presented in bottom left part of Fig. 4. This lattice including sextupoles, magnet fringe fields and linear imperfections was proved to provide an adequate dynamic aperture [11] and good low emittance tuning characteristics [12].

3.5.5 Wiggler Specifications and Performance

Producing the ultra-low horizontal emittance in a compact ring within the machine pulse of 20 ms necessitates the use of damping wigglers. The highest field and relatively short period is needed in order to reach the target emittances. Pure permanent magnets are not able to reach high field (the maximum is around 1.2 T for Sm_2Co_{17}), so pole concentrators are used (e.g. vanadium permendur) to enhance the field to a maximum value of 2.3 T. This maximum field of 2.3T can be reached for a relatively large period of around 140 mm. In that case, the horizontal emittance gets more than doubled and far above the required 500 nm. In order to achieve the target DR performance, the number of wigglers has to be more than doubled, which results to a 40% increase of ring circumference. In this respect, the only way to reach the very small emittance while keeping the ring compact, is the use of high field for high gap/period ratio, necessitating superconducting damping wigglers.

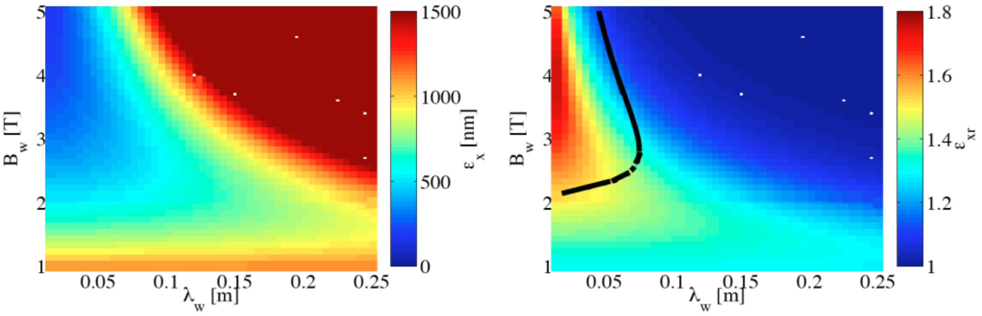

Figure 5: Dependence of the steady state emittance (left) and its ratio with the equilibrium emittance (right) as a function of the wiggler peak field and period. The blue color denote smaller emittances or ratios, whereas the red ones bigger.

In order to explore the dependence of wiggler characteristics on the output horizontal emittance with respect to IBS, a simulation was performed by varying the wiggler peak field and period, while keeping the final vertical and longitudinal ones fixed. The results are shown in Fig. 5. The left plot is colour-coded with the horizontal steady state emittance while the right one with the ratio between the steady-state and the zero-current one. The black curve corresponds to the target emittance of 500 nm and defines the area for which the output emittance is within the budget. The highest field and the shortest period is necessary for reaching the smallest emittance possible. On the other hand, the effect of IBS in that case becomes extremely strong. For reducing the blow-up due to IBS, still the highest fields are interesting but for moderate periods.

In each DR, it is foreseen to install 52 wigglers of peak field 2.5 T and 50 mm period, based on NbTi technology. A short prototype with these characteristics was developed and measured at Budker Institute achieving the field requirements. Another mock-up with more challenging design (2.8 T field, with 40 mm period) wound with Nb_3Sn wire is also under testing at CERN [13].

Around 9kW of total power is produced by each wiggler and an absorption system is necessary and critical to protect machine components and wigglers against quench, but also to lower the photo emission yield for reducing the e-cloud effect in the positron ring. The power limit is set between 1 and 10 W/m, depending the wire technology and the vacuum chamber cooling. A series of horizontal and vertical absorbers are placed downstream of the wigglers. A terminal absorber at the end of the long straight section is absorbing the remaining 100kW of photon power [14].

Full wiggler prototypes with similar magnetic characteristics are expected to be built at BINP and installed at a straight section of the ANKA synchrotron for tests under beam conditions, in an electron storage ring. Of particular interest would be the validation of cooling concept and the resistance of the wiggler to heat load under real beam conditions.

3.5.6 Longitudinal and RF Parameters

The very high peak and average current corresponding to the full train of 312 bunches spaced by 0.5 ns presents a big challenge due to the transient beam loading, especially for a 2 GHz RF system. In this respect, it was decided to consider two bunch trains with 1ns bunch spacing. The RF system with frequency of 1 GHz is more conventional and an extrapolation from existing designs is possible. Nevertheless, the trains have to be recombined in a delay loop downstream the DRs with an RF deflector.

This choice has a positive impact in both the PDRs and the main DRs. Doubling the bunch spacing halves the harmonic number increasing the momentum acceptance. The extraction kicker rise time becomes shorter but it is still long enough (560 ns). The 2-train structure may require two separate extraction kicker systems or one kicker with longer flat top (1 μs). The beam loading is significantly reduced, as the larger bunch spacing reduces peak current and power by a factor of 2. Several beam dynamics issues are also eased due to double bunch spacing. The e-cloud production and instability is reduced, while the fast ion instability will be less pronounced by doubling the critical mass above which particles get trapped. The reduced number of bunches per train reduces the central ion density, the induced tune-shift and the rise time of the instability is getting doubled, thus relaxing the feedback system requirements. Finally, a bunch-by-bunch feedback system is more conventional at 1 than at 2 GHz.

For both frequencies, and in order for the RF bucket to become more linear, the stationary phase has to be kept low. This could be achieved be increasing the RF voltage but this shortens the bunch and increases the impact of collective effects. In order to lower the stationary phase, the dipole field was lowered for reducing the energy loss per turn. At the same time, the momentum compaction is increased and so does the bunch length, leaving some margin for the increase of the voltage.

3.5.7 Collective Effects

3.5.7.1 *Intrabeam Scattering*

One of the main limitations of the CLIC DRs is the effect of intrabeam scattering (IBS) which increases the output emittances in all three dimensions. IBS is a small angle multiple Coulomb scattering effect which depends on the lattice characteristics and the beam dimensions. It is described by a series of theories and approximations [15-18]. A multi-particle tracking code SIRE [19] was developed for evaluating the IBS effect in the emittance, including damping and quantum excitation. This code was compared with classical IBS theories and approximations and the results are presented in Fig.6. The three plots correspond to the behaviour of the horizontal and vertical emittance and the energy spread squared, over one turn of the ring. In all three plots the results from SIRE simulations are shown in dark blue, the results from BM theory in red, the results from Piwinski theory in green and the ones from Bane approximation in black. The results seem to be in very good agreement with the Piwinski theory for all the three planes, while the B-M theory and Bane's approximation seem to overestimate the effect. However, the trend of the emittance evolution is the same. Due to this identical behaviour of the theories and simulations in the arcs and straight sections of the DR, and taking into account that the simulations are quite lengthy, it is convenient to use one of the analytical approaches for understanding and minimising the IBS effect. Thus, the Piwinski theory is used for this purpose, as it seems to be the closest to the simulation results [8].

A measurement campaign in CESRTA and SLS has been initiated for evaluating IBS effect and benchmark theories and simulation codes.

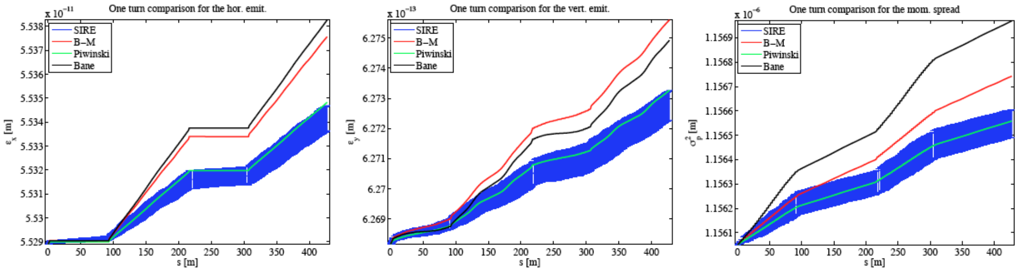

Figure 6: The one turn behaviour of the horizontal emittance (left), vertical emittance (center) and energy spread (right), starting from the zero current values, as computed by SIRE (dark blue), BM (red), modified Piwinski (green) and Bane (light blue) formalisms.

3.5.7.2 *Space Charge*

Due to the very small beam size especially in the vertical plane, the space charge tune-shift can be quite large, and an effort was undertaken in order to reduce the vertical tune-shift to around 0.1. In this respect, the bunch charge and the beam sizes cannot be changed without affecting the collider's performance and the energy was already optimised for reducing the relative impact of IBS, while reaching the required steady state emittances. Consequently, in order for the space charge to be reduced, the ring has to become as compact as possible. At the same time, the bunch length has to be increased without affecting the performance of the downstream bunch compressors. This was achieved by increasing the equilibrium bunch length through combined reduction of the circumference (removing wiggler cells), lowering the harmonic number by reducing the RF frequency and increasing the momentum compaction factor. Note finally that the space charge tune-shift grows to its final large value during the first few ms of damping to the steady state emittance thus forcing the beam core to traverse resonances. Fast pulsing quadrupoles may be necessary, in order to control the coherent tune-shift in order to avoid emittance growth or beam loss.

3.5.7.3 *Electron Cloud Effect and Mitigation*

The positron DR accumulates many densely populated bunches with a narrow spacing. Therefore, electron cloud could be an issue as the positron beam emits synchrotron radiation photons, which create a large number of photoelectrons at the inner chamber wall surface which get scattered inside the vacuum chamber and they can multiply through secondary emission. This causes electrons to be accumulated in the chamber in large amounts with a possible destabilising effect on the circulating beam.

The electron cloud build up was simulated with Factor2 code [20], for elliptical beam pipes. In the dipoles, the electron cloud formation appeared to be largely dominated by the photoemission up to maximum secondary emission yields of 1.8 with central densities between 10^{11} to 10^{13} m^{-3}.

In the wigglers, the situation is more critical because of the smaller pipe radius. The electron cloud build up starts to be dominated by secondary emission for maximum

SEY's around 1.5. Fig. 7 show the electron central densities for three different values of photoemission yield of 90, 99% or 99.9% and maximum SEY of 1.3, 1.5 and 1.8. These studies show that, independently of the initial seed of photoelectrons, extremely high central densities of electrons can be reached for SEY of 1.8. For SEY of 1.3, the electron central density would still be very high if the absorber absorbs less than 99.9% of the emitted synchrotron radiation. Therefore, for maximum SEY below 1.3, the photoelectrons can still be present in large numbers in the wiggler beam pipe, if the absorption is not sufficiently efficient to remove a high fraction of them.

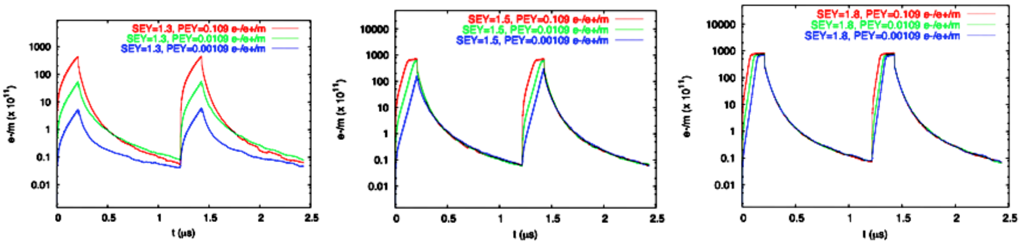

Figure 7: Electron central densities in the wiggler chamber of the CLIC DRs for photoemission yields of 90 (red), 99 (green) or 99.9\% (blue) and secondary electron yield of 1.3 (left), 1.5 (center) and 1.8 (right).

The single bunch electron cloud instability has been studied with an intense simulation campaign showing that the threshold value for the e-cloud density lies at about $5x10^{13}m^{-3}$ in the wigglers, independently of the electron density value in the dipoles. This means that countermeasures are needed to prevent electron accumulation in the wigglers, because when the electron cloud forms it reaches very quickly the critical values to make the beam unstable.

Conventional feedback systems cannot damp the e-cloud instability, as a very wide band is needed. Several mitigation techniques are presently under study[3], including low impedance clearing electrodes, solenoids (only usable in field free regions), low SEY surfaces, grooved surfaces and coatings with NEG and TiN. In particular, an amorphous carbon coating has been extensively tested at SPS [21] and later at CESRTA [22], with promising results, with respect to SEY and photo emission.

It has to be noted that some techniques such as surface coatings, non smooth surfaces or clearing electrodes to fight electron cloud do not come for free and can be serious high frequency impedance sources [23].

3.5.7.4 *Ion Effects*

In the electron DR, the ion oscillation frequency inside the bunch train during the store is in the range of 300 MHz (horizontal plane) to about 1 GHz (vertical plane), to be divided by the the square root of the mass number of the ion However, not all ion types will be trapped in the bunch train and the ones trapped around the beam are those having a mass number above a critcal value, which depends on the location in the ring (due to the different beam sizes). Molecules like N_2 and CO can be trapped almost along the full ring and will accumulate around the electron beam, potentially becoming a source of fast ion instability. The critical masses for trapping are twice as large, reducing the fraction of the ring over which ions like H_2O can be trapped. With the pressure of 1nTorr, the induced tune shift introduced by the ion cloud at the end of the train is moderate. The exponential rise time of the fast ion instability is quite large and equal to a few turns for both options. It would therefore require a very demanding multi-bunch feedback system to be controlled and/or an even lower vacuum pressure through coatings with getters (NEG) or conditioning. The train gaps have also proved to provide a natural cleaning mechanism for the trapped ions.

3.5.7.5 *Instabilities and Impedance Budget*

The broad-band model is used as a first approximation to model the whole ring in order to scan over different impedance values and define the instability threshold and the impedance budget. In these model, the impedance source is assumed to be identical in the horizontal and vertical planes.

In the transverse plane, a strong head-tail instability or Transverse Mode Coupling Instability (TMCI) can occur and cause rapid beam loss. In the case of a round beam and axisymmetric geometry for a short bunch an analytical criterion can be used to predict the TMCI threshold of around 10.7 MΩ/m for the transverse broad-band resonator in the vertical plane.

Simulating the evolution of the bunch centroid for zero chromaticity over several turns for different impedance values, it was found that modes 0 and -1 are observed to move and couple for impedance values of 18 MΩ/m and 7 MΩ/m in the horizontal and vertical plane respectively, causing a TMCI.

Chromaticity is believed to raise the TMCI threshold thanks to the tune spread that it causes and because it locks the coherent modes to their low intensity values, making mode merging weaker. For this reason, a simulation was done for different positive and negative values of chromaticity. As expected, the presence of chromaticity causes the modes to move less and not to merge and by consequence to avoid a TMCI, but another type of instability, the head-tail instability, is occurring. The TMCI quickly becomes very fast above the threshold for the onset, but for the case of head-tail instability the calculation of its rise time is needed and the damping time of 2 ms defines an instability threshold at 6.5 MΩ/m and 6 MΩ/m in the horizontal and vertical plane respectively. For even higher chromaticity, the threshold drops to 4 MΩ/m in both planes, which is a safe value to consider as a transverse impedence budget.

The resistive wall in the wiggler sections with 6 mm vertical half aperture is expected to be a strong source of impedance. Because of the small aperture, compared to 9 mm for other parts of the ring, the contribution of the wigglers is expected to take a significant fraction of the available impedance budget. Moreover, layers of coating materials, which are necessary for e-cloud mitigation or good vacuum, can significantly increase the resistive wall impedance especially in the high frequency regime. The materials used in these simulations are stainless steel (ss) and copper for the pipe of the wigglers, which is assumed to be flat. Amorphous carbon (aC), used for e-cloud mitigation, and non-evaporated getter (NEG), used for good vacuum, were chosen as coating materials. Different material and coating combinations were tried, in order to study the effect of coating on the threshold. For the case of copper, the thresholds are higher compared to those of stainless steel making it a better choice in terms of instabilities but also a more expensive material. Adding a layer of coating material on the beam pipe reduces the intensity thresholds and in fact the thicker the coating is, the more the threshold is reduced, corresponding to an extra 1MΩ/m reduction in the impedance budget.This budget is expected to be further reduced if all the different contributions from the DR are taken into account.

The rise time of the coupled bunch modes caused by resistive wall are estimated to be 0.3 ms corresponding to about 210 turns and can be damped with a transverse feedback. The rise time was simulated to be quite larger than the calculated one (by a factor 5-10), as the simulation takes into account the real wiggler and the train length.

3.5.8 **Injection/Extraction**

The injection and extraction process is quite simple with only one pulse stored in the damping ring per cycle. This pulse contains two trains of 156 bunches with 1GHz structure. Each train which is supposed to be symmetrically spaced in the DR, covers a small fraction of the circumference of only 11%. The injection and extraction system is located at symmetric locations, at the end of the arc, after the dispersion suppressor and upstream of the super-conducting wigglers to avoid that synchrotron radiation damages the sensitive injection/extraction elements. The kickers can be placed at maximum horizontal beta functions for minimising the deflection angle. For the same reason, the phase advance between injection (extraction) septa and kickers are set to around π/2. Additional space can be added in order to install longer elements thus reducing the available voltage needed and accommodate protection systems.

An extraction kicker ripple produces a beam size jitter which is propagated up to the collider IP. On the other hand, injection kicker jitter is translated to reduction of the beam stay clear, during the injection process. For both processes, a typical tolerance of 10\% of the beam size at extraction or injection is considered, although in the case of injection, it can be relaxed to even higher values (e.g. 20-30%). Taking into account that the extracted beam size for the required normalised emittance of 500~nm corresponds to a few tens of microns, the kicker stability tolerance is around 10^{-4}.

A similar tolerance can be established for the kicker roll, which will induce a vertical beam size jitter. The extracted vertical beam size is of the order of a few μm and to keep the distortion to the order of a few hundred nm, the kicker alignment should be better than a few tens of μrad. Future refinement in the lattice of the damping rings will not change significantly the kicker specifications, especially the stringent required stability.

To ease this very tight requirement, a 2nd identical kicker powered by the same pulser can be installed in the extraction line, at a phase advance of π for jitter compensation. This solution was already proposed in the case of the NLC damping rings [1], which required similar stability tolerances. A double strip-line kicker system was at ATF with similar stability requirements but for shorter rise/fall times and flat top [24].

3.5.9 **Delay Loop**

The two trains of the CLIC DR have to be recombined in a single delay loop for both species, using RF deflectors. A unique α-shape loop, as in CTF3, is considered, for both species with a circumference of 263m, i.e. half of the damping rings. The optics is tuned to achieve high-order iso-chronism and is based on TME cells and sextupole tuning. The emittance growth due to synchrotron radiation is negligible due to the low energy and relatively short length of the loop. The path length correction is very critical and a wiggler, orbit correctors or a chicane may be considered in order to control it down to a few mm. The systematic energy loss is roughly half of the DR and can be corrected with RF cavities of a few hundred kV. As the beam stability requirement is quite low, this imposes tight jitter tolerances for the RF deflector (around 10^{-3} . This tolerance is within the capability of modern clystrons. It will necessitate a demonstration through measurements in CTF3 which are equipped with similar RF deflectors for the drive beam recombination and frequency multiplication [24].

3.5.10 **Acknowledgements**

We would like to thank all the members of the CLIC damping ring design team and the Low Emittance Rings collaborators for their numerous contributions to this work and in particular F. Antoniou, M. Barnes, S. Calatroni, P. Chiggiatto, R. Corsini, A. Grudiev, E. Koukovini-Platia, T. Lefevre, N. Mounet, G. Rumolo, S. Russenchuck, H. Schmickler, D. Schoerling, D. Schulte, M. Taborelli, G. Vandoni, F. Zimmermann (CERN), Y.M. Boland, R. Dowd, R. Rassool, E. Tan, K. Wooton (ACAS, Melbourne, Australia), A. Bragin, E. Levichev, D. Shatilov, S. Siniatkin, S. Piminov, P. Vobbly, K. Zolotarev (BINP), M. Billing, J. Calvey, J. Crittenden, G. Dugan, M. Palmer, D. Rubin, J. Shanks (Cornell), F. Torral (CIEMAT), M. Korostelev (Cockroft), M. Wendt (FNAL), C. Belver-Aguilar, A. Faus-Golfe (IFIC-Valencia), D. Alesini, M. Biagini, S. Guiducci, S. Liuzzo (INFN-LNF), P. Raimondi (ESRF), R. Bartolini (DIAMOND), K. Kubo, T. Naito, N. Terunuma, J. Urakawa (KEK-ATF), A. Bernard, A.S. Muller (KIT-ANKA), E. Wallen, A. Anderson (Maxlab), M. Aiba, M. Boege, N. Milas, L.Rivkin, A. Streun (PSI-SLS).

3.5.11 **References**

1. N. Phinney, N. Toge, N. Walker, ILC Reference Design Report Vol. 3 -Accelerator, arXiv:0712.2361, http://arxiv.org/pdf/0712.2361.pdf.
2. Next Linear Collider Zeroth-Order design report, SLAC-R-474, 2002.
3. Low Emittance Rings Workshop 2010, http://ler2010.web.cern.ch.
   Low Emittance Rings Workshop 2011, http://lowering2011.web.cern.ch.
4. A. Streun et al., submitted to Physical Review Letters.
5. F. Antoniou and Y. Papaphilippou, "Design considerations for the CLIC pre-damping rings", PAC'09, Vancouver, May 2009.
6. H. Braun et al., CLIC 2008 parameters, CLIC-Note-764.
7. Y. Papaphilippou, H.H. Braun and M. Korostelev, "Parameter scan for the CLIC damping rings", EPAC'08, Genova, June 2008, p.679.
8. F. Antoniou, M. Martini, Y. Papaphilippou and A. Vivoli, "Parameter scan for the CLIC Damping Rings under the influence of intrabeam scattering", IPAC'10, Kyoto, 2010.
9. Y. Papaphilippou et al., "Lattice options for the CLIC damping rings", PAC'09, Vancouver, May 2009.
10. Y. Papaphilippou et al., "Design Optimization for the CLIC Damping Rings", IPAC2010, Kyoto, Japan, 2010.
11. Y. Renier et al. Proc. of IPAC 2011, p. 2205, San Sebastian, Spain, 2011.
12. K.P. Wooton, et al., Proc. of IPAC 2011, p. 1102, San Sebastian, Spain, 2011.
13. D. Schoerling et al, Design and System Integration of the Superconducting Wiggler

Magnets for the CLIC Damping Rings, PRST-AB, 2012, (in press).
14. K. Zolotarev, et al., CLIC Note, 2009, in preparation.
15. A. Piwinski, Handbook of Accelerator Physics, World Scientific (1999) 125.
16. M. Martini, Tech. Rep. PS/84-9(A4), CERN, 1984.
17. J. Bjorken and S. Mtingwa, Part. Accel., 13 (1983) 115.
18. K. Bane, SLAC-PUB-9226, June 2002.
19. A. Vivoli and M. Martini, Proc. of IPAC 2010, p. , Kyoto, Japan, 2010.
20. G. Rumolo, et al., "Electron Cloud Build Up and Instability in the CLIC Damping Rings", EPAC'08, Genova, June 2008.
21. E. Shaposhnikova, et al., "Experimental studies of carbon coatings as possible means of supressing beam induced electron multi-pacting in the CERN SPS", PAC'09, Vancouver, May 2009.
22. M. Palmer et al., "Electron Cloud at Low Emittance in CesrTA", IPAC'10, Kyoto, Japan, 2010.
23. N. Mounet and E. Metral, Proc. of IPAC 2011, p. , San Sebastian, Spain, 2011.
24. T. Naito et al, "Multi-bunch Beam Extraction by using Strip-line Kicker at KEK-ATF", IPAC'10, Kyoto, Japan, 2010.
25. D. Alesini and F. Marcellini, "RF deflector design of the CLIC test facility CTF3 delay loop and beam loading effect analysis", PRSTAB12 031301, 2009.

3.6 Nonlinear Dynamics Optimization in Low Emittance Rings: Theory and Modelization (a Geometric Point of View)

Johan Bengtsson, BNL, Upton, NY 11973-5000
Mail to: bengtsson@bnl.gov

3.6.1 Introduction: Analytical vs. Numerical and Experimental Methods

We outline a control theory for the nonlinear dynamics governing synchrotrons. Starting from the relativistic Hamiltonian for a charged particle in an external electromagnetic field, instead of evaluating the corresponding Poincaré map by classical perturbation theory [1], the map is expressed as a Lie series [2], where the Lie generators (aka "driving terms") codifies the dynamics. The control problem for the system of nonlinear ODEs (Ordinary Differential Equations) is thus transformed into a system of (over constrained) nonlinear algebraic equations in the multipole strengths [3]. In other words, the coefficients in the equations of motion are tailored directly, rather than in perturbative, or numerical solutions.

Regardless, numerical techniques for 6D phase-space tracking [4-6] are crucial for (in-depth) validation of analytical results from simplified models. Typically, by attempting to "unveil" some underlying "harmonic oscillator" and the (implicit) use of linear superposition.

However, since numerical integration provide little insight into how to fix a flawed design, Truncated Power Series Algebra (TPSA) [7-8] (aka Automatic Differentiation) is useful for analysis of the resulting dynamics for a realistic lattice (i.e., with engineering tolerances, etc.) by e.g. extracting arbitrary order Taylor maps and the corresponding Lie generators.

Alternatively, a "brute force" (direct) numerical optimization of tracking data using Genetic Algorithms with Multi-Objective optimization (MOGA) and parallel computation can be used [9-10]. In fact, the approach is known to be an effective solution of the: sorting, swapping, and shimming problem for Insertion Devices (IDs) [11].

Furthermore, by using turn-by-turn BPM data and modern signal processing techniques [12], or Orbit Response Matrix (ORM) measurements [13-14], the driving term method can (with care) be used on-line as well; i.e., "closing-the-loop" [1,15-20]. For a complementary approach, see Frequency Map Analysis (FMA) [21].

Note, in the following by a first or second order achromat, we mean in terms of the 6D space-space coordinates ($\bar{x} \equiv \lfloor x, p_x, y, p_y, \delta, c_0 t \rfloor$) for the map. The corresponding Lie generator is one order higher (2nd or 3rd). For the driving terms (Lie generators), first and second order are in terms of the sextupole strength $b_3 L$, or more generally, the multipole strength $b_n L$.

3.6.2 Avoiding the "TME Trap": A Systems Approach

The "TME trap" (Theoretical Minimum Emittance cell), i.e., the resulting "chromaticity wall", can be avoided by a first principles approach. Roughly, the linear chromaticity ξ_x becomes uncontrollable by a leading order (transverse) minimization of ε_x. An artifact created by ignoring leading order (linear) chromaticity; a reductionist approach. Hence, we will refer to it as the $\langle \mathcal{H}_x \rangle^{\min}$-cell ($\mathcal{H}_x$ is the dispersion action). Note, while the (linear) chromaticity for the FODO cell is a straightforward (linear algebra) exercise ($\xi_x = -\tan(\Delta\mu_x/2)/\pi$), it is not for *N*-Bend-Achromats (*N*-BA). For an analysis of the scaling properties of a periodic $\langle \mathcal{H}_x \rangle^{\min}$-cell, see refs. [22-23].

3.6.3 First Example: SLS Re-Baselining

The method was originally developed to address the "DA problem" (Dynamic Aperture) for the initially proposed Swiss Light Source (SLS) [24] lattice. A $\langle \mathcal{H}_x \rangle^{\min}$ driven 7BA design with 6 arcs (7BA-6) [25] => not robust when e.g. engineering tolerances were included. While we did establish an "academic solution" (by introducing 33 sextupole families and 4 phase trombones [26]), the highly strained lattice was resolved by re-baselining to a (robust) Triple-Bend-Achromat (TBA) [27]. For a "systems approach", we used the normalized (linear) chromaticity ($|\xi_x|/\nu_x$) per cell to guide the linear optics design. The design effort was also streamlined by porting the software modules (in Pascal at the time) for controlling (the driving terms) and analyzing the nonlinear dynamics (by FFT and signal processing of tracking data) to the local code used (and improved, in Pascal as well) for *interactive* optics design [28]; interleaving the (linear) optics design with the (nonlinear) control problem.

3.6.4 Second Example: NSLS-II Re-Baselining

Later, the approach was refined (higher order achromats [29]) for robust design of NSLS-II [30]; requiring another re-baselining (of a $\langle \mathcal{H}_x \rangle^{\min}$ driven TBA-24,

$C = 500 \rightarrow 750\,\mathrm{m}$ [31-33]). In particular, while doubling the number of dipoles for a proven design e.g. 2×TBA-12 -> TBA-24 gives

$$\varepsilon_x = 5\,\mathrm{nm}\cdot\mathrm{rad}/2^3\ @2.4\,\mathrm{GeV} \rightarrow 1\,\mathrm{nm}\cdot\mathrm{rad}\ @3\,\mathrm{GeV}\,, \tag{1}$$

it reduces the dispersion in the sextupoles as well. Hence, the "DA problem" does not scale. A parallel pursuit of a DBA-30 with Damping Wigglers (DWs) also led to a robust design [34] which eventually was chosen [35]; a counter intuitive solution for a $\langle \mathcal{H}_x \rangle^{\min}$ approach. As a (conservative) guideline for the parametric studies for the CDR work (DBAs with 32 down to 24 cells & DWs), we used: $|\xi_x| \sim 3$ per DBA and $\hat{\eta}_x \sim 0.3\,\mathrm{m}$ for the peak dispersion [30].

3.6.5 The Chromatic Control Problem: A Measure for Stiffness

It is known that (fixed ρ_b) [36]

$$\varepsilon_x[\mathrm{nm{\cdot}rad}] = 1470\cdot\frac{(E\,[\mathrm{GeV}])^2\langle\mathcal{H}_x\rangle^{\min}}{\rho_\mathrm{b} J_x} = 1470\cdot\frac{(E\,[\mathrm{GeV}])^2(2\pi)^3 F}{12\sqrt{15}J_x N_\mathrm{b}^3} \tag{2}$$

where N_b is the total number of dipoles and [37]

$$F_\mathrm{CB} = 1,\quad F_\mathrm{EB} = 3,\quad F_{N-\mathrm{BA}} = \left(\frac{N}{2+(N-2)\cdot 3^{1/3}}\right)^3 F_\mathrm{EB} \tag{3}$$

for a "center bend", "end bend", and N -BA, respectively.

As a measure for the *stiffness* of the chromatic control problem, we introduce

$$S \equiv \frac{|\xi_x|}{\nu_x\sqrt{\langle\mathcal{H}_x\rangle}} \sim \frac{1}{\mathrm{DA}}\,. \tag{4}$$

Note that the DA has a minimum for the $\langle \mathcal{H}_x \rangle^{\min}$-cell. A survey of F_rel (= 1 for $\langle \mathcal{H}_x \rangle^{\min}$) vs. S is summarized in Tab. 1. For the operating facilities we find: $S = 49 \pm 23$.

Table 1: Survey of F_{rel} vs. Stiffness S for some Storage-Ring Light Sources.

Lattice	Type	E [GeV]	ε_x [nm·rad]	ε^*_x [nm·rad]	J_x	$\langle\mathcal{H}_x\rangle$ [$\times10^{-3}$]	F_{rel}	ξ_x/ν_x	S
SPring-8	11×DB-4	8	3.4	3.7	1.0	1.42	4.6	2.2	58
ESRF	DB-32	6	3.8		1.0	1.68	3.5	3.6	89
APS	DB-40	7	2.5	3.1	1.0	1.35	3.3	2.5	69
PETRA III	Mod. FODO	6	1		1.0	3.62	39.8	1.2	20
SPEAR3	DB-18	3	11.2		1.0	5.73	7.4	5.5	73
ALS	TB-12	1.9	6.3	6.4	1.0	4.99	10.4	1.7	24
BESSY II	TBA-10	1.9	6.1		1.0	4.83	2.9	2.8	40
SLS	TBA-12	2.4	5		1.0	3.38	2.6	3.2	56
DIAMOND	DB-24	3	2.7		1.0	1.46	4.2	2.9	76
ASP	DB-14	3	7		1.4	5.60	3.0	2.1	28
ALBA	DB-16	3	4.3		1.3	2.96	2.6	2.1	39
SOLEIL	DB-16	2.75	3.7	5.5	1.0	1.79	2.0	2.8	67
CLS	DBA-12	2.9	18.3		1.6	16.79	2.0	1.3	10
ELETTRA	DBA-12	2	7.4		1.3	9.12	1.4	3.0	31
TPS	DB-24	3	1.7		1.0	1.08	2.7	2.9	87
NSLS-II	DBA-30	3	2		1.0	3.78	2.0	3.1	50
MAX-IV	7BA-20	3	0.33		1.9	0.40	18.1	1.2	59
PEP-X (TME)	4×8TME-6	4.5	0.095		1.0	0.34	3.3	1.7	90
PEP-X (USR)	8×7BA-6	4.5	0.029		1.0	0.10	5.3	1.4	145
TeVUSR	30×7BA-6	11	0.0031		2.4	0.02	12.0	1.4	360
TeVUSR	30×7BA-6	9	0.0029		2.7	0.02	18.4	1.4	281

A few observations:

1. While ELETTRA has gradient dipoles, the phase advance for the DBA was increased by adding a quadrupole at the center.
2. ALS has superbends; which increases the emittance.
3. Upgrades of former High-Energy Physics (HEP) facilities have been successful: SPEAR 3 (by re-using the tunnel) [38], and PETRA III (by modifying 1/8th of the existing ring and introducing DWs) [39]; despite the constraints from legacy.
4. Since NSLS-II is using DWs, the straights must be achromatic ($F_{\mathrm{rel}} = 2, S = 50$).
5. MAX IV [40] is based on a compact, robust 7BA; the result of a systems approach. In particular, by ignoring $\langle \mathcal{H}_x \rangle^{\min}$ ($F_{\mathrm{rel}} = 18, S = 59$), and instead focusing on: $1/N_b^3$, robust design and innovative (cost effective) engineering (e.g. concrete “girders”). With a proof-of-concept by MAX-III [41] (magnets built-to-print); adopted by SOLARIS [42]. A product of “engineering-science” [43]; i.e., MAX I -> MAX IV. Initially a 7BA-12 [44], successfully scaled (for more straight sections) to a 7BA-20 [45]. The (conceptual) design is actually quite conservative [46]; e.g. $\tau_{\mathrm{Touschek}} \sim 20\ \mathrm{hrs}$. Note, a $\langle \mathcal{H}_x \rangle^{\min}$ approach would not have led to this solution; hence a “paradigm shift”.

6. Conceptual studies include PEP-X ($\langle \mathcal{H}_x \rangle^{\min}$ based, $F_{\text{rel}} = 3.3, S = 90$) [47] which, inspired by the compact 7BA for MAX IV, recently re-baselined to 3.4×MAX IV (6 arcs w/ 8×7BA) [48]. But pushed it considerable ($F_{\text{rel}} = 5.3, S = 145$); a $\langle \mathcal{H}_x \rangle^{\min}$ approach.
7. Similarly for a Tevatron-sized 9×MAX IV (6 arc w/ 30×7BA) [49]. At least for the preliminary studies ($F_{\text{rel}} = 12, S = 496$). On the other hand, workable solutions emerge (for on-axis injection) by relaxing the optics to $F_{\text{rel}} = 18.4, S = 281$.

To summarize, for established facilities (optimized over some 20 years), we conclude that $S < 100$ (2 sigma) for robust designs. However, by using e.g. on-axis injection, this might be revised.

3.6.6 **Design Philosophy**

Design a system which is controllable & observable. This requires: a realistic model, robust design, effective "knobs" (controls), diagnostics, and signal processing techniques:

1. To avoid instabilities, transition to chaos, etc.
2. For efficient injection and satisfactory Touschek lifetime.

For an effective approach, the entire facility must be considered: a complex, tightly coupled system. Note the complementary (hybrid) approach for MAX IV: a 1.5 Gev & 3 GeV rings with a full energy linac injector (=> FEL). A reductionist approach is inadequate because "the sum is more than the parts": $f(a+b) = f(a) + f(b) + \ldots$; i.e., nonlinear dynamics does (in general) not scale. The $\langle \mathcal{H}_x \rangle^{\min}$ approach leads to a "chromaticity wall". For example, for a FODO cell $\xi_x = -\tan(\Delta\mu_x/2)/\pi \to \infty$ for $\langle \mathcal{H}_x \rangle^{\min}$ => $\Delta\mu_x = 180°$. For a systems approach, see refs. [22-23]. For inspiration e.g.:

- J.C. Maxwell "On Governors" (1868): Control Theory for steam engines; today used for diesel engines.
- "The Birth of Flight Control: An Engineering Analysis of the Wright Brothers 1902 Glider": inventors of the ailerons (by wing warping); aka 3-axis control.

3.6.7 Lattice Design: A “Feedback System”

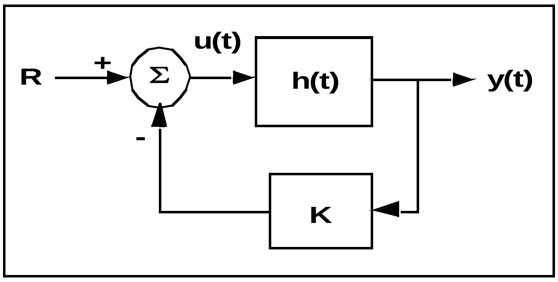

Figure 1: “Closing-the-Loop”.

For an analogy, one may view the lattice design process as a “feedback system”, see Fig. 1, where $h(t)$ (transfer function) is the lattice described by a Hamiltonian $H(\bar{x};s)$, R (input): desired injection efficiency, orbit stability, emittance, beam lifetime, etc., $y(t)$ (output): actual injection efficiency, etc. And $u(t)$ (error signal) the gap between the desired and actual design goals. Strategies include:

1. Design ("feed-forward”): model, guidelines, engineering, reality checks, etc.
2. On-line control (“feed-back”, e.g. commissioning): model-based control, turn-by-turn BPM data, orbit response matrix, etc. and successive refinements by an iterative process.

3.6.8 Linear Optics: Betatron Motion

Hill’s equation can be written as two first order ODEs

$$x'' + K(s)x = 0 \quad \Leftrightarrow \quad \begin{cases} x' = p_x, \\ p_x' = -K(s)x \end{cases} \tag{5}$$

which are generated by the quadratic Hamiltonian ($\bar{x} \equiv [x, p_x]$)

$$H_2(\bar{x};s) = \frac{p_x^2}{2} + K(s)\frac{x^2}{2}, \quad \begin{cases} x' = \partial_{p_x} H_2(\bar{x};s), \\ p_x' = -\partial_x H_2(\bar{x};s) \end{cases}. \tag{6}$$

For piece-wise constant $K(s)$, the solutions are

$$\bar{x}_1 = M\bar{x}_0 \tag{7}$$

where

$$M = \begin{bmatrix} \cos\left(\sqrt{K}L\right) & \frac{1}{\sqrt{K}}\sin\left(\sqrt{K}L\right) \\ -\sqrt{K}\sin\left(\sqrt{K}L\right) & \cos\left(\sqrt{K}s\right)L \end{bmatrix} \rightarrow \begin{bmatrix} 1 & L \\ 0 & 1 \end{bmatrix}, \quad K \rightarrow 0 \tag{8}$$

and $\sin\left(\sqrt{K}L\right) \rightarrow -\sinh\left(\sqrt{|K|}L\right)$ and $\cos\left(\sqrt{K}L\right) \rightarrow \cosh\left(\sqrt{|K|}L\right)$ for $K < 0$.

3.6.9 **The Poincaré Map**

By introducing the differential operator (Lie derivative)

$$\mathcal{D}(\bar{x}) = x'\partial_x + p_x'\partial_{p_x} = \left(\partial_{p_x} H(\bar{x};s)\right)\partial_{x_0} - \left(\partial_x H(\bar{x};s)\right)\partial_{p_{x0}} \tag{9}$$

and the Taylor expansion

$$e^{\mathcal{D}(\bar{x})} \equiv I + \frac{\mathcal{D}(\bar{x})}{1!} + \frac{\mathcal{D}^2(\bar{x})}{2!} + \ldots, \quad I\{f(x)\} = f(x), \tag{10}$$

where I is the identity function, the (formal) solution can be written (Lie series)

$$\bar{x}(\Delta s) = e^{\Delta s \mathcal{D}(\bar{x}_0)} \bar{x}_0 \equiv \mathcal{M}_{\Delta s} \bar{x}_0 \, . \tag{11}$$

For example, in the linear case ($\mathcal{M}$ is a functional map)

$$\mathcal{M} = e^{\mathcal{D}_{H_2}} = \mathcal{A}^{-1} e^{\mathcal{D}_{K_2}} \mathcal{A} = \mathcal{A}^{-1} e^{\mathcal{D}_{-2\pi\bar{\nu}\cdot\bar{J}}} \mathcal{A} = \mathcal{A}^{-1} \mathcal{R} \mathcal{A} \tag{12}$$

and the motion is stable if $\left|\mathrm{Tr}\{M\}\right| < 2$ (elliptic vs. hyperbolic).

3.6.10 **The Lie Generator: A Geometric Point of View**

The Lie generator has a simple geometric interpretation for some special cases:

1. Translations (drift): $H_\mathrm{d} = p_x^2/2, \quad \mathcal{M}_\mathrm{d} = e^{L\mathcal{D}_{H_\mathrm{d}}} x_0 = x_0 + L p_{0x}$.
2. Thin kick: $H_\mathrm{tk} = b_n x^n \delta(s)/n, \quad \mathcal{M}_\mathrm{tk} = e^{b_n \mathcal{D}_{H_\mathrm{tk}}} x_0 = p_{0x} - b_n x^{n-1}$.
3. Rotation: $H_\mathcal{R} = \frac{1}{2}\left(x^2 + p_x^2\right), \quad \mathcal{R} : \begin{cases} x = e^{\mu\,\mathcal{D}_{H_\mathcal{R}}} x_0 = x_0 \cos(\mu_x) + p_{0x} \sin(\mu_x), \\ p_x = e^{\mu\,\mathcal{D}_{H_\mathcal{R}}} p_{0x} = -x_0 \sin(\mu_x) + p_{0x} \cos(\mu_x). \end{cases}$

see Fig. 2.

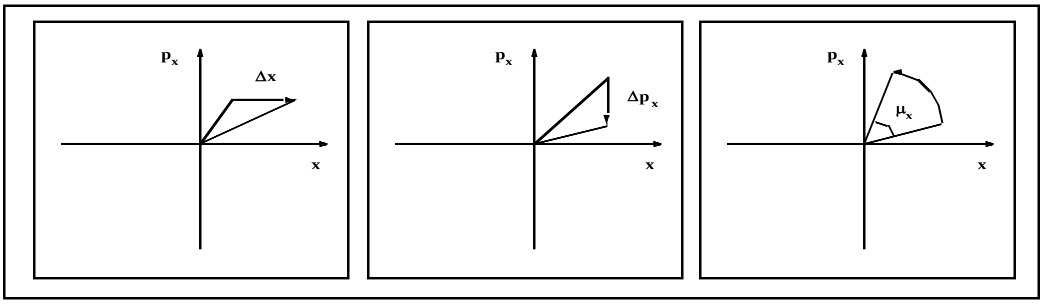

Figure 2: Geometry for a: Drift, Thin Kick, and Phase-Space Rotation.

3.6.11 **Symplectic Integrators: A Geometric View**

The Hamiltonian for a multipole can be split into a “drift” and a “kick”

$$\mathcal{M}_{\mathrm{mag}} = e^{L/2\mathcal{D}_{\mathrm{d}}} e^{(b_2 L)\mathcal{D}_{\mathrm{d}}} e^{L/2\mathcal{D}_{\mathrm{d}}} + O\left(L^3\right) = \left(e^{L/2n\mathcal{D}_{\mathrm{d}}} e^{(b_2 L)/n\mathcal{D}_{\mathrm{d}}} e^{L/2n\mathcal{D}_{\mathrm{d}}}\right)^n + O\left(\left(\frac{L}{n}\right)^3\right) \qquad (13)$$

where the second expression is for n integration steps, i.e., a 2nd order symplectic integrator, see Fig. 3.

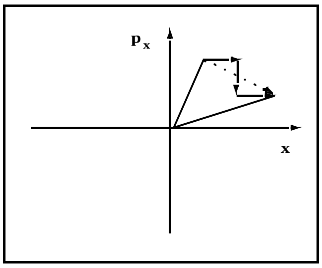

Figure 3: The Geometry of a Second Order Symplectic Integrator.

Generalizing, a $(2N+2)$th order is obtained from a $2N$th by [5]

$$S_{2N+2} = S_{2N}(z_1 L)_{2N}(z_0 L)_{2N}(z_1 L) + O\left(L^{2N+3}\right), \quad \begin{cases} z_0 = -\dfrac{2^{1/(2N+1)}}{2-2^{1/(2N+1)}}, \\ z_1 = \dfrac{1}{2-2^{1/(2N+1)}} \end{cases} \qquad (14)$$

where $z_0 + 2z_1 = 1$. In particular, a 4th order is obtained from Eq. (13); a carefully balanced sequence of “drifts” and “kicks”.

3.6.12 **Action-Angle Variables**

The (linear) one-turn map, obtained by concatenation, can be diagonalized:

$$M=ARA^{-1},\quad A=\begin{bmatrix}\sqrt{\beta_x} & 0\\ -\dfrac{\alpha_x}{\sqrt{\beta_x}} & \dfrac{1}{\sqrt{\beta_x}}\end{bmatrix},\quad R=\begin{bmatrix}\cos(2\pi\nu_x) & \sin(2\pi\nu_x)\\ -\sin(2\pi\nu_x) & \cos(2\pi\nu_x)\end{bmatrix}. \tag{15}$$

The action-angle variables $[\phi_x, J_x]$ (constants of motion) are (normalized phase-space)

$$\tilde{x}\equiv A^{-1}\bar{x}=\begin{bmatrix}\sqrt{2J_x}\cos(2\pi\nu_x+\phi_x)\\ -\sqrt{2J_x}\sin(2\pi\nu_x+\phi_x)\end{bmatrix},\quad \begin{cases}(2J_x)=\tilde{x}^2+\tilde{p}_x^2,\\ \phi_x=-\tan(-\dfrac{\tilde{p}_x}{\tilde{x}_x})\end{cases}. \tag{16}$$

see Fig. 4, and the Hamiltonian simplifies to

$$K_2(J_x)=2\pi\nu_x J_x,\quad \begin{cases}\phi'_x=\partial_{J_x}K_2=2\pi\nu_x,\\ J'_x=-\partial_{\phi_x}K_2=0\end{cases} \tag{17}$$

which is stable for $\nu_x \neq \text{int}$. To summarize, by introducing the action-angle variables, the s-dependent Hamiltonian $H_2(\bar{x};s)$, Eq. (6) is transformed to an invariant $K_2(J_x)$.

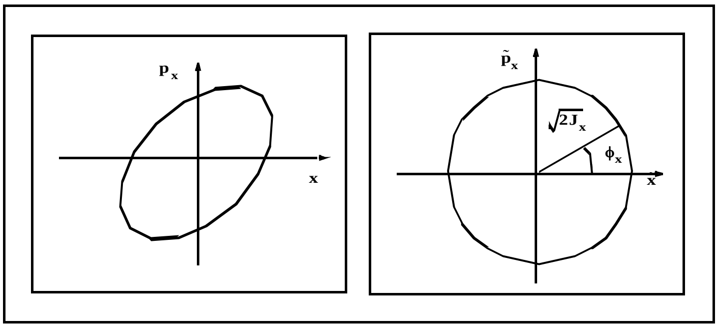

Figure 4: Phase-Space and Normalized Phase-Space (aka Floquet Space).

Similarly, the dispersion action is

$$\tilde{\eta}\equiv A^{-1}\bar{\eta},\quad \bar{\eta}\equiv[\eta_x,\eta'_x]^{\mathrm{T}},\quad \mathcal{H}_x=\tilde{\eta}^{\mathrm{T}}\tilde{\eta} \tag{18}$$

3.6.13 **Non-Linear Maps**

Generalizing, the generator $H(\phi_x, J_x)$ of the Lie generator $\mathcal{D}_H$ is a nonlinear invariant

$$e^{\mathcal{D}_H}H(\phi_x,J_x)=H(\phi_x,J_x),\quad \mathcal{D}_H\equiv\left(\partial_{J_x}H(\phi_x,J_x)\right)\partial_{\phi_x}-\left(\partial_{\phi_x}H(\phi_x,J_x)\right)\partial_{J_x} \tag{19}$$

For example, starting from the linear map

$$\mathcal{M}=\mathcal{A}^{-1}e^{\mathcal{D}_{K_2}}\mathcal{A},\quad \mathcal{D}_{K_2}\equiv 2\pi\nu_x\partial_{\phi_x}, \tag{20}$$

we may add a thin octupole kick

$$V(\tilde{x};s) = -\frac{(b_4L)}{4}\tilde{x}^4\delta(s) = -\frac{(b_4L)}{4}\left(3+4\cos(2\phi_x)+\cos(4\phi_x)\right)\delta(s), \tag{21}$$

and, by using the CBH theorem for non-commuting operators, we obtain

$$\mathcal{M} = \mathcal{A}^{-1}e^{\mathcal{D}_V}e^{\mathcal{D}_{K_2}}\mathcal{A} = e^{\mathcal{D}_{K_2}+\mathcal{D}_V+[K_2,V]/2+\dots}\mathcal{A}, \tag{22}$$

aka Birkhoff series; which in general does not converge. One exception is the one-resonance map; academic. So, instead we control the system by

$$e^{\mathcal{D}_V} \to I \tag{23}$$

3.6.14 One-Resonance Theory (Academic)

Close to a resonance $e = 4\nu_x - p$ for some integer p, it can be simplified to

$$\mathcal{M} = \mathcal{A}^{-1}e^{\mathcal{D}_{K_2}+\mathcal{D}_V+\dots}\mathcal{A} = \mathcal{A}^{-1}e^{\mathcal{D}_{K_2+V}+\mathcal{D}_V+\dots}\mathcal{A} = \mathcal{A}^{-1}e^{\mathcal{D}_H}\mathcal{A} \tag{24}$$

where

$$H(\phi_x,J_x) = \frac{\pi e}{3}J_x - \frac{(b_4L)}{8}J_x^2\left(3+\cos(4\phi_x)\right), \quad \nu_x(J_x) = \frac{\partial H}{2\pi\partial J_x} = \frac{1}{4}\left(e-3(b_4L)J_x\right) \tag{25}$$

with $H(\phi_x,J_x)$ an invariant and $\nu_x(J_x)$ anharmonic.

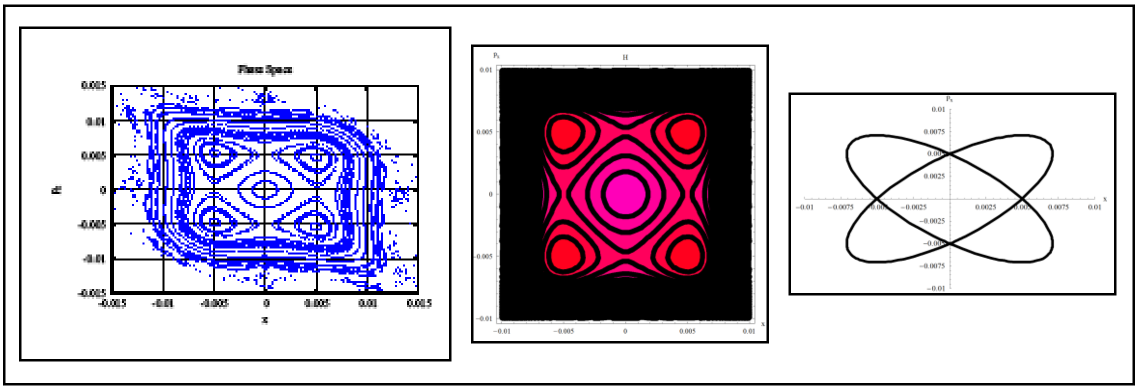

Figure 5: Tracking ($4\nu_x$ and $2\nu_x$), Invariant $H(\phi_x,J_x)$, and Separatrix ($\partial H/\partial J_x = \partial H/\partial\phi_x = 0$).

To summarize, this case is simple enough to be fully understood analytically. On the other hand, for a realistic 6D model the best approach is phase-space tracking; by a (straightforward) direct numerical integration of the equations of motion. In particular, the relativistic equations of motion in the co-moving, curvilinear reference frame (Eq. (33) p. 10 in ref. [1]). And, depending on the time scale, using a symplectic integrator.

3.6.15 **Control of the Dynamics: Poincaré Map Generators**

To summarize:

1. The action-angle variables are the invariants for the linearized equations of motion described by the quadratic Hamiltonian.
2. The differential operator is known as the Lie derivative, i.e., the derivative along a vector (Hamiltonian) flow: $\left[\partial_{J_x} H(\phi_x, J_x), -\partial_{\phi_x} H(\phi_x, J_x)\right]$. The generator $H(\phi_x, J_x)$ is a non-linear invariant.
3. The corresponding (formal) power series solution is called a Lie series.
4. Using this approach, the dynamics can be evaluated by a direct analysis of the *generators for the Poincaré map,* i.e., the source of the (non-linear) terms in the equations of motion. Rather than first having to find perturbative solutions to the non-linear equations of motion; around the lattice. And then analyze the effects (phenomenology) of those terms in the corresponding *trajectories*.
5. The dynamics can be controlled (directly), by controlling the coefficients for the generators. In other words, the dynamics is governed by a system of (over-constrained) non-linear algebraic equations.

For example, the leading order tune shift in 2 D.O.F. (Degrees of Freedom) with mid-plane symmetry (=> no skew multipoles) is generated by

$$K(\bar{J}) = 2\pi\bar{\nu}\cdot\bar{J} + a_{xx}J_x^2 + a_{xy}J_xJ_y, \quad \begin{cases} \nu_x(\bar{J}) = \dfrac{1}{2\pi}\dfrac{\partial H}{\partial J_x} = \nu_{0x} + \dfrac{a_{xx}}{\pi}J_x + \dfrac{a_{xy}}{2\pi}J_y, \\ \nu_y(\bar{J}) = \dfrac{1}{2\pi}\dfrac{\partial H}{\partial J_y} = \nu_{0y} + \dfrac{a_{xy}}{2\pi}J_x \end{cases} \tag{26}$$

Note also that e.g. a finite (positive) linear chromaticity

$$K(\bar{J}) = 2\pi\bar{\nu}\cdot\bar{J} + 2\pi\bar{\xi}\cdot\bar{J}\delta, \quad \begin{cases} \bar{\nu} = \dfrac{1}{2\pi}\dfrac{\partial H}{\partial \bar{J}} = \bar{\nu}_0 + \bar{\xi}\delta, \\ c_0\Delta t = -\dfrac{\partial H}{\partial \delta} = -2\pi\bar{\xi}\cdot\bar{J} \end{cases} \tag{27}$$

leads to a considerable path dependence on the betatron motion; due to the symplectic flow.

3.6.16 **Sextupoles: The Driving Terms (Lie Generators)**

The Hamiltonian for a sextupole is

$$V(x;s) = \frac{b_3(s)}{3}\left(x^3 - 3xy^2\right), \quad \tilde{x} = \mathcal{A}^{-1}x \equiv \frac{1}{2}\left(h_x^+ + h_x^-\right), \quad h_x^\pm \equiv \sqrt{2J_x}e^{\pm i\varphi_x} \tag{28}$$

and similarly for y. Summing up the leading order generators around the lattice

$$\mathcal{M} = \mathcal{A}^{-1} e^{\mathcal{D}_V + \cdots} e^{\mathcal{D}_{K_2}} \mathcal{A} \tag{29}$$

gives (generators)

$$V(\phi_x, J_x) = \sum_{|\bar{I}|=3} h_{\bar{I}} h_x^{+i_1} h_x^{-i_2} h_y^{+i_3} h_y^{-i_4} \delta^{i_5}, \quad I \equiv [i_1, i_3, i_3, i_4, i_5], \quad |I| = \sum_{k=1}^{5} i_k \tag{30}$$

where (driving terms)

$$h_{i_i i_2 i_3 i_4 i_5} = h^*_{i_2 i_1 i_4 i_3 i_5} \sim \sum_{\mathrm{k}=1}^{\mathrm{N}} (\mathrm{b}_{3\mathrm{k}} L) \beta_{xk}^{(i_1+i_2)/2} \beta_{yk}^{(i_3+i_4)/2} \eta_{xk}^{i_5} e^{i[(i_1+i_2)\mu_{xk} + (i_3+i_4)\mu_{yk}]} \tag{31}$$

depends only on the lattice properties, i.e., the sextupole strengths and optics. For a geometric view, they can be represented as phasors $[\mathrm{Re}\{h_{\bar{I}}\}, \mathrm{Im}\{h_{\bar{I}}\}]$ being summed up around the lattice; see below.

3.6.17 Sextupoles: Inventory and Phenomena

An inventory of the first and second order driving terms and related phenomena are summarized in Table 2.

Table 2: First and Second Order (in $b_3 L$) Sextupolar Driving Terms.

Order	Driving Term	Phenomena
1	h_{11001}, h_{00111}	$\partial \bar{\nu} / \partial \delta$
1	h_{20001}, h_{00201}	$\partial \bar{\beta} / \partial \delta$
1	h_{10002}	$\partial^2 \eta_x / \partial \delta^2$
1	$h_{10110}, h_{21000}, h_{30000}, h_{10020}, h_{10200}$	$\nu_x, 3\nu_x, \nu_x \pm 2\nu_y$
2	$h_{22000}, h_{11110}, h_{00220}$	$\partial \bar{\nu} / \partial J_{x,y}$
2	h_{11002}, h_{00112}	$\partial^2 \bar{\nu} / \partial \delta_2$
2	$h_{20110}, h_{11200}, h_{20020}, h_{20200}$	$2\nu_x, 2\nu_y, 2\nu_x \pm 2\nu_y$

3.6.18 Lattice Design and Chromatic Correction: Symmetry

Challenge: How to control the swamp of undesirable terms generated by (linear) chromatic correction for a strongly focusing lattice?

$$\mathcal{M} = \mathcal{A}^{-1} e^{\mathcal{D}_V + \cdots} e^{\mathcal{D}_{K_2}} \mathcal{A} \tag{32}$$

Solution: zero the undesirable terms in V; a highly over constrained problem. The most effective approach: use symmetry (reduces *all* terms). Note, since the amplitude dependent tune shift is a second order effect, it scales with the square of the number of sextupoles N_{b_3}. Whereas for a periodic lattice, it scales with the number of cells N_{cell}, i.e., linearly with the number of sextupoles per cell $N_{b_3,\text{cell}}$.

For example, linear achromats (in the phase-space variables): *N*-Bend-Achromats (DBA, TBA, and 7BA).

Traditional design strategies:

1. Avoidance (weakly focusing rings with high periodicity): Introduce two chromatic families and choose the working point so that systematic resonances are avoided.
2. Anti-symmetry (FODO lattices): Introduce two chromatic families separated by a hor. and ver. phase advance of $k\pi, k = \text{odd}$. However, this will systematically drive h_{20001} and h_{00201}.
3. Higher order achromats (strongly focusing lattices): define a unit cell, repeat it N times, and choose the phase advance so that all the (phase dependent) driving terms are cancelled over a structure, e.g. an arc. However, if this is done over an entire ring, the working point is now on an integer. For how to avoid this, see below.

3.6.19 **Example: 5-Cell Second Order Achromat**

1. Introduce two chromatic sextupole families.
2. Cancel the first order driving terms according to e.g. Tab. 3. For an example, see Fig. 6.

Table 3: 5-Cell Second Order Achromat.

Cell	$\bar{\nu}$	ν_x	$2\nu_x$	$2\nu_y$	$3\nu_x$	$\nu_x - 2\nu_y$	$\nu_x + 2\nu_y$
1	$[8/5, 3/5] = [1.6, 0.6]$	1.6	3.2	1.2	4.8	0.4	2.8
2		3.2	6.4	2.4	9.6	0.8	5.6
3		4.8	9.6	3.6	14.4	1.2	8.4
4		6.4	12.8	4.8	19.2	1.6	11.2
5		8	16	6	24	2	14

3. Introduce 1 more chromatic and 5 geometric (i.e., a total of 9 families => *full control of all the first order diving terms*) to provide leeway for the choice of working point; hence the 9 sextupole families for SLS [3].
4. The required number of sextupole (multipole) families, placement, etc. can be evaluated and optimized by analyzing the rank conditions for the Jacobian of the (algebraic) system for the driving terms [27,29].
5. Also, with care, higher order multipoles can also be beneficial, e.g. octupoles, see MAX-IV.

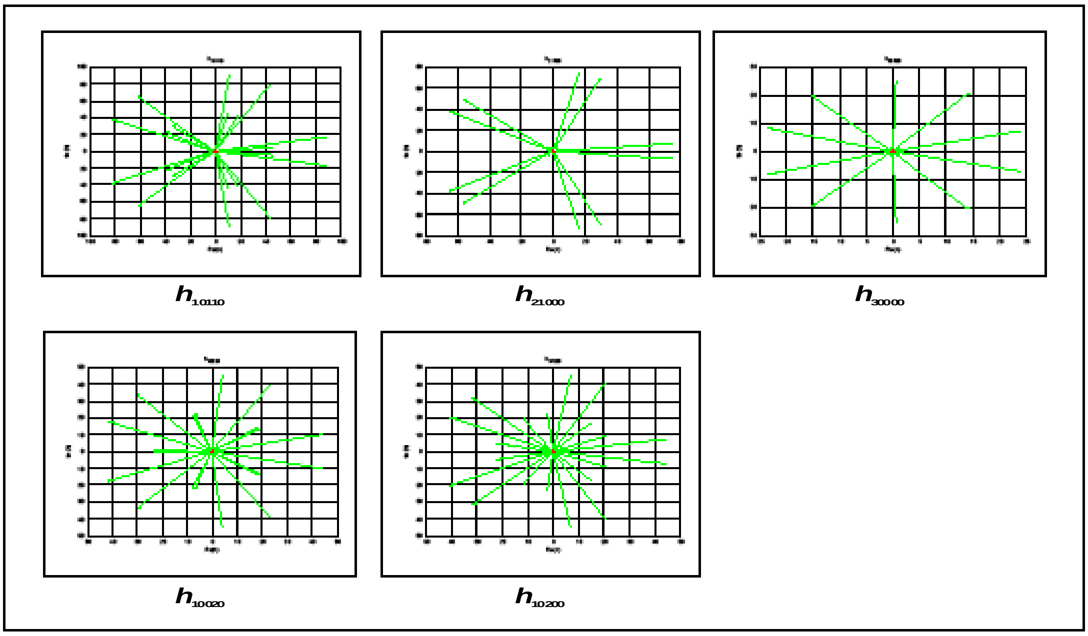

h_{10110} h_{21000} h_{30000} h_{10020} h_{10200}

Figure 6: First Order Geometric Sextupolar Effects Cancelled over 5 Cells.

3.6.20 **Conclusions**

- We have outlined a design philosophy based on a systems approach; rather than the traditional $\langle \mathcal{H}_x \rangle^{\min}$ (reductionist) approach.
- And provided two examples NSLS-II and MAX-IV that are counter intuitive to the traditional approach. The result of global vs. local optimizations. In particular, by a tempered approach, guided by the scaling properties of a complex system to e.g. balance $\mathrm{Min}\{\langle \mathcal{H}_x \rangle\}$ vs. $\mathrm{Min}\{S\}$, rather than the pursuit of a local minima for some particular aspect.
- We also pointed out how the pursuit of “engineering-science” has enabled the latter to mediate the technical risks.
- For the modeling aspects, we have pointed out the complementary aspects of analytical and numerical methods. And illustrated the importance of a geometric point of view to abstract math (differential geometry). See e.g. ref. [8] regarding confusing Truncated-Power-Series-Algebra [7] with differential algebra. Hence our use of Lie series (a differential algebra), Eq. (10), for the symplectic group. In other words, consistent with Leibniz’ rule ($\partial(ab) = \partial(a)b + a\partial(b)$).
- We have also emphasized how the outlined method(s) for the chromatic control problem can be pursued into the control room: i.e., “closing-the-loop”.

3.6.21 **References**

1. J. Bengtsson “Non-Linear Transverse Dynamics for Storage Rings with Applications to the Low-Energy Antiproton Ring (LEAR) at CERN” CERN 88-05.
2. J. Bengtsson, J. Irwin “Analytical Calculation of Smear and Tune Shift” SSC-232 (1992).
3. J. Bengtsson “The Sextupole Scheme for the Swiss Light Source (SLS): An Analytic

Approach” SLS Note 9/97.

4. E. Forest, R.D. Ruth “Fourth-Order Symplectic Integration” Physica D 43 (1), 105-117 (1990).
5. H. Yoshida “Construction of Higher Order Symplectic Integrators” Phys. Lett. A 150 (5-7), 262-268 (1990).
6. E. Chacon-Golcher, F. Neri “A Symplectic Integrator with Arbitrary Vector and Scalar Potentials” Phys. Lett. A 372 (26), 4661-4666 (2008).
7. M. Berz “The Method of Power Series Tracking for the Mathematical Description of Beam Dynamics” NIM A258 (3), 431-436 (1987).
8. V. Garczynski “Remarks On Differential Algebraic Approach to Particle Beam Optics by M. Berz” NIM A334, 294-298 (1993).
9. M. Borland et al “Direct Methods of Optimization of Storage Ring Dynamics and Momentum Aperture” Proc. PAC09, 3850-3852.
10. L. Yang et al “Multiobjective Optimization of Dynamic Aperture” PR ST-AB 14, 054001 (2011).
11. O. Chubar et al “Application of Genetic Algorithms to Sorting, Swapping and Shimming of the SOLEIL Undulator Magnets” AIP Conf. Proc. 879, 359-362 (2007).
12. E. Asséo, J. Bengtsson, M. Chanel “LEAR Beam Stability Improvements Using FFT Analysis” Proc. EPAC88, 541-543.
13. J. Bengtsson, M. Meddahi “Modeling of Beam Dynamics and Comparison with Measurements for the Advanced Light Source (ALS)” Proc. EPAC94, 1021-1023.
14. J. Safranek “Experimental Determination of Storage Ring Optics Using Orbit Response Measurements” NIM A388 (1-2), 27-36 (1997).
15. Y. Luo et al “Measurement and Correction of Third Resonance Driving Term in the RHIC” Proc. PAC07, 4351-4353.
16. R. Bartolini et al “Correction of Multiple Nonlinear Resonances in Storage Rings” PRST-AB 11, 104002 (2008).
17. A. Streun et al “Nonlinear Beam Dynamics Studies at the SLS” 2nd Workshop on Nonlinear Beam Dynamics in Storage Rings, DIAMOND Nov 2–4, 2009.
18. A. Franchi et al “Vertical Emittance Reduction and Preservation in Electron Storage Rings via Resonance Driving Terms Correction” PRST-AB 14, 034002 (2011).
19. J. Bengtsson, E. Forest “Global Matching of the Normalized Ring” AIP Conf. Proc. 255, 329-233 (1991).
20. D. Robin et al “Model Calibration and Symmetry Restoration of the Advanced Light Source” Proc. EPAC96.
21. C. Steier et al “Measuring and Optimizing the Momentum Aperture in a Particle Accelerator” Phys. Rev. E. 65, 056506 (2002).
22. E. Levichev, V. Kvardakov “Nonlinear Characteristics of the TME Cell” Proc. RuPAC06, 327-329.
23. R. Talman “Accelerator X-Ray Sources” Fig. 11.10, p. 355 (Wiley-VCH, Berlin, 2006).
24. A. Streun “A Standard Method of Nonlinear Lattice Optimization and Application to the Swiss Light Source Storage Ring” this newsletter.
25. W. Joho et al “Design of a Swiss Light Source (SLS)” Proc. EPAC94, 627-629.
26. J. Bengtsson et al “Status of the Swiss Light Source Project SLS” Proc. EPAC96.
27. J. Bengtsson et al “Increasing the Energy Acceptance of High Brightness Synchrotron Light Storage Rings” NIM A404 (2-3), 237-247 (1998).
28. A. Streun OPA.
29. J. Bengtsson “NSLS-II: Control of Dynamic Aperture” BNL-81770-2008-IR (2008).
30. NSLS-II CDR (2006).
31. J.B. Murphy et al “NSLS-II: A Future Source for the NSLS” Proc. EPAC04, 2457-2459.
32. J. Bengtsson “A Control Theory Approach for Dynamic Aperture” Proc. EPAC06, 3478-3480.

33. S.L. Kramer, J. Bengtsson "Optimizing the Dynamic Aperture for Triple Bend Achromatic Lattices" Proc. EPAC06, 3481-3483.
34. S. Krinsky, J. Bengtsson, S. Kramer "Consideration of a Double Bend Achromatic Lattice for NSLS-II" Proc. EPAC06, 3487-3489.
35. S. Ozaki et al "Philosophy for NSLS-II Design with Sub-Nanometer Horizontal Emittance" Proc. PAC07, 77-79.
36. M. Sommer "Optimization of the Emittance of Electrons (Positrons) Storage Rings" LAL/RT/83-15 (1983).
37. S.Y. Lee "Emittance Optimization in Three- and Multiple-Bend Achromats" Phys. Rev. E 54, 1940-1944 (1996).
38. SPEAR 3 Design Report (2002).
39. PETRA III Technical Design Report (2004).
40. S. Leeman "The MAX IV 3 GeV Storage Ring" this newsletter.
41. M. Sjöström, E. Wallén, M. Eriksson, L.-J. Lindgren "The MAX III Storage Ring" NIM A601 (3), 229-244 (2009).
42. "SOLARIS The First Synchrotron in Poland" Joint US-CERN-Japan-Russia School Erice, Italy, 6–15 April 2011.
43. S.T. Corneliussen "The Transonic Wind Tunnel and the NACA Technical Culture" NASA SP-4219 (1998).
44. M. Eriksson et al "The MAX-IV Design: Pushing the Envelope" Proc. PAC07, 74-76.
45. "Revised Design of the MAX IV Facility" MAX-lab (2009).
46. S.C. Leemann et al "Beam Dynamics and Expected Performance of Sweden's New Storage-Ring Light Source: MAX IV" PRST-AB 12, 120701(2009).
47. K. Bane et al "A Design Report of the Baseline for PEP-X: an Ultra-Low Emittance Storage Ring" SLAC-PUB-13999 (2010).
48. Y. Cai et al "PEP-X: An Ultimate Storage Ring Based on Fourth-Order Geometric Achromats" SLAC-PUB-14785 (2011).
49. M. Borland "Exploration of a Tevatron-Sized Ultimate Light Source" this newsletter.

3.7 Methods and Tools to Simulate, Optimize and Analyze non-linear Dynamics in low Emittance Storage Rings

Laurent S. Nadolski
Synchrotron SOLEIL, Gif-sur-Yvette, France
Mail to: nadolski@synchrotron-soleil.fr

3.7.1 Introduction

Optimizing the key parameters for the accelerator performance such as emittance for damping rings, luminosity for colliders or brilliances for light sources has always been very challenging over the years. Following the progress made in the understanding of the transverse beam dynamics, the accelerator parameters are constantly pushed to the limit set by the technologies of, among others, manufacturing magnets, magnetic measurements, alignment in the tunnel and beam based measurement benefiting from the improvement of diagnostic equipment such as beam position monitors (BPMs). Lattice design of today's and tomorrow's accelerators like third generation light sources (3GLS) is very demanding (see requirements in Ref. [1]) and still occupies the major part of the work of accelerator physicists. In this paper a selection of recent new approaches and tools to model and optimize the non-linear transverse dynamics is presented. The used material is largely taken from a talk given last year during the IPAC’11 International Particle Conference in San Sebastian.

3.7.2 Requirements for Modern Light Sources

Over the last 60 years the ring-based light sources have evolved from first generation where synchrotron light was used as a parasite mode of operation of the high energy physics, to second and third generations with dedicated storage rings producing synchrotron light and serving many users at the same time. If for today’s 3GLSs the photon beam is diffracted limited in the vertical plane for photons around a few Angstroms, a new class of storage rings will soon emerge with ultra-low horizontal emittance in order to reach a diffracted limited photon beam in both transverse planes. This class could be named 3+ to distinguish these facilities from the forth-generation light sources based on LINAC or recirculation schemes. The lowest horizontal emittance is reached today by the Petra-III facility with an emittance value of 1 nm.rad. Table 1 gives the expected horizontal emittances of forthcoming 3+GLSs with emittances a factor 100 smaller.

Table 1: Expected horizontal emittance for future ring-based light sources.

Future Storage Ring Facility	*Energy (GeV)*	*Horizontal emittance (*pm.rad)
NSLS-II	3	600
MAX-IV	3	300
PEPX	4.5	12
Spring8 upgrade	6	10
APS upgrade	7	15

To achieve such a low horizontal emittance value, the arrangement of the magnets, namely the lattice, becomes more and more compact and complex using optics blocks such as theoretical minimum emittance, multi-bend achromat structures and/or smart combinations of both of them [2, 3]. Introduction of damping wigglers is also an option to reduce further down the emittance [4-7]. The reader should be aware that this is a significant step from relatively simple lattices, like the triple bend lattice of the ALS [8] using only two families of sextupoles to correct for the linear chromaticities to highly complex multi-parameter lattices with a very large number of sextupoles and even octupoles in the case of MAX-IV [9]. All these additional multipoles are solely introduced to compensate for the large chromaticities introduced by the strong focusing lattices and at the same time to reduce as much as possible the resonance driving terms inherent of the multipoles.

Among all the parameters needed to be fulfilled to design state of the art low emittance storage rings providing the user community with high photon flux and brilliance, two of them are very significant: The horizontal dynamic aperture should be large enough to allow injection off-axis (typically 15-25 mm) as long as any technical solution is devised for on-axis injection; Long enough beam lifetime is another requirement. For such strong focusing optics Touschek lifetime becomes the dominant regime asking typically for a 2 to 4% transverse momentum aperture. This point is critical even for facilities running Top-up injection since long lifetime contribute to a reduction of the beam losses, activation in the tunnel and running cost of such facilities.

One of the challenges of light sources is to optimize simultaneously on- and off-momentum dynamic apertures. On the hand, the lattice has to be very robust with respect to alignment errors, multipole errors, and on the other hand, it has to keep its nominal performance when powerful and new types of insertion devices (IDs) are introduced in the lattice. The IDs are the dominant photon sources in 3GLSs. Examples are low gap in-vacuum undulators, Apple-II, Apple-III, Figure-8 undulators, high-field wigglers and fast switching electromagnetic undulators. Today's low vertical emittance and tomorrow's low horizontal emittance constrain even more the requirements to keep the ring performance against dynamical configurations of tens of undulators freely controlled by the users.

In the next section, the modeling of magnets and IDs will be briefly discussed. Then major strategies for optimizing non-linear transverse beam dynamics will be described by emphasizing three tools: frequency map analysis, resonance driven term methods, and genetic algorithms.

3.7.3 **Modeling of Magnets and Insertion Devices**

3.7.3.1 ***Main Magnets***

Tracking codes are essential simulation tools for predicting the on- and off-momentum transverse beam dynamics of particles circulating in an accelerator. Non-spurious effects, energy conservation for long term tracking codes are relevant features to accurately compute dynamic aperture (DA), to estimate resonance widths or to calculate Touschek lifetime. Due to a relatively short damping time of a few milliseconds in electron storage rings, tracking over a few thousand of turns is enough providing that a stability index such as the diffusion index of frequency map analysis is used. Most of the modern tracking codes, such as MADX/PTC [10], TRACY-III [11], LEGO [12], ELEGANT [13], SAD [14], are based on symplectic integration schemes. Ruth and Forest have popularized symplectic integrators in the 1983–1990 [15, 16]. Then Neri introduced the use of Lie Algebra (1988) [17] and Yoshida techniques to build arbitrary high order integrators (1990) [18]. Implicit and explicit integration schemes are possible. McLachlan [19] and Laskar [20] have proposed even more stable schemes. All these classes of integrators have the required properties of long term integration such as energy preservation, bounded errors, phase stability (see Ref. [21] and references therein for more details).

3.7.3.2 ***Insertion Devices***

Modeling insertion device has slowly shifted from Halbach formalism to more accurate methods due to the complexity of the IDs in term of non-linear fields, short periods, narrow pole widths, aperiodicity, polarization, and lower gaps. Symplectic integration schemes are based either on Taylor expansion of the electromagnetic field or on kick maps [22-24].

Moreover the assembling of the IDs has significantly changed in order to reduce all non-linear perturbations. Evolutionary algorithms [25] can be used to sort the magnet blocks during the assembly phase to minimize several merit functions such as: first and second order field integrals, normal, skew gradients, phase errors. Special sets of magnets (magic fingers) are usually placed at the ends of the IDs to reduce the impact of higher order field integrals at large transverse amplitudes. Additional active (dedicated correction coils, multipole wires) or passive corrections are introduced if required, and can be included in tracking codes.

3.7.4 Diagnostics Tools and Means for Optimization

3.7.4.1 *Data Acquisition Using Turn-by-Turn BPMs*

Thanks to the improvement of the BPM electronics, turn-by-turn (TbT) data have become a valuable tool to analyze non-linear beam dynamics. Typically TbT BPM resolution is 10 μm for a few milli-amperes of stored beam. An additional constraint when carrying out beam-based experiments is the beam smearing due to the fact that the kicked beam is a bunch of particles. With a slightly different energy and transverse amplitude, each particle encounters various non-linear magnetic fields. As a result the motion of the centroid of the particles is shifted from coherent to incoherent. Its amplitude of oscillation then decreases much faster than the damping time: in a few tens or hundreds of turns. Algorithms to precisely determine betatron tunes lose their precision [26]. Lines in the frequency domain excited by resonance of order m decohere m times faster than the tune line [27]. Moreover artifacts from the BPM themselves like mixing between turns, cross-talks between RF-channels of the BPM front-end, RF-channel gain or non-linear response due to the asymmetry of the vacuum chamber hosting the BPM make the analysis difficult [28]. All these facts need to be evaluated and corrected carefully before drawing any conclusion from the TbT data analysis of the non-linear motion of the beam.

3.7.4.2 *Frequency Map Analysis*

Frequency Map Analysis (FMA [29-31]) is a refined Fourier technique to build a quasi-periodic decomposition of a signal over time. For accelerators, the first frequencies of the decomposition are the betatron tunes; the others are related to resonance driving terms (RDTs). FMA builds a two-dimension mapping between the dynamic aperture and the tune-space and gives a global and detailed view of the transverse beam dynamics. Its convergence speed distinguishes FMA from other techniques: it goes as the fourth power of the number of turns used for the analysisfor data filtered with a Hanning window [31]. The so-called diffusion index is the tune variation with respect to time and can be coded as a color in the DAs and FMAs. It makes easy and intuitive the distinction of linear motion from non-linear or chaotic motion, resonances limiting the on- or off-momentum apertures. FMA features are specially adapted to reduce the number of turns tracked in simulation and are suitable for getting useful information even if the experimental data points are limited because of beam smearing. FMA is now widely used from design stage to beam-based measurements [32-34]. It is worth noting that a very accurate description of the machine model of BESSY-II was obtained and experimentally validated with FMA only after introducing fringe field of dipoles and quadrupoles, systematic errors like octupoles in quadrupoles and decapoles in correctors hosted in sextupoles. This is an example of the very good agreement that can be reached today between model and experiment for on-momentum dynamics [35]. Similarly, agreement for off-momentum dynamics can be as good as a few percent [36, 37] while a factor two was widely accepted 10 or 20 years ago (Fig. 1).

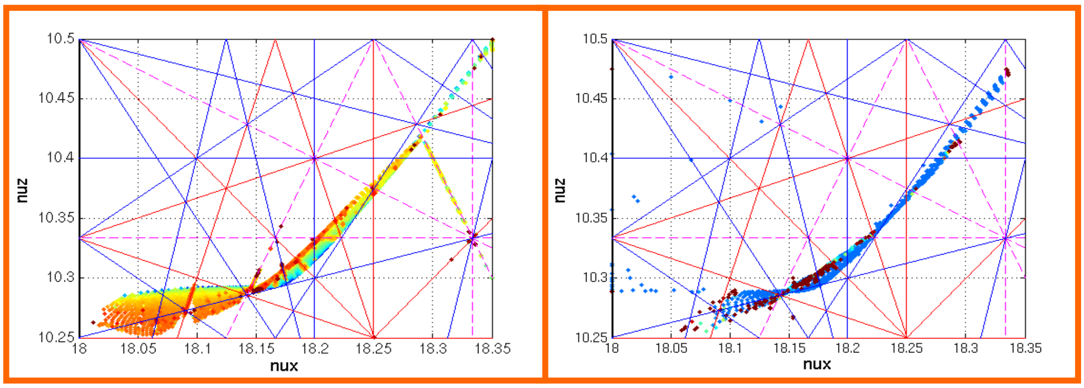

Figure 1: Off-momentum frequency maps associated with the energy/horizontal acceptance (dp/p, x) of the SOLEIL storage ring. The comparison between the model (left) and the measurement (right) gives a very good agreement for the working point 18.202/10.317. The same network of resonances is displayed by both maps giving an energy acceptance of 4% for the lattice without any insertion devices [36].

3.7.5 Optimization Methods and Selected Results

3.7.5.1 *Sextupole Optimization and Resonant Driving Terms*

The standard method for optimizing sextupoles, main non-linear elements introduced for correcting the chromaticities, is based on an analytical approach: the perturbation theory that allows to compute the resonant driving terms excited by such multipoles [38, 39]. When applying this technique to sextupoles, 7 and 13 driving terms are excited to the first and second orders of the theory. More precisely, at first order these terms are the 2 linear chromaticities and 2 and 3 terms related to respectively the first and third order resonance. Second order terms are the 2 non-linear chromaticities, the 3 tune-shifts with amplitude, and 2x4 terms related to respectively second and fourth order resonant driving terms.

Usually lattice designers use least-squared-like minimization algorithms to optimize all these driving terms. Their work is complicated due to the complexity of the adjustment between linear and non-linear optics on one hand, and of on- and off-momentum dynamics optimization on the other hand. Even if powerful tools are now available, this works, although proven to be successful, is still not automated, can be tedious and requires a lot of manual iterative steps. Results will mainly depend on the weights put on each RDT and the accelerator physicist’s experience.

In addition, since this optimization is based on perturbation approach, it does not guarantee the best results. Future challenging 3GLSs are required to have extra knobs in order to reduce furthermore the RDTs such as non-linear chromaticity or octupolar terms. For instance SLS then MAX-IV facilities have proposed to re-cable unused extra binding of sextupole magnets as sextupoles and skew quadrupoles [40, 41]. A very nice result has been obtained at SLS. The lifetime reduction was recovered for the operation mode, this means an improvement by a factor 2 of the beam lifetime normalized by the stored current. Equipping the storage ring with individual power supply sextupole is also a way to increase the tuning flexibility of the non-linear dynamics.

Another approach consists in choosing specific phase advanced between sextupoles of a same family (interleaved sextupoles) to cancel by construction the RDTs. When doable, the introduction of geometric achromats eliminates all the geometric third order terms and can even be extended to cancel out almost all the fourth order geometric terms [42].

3.7.5.2 *Using FMA to Reduce the RDTs*

Thanks to the improvement of the turn-by-turn BPM precision, new methods for minimizing RDTs directly based on TbT data have been proposed and are very promising [43]. For comparing real and model lattices the code LOCO [44] has been proven to be very successful for small and medium circumference storage rings where beta-beat is corrected below 1% RMS. For large facilities, computation issues become a brake to such a method. It is only based on closed orbit data (orbit response matrix and dispersion function). Similarly, using turn-by-turn data, FMA-like algorithms give amplitude and phase of the spectral lines of the betatron motion that can be used to compare and correct the real accelerator with respect to the model. The knobs are skew quadrupoles, sextupoles, and higher order multipoles. This technique should allow us, in the future, to calibrate the non-linear model and give a large control of the non-linear resonances [26, 27]. A first application at DIAMOND light source has given slight improvement of the lifetime. With better resolution of BPM TbT data, this method will open new doors to characterize and tune the non-linear beam dynamics using directly the beam [37]. BPM resolution is already good enough for tuning betatron coupling using skew quadrupoles (see for instance the low vertical emittance preservation at ESRF [45]). Another application could give a way to online monitor and tune the multipoles of the storage ring [46].

3.7.5.3 *Global Analysis of a Given Lattice*

New methods for optimizing lattices have appeared over the last decades. An example developed at the ALS is the GLASS technique that stands for GLobal scan of All Stable Settings [47]. This technique is well adapted for highly periodic lattices when only a few parameters are scanned due to computation time limitation. In the work reported in Ref. [47], a billion lattices were scanned using 3 quadrupole and 2 sextupole families. After one day of computation, one million stable linear solutions were identified. Then their main properties were computed to build up a large and exhaustive database. Solutions were then sorted by emittance, brilliance values, tunes, DA sizes, momentum compaction values, and so on. In that way a global view of all the performances reachable with the ALS lattice was obtained in a very practical manner. Output of this study gave 13 stable areas (Fig. 2), among them only 2 were known before, others are promising or even counter-intuitive. For example, it was discovered that ALS could still run while switching off one or two families of quadrupoles. New potential capabilities enhancing the brilliance were suggested with low horizontal beta-function and lower emittance. However this method cannot be directly applied to most of 3GLSs since the parameter space is too large (typically ten families of quadrupoles and sextupoles).

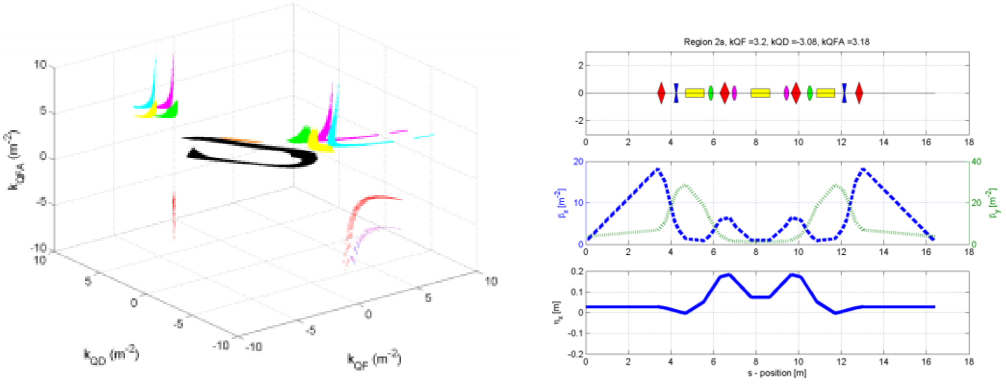

Figure 2: The application of the GLASS technique on the ALS lattice gives 13 stable areas (left side) represented by different colours in the parameter space (three families of quadrupoles). Seven of these regions give a horizontal emittance below 10 nm.rad. An example of the linear lattice for a low emittance lattice with mini beta function at injection is given by the right figure (Top: lattice structure; Middle: beta functions; Bottom: horizontal dispersion function) [47].

3.7.5.4 *Genetic Algorithms*

Genetic algorithms are a very promising solution to alleviate the limitation of GLASS. They are based on direct tracking. The focus was first on optimization of the non-linear dynamics. They become very attractive because they open new windows of optimization and give solutions never thought before. Moreover beam-based experiments have started to confirm these findings. Multi-Objective Genetics Algorithms (MOGA) applied to accelerator physics are the results of a long and continuous effort, more than ten years, first started at APS and then followed by others: ALS, BNL, … [48] (see Ref. [49] for a tutorial to MOGA). Thanks to development of computer clusters and improvement of CPUs, access to massive and parallel computation has become affordable.

Definition of suitable objective functions is essential for direct tracking methods. The most popular and successful functions of merit are on- and off-momentum dynamic apertures. Recently including tune-shifts with amplitude has been shown to speed up the algorithm convergence [50]. Addition of other driving terms is not required even if they can help. To reduce the time for computing dynamic aperture different algorithms have been developed. Only a small number of turns are typically used (64 to 128), which has been proven to be enough as a first step to narrow down the number of solutions. As a second step, long-term tracking (1 000 to 2 000 turns) and FMA are used to select the best and most robust solutions. As reported in Ref. [50], in the case of NSLS-II, starting with population of 6 000, computation of 300 generations takes less than a week on a Sun Grid Engine Cluster made of 96 standard CPUs. Results give large enough dynamic apertures with flat amplitude tune-shift to avoid crossing resonance lines. An interesting result is that small RDTs are a necessary but not a sufficient condition for getting large DAs. Multi-objective optimization is effective and has been shown to be robust to errors. Experimental results at APS give an increase of the beam lifetime by 25 % and 10 % respectively for 24-bunch and hybrid filling patterns used in operation [48]. Amazingly, it is demonstrated that a slight symmetry break of the SR periodicity results in a 25% lifetime improvement without any reduction of the injection efficiency (90–100 %) at APS. Application to an intermediate energy 3GLS, namely DIAMOND, has also given an experimental increase of 25% of the lifetime [51]. These results are the proof that genetic algorithms have become mature techniques for optimizing simultaneously on- and off-momentum apertures. A step forward has been reached at ALS with the optimization of both linear and non-linear beam dynamics using MOGA and the diffusion index obtained through FMA as a merit function [52] (Fig. 3).

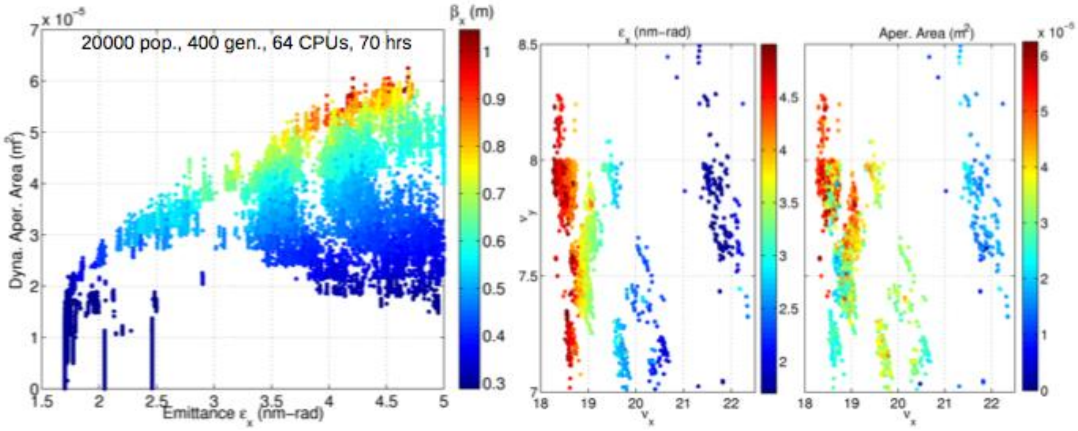

Figure 3: Ultimate ALS lattice as a result of the application of MOGA technique to simultaneously optimize the linear and nonlinear transverse beam dynamics. Seven parameters are used: 3 quadrupole and 6 sextupoles families. On the left the dynamics aperture is shown versus the emittance. On the right the tune space is painted using a colour index to denote emittance values and dynamics apertures [52].

3.7.6 Conclusion and Perspectives

Over the last 20 years tracking codes have become much more trustable. Agreement between real and modeled lattices has shifted from a factor 2 down to a few percent for tune-shifts with amplitude and energy, on- and off-momentum dynamic apertures. This tremendous step forward is partly due to the significant progress in diagnostics: the turn-by-turn BPM data and the development of fast dedicated kicker magnets for probing and studying non-linear dynamics. Nowadays, accelerator physicists are well equipped for predicting the performance of a lattice and the effect of the introduction of new equipment such as insertion devices in a storage ring. FMA like techniques give a global and comprehensible view of the non-linear beam dynamics. Promising results have been obtained using RDTs based on turn-by-turn data. This trend will strongly benefit from future higher resolution BPMs. MOGA like algorithms enable us to optimize simultaneously the on- and off-momentum apertures. This is a significant shift from sequential to parallel optimization. These new ways of optimization have opened new horizon windows with sometime unpredictable and amazing results. So the improvement in lattice modeling combined with the latest simulation techniques and progress on accurate beam based measurements using TbT data makes us confident for the design and the operation of ever brighter light sources, diffracted limited in both horizontal and vertical planes.

3.7.7 Acknowledgement

The author would like to thank M. Borland, L. Emery, P. Kuske, X. Huang, Y. Cai, J. Safranek, C. Steier, D. Robin, L. Yang, K. Sotome, S. Leemann, A. Streun, R.

Bartolini, A. Franchi, R. Tomàs, Y. Papaphilippou, A. Kling, and M. Chiu for providing materials for this article and many useful discussions. The author expresses his gratitude to A. Nadji and R. Nagaoka for very stimulating interactions.

3.7.8 References

1. M. Bei et al., “The Potential of an Ultimate Storage Ring for Future Light Sources”, Nucl. Intrum. & Methods A, Vol. 622, Issue 3, pp. 518-535 (2010).
2. S. C. Leemann and A. Streun, “Perspectives for future light source lattices incorporating yet uncommon magnets”, Phys. Rev. ST Accel. Beams, 14:030701, Mar 2011.
3. Y. Cai. “Single-particle dynamics in electron storage rings with extremely low emittance. Nuclear Instruments and Methods”, Nucl. Intrum. & Methods A, Vol. 645(1), pp. 168-174 (2011).
4. H. Wiedemann, “An Ultra-Low Emittance for PEP using Damping Wigglers”, Nucl. Intrum. & Methods A, Vol. 266 (1988).
5. M. Tischer et al., “Damping Wigglers for the PETRA-III Light Source”, PAC'05, Knoxville, pp. 2446-2448, (2005).
6. S. Ozaki et al., “Philosophy for NSLS-II design with sub-nanometer horizontal emittance”, PAC'07, Albuquerque, pp. 77-79 (2007).
7. S. C. Leemann et al., “Beam Dynamics and Expected Performance of the Sweden's new Storage-Ring light source: MAX-IV”, Phys. Rev. ST Accel. Beams, 12:120701, Dec 2009.
8. “Advanced Light Source 1-2 GeV Synchrotron Radiation Source”, Conceptual Design Report, LBNL publication PUB-5172, Berkeley (1986).
9. MAX-IV Detailed Design Report, available for download at http://www.maxlab.lu.se/maxlab/max4/index.html.
10. MAD home page, http://mad.web.cern.ch/mad.
11. J. Bengtsson, Tracy-2 User's Manual (unpublished).
12. Y. Cai et al., “LEGO: A Modular Accelerator Design Code”, SLAC-PUB-7642, August 1997.
13. M. Borland, “Users Manual for Elegant”, APS LS-231, May 6, 1993.
14. SAD home page, http://acc-physics.kek.jp/SAD/
15. R. D. Ruth, “A canonical Integration Technique”, IEEE Trans. Nucl. Sci., Ns-30, pp. 2669-2671 (1983).
16. E. Forest and R. D. Ruth, “Fourth-order symplectic integration”, Physica D, Nol. 43(1), pp. 105-117 (1990).
17. F. Neri, “Lie algebras and canonical integration”, Dept. of Phys., Maryland University (1987).
18. H. Yoshida, “Construction of high order symplectic integrators”, Phys. Let. A, Vol. 150, No 5-7, pp. 262-268 (1990).
19. R. I. McLachlan, “Composition methods in the presence of small parameters”, BIT Vol. 35, No. 2, pp. 258-268 (1995).
20. J. Laskar and P. Robutel, “High order symplectic integrators for perturbed Hamiltonian systems”, Celestial Mechanics, Vol. 80, pp. 39-62 (2001).
21. E. Forest, “Geometric integration for particle accelerators”, J. Phys. A: Math. Gen. 39 5321(2006).
22. P. Elleaume et al., “A new approach to the electron beam dynamics in undulators and wigglers”, EPAC'92, pp. 661-663 (1992)
23. Y. K. Wu, E. Forest, and D. S. Robin, “Explicit symplectic integrator for s-dependent static magnetic field”, Phys. Rev. E, 68:046502, Oct 2003.
24. J. Bahrdt and G. Wüstefeld, “Symplectic tracking and compensation of dynamic field

integrals in complex undulator structures", Phys. Rev. ST Accel. Beams,14:040703, Apr 2011.

25. O. Rudenko and O. Chubar, "An Evolutionary Approach to Shimming Undulator Magnets for Synchrotron Radiation Sources", Proceedings of 9th Int. Conf. on Parallel Problem Solving from Nature PPSN IX, p. 362 (2006).
26. R. Bartolini et al., "Precise Measurement of The Betatron Tune", Part. Acc. Vol. 55, pp. 247-256 (1995).
27. R. Tomàs, "Direct Measurement of Resonance Driving Terms in the Super Proton Synchrotron of CERN using Beam Position Monitors", Ph.D. Thesis Dissertation (2002).
28. R. W. Helms and G. H. Hoffstaetter, "Orbit and optics improvement by evaluating the non-linear beam position monitor response in the Cornell electron storage ring", Phys. Rev. ST Accel. Beams, 8:062802, Jun 2005.
29. J. Laskar, "Secular evolution of the solar system over 10 million years", Astronomy & Astrophysics, Vol. 198, pp. 341-362 (1988).
30. J. Laskar, "The chaotic motion of the solar system. A numerical estimate of the size of the chaotic zones", Icarus, Vol. 88, pp. 266-291 (1990).
31. J. Laskar, "Introduction to Frequency Map Analysis", Proceedings of 3DHAM95 NATO Advanced Institute, S'Agaro, June 1995, C. Simo Ed., pp. 134-150.
32. D. S. Robin et al., "Global Dynamics of the Advanced Light Source Revealed through Experimental Frequency Map Analysis", Phys. Rev. Lett. 85, 558-560 (2000).
33. C. Steier et al., "Measuring and optimizing the momentum aperture in a particle accelerator", Phys. Rev. E, 65, 056506 (2002).
34. L. Nadolski and J. Laskar, "Review of single particle dynamics for third generation light sources through frequency map analysis", Phys. Rev. ST Accel. Beams 6, 114801 (2003).
35. P. Kuske, "Effects of Fringe Fields and Insertion Devices revealed through experimental Frequency Map Analysis", Proceedings of PAC'05, Knoxville, pp. 266-268 (2005).
36. P. Brunelle et al., "Nonlinear beam dynamics studies at SOLEIL using experimental frequency map analysis", Proceedings of IPAC'10, Japan, pp. 4653-4655 (2010).
37. R. Bartolini et al., "Calibration of the non-linear ring model at the Diamond light source", Phys. Rev. ST Accel. Beams, 14:054003, May 2011.
38. J. Bengtsson, "Non-linear transverse dynamics for storage rings with applications to the Low-Energy Antiprotron Ring (LEAR) at CERN", CERN 88-05, August 1988.
39. J. Bengtsson, "The sextupole scheme for the Swiss Light Source (SLS): An Analytic approach", SLS-Note 9/97, March 1997.
40. A. Streun, "Nonlinear Beam Dynamics Studies at the SLS", Proceedings of Non-linear Beam Dynamics Workshop, Diamond, 2009, http://www.diamond.ac.uk/Home/Events/Past_events/ NBD_workshop.html.
41. A. Streun, "Non-linear dynamics at the SLS Storage Ring", Proceedings of the Low Emittance Rings Workshop 2010, http://ler2010.web.cern.ch.
42. Y. Cai et al., "PEP-X: An ultimate Storage Ring Based on Fourth-Order Geometric Achromats", SLAC-PUB-14785 (2011).
43. R. Bartolini and F. Schmidt. "Non-linear ring model calibration with frequency analysis of betatron oscillations". Proceedings of PAC'05, Knoxville, pp. 1452-1454 (2005).
44. J. Safranek, "Experimental Determination of Storage Ring Optics using Orbit Response Measurements", Nucl. Inst. And Meth. A388, 27 (1997).
45. A. Franchi et al, "Vertical emittance reduction and preservation in electron storage rings via resonance driving terms correction", Phys. Rev. ST Accel. Beams, 14:034002 (2011).
46. A. Franchi, R. Tomàs, and F. Schmidt, "Magnet strength measurement in circular accelerators from beam position monitor data", Phys. Rev. ST Accel. Beams,

10:074001 (2007).
47. D. S. Robin et al., “Global analysis of all linear stable settings of a storage ring lattice”, Phys. Rev. ST Accel. Beams, 024002 (2008).
48. M. Borland et al, “Direct Method of Optimization of Storage Ring Dynamic and momentum Aperture”, Proceedings of PAC'09, Vancouver, pp. 3850-3852 (2009).
49. A. Konak et al, “Multi-objective optimization using genetic algorithms: A tutorial”, Reliability Engineering and system Safety, Volume 91, Issue 9, pp. 992-1007 (2006), ISSN 0951-8320, 10.1016/j.ress.2005.11.018.
50. L. Yang, Y. Li, W. Guo, and S. Krinsky. “Multiobjective optimization of dynamic aperture”, Phys. Rev. ST Accel. Beams, 14:054001 (May 2011).
51. Courtesy of Riccardo Bartolini.
52. C. Sun, “Dynamics Aperture Optimization using Genetic Algorithms”, Proceeding of PAC'11, New York (2011).

3.8 A Standard Method of Nonlinear Lattice Optimization and Application to the Swiss Light Source Storage Ring

Andreas Streun
Paul Scherrer Institut, 5232 Villigen, Switzerland
Mail to: andreas.streun@psi.ch

3.8.1 Introduction

Low equilibrium emittance in a storage ring requires a large number of bending magnets with a horizontal beam focus at each and thus a large number of strong quadrupoles. The momentum dependence of the quadrupoles’ focusing strength causes large negative chromaticities, which have to be corrected by strong sextupoles in dispersive regions in order to suppress the head-tail instability. The nonlinear recursion of a particle orbiting in a lattice with sextupoles can lead to unstable motion beyond some amplitude, called the dynamic acceptance of the lattice. Small transverse acceptance impedes injection into the ring and accumulation of beam, and small lattice momentum acceptance, i.e. the momentum dependent transverse acceptance, leads to short beam life time due to Touschek scattering.

Optimization of the dynamic acceptance is probably the most critical challenge in the design of any low emittance ring. During the past decades a “standard method” has been established, which will be described together with its practical implementation in the code OPA, and its application to both the design and operation of the SLS and to the design of MAX IV.

3.8.2 The Standard Method of Nonlinear Optimization

3.8.2.1 *The Single Particle Hamiltonian*

The commonly used transverse Hamiltonian for the paraxial motion of a highly relativistic particle in a flat storage ring is given by

$$H = \frac{P_x^2 + P_y^2}{2(1+\delta)} - b_1 x\delta + \frac{b_1^2}{2} + \Re\left(\sum_{n\geq 2} \frac{b_n}{n}(x+iy)^n\right) \quad , \qquad (1)$$

with $P_{x,y} = p_{x,y}/p_o$ and $\delta = p/p_o$ the transverse and total momenta normalized to a reference momentum p_o. The magnetic fields are assumed to be static and piecewise constant, having either a cartesian symmetry or a cylindrical symmetry of low curvature. They are decomposed into regular multipoles including chromatic aberrations

$$b_n = \frac{1}{(1+\delta)}\left(\frac{e}{p_o}\right)\frac{1}{(n-1)!}\left.\frac{\partial^{(n-1)} B_y(x, y=0)}{\partial x^{(n-1)}}\right|_{x=0}. \tag{2}$$

3.8.2.2 *First Order Sextupole*

Introducing the linear optics ($b_{(n>2)} = 0$) solutions for a flat lattice in resonance basis, with $\beta_{x,y}$ the beta functions, η the [horizontal] dispersion and $\mu_{x,y}$, $2J_{x,y}$ the betatron phases and amplitudes,

$$x = \frac{1}{2}\left(h_x^+ + h_x^-\right) + \eta\delta, \quad y = \frac{1}{2}\left(h_y^+ + h_y^-\right) \text{ with } h_z^{\pm} = \sqrt{(2J_z)\beta_z}\, e^{\pm i\mu_z}, \quad (z = x, y) \tag{3}$$

and expanding up to 3rd order in coordinates x, y, δ provides the ten terms of first order in sextupole strength

$$\begin{aligned} h_{jklmp} = a_{jklmp}(2J_x)^{(j+k)/2}(2J_y)^{(l+m)/2} \cdot \Bigg(& \sum_n^{N_{sext}} (b_3L)_n \beta_{xn}^{(j+k)/2} \beta_{yn}^{(l+m)/2} e^{i\{(j-k)\mu_{xn}+(l-m)\mu_{yn}\}} \\ & - \left[\delta^p \cdot \sum_n^{N_{quad}} (b_2L)_n \beta_{xn}^{(j+k)/2} \beta_{yn}^{(l+m)/2} \eta^p e^{i\{(j-k)\mu_{xn}+(l-m)\mu_{yn}\}} \right]_{\text{if } p>0} \Bigg) \end{aligned} \tag{4}$$

with j, k, l, m, p integers and a_{jklmp} a constant. Each sextupole kick (in modeling, there may be many kicks from one thick sextupole) corresponds to a vector in the complex plane, with the local optical functions and its integrated strength (b_3L) defining the length and local betatron phases defining the angle. For $p > 0$ there are also contributions from quadrupoles. We find five chromatic terms ($p > 0$) which also contain quadrupole contributions. Two of these, h_{11001} and h_{00111}, are real and phase independent, and essentially equate to the chromaticities. h_{20001} and h_{00201} drive momentum dependant beta-beat and, as a 2nd order effect, the 2nd order chromaticities, while h_{10002} drives the 2nd order dispersion. The five geometric terms h_{21000}, h_{30000}, h_{10110}, h_{10200} and h_{10020} drive the sextupole resonances Q_x, $3Q_x$, $Q_x \pm 2Q_y$: resonance denominators appear when calculating N periods, i.e. h_{jklmp}^N [1]. To all resonant (i.e. phase dependent) terms exists a complex conjugate of same magnitude and opposite phase $h_{jklmp}{}^* = h_{kjmlp}$.

Early approaches continued with a Fourier transformation of the h_{jklmp} terms to find and suppress driving terms for single resonances in the vicinity of the working point. This however works mainly for machines of large periodicity. In general, it is preferable to suppress the complete non-linear Hamiltonian as source of all the resonances.

3.8.2.3 *Phase Cancellation Schemes*

Ideally, the two chromatic terms are set to the desired values (usually slightly positive) and the others to zero. Since the terms are linear in sextupole strength they may be arranged as a linear system of equations. In general, 2 real and 8 complex terms give 18 equations. But often lattices are symmetric, i.e. each sextupole has its counterpart at opposite phase, so the imaginary parts cancel and 10 equations are left.

With M families of sextupoles a $10{\times}M$ system is thus obtained, which is then analyzed and solved by a suitable algorithm like Singular Value Decomposition (SVD), which also works for over- or underdetermined systems and provides a vector of weight factors revealing possible degeneracy.

In lattices with dispersion-free straight sections sextupole families form two groups: chromatic families in the arcs making use of dispersion for chromaticity correction, and harmonic families in the straights for compensation of the adverse effects of the chromatic sextupoles. In a low emittance lattice the horizontal phase advance per cell approaches 180° in order to provide a focus in each bending magnet. As a result, the h_{20001} term becomes proportional to the horizontal chromaticity h_{11001}, because $e^{i2\mu_x} \approx 1$. Thus the linear system is degenerate and can not be solved for the vector of sextupole strengths. The strong h_{20001} will introduce momentum dependent variation of beta functions and thus cause large 2nd order horizontal chromaticity leading to an insufficient momentum acceptance.

A way out is to exploit suitable phase advances between sextupoles for cancellation, and this requires to go back to the linear optics design. Many cancellation schemes have been proposed. Taking into account space limitations, the two most useful are periodicity and symmetry as shown in Figure 1: In a series of N identical cells, a cell phase advance of $\Delta\mu_x = 2\pi \cdot n_x/N$ and $\Delta\mu_y = \pi \cdot n_y/N$, with n_x, n_y integers, would eliminate all terms except the chromatic ones. (Since all regular sextupole resonances contain only even multiples of the vertical tune, the total vertical phase can be any multiple of π, whereas an even multiple is required horizontally.) In other lattices, a lattice section and its mirror image cancel the problematic h_{20001} if the phase advance is $\Delta\mu_x = 2\pi \cdot (2n_x+1)/4$. Doing the same vertically cancels h_{00201} too, and appending another pair of sections finally cancels all resonant terms. This scheme was applied to the TBA lattice of the SLS storage ring (see below).

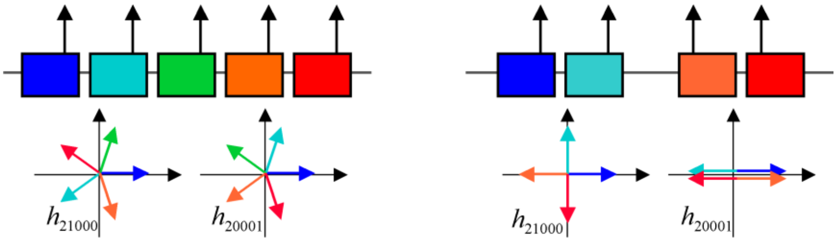

Figure 1: Cancellation of some sextupole terms by proper phase advance: in a periodic structure (left; $N = 5$, $n_x = 2$) and in a symmetric structure (right; $n_x = 1$)

Lattices with dispersion-free straights like the SLS were designed in the earlier years, when there was concern about synchro-betatron resonances from dispersion in RF cavities and translation of energy jitter to transverse noise for the experiments. Later, when both problem were handled by improvements on RF cavities and amplifiers, distributed dispersion lattices like SOLEIL or ALBA were realized to obtain even lower emittance. Since all sextupoles are chromatic, the degeneracy problem was alleviated. However, the latest designs for ultra low emittances < 1 nm like MAX IV and NSLS-II, or even lower like PEP-X, have to return to dispersion free straights to avoid emittance increase from insertion devices and thus face this degeneracy issue once again.

It is important to note, that the nonlinear optimization is not a second design step following the linear lattice design, but both have to be iterated alternately.

3.8.2.4 *Second Order Sextupole*

The first order sextupole terms perturb the linear particle motion. Introducing the perturbed motion into the sextupole Hamiltonian produces effects of 2nd and higher order in sextupole strength. They correspond to cross-talks between sextupole kicks and thus occur already in a single thick sextupole. Derivation is done by 2nd order perturbation theory [1] or by Lie algebra techniques [2] and reveals that the 2nd order terms are products of 1st order terms.

Five phase independent terms are found, h_{11002} and h_{00112} cause the 2nd order chromaticities $\partial^2 Q_{x,y} / \partial\delta^2$, and h_{22000}, h_{11110} and h_{00220} cause the amplitude dependent tune shifts (ADTS) $\partial Q_x / \partial(2J_x)$, $\partial Q_x / \partial(2J_y) = \partial Q_y / \partial(2J_x)$, $\partial Q_y / \partial(2J_y)$. These terms describe how the "footprint" of the beam in the tune diagram sprawls with increasing betatron amplitudes ($2J_{x,y}$) or momentum deviation δ. When particles then meet major resonances they may get lost, which determines the acceptances of the lattice. Furthermore, eight on-momentum resonant terms are found driving octupole resonances $2Q_{x,y}$, $4Q_{x,y}$, $2Q_x \pm 2Q_y$, and the eight first order sextupole [and quadrupole] resonant terms reappear as 2nd order off-momentum terms at one order higher in momentum.

3.8.2.5 *Octupoles and Decapoles*

The beam footprint has to be restricted in order to provide sufficient lattice acceptance, thus much effort in optimization of the sextupole pattern is spent on controlling 2nd order chromaticities and ADTS, which appears quite awkward since these are 2nd order effects only and thus difficult to manipulate. For octupoles, these effects are 1st order, and a linear system can be set up in analogy to the 1st order sextupole system. This has been done at MAX IV to control the ADTS [4].

Decapoles affect in 1st order the 3rd order chromaticities and may be useful to "fold" the beam footprint into a small tune interval in cases where a machine has to run at large positive linear chromaticities for Landau-damping of transverse coupled bunch instabilities, but have not yet been applied for that purpose.

3.8.2.6 *Practical Formulae*

Formulae for the 1st order sextupole terms (Eq.4) can be directly derived from Eqs.2 and 3, but can also be looked up in [2]. 2nd order sextupole terms are derived in [2] and explicitly given in [3]. Practical expressions for the ADTS can be found in [1,2]. Octupole and decapole 1st order terms are given in [4].

Note that all terms depend on betatron amplitudes and momentum deviations like

$$h_{jklmp} \propto (2J_x)^{(j+k)/2} (2J_y)^{(l+m)/2} \delta^p \tag{5}$$

which is often omitted assuming normalization to betatron amplitudes of 1 m and $\delta = 1$.

There may be confusion whether J or ($2J$) is considered as betatron amplitude. From a practical point of view it is preferable to call $(2J_x) = \beta_x x'^2 + 2\alpha_x x x' + \gamma_x x^2$ the amplitude. From a theoretical point of view it would be more logical to consider J as amplitude,

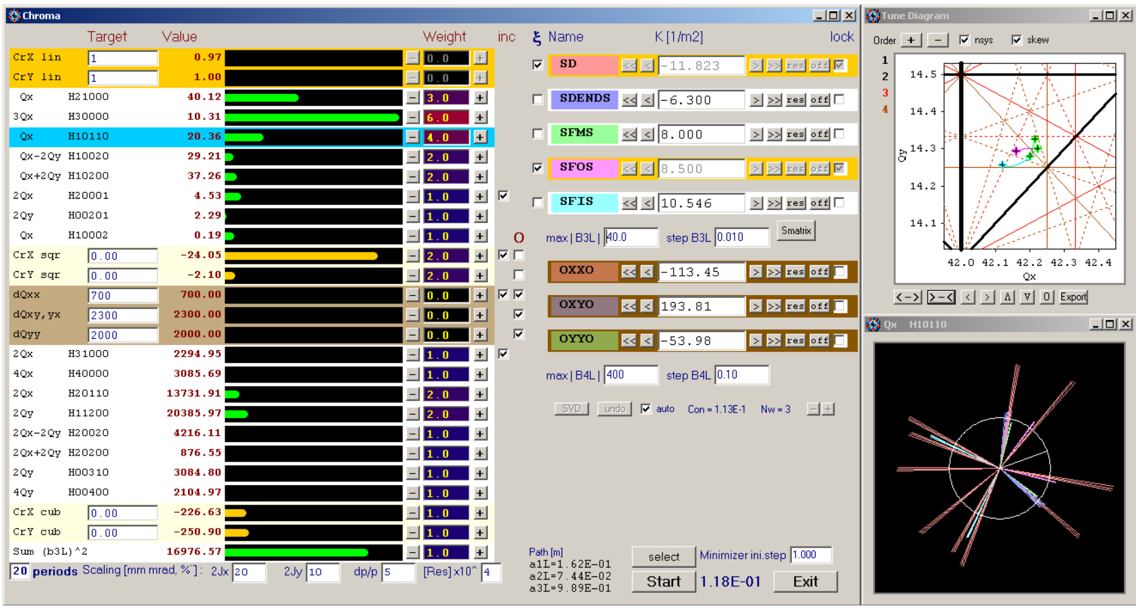

		Target	Value	Weight	inc	O
CrX lin		1	0.97	0.0		
CrY lin		1	1.00	0.0		
Qx	H21000		40.12	3.0		
3Qx	H30000		10.31	6.0		
Qx	H10110		20.36	4.0		
Qx-2Qy	H10020		29.21	2.0		
Qx+2Qy	H10200		37.26	2.0		
2Qx	H20001		4.53	1.0	☑	
2Qy	H00201		2.29	1.0		
Qx	H10002		0.19	1.0		
CrX sqr		0.00	-24.05	2.0	☑	☐
CrY sqr		0.00	-2.10	2.0		☐
dQxx		700	700.00	0.0	☑	☑
dQxy,yx		2300	2300.00	0.0		☑
dQyy		2000	2000.00	0.0		☑
2Qx	H31000		2294.95	1.0	☑	
4Qx	H40000		3085.69	1.0		
2Qx	H20110		13731.91	2.0		
2Qy	H11200		20385.97	2.0		
2Qx-2Qy	H20020		4216.11	1.0		
2Qx+2Qy	H20200		876.55	1.0		
2Qy	H00310		3084.80	1.0		
4Qy	H00400		2104.97	1.0		
CrX cub		0.00	-226.63	1.0		
CrY cub		0.00	-250.90	1.0		
Sum (b3L)^2			16976.57	1.0		

20 periods Scaling [mm mrad, %]: 2Jx 20 2Jy 10 dp/p 5 [Res]x10^ 4

ξ	Name	K [1/m2]	lock
☑	SD	-11.823	☑
☐	SDENDS	-6.300	☐
☐	SFMS	8.000	☐
☑	SFOS	8.500	☑
☐	SFIS	10.546	☐

max | B3L | 40.0 step B3L 0.010

	Name	K [1/m2]	lock
	OXXO	-113.45	☐
	OXYO	193.81	☐
	OYYO	-53.98	☐

max | B4L | 400 step B4L 0.10

☑ auto Con = 1.13E-1 Nw = 3

Path [m]
a1L=1.62E-01
a2L=7.44E-02
a3L=9.89E-01

Minimizer ini.step 1.000

1.18E-01

Figure 2: Graphical user interface of the OPA module for nonlinear optimization.

since it is the canonical action variable which allows to write the Hamiltonian as $H = J/\beta$ and defines $\varepsilon = \langle J \rangle$ as the emittance of a Gaussian beam.

3.8.3 The OPA Code

Unlike most other beam dynamics codes, OPA [5] was made for interactive, visual design and optimization of a storage ring lattice, whereas the underlying models were kept quite simple. Driven by the SLS design in the 90's and later by MAX IV design, in particular the module for nonlinear optimization was extended and designed for interactive use. Figure 2 shows the graphical user interface (GUI): the 1st and 2nd order terms of the sextupole Hamiltonian are calculated in response to manual or automatic variation of M sextupole family strengths using pre-calculated matrices relating the M-vector of sextupoles to the 1st order terms and relating the M^2-vector of all sextupole combinations to the 2nd order terms. The chromaticities are calculated by numeric differentiation of the closed orbit up to 3rd order. The values displayed are absolute values and normalized to betatron amplitudes of $(2J_{x,y}) = 1\,\mathrm{m}$ and a momentum deviation of $\delta = 1$. Realistic values may be entered and are applied according to Eq.5 in order to provide the bar chart for relative comparisons. A gradient search of Powell type [6] can be used to minimize a penalty function composed of selected terms with relative weight factors to be entered. During minimization chromaticities can be locked by assigning a pair of sextupoles.

Octupoles can be assigned to correct 2nd order chromaticities and/or ADTS, and a SVD routine will follow the requested target values during sextupole optimization. Resonant octupole terms are calculated too and added by absolute values to the 2nd order sextupole terms. Decapoles affect only the 3rd order chromaticities.

OPA is an aged code based on an outdated environment. An open source project has been started [7] in order to rebuild and extend OPA's interactive functionality by connecting a GTK+ [8] GUI to the TRACY-3 beam dynamics library with MPI [9] for parallel computation.

3.8.4 Applications

3.8.4.1 *SLS Storage Ring Lattice Design*

Earliest consideration for a Swiss Light Source were driven by user requirements at that time and did not yet consider nonlinear beam dynamics [10]. For the conceptual design report 1993, a hexagon shaped lattice consisting of six 7-bend achromats and six straight sections was optimized [11]. Each arc was composed of five full cells at the arc center and two half cells for matching to the dispersion-free straights, cf. Figure 6/top. Cancellation of all first order sextupole terms could be achieved in the five center cells if cell phase advances were adjusted to $\Delta\mu_x = 144° = 2/5 \cdot 2\pi$ and $\Delta\mu_y = 36° = 1/5 \cdot \pi$, see Figure 1/left. However, the target emittance of about 3 nm at 2.1 GeV following user request moved the horizontal phase advances towards 160°. As a consequence, the h_{20001} term could not be cancelled and the momentum acceptance was insufficient. As a way out, the lattice circumference was increased from 252 m to 270 m introducing short straights to be used as “phase trombones” to provide the appropriate phase advance such that the h_{20001} term would cancel over a wide range of $\Delta\mu_x = 144°\ldots173°$ with the possibility to reach an emittance as low as 2.3 nm at 2.1 GeV [12]. Finally, the 7BA-achromat lattice was abandoned due to the complexity of the lattice incorporating a large number of sextupole families, and also because a six straight sections limit would be too few for the fast growing community of prospective users.

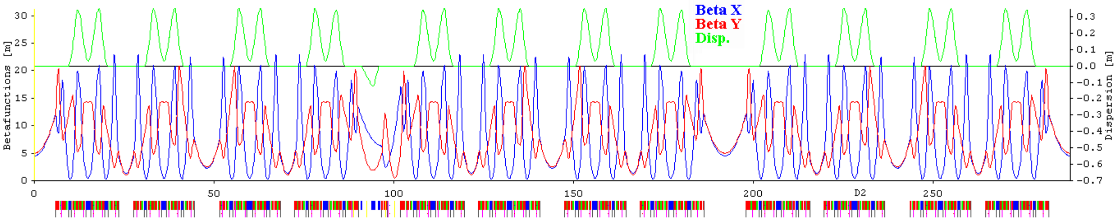

Figure 3: Optics of the lattice of the SLS storage ring comprising 12 TBAs and 3 long (11 m), 3 medium (7 m) and 6 short (4 m) straight sections. The chicane between the 4th and 5th TBA was introduced for the FEMTO laser beam slicing installation.

A new design started from scratch in 1996 and resulted in a 12-TBA lattice of

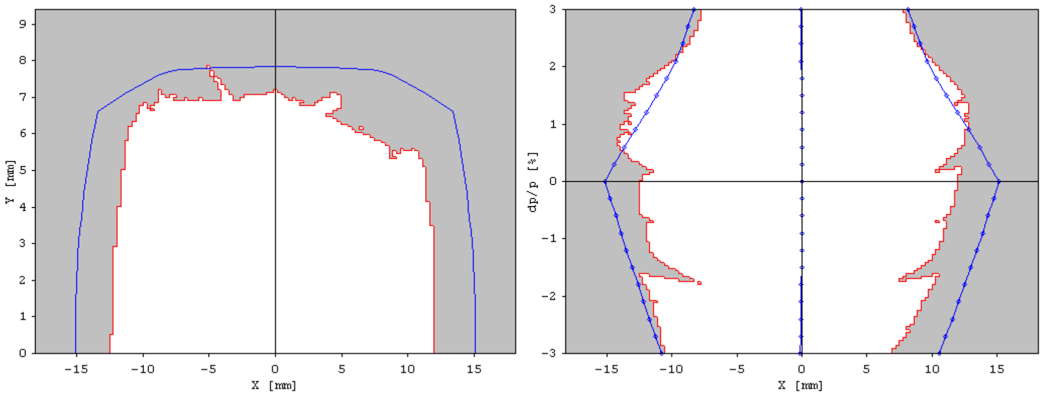

Figure 4: Dynamic apertures of the SLS TBA lattice in (x,y) and (x,δ) planes. ($\beta_x = 4.5$ m, $\beta_y = 5.0$ m at track point for $\delta = 0$)

288 m circumference with 12 straight sections providing 5 nm at 2.4 GeV as the best compromise between performance and available area on site [13], cf. Figure 3, which then was realized and commissioned [14]. In this lattice, phase advances close to $\Delta\mu_x = 7/4 \cdot 2\pi$ and $\Delta\mu_y = 3/4 \cdot 2\pi$ per TBA largely suppress h_{20001} and h_{00201} over 2 TBAs, and the other 1st order resonant terms over 4 TBAs as indicated in Figure 1/right. Figure 4 shows the dynamic aperture in the (x,y) and (x,δ) planes. From design, it provides 100% injection efficiency and a Touschek lifetime of 9.7 hrs (TRACY 6D-tracking) in the standard operation mode (400 mA in 390 bunches, 2.1 MV 500 MHz RF, 3rd harmonic cavity for factor 2.2 bunch lengthening and 0.1% emittance coupling).

3.8.4.2 ***Linear and Nonlinear Optimization of the SLS Lattice***

Linear optimization covers orbit correction, optics correction and coupling suppression. All these measures will not be described here, only a few key issues will be briefly mentioned: single power supplies for each of the 177 quadrupoles and the turn by turn capability of the BPM system eased measurement and correction of optical functions by different methods [15]. The dynamic alignment system of the SLS allows moving the magnet girders remotely with stored beam. A vertical girder realignment based on survey data was performed with running orbit feedback [16] and a reduction of the vertical corrector currents by a factor 4 was observed. A suppression of vertical dispersion and betatron coupling using 36 skew quadrupoles by model dependent (LOCO) and independent (random walk) methods recently achieved a new record for vertical emittance of about 1 pm, only a factor 5 larger than the natural quantum limit [17].

Nonlinear optimization was hindered by the fact that the sextupoles were hardwired to 9 families which are symmetrically distributed, such that, seen from a symmetry point of the lattice, $\Im(h) = 0 \ \forall \ h$. So in the real lattice, possible perturbations of symmetries could not be corrected. Furthermore, the situation was aggravated by the necessity to operate the storage ring at positive chromaticities of $\xi_x = \xi_y = +5$ in order to suppress coupled bunch instabilities, and by the FEMTO insertion for laser beam slicing

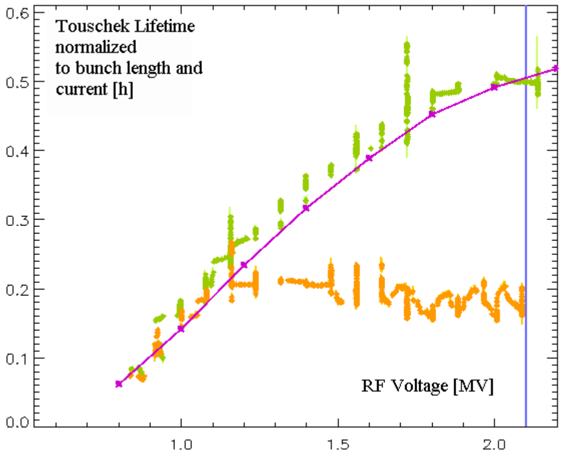

Figure 5: SLS beam lifetime as a function of RF voltage before (orange dots) and after (green dots) optimization of skew quadrupoles and auxiliary sextupoles, and comparison to a 6-D TRACY tracking of the ideal lattice (magenta line).

which made the period-3 lattice essentially period-1 although the modification was largely hidden from the sextupoles by applying the “π-trick”, i.e. a local betatron phase change of $\Delta\mu_x = 0$ and $\Delta\mu_y = \pi$ [18]. As a consequence, resonances in the beam footprint, in particular $3Q_x = 61$, cut the momentum acceptance and thus reduced the Touschek lifetime.

The 120 sextupoles of the SLS storage ring are all equipped with two sets of additional coils. In 72 sextupoles these coils were employed as horizontal and vertical orbit correctors, in 36 as skew quadrupoles. The remaining 12, which are all members of the family for horizontal chromaticity correction, were wired as “auxiliary sextupoles” and an SVD based tool was provided for interactive variation of amplitude and phase of h_{21000}, h_{30000}, h_{10020} and h_{10200} while maintaining ξ_x. h_{10110} can not be varied independently since it is degenerate with h_{21000}, because all auxiliary sextupoles have identical beta-functions and dispersion. The tool was used to empirically optimize beam life time, and finally, mainly by tuning h_{30000}, restored the lattice momentum acceptance of 3%. The beam lifetime followed the RF voltage in excellent agreement with simulations for the ideal lattice [19], see Figure 5.

3.8.4.3 *Multi-bend Achromat Lattices*

The 7BA lattice failed for the CDR-version of the SLS because at that time (1993), a conservative magnet design (large apertures, no gradient bends) allowed only six arcs

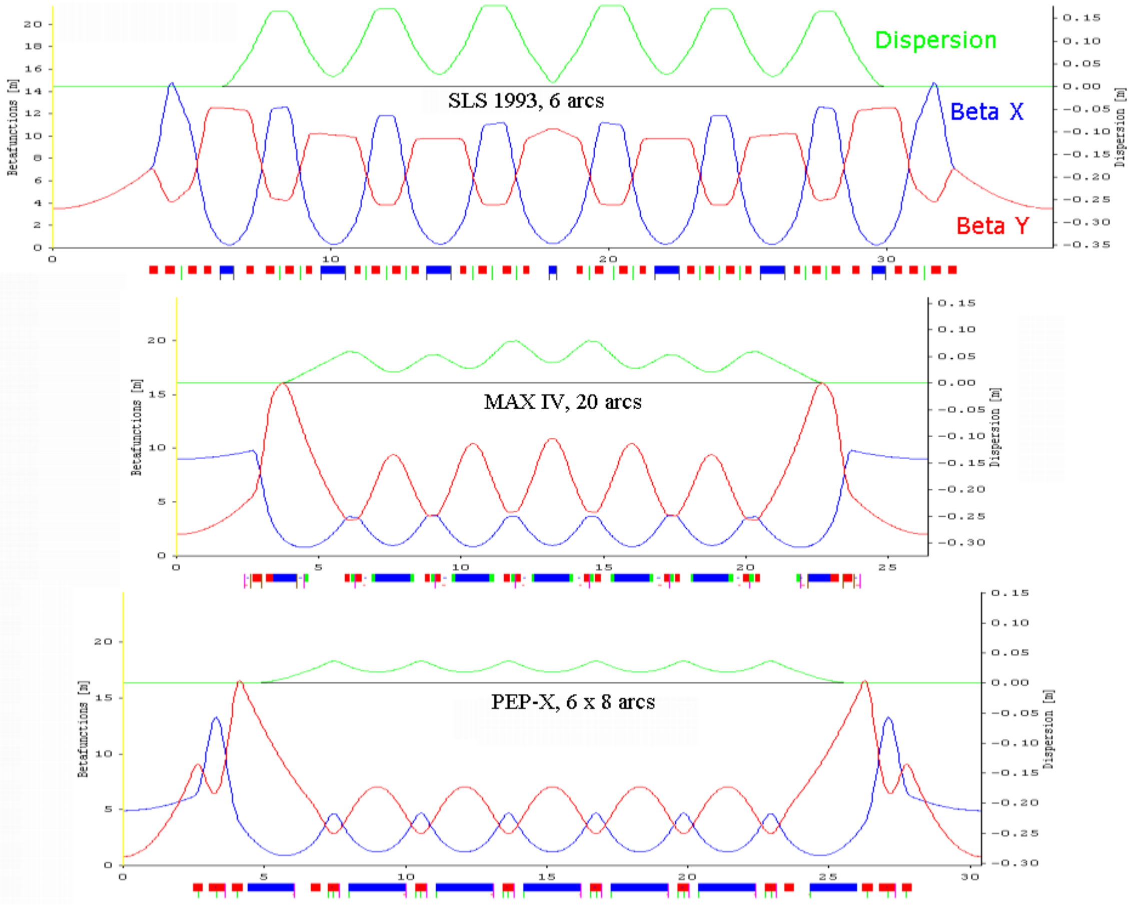

Figure 6: Evolution of the 7-BA arc (approx. to scale)

given the available site for the machine. Thus achieving a sufficiently small emittance required an overstrained optics, indicated by large normalized chromaticities of $\xi_x/Q_x = -2.7$, $\xi_y/Q_y = -3.4$, and inconvenient cell phase advance.

Increasing the number of arcs opens a positive feedback cycle [20]: reduced deflection angle per bending magnet gives lower dispersion and thus requires less physical aperture. So magnets can be scaled down and allow higher gradients. So the cells can be shorter and more arcs can be realized for a given machine size. Gradient magnets further compact the lattice. Since emittance scales cubically with the deflection angle per bending magnet, a very low emittance can be realized even with a quite relaxed arc optics. This concept was followed in the designs of MAX IV and PEP-X, which are both based on 7BA arcs, see Figure 6. However, the strength of the chromatic sextupoles increases as the dispersion is reduced, because the chromaticity generated by each quadrupole does not depend much on the deflection angle per bending magnet. Thus nonlinear optimization becomes more challenging as the number of arcs is increased.

MAX IV [21] has 20 arcs providing 326 pm emittance (bare lattice without damping wigglers) at 3 GeV with normalized chromaticities of –1.2/–3.1. The phase advances per arc including the adjacent straights as shown in Figure 6/middle are $\mu_x/\mu_y = (2.11/0.81) \times 2\pi$ [22]. Counting only the arc cells, the phase advances are $\approx 4\pi$ horizontally and $\approx \pi$ vertically, so all 1st order terms are cancelled within the arc independently of the optics in the straight sections. (Since all regular sextupole terms contain even multiples of vertical phase, any multiple of π provides cancellation whereas a multiple of 2π is required horizontally.) Suppression of all 1st order terms largely suppresses 2nd order terms too, since they are cross-talks of the 1st order terms [2]. Sufficient suppression of the ADTS however could not be achieved in 2nd order sextupole optimization alone, therefore three families of octupoles were introduced near the end bends at locations where $\beta_x > \beta_y$, $\beta_x \approx \beta_y$, and $\beta_x < \beta_y$ respectively, in order to independently control the three ADTS terms. Sextupole thus became free and, besides adjusting chromaticities and suppressing other 1st order effects, were used to tailor 2nd and 3rd order chromaticities for folding the chromatic beam footprint into a minimal region in the tune diagram, thus providing a momentum acceptance of more than ±5% and correspondingly long Touschek lifetime [4]. In view of commissioning, “ADTS-knobs” in the control room may be quite helpful for machine development.

Finally, it is also appropriate to mention the design studies for PEP-X [23,24], where the 7BA arc is further promoted in order to achieve an ultra-low natural emittance of 29 pm at 4.5 GeV (bare lattice without damping wigglers). Here, the ring is composed of 48 arcs arranged in 6 super-arcs (sextants) of 8 arcs separated by 6 very long straight sections for matching the lattice to the footprint of the existing PEP-II facility. Non-linear optimization is challenged by the extremely small dispersion in the arcs (cf. Figure 6/bottom). Nevertheless the designer succeeds in realizing ±2% momentum acceptance, thereby providing several hours of Touschek lifetime, and a horizontal acceptance which is sufficient for off-axis injection due to a wider beam ($\beta_x \approx 200$ m) at the location of the injection septum.

3.8.5 **References**

1. J. Bengtsson, “Non-linear transverse dynamics for storage rings with applications to the

Low-Energy Antiproton Ring (LEAR) at CERN”,
CERN 88-05 (1988).

2. J. Bengtsson, “The sextupole scheme for the Swiss Light Source: an analytic approach”, Internal report SLS-Note 9/97, Paul Scherrer Institut, 1997.
3. Chun-xi Wang, “Second-order driving terms due to sextupoles and chromatic effects of quadrupoles”, Internal report ANL/APS/LS-330, Argonne 2012.
4. S. C. Leemann and A. Streun, “Perspectives for future light sources incorporating yet uncommon magnets”, Phys. Rev. Special Topics Accelerators and Beams 14, 030701 (2011).
5. OPA code and user guide: people.web.psi.ch/streun/opa/.
6. Numerical recipes: www.nr.com/.
7. Mau-Sen Chiu and Ho-Ping Chang, “New Features of the Parallel TRACY for Nonlinear Beam Dynamics”, to be presented at the 2012 International Particle Accelerator Conference, New Orleans (2012).
8. GTK+ www.gtk.org.
9. MPICH2 www.mcs.anl.gov/research/projects/mpich2/.
10. R. Abela, W. Joho, P. Marchand, S. V. Milton, L. Z. Rivkin, “Design Considerations for a Swiss Light Source (SLS)”, proceedings of the 1992 European Particle Accelerator Conference, Berlin (1992).
11. W. Joho, P. Marchand, L. Rivkin, A. Streun, “Design of a Swiss Light Source (SLS)”, proceedings of the 1994 European Particle Accelerator Conference, London (1994).
12. J. Bengtsson, W. Joho, P. Marchand, L. Rivkin, A. Streun, “Status of the Swiss Light Source Project SLS”, proceedings of the 1996 European Particle Accelerator Conference, Sitges/Barcelona (1996).
13. The SLS Design Handbook, ados.web.psi.ch/slsdhb/.
14. A. Streun et al., “Commissioning of the Swiss Light Source”, proceedings of the 2001 Particle Accelerator Conference, Chicago (2001).
15. M. Aiba, M. Böge, J. Chrin, N. Milas, T. Schilcher, A. Streun, “Comparison of linear optics correction means at the SLS”, proceedings of the 2011 International Particle Accelerator Conference, San Sebastian (2011).
16. M. Böge, M. Aiba, N. Milas, A. Streun, S. M. Liuzzo, “SLS vertical emittance tuning”, proceedings of the 2011 International Particle Accelerator Conference, San Sebastian (2011).
17. M. Aiba, M. Böge, N. Milas, A. Streun, “Random Walk Optimization in Accelerators - Vertical Emittance Tuning at SLS”, , to be presented at the 2012 International Particle Accelerator Conference, New Orleans (2012).
18. A. Streun et al., “Sub-Picosecond X-ray Source FEMTO at SLS”, proceedings of the 2006 European Particle Accelerator Conference, Edinburgh (2006).
19. M. Böge, J. Chrin, A. Lüdeke, A. Streun, “Correction of Imperfections in the SLS Storage Ring”, proceedings of the 2009 Particle Accelerator Conference, Vancouver (2009).
20. M. Eriksson et al., “Some small-emittance light-source lattices with multi-bend achromats“, Nucl. Instr. and Meth. A 587 (2008) 221−226.
21. S. C. Leemann, “The MAX IV 3 GeV Storage Ring”, this newsletter.
22. S. C. Leemann, “Recent Improvements to the Lattices for the MAX IV storage ring”, proceedings of the 2011 International Particle Accelerator Conference, San Sebastian (2011).
23. Y. Nosochkov et al., “Lattice Design for PEP-X Ultimate Storage Ring Light Source”, proceedings of the 2011 International Particle Accelerator Conference, San Sebastian (2011).
24. Min-Huey Wang et al., “Dynamic Aperture and Tolerances for PEP-X Ultimate Storage Ring Design”, proceedings of the 2011 International Particle Accelerator Conference,

San Sebastian (2011).

3.9 Vertical Emittance Reduction and Preservation in the ESRF Electron Storage Ring

Andrea Franchi and Laurent Farvacque
ESRF, Grenoble, France
Mail to: andrea.franchi@esrf.fr and laurent.farvacque@esrf.fr

3.9.1 Introduction

The last two years saw major efforts in reducing dramatically betatron coupling and the vertical emittance in the ESRF electron storage ring. Benefits have been manifold: higher brilliance, lower radiation dose during injections and, possibly, higher photon flux towards high energies by further reducing the vertical aperture of in-vacuum undulators. After reviewing the physics of betatron coupling and describing the novel correction scheme, results obtained in this two-year campaign will be reported. The ultra-low vertical emittance (3-4 pm, with a horizontal emittance of 4 nm at 6 GeV) is routinely achieved after a weekly correction based on the orbit response matrix (ORM) and the minimization of vertical dispersion and coupling Resonance Driving Terms (RDTs). These values could be preserved during beam delivery only through the implementation of feedback and feed-forward loops on the corrector skew quadrupoles to compensate on the fly the coupling induced by moving insertion devices (IDs).

Focus will be given to the difficulty of evaluating betatron coupling from the measurement of the vertical beam size at one or few locations, without an independent analysis of lattice errors (via ORM measurement or harmonic analysis of turn-by-turn beam position data, for instance). Indeed, it will be shown how in modern lepton colliders and light sources based on storage rings betatron coupling renders the vertical emittance no longer an Observable. More important, doubts will be cast on the reliability of indirect measurements of vertical emittance based on lifetime and closest-tune approach. Indeed, both measurements rely on the wrong assumption that betatron coupling excites the difference resonance only, whereas it will be shown that in modern lepton machines the (destructive) sum resonance plays a comparable (if not dominant) role. It is the coexistence of both resonances in those accelerators aiming at even smaller horizontal emittances that renders the vertical emittance not observable in presence of coupling. Last, a discussion on the risks incidental to the evaluation of the vertical emittance from the measurement of the Touschek lifetime is presented.

3.9.2 Vertical Emittances in the Presence of Coupling

Because of radiation damping and diffusion, accelerator lattices define specific equilibrium (or eigen)emittances ($\mathcal{E}_u$, $\mathcal{E}_v$), which are constant in time and along the ring. In absence of magnet errors, the two planes are decoupled and vertical dispersion D_y is everywhere zero. This in turn leads to almost zero (up to the quantum limit) ideal vertical eigenemittance, $\mathcal{E}_v \approx 0$. The impact of scattering effects, with residual gas as well as intra-beam collisions, is not taken into account here. Beam profile monitors provide root-mean-square (RMS) beam sizes, $\sigma^2_r = \langle r^2 \rangle - (\delta D_r)^2$, where r stands for either x or

y, D_r is the dispersion function, and δ is the relative RMS beam energy spread. Throughout the paper, all RMS quantities denoted with σ refer to the betatronic part, hence assuming that dispersion terms have been already subtracted. In the ideal uncoupled lattice, the eigenemittance $\mathcal{E}$ is equivalent to the RMS beam emittance ε,

$$\varepsilon_r = \sqrt{\sigma_r(s)\sigma_p(s) - \sigma_{rp}^2(s)}\ ,$$

where σ_p and σ_{rp} are the RMS beam divergence and cross-term moment, respectively. The stored beam being matched to the focusing lattice, the measured normalized RMS beam size is sufficient to characterize the RMS emittance, since

$$\varepsilon_r = \frac{\sigma_r^2(s)}{\beta_r(s)} = \frac{< r^2(s) > -[\delta D_r(s)]^2}{\beta_r(s)}\ , \tag{1}$$

where β_r is the Twiss parameter. Betatron coupling has in this context four main effects:

- The vertical equilibrium emittance is no longer zero, $\mathcal{E}_v \neq 0$;
- RMS emittance and eigenemittance are no longer equivalent, $\varepsilon_r \neq \mathcal{E}_r$;
- RMS emittance and normalized RMS beam size are no longer equivalent, $\varepsilon_r \neq \sigma^2_r/\beta_r$;
- RMS emittance varies along the ring, i.e., depends on the coordinate s, $\varepsilon_r = \varepsilon_r(s)$.

While the differences are almost negligible among the horizontal quantities, they are of importance in the vertical plane. The literature related to this topic is already vast, both in terms of mathematical modeling and practical cures aimed at minimizing coupling effects. [1–5]. Formulas for the numerical evaluation of the equilibrium beam distribution parameters of Refs. [2,3] were already implemented in optics codes, such as Accelerator Toolbox (AT) [6] and MADX [7]. Works on coupling correction and vertical emittance minimization [8–10] are based on beam size measurements at one or few locations. In Ref. [10] it is acknowledged that measurements of σ^2_y / β_y are only an approximation of ε_y and both differ from the vertical eigenemittance $\mathcal{E}_v$ obtained from the model. Nevertheless, no direct estimation of such an approximation is made.

As discussed in Ref. [11], with coupling the usual notion of emittance is replaced by three separate quantities. For the sake of clarity, it is worthwhile distinguishing the nomenclature before analyzing them in details.

- The RMS *apparent* emittance E_r is the observable quantity, derived from beam profile measurements

$$E_r = \frac{\sigma_r^2(s)}{\beta_r(s)} = \frac{< r^2(s) > -[\delta D_r(s)]^2}{\beta_r(s)}\ . \tag{2}$$

- The RMS *projected* emittance ε_r is the second-order statistical moment representing the surface of the beam phase space

$$\varepsilon_r = \sqrt{\sigma_r(s)\sigma_p(s) - \sigma_{rp}^2(s)}\ , \tag{3}$$

- The *eigenemittance* or *equilibrium emittance* $\mathcal{E}_r$ is the true invariant (i.e. independent of *s*) and an intrinsic property of the accelerator lattice.

Betatron coupling is generated by skew quadrupole fields present in the ring and originated by quadrupole tilts, sextupole misalignments (or vertical closed orbit distortion at their locations), IDs, and corrector skew quadrupoles already powered. They are usually modeled as integrated magnetic strengths of zero-length elements, J_1, distributed along the machine. They excite two RDTs, f_{1001} and f_{1010}, for the difference and sum resonance respectively,

$$f_{\substack{1001\\1010}} = \frac{\sum_{w}^{W} J_{w,1}\sqrt{\beta_x^w \beta_y^w}\, e^{i(\Delta\phi_{w,x} \mp \Delta\phi_{w,y})}}{4(1-e^{2\pi i(Q_u \mp Q_v)})} = \left|f_{\substack{1001\\1010}}\right| e^{iq_{\mp}} \tag{4}$$

where $\beta_{x,y}$ are the Twiss parameters corresponding to the location of the skew quadrupole kick, $\Delta\phi_w$ is its phase advance with respect to the position where the RDTs are either measured or evaluated. $Q_{u,v}$ are the eigentunes, which in first approximation are equivalent to the betatron tunes, whereas $q_{\pm}$ are the phase of the two RDTs. In first (but usually already robust) approximation, both β and ϕ refer to the ideal, uncoupled lattice. One of the most peculiar features of the RDTs is their dependence on the coordinate *s*. The presence in Eq.(4) of the phase advances $\Delta\phi_w$ makes the RDTs change abruptly when the skew quadrupole kick number *w* is crossed, since both $\Delta\phi_{w,x}$ and $\Delta\phi_{w,y}$ change sign when moving from upstream to downstream the skew quadrupole source $J_{w,1}$, hence changing the value of the overall summation in the numerator. In Ref. [12] it was shown how actually the amplitude of the RDTs remains constant in the region between two sources of coupling, while an abrupt jump occurs when one is crossed. Both f_{1001} and f_{1010} are complex quantities that can be either measured from the harmonic analysis of turn-by-turn beam position data [12,13] or evaluated from an error lattice model, i.e. from $J_{w,1}$, $\beta_{x,y}$, $\Delta\phi_w$ and the tunes inferred from ORM measurements, through Eq. (4). They are rather straightforward to evaluate and represent the basic ingredients for the comprehension of all subtleness incidental to the multiple definitions of vertical emittance, efficient coupling correction, and interpretation of indirect measurements of the vertical emittance.

Before introducing the formulas describing its various definitions, it is worthwhile introducing some other handy quantities evaluable directly from the RDTs

$$\begin{aligned} \mathcal{C} &= \cosh(2\mathcal{P})\,, & \mathcal{P} &= \sqrt{-|f_{1001}|^2 + |f_{1010}|^2}\,, \\ \mathcal{S}_- &= \frac{\sinh(2\mathcal{P})}{\mathcal{P}}|f_{1001}|\,, & \mathcal{S}_+ &= \frac{\sinh(2\mathcal{P})}{\mathcal{P}}|f_{1010}|\,, \end{aligned} \tag{5}$$

Even though all quantities in Eq.(5) are complex numbers and dependent on the coordinate *s*, the following relations holds

$$1 = \mathcal{C}^2 + \mathcal{S}_-^2 - \mathcal{S}_+^2\,; \qquad \mathcal{C}^2,\, \mathcal{S}_-^2,\, \mathcal{S}_+^2,\, \mathcal{S}_-\mathcal{S}_+ \in \Re\,, \tag{6}$$

Whenever f_{1001} (difference resonance) is greater in absolute value than f_{1010} (sum resonance), $\mathcal{P}$ is purely imaginary and $\mathcal{C}$, $\mathcal{S}_{\pm}$ contain trigonometric functions. When the contrary is true, $\mathcal{P}$ is a real number and $\mathcal{C}$, $\mathcal{S}_{\pm}$ contain hyperbolic functions. One way, hence, of evaluating the play of forces between the sum and difference resonances is represented by the comparison between the absolute value of the two RDTs along the ring. If $|f_{1001}|>>|f_{1010}|$ anywhere in the machine, the sum resonance may be neglected. If, on the contrary, $|f_{1001}|<<|f_{1010}|$, the sum resonance is dominant (rare case in modern circular accelerators). If, eventually, $\mathcal{P}^2$ continuously changes signs along the ring (i.e., $\mathcal{P}$ passes from real to purely imaginary), none of the two resonances may be neglected. It will be shown that the former case applies to hadron machines, while the latter is encountered in modern lepton machines.

In Ref. [11] explicit analytical expressions for the three different types of vertical emittances were derived.

- The RMS apparent emittance E_y :

$$\mathrm{E}_{\mathrm{y}}(s)=\mathcal{C}^2\mathcal{E}_v+\left[\mathcal{S}_-^2+\mathcal{S}_+^2-2\mathcal{S}_-\mathcal{S}_+\cos(q_+-q_-)\right]\mathcal{E}_u\ . \tag{7}$$

- The RMS projected emittance ε_y :

$$\varepsilon_y(s)=\sqrt{(\mathcal{C}^2\mathcal{E}_v+\left[\mathcal{S}_-^2+\mathcal{S}_+^2\right]\mathcal{E}_u)^2-(2\mathcal{S}_-\mathcal{S}_+\mathcal{E}_u)^2}\ . \tag{8}$$

- The invariant eigenemittance or equilibrium emittance $\mathcal{E}_v$:

$$\mathcal{E}_v=\frac{1}{2}\frac{\oint \mathrm{d}(s)\left\{\mathcal{C}^2\mathcal{H}_y^2(s)+\left[\mathcal{S}_-^2+\mathcal{S}_+^2\right]\mathcal{H}_x^2(s)\right\}ds}{\oint\left\{\mathrm{b}_{\mathrm{RF}}(s)-\mathcal{C}^2D_y(s)\mathrm{b}_{\delta\mathrm{y}}(s)-\left[\mathcal{S}_-^2-\mathcal{S}_+^2\right]D_x(s)\mathrm{b}_{\delta\mathrm{x}}(s)\right\}ds}\ . \tag{9}$$

in which d(s) is the diffusion coefficient, $\mathcal{H}$ and D are the dispersion invariant and function respectively, while b_{RF}, $\mathrm{b}_{\delta\mathrm{x}}$ and $\mathrm{b}_{\delta\mathrm{y}}$ are the damping terms generated by RF cavities and bending magnets, see Refs. [5,11] for their explicit definitions. Equation (9) was verified against the eigenemittance computed by the MADX code, through the `emit` module implementing the formulas of Ref. [2]. Equations (7) and (8) were tested against the equivalent RMS quantities evaluated by the AT code, through the function `ohmienvelope` which computes the equilibrium beam envelope using the formalism of Ref. [3]. This function provides a 6x6 matrix containing the normalized equilibrium RMS moments: The apparent emittances E_x and E_y are then the matrix elements O_{11} and O_{33}, respectively, while the projected emittances ε_x and ε_y are the determinants of the first and second 2x2 diagonal projections, respectively. It is clear that the deviations between the three definitions in the horizontal plane (to be found in Ref.[11]) are practically negligible, being in general $\mathcal{C}\approx 1>>\mathcal{S}_\pm$, $\mathcal{E}_y<<\mathcal{E}_x$ and hence $\varepsilon_x\approx \mathrm{E}_x\approx\mathcal{E}_x$. The same is not true in the vertical plane, unless coupling is suppressed. In Fig. 1 the (measurable) apparent and the (non-measurable) projected emittances as computed from Eqs.(7)-(8) along the ESRF storage ring are displayed for two different cases, with low coupling (vertical eigenemittance or $\mathcal{E}_y$=3 pm) and large coupling ($\mathcal{E}_y$=9 pm). The difference between the two quantities is clearly visible and more important when coupling is larger. Two peculiar locations have been chosen to show how a single evaluation of the apparent emittance from the measurement of the vertical beam size may largely underestimate or overestimate the projected emittance. By trying to interpret the measured apparent emittance at the location of the black triangles as the eigenemittance obtained from the lattice model would induce an unjustified discrepancy of about a factor two.

As suggested by the two plots of Fig. 1, the (measurable) apparent emittance averaged along the ring is a good approximation of the (non-measurable) mean projected emittance: the lower the coupling and the larger the number of measurement points, the better the approximation. The ESRF storage ring is equipped with an unusually large number of emittance monitors distributed rather uniformly around the machine (see left picture of Fig. 2): two pinhole cameras and 11 dipole radiation projection monitors (IAX). The right plot of Fig. 2 shows a comparison between the measured apparent emittance E_y and the prediction from the model: the pattern is well reproduced, whereas a comparison with the computed projected emittance ε_y would show a much poorer agreement. Interpreting the measured values as the (constant) eigenemittance obtained from the model ($\mathcal{E}_y$=15 pm) would be nonsense. For these reasons, at the ESRF the apparent emittance averaged over all monitors, $<E_y>$, is displayed and referred as the machine emittance ε_y and one figure of merit for coupling.

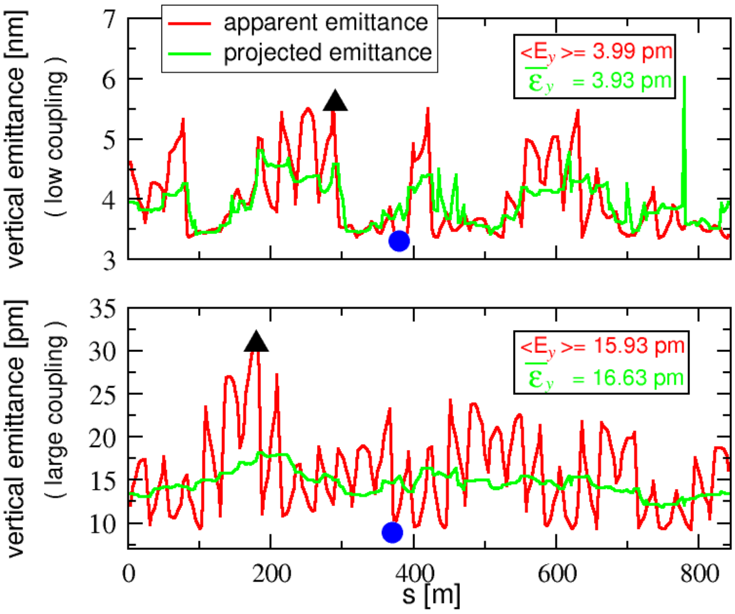

Figure 4: E_y (red) from Eq. (7) and ε_y (green) from Eq. (8) plotted along the ESRF storage ring for two different amounts of coupling inferred from ORM measurements, corresponding to eigenemittances of E_y=3 pm (top) and E_y=9 pm (bottom). The black triangles indicate the positions where E_y would overestimate the projected emittance ε_y, that would be instead underestimated by measurements at the blue circles.

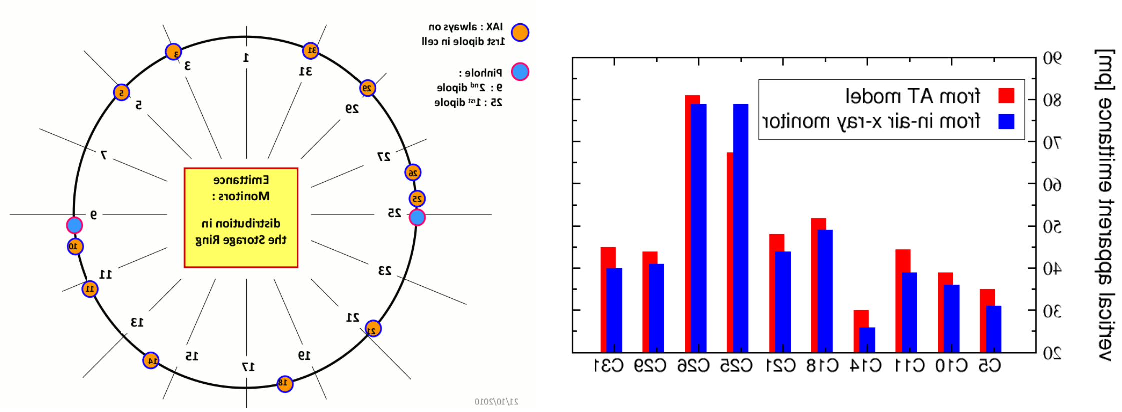

Figure 5: Left: distribution of the 13 emittance monitors around the ESRF storage ring. Right: comparison between the apparent emittances E_y (before coupling correction) measured at ten available IAX detectors (blue) and the predictions of AT (red) after creating the lattice error model from the ORM measurement of January 16, 2010.

However, the use of the averaged emittance alone may not be sufficient to quantify the coupling in the machine. When operating in uniform mode (992 bunches without empty buckets) the ESRF storage ring experiences vertical instabilities induced by ion trapping: the higher the current of the stored beam (and the poorer the vacuum), the stronger the instability and the vertical coherent motion. The latter causes an artificial emittance blowup due to the monitor integration time, which is much larger than the vertical beam motion. Typical values are reported in the left part of Tab. 1: the fact the vertical bunch-by-bunch orbit feedback restores the low emittance is an evidence of this artifact. For comparison, one corrector skew quadrupole was trimmed at low beam current so to reproduce the same average emittances. By merely looking at this figure, hence, it would be difficult to disentangle coupling and instability. The standard deviation between the 11 monitors, instead, seems to be a better identifier. In the ion-trapping case the 17.2 pm are measured with a deviation of 1.8 pm only, whereas when increasing coupling to reach the same value, a larger spread of 3.2 pm is observed: the large the coupling, the larger the spread, as already suggested by Fig. 1.

Table 1: Measured vertical emittance (average over 11 monitors) against stored beam current (left) inducing ion-trapping vertical instabilities, and against coupling (right). The average emittance is reported together with the standard deviation between the monitors (STD) and the RMS fluctuation over 30 s of their 1-Hz sampling (F).

beam current [mA]	**measured vertical emittance [pm] INCREASING ION TRAPPING**	**skew quad current [A]**	**measured vertical emittance [pm] INCREASING COUPLING**
20	3.0 ± 1.5 (STD) ±0.15 (F)	0	3.1 ± 1.5 (STD) ±0.20 (F)
100	5.7 ± 1.7 (STD) ±0.07 (F)	0.08	5.7 ± 1.8 (STD) ±0.20 (F)
160	10.1 ± 2.0 (STD) ±0.12 (F)	0.15	10.0 ± 2.7 (STD) ±0.20 (F)
200	17.2 ± 1.8 (STD) ±0.35 (F)	0.18	17.2 ± 3.2 (STD) ±0.20 (F)
200*	4.2 ± 1.4 (STD) ±0.05 (F)	* with bunch-by-bunch feedback on	

3.9.3 Coupling Correction via Resonance Driving Terms

Correction of coupling and vertical dispersion is performed by means of independent skew quadrupoles (trim coils), distributed rather uniformly around the ring, 32 until 2010, 64 as of 2011. Until the end of 2009 coupling used to be corrected by minimizing either the vertical eigenemittance or the apparent one along the ring (both computed by the AT code), via the Matlab function `FMINSEARCH`. The dependence of the vertical emittances on the corrector strengths being in first approximation quadratic, this resulted in a nonlinear multidimensional minimization over 32 parameters. The main drawbacks of this approach are CPU time (about 10 min for 500 iterations) and the risk of limited improvements whenever a local minimum (not necessarily the lowest) is found.

Equations (7) and (8) suggest an intuitive consideration: the lower the RDTs (i.e. the coupling), the lower the vertical emittance, as the contribution from the large horizontal equilibrium emittance $\mathcal{E}_u$ is minimized. A setting for the corrector skew quadrupoles may be then found to minimize as uniformly as possible both f_{1001} and f_{1010} along the ring. Equation (4) shows how this task becomes much simpler than the previous, the system relating RDTs and corrector strengths being linear, hence straightforward to invert, via SVD for instance. By itself coupling correction implies that $\mathcal{C}^2 \approx 1$, $\mathcal{S}_+ \approx \mathcal{S}_- \approx 0$, and hence that $E_y \approx \varepsilon_y \approx \mathcal{E}_v$. This, however, is not sufficient, as the eigenemittance $\mathcal{E}_v$ is minimized only after a further correction of vertical dispersion, i.e., after minimizing $\mathcal{H}_y$, see Eq. (9). Skew quadrupoles may still be used to this end. The dependence of D_y on the skew quadrupole strengths being also linear, the system to be resolved reads

$$\begin{pmatrix} a_1 \vec{f}_{1001} \\ a_1 \vec{f}_{1010} \\ a_2 \vec{D}_y \end{pmatrix} = -\mathbf{M}\vec{J}_c \quad , \tag{10}$$

where the vector on the l.h.s. contains the (complex) RDTs and the (real) vertical dispersion measured (or evaluated) at all beam position monitors (BPMs), the weights $a_2=1-a_1$ are introduced in order to determine the best compromise between dispersion suppression and deterioration of coupling. Their determination is empirical. The vector on the r.h.s contains the strengths of the corrector skew quadrupol es. **M** is a response matrix that can be evaluated through Eq. (4) and any optics code.

3.9.4 Application in the ESRF Storage Ring: Achieving and Preserving Ultra-low Vertical Emittance

At the ESRF storage ring ORM measurements are carried out weekly in preparation of the following beam delivery. The error lattice model so inferred is then loaded in the AT code and the RDTs are evaluated from Eq. (4). These and the measured vertical dispersion are inserted in the system of Eq. (10) and inverted. The first test was carried out on January 16th 2010, when all correctors (both 32 normal and 32 skew quadrupoles) were switched off. Despite the large errors (beta beating of about 50% and vertical apparent emittance of the order of hundreds of pm) stable beam could be stored. The vertical apparent emittance measured along the ring before the first correction is shown in the upper left plot of Fig. 3, providing an average value of 237 ± 122 pm. Error bars on individual monitors are (pessimistically) derived from the inferred beta beating. After a first correction, this went down to about 8% and the vertical (average) emittance reduced to 23.6 ± 6.3 pm. A second ORM measurement and correction was then applied providing the usual beating of 5% and an emittance of 11.5 ± 4.3 pm (bottom left plot of Fig. 3). The plots in the right column of Fig. 3 show the coupling RDTs before and after correction and prove how the sum RDT f_{1010} is stronger and the difference RDT f_{1001} without correctors, while they are comparable after the second correction. An evidence that at ESRF storage ring the sum resonance may not be ignored. After a few months of iterations and fine tuning (for both the weights $a_{1,2}$ of Eq.(10) and the calibration of the skew quadrupoles) a beam with a vertical emittance of about 7 pm could be provided to users in the most used filling mode (multi-bunch train filling 7/8 of the ring plus a single intense bunch at the centre of the gap).

As already mentioned in the Introduction, coupling correction at fixed ID gaps may not last during beam delivery, because of the continuous changes of their vertical apertures. The residual magnetic imperfections in some IDs may include gap-dependent skew quadrupoles terms. This concerns mainly high-field wigglers installed more than ten years ago or small-gap devices such as in-vacuum undulators. An example of the impact of ID gap movements on the apparent vertical emittance recorded at 12 monitors on January 20th 2010 during normal beam delivery is shown in the left plot of Fig. 4. The sudden closure of ID13 augments coupling: Both the mean emittance and its spread increase of about a factor two. The further closure of ID6 about 1 h later compensates partly the impact of ID13, by reducing both values of about 20%.

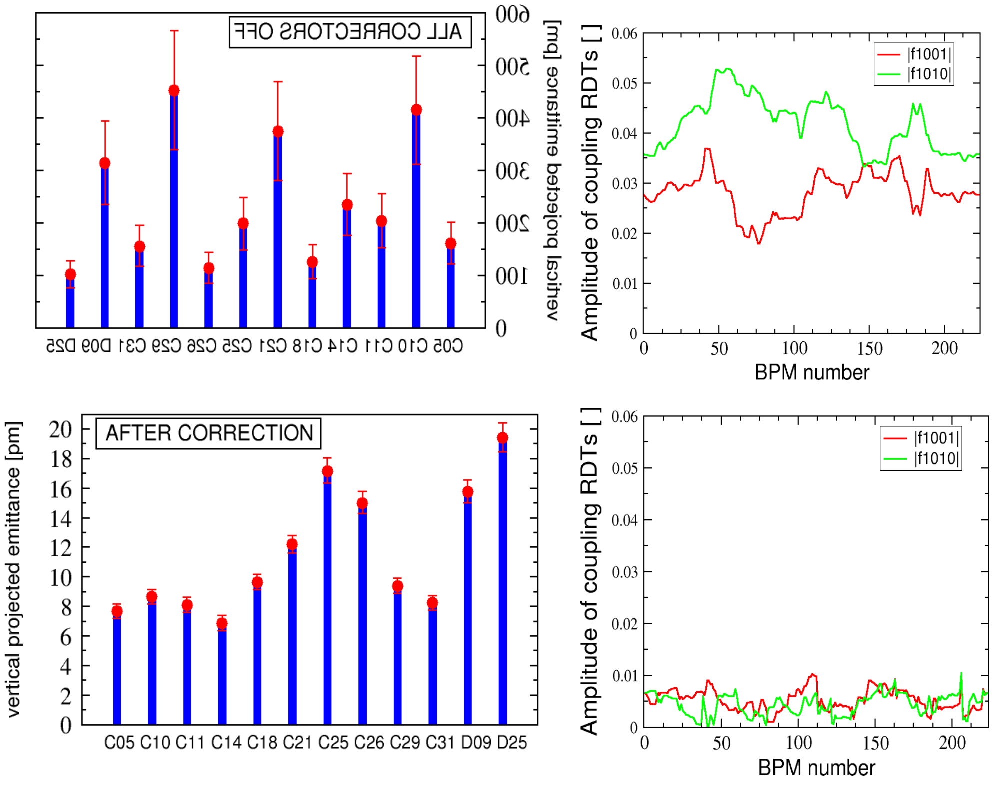

Figure 6: Left column: Vertical apparent emittances Ey measured along the ESRF storage ring with all correctors off (upper plot) and after a correction (bottom plot). The names in the abscissa refer to the used monitors: ten (out of 11) in-air x-ray monitors (from C05 to C31) and two pinhole cameras (D09 and D25). Right column: Amplitude of the corresponding coupling RDTs.

For the time being, ORM and RDTs may not be measured and corrected during beam delivery. In order to minimize the variations of the vertical emittance during normal operation, a feed-forward loop was tested on two IDs known to be among the main sources of coupling. Two dedicated corrector steerers installed at both ends of their straight sections were configured as skew quadrupoles and their strengths defined by look-up tables (created from beam-based measurements) against the undulator vertical aperture. The right plot of. Fig. (4) shows the effectiveness of this scheme. Operators may also trim the other 32 corrector skew quadrupoles to minimize the vertical emittance during normal operations. This is done through a software application that trims the corrector currents so to vary the two coupling vectors C^+ and C^- [14] for the sum and difference resonances, respectively. Until November 2010, operators would trim the C^- vector by trials and errors. Recently, a coupling feedback loop was installed to periodically vary C^- to minimize the vertical emittance, which is measured each second. The left plot of Fig. 5 shows a comparison between the vertical emittance evolution during one week of beam delivery with and without the coupling feedback. In the later case, uncompensated ID gap movements during the first day caused the mean vertical emittance to reach 30 pm (from the initial 6 pm), whereas the coupling feedback prevents any unwanted increase.

During the winter shutdown of 2011 32 additional corrector skew quadrupoles were installed (bringing the total number to 64) and included in the correction. In machine dedicated studies a mean vertical emittance of 2.8 ± 1.1 pm could be achieved, whereas in normal user mode values between 3.2 and 4.5 could be provided in the standard 7/8 +1 mode. With these values the beam lifetime experienced an important reduction from about 55 h (at 200 mA until 2009) to about 30 h. This led to the decision to add one refill per day on top of the traditional two. However, in spring 2011 thanks to a new correction of the sextupolar resonances, a lifetime of about 45 h could be retrieved (see right plot of Fig. 5), hence allowing the removal of the additional third refill.

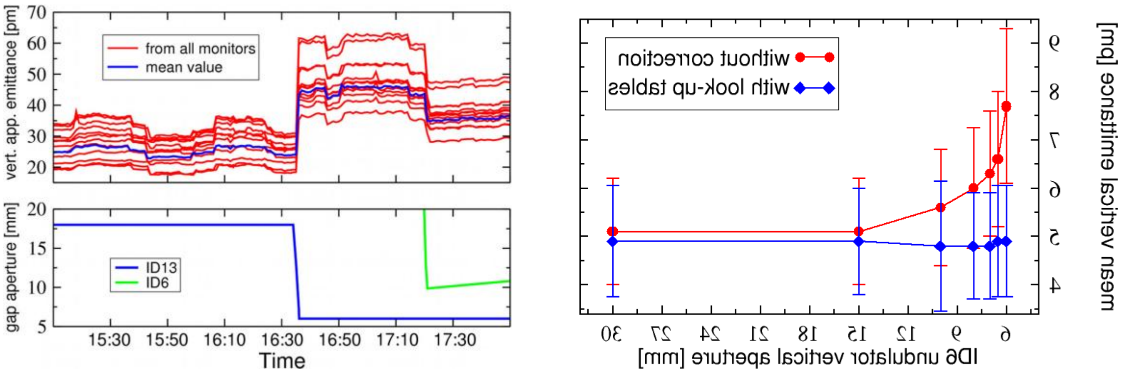

Figure 7: Left: example of vertical apparent emittance abrupt jumps (top plot, measured at 12 monitors, red lines, with the corresponding mean value depicted in blue) following two ID gap movements (bottom). Right: mean vertical emittance measured against the vertical aperture of the ID6 in-vacuum undulator without correction (red circles) and with automatic coupling compensation (blue diamonds). Error bars correspond to the spread among the monitors.

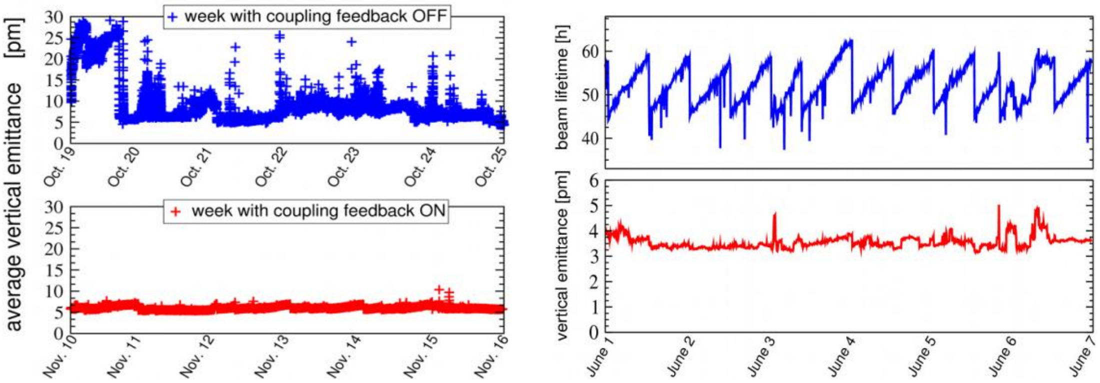

Figure 8: Left: comparison between the mean vertical emittance measured during beam delivery in 2010 without (top) and with (bottom) the coupling feedback. Right: beam lifetime (top) and mean vertical emittance measured during a week of beam delivery in 2011 (7/8 +1 filling mode) with coupling feedback and feed-forward, and 32 additional corrector skew quadrupoles

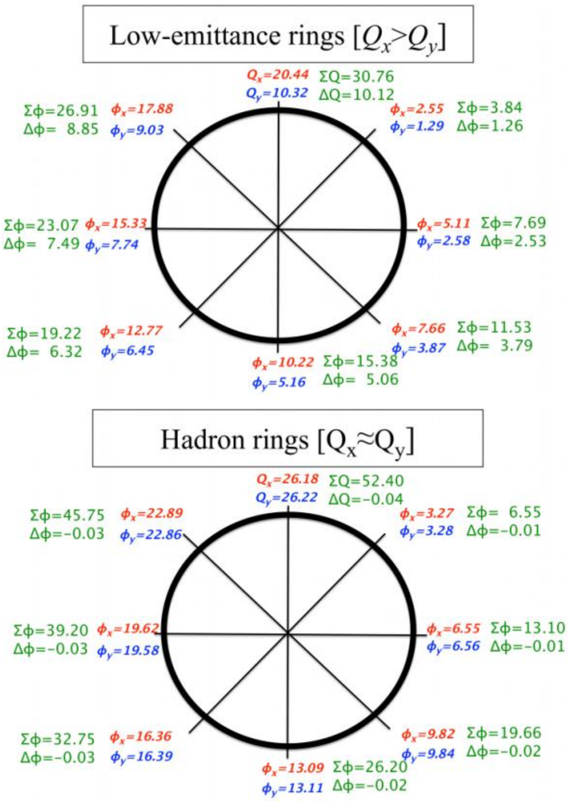

Figure 9: Schematic view of the different evolution of the betatron phases along typical low-emittance rings (left) and hadron machines (right): the unsplit tunes in the later case makes the $\Delta\Phi$ terms be almost zero along the entire path.

3.9.5 Betatron Coupling: Hadron vs Lepton Circular Accelerators

This section is an attempt to understand why in hadron accelerators the sum resonance is barely excited whereas in modern lepton machines it is as strong as the difference resonance. The answer proposed here is: It depends on the difference between the integer parts of the tunes. The design on modern lepton machines is based on the production of even smaller horizontal emittances, which requires even stronger horizontal focusing, with less stringent requirements on the vertical plane. This in turn leads to horizontal tunes much larger than the vertical ones. In the case of the ESRF storage ring Q_x=36.44 and Q_y=13.39 with a difference Q_x - Q_y= 23.05. Hadron machines generally do not require stronger horizontal focusing and usually operate with almost "round" beam, i.e. with similar horizontal and vertical emittances. Focusing is then similar in both planes, leading to unsplit tunes (i.e. with the same integer parts) or split by one or a few units. In the CERN SPS, for instance, Q_x=26.18 and Q_y=26.22 with a difference Q_x - Q_y= - 0.04. The influence on the two resonances may be evaluated from the two coupling vectors C^+ and C^-

$$
\begin{aligned}
C^- &= \frac{1}{2\pi}\oint ds\, j_1(s)\sqrt{\beta_x(s)\beta_y(s)}\,e^{i(\phi_x(s)-\phi_y(s))+is/R\Delta} \quad , \\
C^+ &= \frac{1}{2\pi}\oint ds\, j_1(s)\sqrt{\beta_x(s)\beta_y(s)}\,e^{i(\phi_x(s)+\phi_y(s))+is/R\Delta} \quad .
\end{aligned}
\tag{11}
$$

The two integrals contain a common term $j_1(s)\sqrt{\beta_x(s)\beta_y(s)}$ and two different complex functions: The integrand in C^- oscillates with the difference between the betatron phases ($\Delta\Phi=\Phi_x-\Phi_y$), whereas the other oscillates with their sum ($\Sigma\,\Phi=\Phi_x+\Phi_y$). As depicted in Fig. 6, in lepton machines the number of oscillations performed by $\Sigma\,\Phi$ along the ring, i.e. along the integral path of Eq. (11), is comparable to the ones of $\Delta\Phi$, about 31 and 10 respectively. Hence, the two integrals are of comparable amplitude (actually in the ESRF storage ring, after correction, typical values are $|C^+|\approx 3\times10^{-3}$ and $|C^-|\approx 0.9\times10^{-3}$). In hadron rings with unsplit tunes, instead, $\Delta\Phi$ remains almost zero along the path, making the exponential term in the integral of C^- being equal to 1, whereas the integrand of C^+ executes a large number of oscillations, 52 in the example of Fig. 6. These make $|\,C^+| << |\,C^-|$ (Riemann–Lebesgue lemma). The same is true for hadron accelerators with tunes split by one or a few units. Parenthetically, in machine with unsplit tunes C^- is approximately a real number, which in turns requires just one family of corrector skew quadrupoles to be minimized.

3.9.6 Indirect Measurements of Vertical Emittance

Effective correction of coupling and dispersion may lead to vertical emittances smaller than the resolution of the available diagnostic, preventing a direct measurement. In accelerators experiencing such a shortcoming it is hence necessary to infer the vertical emittance from indirect measurements. In this section we review the three most common procedures, discussing their limits of applicability following the considerations made in the previous sections.

In the early nineties Guignard offered a comprehensive work with several handy formulas for the evaluation of betatron coupling and vertical emittance in the large electron-positron (LEP) collider of CERN [15]. By assuming that both the sum resonance and the contribution of the vertical dispersion to the vertical eigenemittance are negligible, the following relations were derived

$$
\varepsilon_y = g\varepsilon_x \ , \qquad g = \frac{(|C^-|/\Delta)^2}{(|C^-|/\Delta)^2+2} \ , \tag{12}
$$

where the (large) horizontal emittance ε_x is measurable, along with the coupling coefficient g. The latter may indeed by inferred from $|C^-|$ (measurable from the closest-tune approach) and the distance between the fractional parts of the tunes $\Delta=Q_x-Q_y$. The first assumption (negligible sum resonance) was satisfied by all CERN chain of accelerators, these having either unsplit tunes (PS booster, PS, and SPS) or similar tunes (in LEP Q_x=70.4 and Q_y =78.4). As discussed above, this condition is in general no longer met by modern lepton colliders and light sources based on storage ring. In the case of the ESRF the second assumption is not met either, the main source of vertical emittance being presently identified in the vertical dispersion.

Another indirect measurement is based on the evaluation of the beam lifetime before and after coupling correction. This smaller emittance shall increase the probability of the Møller scattering among the electrons within a bunch hence reducing the Touschek lifetime. The dependence of the latter from the vertical emittance being the inverse of its square root, the following relations hold

$$K=\frac{\varepsilon_y}{\varepsilon_x}\ ,\qquad K_A=\frac{\tau_A^2}{\tau_B^2}K_B\ , \tag{13}$$

where K and τ are the coupling coefficient and the Touschek lifetime, while B and A refer to their measurement, before and after coupling correction, respectively. As for the previous method, from the measurable horizontal emittance and K_A it is possible to infer the ε_y. Beside the improper mixture of eigenemittance in the first formula and the apparent emittance that should be used when invoking the Touschek lifetime, this approach assumes that any deterioration of lifetime is induced exclusively by the stronger Touschek effect. Unfortunately, the sum resonance is destructive and may lead to a simultaneous emittance increase and lifetime decrease, if overcompensated. Without a separate evaluation of the two RDTs (or, alternatively, of the two resonance stop-bands) showing that $|f_{1010}|<<|f_{1001}|$ along the ring (or that $|C^+|<<|C^-|$), this approach may underestimate the vertical emittance.

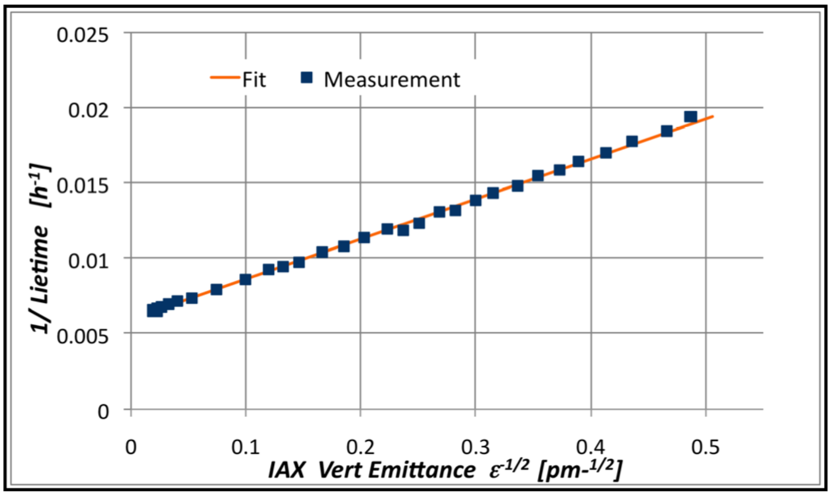

Figure 10: Inverse of the beam lifetime measured at the ESRF storage ring against the inverse square root of the mean vertical apparent emittance. The latter is artificially increased with a vertical shaker leaving the (low) coupling unchanged.

The third method is based on the direct measurement of the Touschek lifetime against different values of the vertical emittance. The inverse beam lifetime reads

$$\frac{1}{\tau}=\frac{\mathrm{A}}{\sqrt{\varepsilon_y}}+\frac{1}{\tau_{Vac}} \quad , \tag{14}$$

where τ_{Vac} denotes the residual vacuum lifetime, the first term in the r.h.s. is the Touschek lifetime and *A* is constant that depends on several RF-related parameters (such as bunch length, RF acceptance and dynamic aperture) and on the Twiss parameters $\beta_{x,y}$. Since the Møller scattering depends on the bunch volume, the Touschek lifetime depends on the two RMS beam sizes, $\sigma_{x,y}$, and the bunch length. Hence, by introducing the vertical emittance in the formula, one is implicitly referring to the apparent emittance $\mathrm{E_y}= \sigma^2_{y}/\beta_y$. This, and not the eigenemittance, shall then be used as independent variable when measuring the Touschek lifetime. More precisely, being the latter the result of an integral over the path length, and being the main sources of scattering the regions with low horizontal beta functions, the Touschek lifetime depends on the vertical apparent emittance averaged along the low-beta regions. The evaluation of *A* necessitates also separate measurements requiring a (sometime subjective) evaluation of parameters such as the RF acceptance and the dynamic aperture. Moreover, if the vertical emittance is varied with coupling, *A* is no longer constant (specially at large coupling) since the Twiss parameters $\beta_{x,y}$ are mixed and the additional vertical dispersion remains unaccounted. In order to overcome this series of problems, at the ESRF storage ring a vertical shaker (excited with white noise) is used to blow up the vertical beam size of a machine with corrected coupling. The average apparent emittance inferred from the 11 monitors distributed along the ring is used as independent variable and plotted as $1/\sqrt{E_y}$ along with $1/\tau$. Displaying Eq. (14) in this way results in a linear curve, where the vacuum term is inferred from the intercept coefficient in the liner fit, *A* from the slope (hence requiring no separate measurement of its terms). The real vertical emittance is inferred after extrapolating the linear fit to the measured lifetime. On February 1st 2011 such a measurement was carried out in the ESRF storage ring to asses the reliability of the IAX monitors at the 4 pm level, as the lower limit for this device was expected to be around 10 pm. The vertical emittances evaluated from the Touschek lifetime resulted in 3.9 pm, highly compatible with the value obtained from the 11 IAX monitors, 4.2 ±1.2 and those from two pinhole cameras, 3.64 and 3.75 pm. The eigenemittance evaluated from the lattice error model was a mere 2.4 pm.

3.9.7 **Conclusion**

The resonance driving terms (RDT) formalism applied to betatron coupling in electron storage rings establishes an unambiguous correlation between the different definitions of vertical emittance. On the wake of this, a correction scheme was conceived for coupling correction and vertical emittance minimization. The application in the ESRF storage ring of this scheme together with a combination of coupling feedback and feed-forward resulted in an ultra-low vertical emittance of about 3-4 pm delivered routinely to users. The presence and the role of the coupling sum resonance in modern lepton machines were pointed out, stressing their implications in the evaluation of the vertical emittance from some indirect measurements.

3.9.8 References

1. M. Sands, SLAC Report No. SLAC-121 (1970).
2. A. W. Chao, J. Apl. Phys. vol. 50, p 595 (1979).
3. K. Ohmi, K. Hirata and K. Oide, Phys. Rev. E, vol. 49 N. 1, p 751 (1994).
4. H. Tanaka and A. Ando, Proc. of the Tamura Symposium on the Future of Accel. Phys., AIP Conf. Proc. vol. 356 N. 1, p. 138, Austin, Texas, USA (1996).
5. B. Nash, J. Wu, and A. W. Chao, Phys. Rev. ST-AB, vol. 9, 032801 (2006). B. Nash, PhD thesis, SLAC-R-820.
6. A. Terebilo, Proceedings of PAC01, p 3203, Chicago, Illinois, USA (2001).
7. W. Herr, F. Schmidt, CERN AB Note, CERN-AB-2004-027-ABP (2004)
8. C. Steier *et. al.*, Proceedings of PAC03, p 3123, Portland, Oregon, USA (2003). A˚. Andersson, M. Böge, A. Lüdeke, V. Schlott, and A. Streun, Nucl. Instr. and Meth. A, 591-3, p 437 (2008).
   C. Thomas, G. Rehm, I. Martin and R. Bartolini, Phys. Rev. ST-AB vol. 13, 022805 (2010).
9. J. Safranek and S. Krinsky, Proceedings of the Orbit Correction and Analysis Workshop, AIP Conf. Proc. vol. 315, pp. 163-169 (1994).
10. K. Kubo *et. al.*, Phys. Rev. Lett. vol. 88, N. 19, 194801 (2002). Y. Honda *et. al.*, Phys. Rev. Lett. vol. 92, N. 5, 054802 (2004).
11. A. Franchi *et. al.*, Phys. Rev. -AB, vol. 14, 034002 (2011).
12. R. Tomás García, PhD thesis, CERN-THESIS-2003-010 (2003).
13. A. Franchi, PhD thesis, GSI DISS 2006-07 (2006).
14. M. Minty and F. Zimmermann, “Measurement and Control of Charged Particle Beams”, Springer, Berlin, 2003 (ISBN 3-540-44197-5).
15. G. Guignard, Phys. Rev. E, vol. 51, N. 6, p. 6104 (1995).

3.10 Ion Effects in Low Emittance Rings

Lanfa Wang
SLAC, 2575 Sand Hill Road, Menlo Park, CA 94025
Mail to: wanglf@slac.stanford.edu

3.10.1 Introduction

In an electron accelerator, ions generated from the residual gas molecules can be trapped by the beam. Then these trapped ions interact resonantly with the beam and cause beam instability and emittance blow-up. Most existing light sources use a long single bunch train filling pattern, followed by a long gap to avoid multi-turn ion trapping. However, such a gap does not preclude ions from accumulating during one passage of the single bunch train beam, and those ions can still cause a Fast Ion Instability (FII) as first predicted by Raubenheimer and Zimmermann [1]. FII has been observed later in ALS[2] and PLS[3,4] by artificially increasing the vacuum pressure by injecting helium gas into the vacuum chamber [2,3,4] or by turning off the ion pumps [3] in order to observe the beam ion instability. However, When the beam emittance becomes smaller, the FII can occur at nominal vacuum pressure as observed in PLS [5], SOLEIL [6], and SSRF [7]. This letter first briefly reviews the beam ion instability theory, and then reports the observations of beam ion instabilities in SPEAR3. Finally, simulations are given to benchmark with the observations.

3.10.2 **Beam Ion Instability Theory**

3.10.2.1 ***Single Bunch Train Instability***

The beam ion instability with single bunch train beam, which is often called Fast Beam Ion Instability (FBII), has been first predicted in 1995[1]. The predicted beam oscillation amplitude has a quasi-exponential growth with time $\tilde{y}(z) \propto \exp\left(+z/l_{train}\sqrt{t/\tau_c}\right)$, where z is the position along the bunch train with a bunch train length l_{train}. The growth rate is given [1]

$$\frac{1}{\tau_c} = \frac{4cr_e r_p^{1/2} \lambda_i \beta_y N^{1/2} n_b S_B^{1/2}}{3\sqrt{3}\gamma\sigma_y^{3/2}\left(\sigma_x + \sigma_y\right)^{3/2} A^{1/2}}. \tag{1}$$

Here, β_y is beta-function, γ is gamma factor, r_e is the classical electron, A is mass number of ion, n_b is number of bunches, N is number of electrons per bunch and λ_i is the ion line density

$$\lambda_i = \sigma_i \frac{P}{kT} N n_b \tag{2}$$

Here P is the pressure, σ_i is the ionization cross-section.

Eq. (1) works in the linear regime of the space charge force, which means the beam's amplitude is smaller than the beam size. A constant beam size is assumed. Figure 1 shows a simulation of FBII with a FODO cell optics. The simulation agrees with the predictions in many ways, although the growth time by simulation is slightly longer. As shown by the simulation, the growth of the beam's amplitude is a quasi-exponential growth in time and exponential growth along the bunch train as predicted.

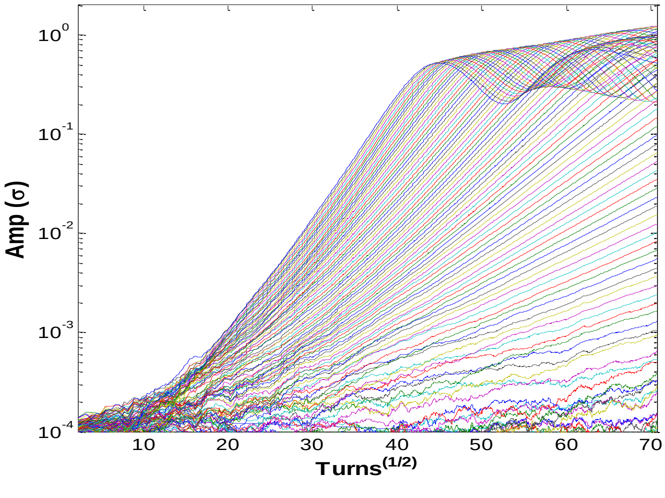

Figure 1: FBII by simulation. Different lines are for different bunches along the single bunch train. Vertical axis is the beam oscillation amplitude in the unit of beam size. Note that horizontal axis is square root of time (number of turns here).

The variation of beam size along the ring can cause damping to the instability, when this damping is very strong, the growth of oscillation amplitude become exponential with a growth time [8]

$$\frac{1}{\tau_e} \approx \frac{1}{\tau_c} \frac{c}{2\sqrt{2} l_{train} \Delta\omega_i / \omega} \tag{3}$$

Here $\Delta\omega_i / \omega_i$ is the relative frequency variation due to the variation of beam size. Note that the above formula works only when this damping effect is much strong. In most cases, the FBII follows quasi-exponential growth.

3.10.2.2 *Multi-Bunch Train Instability*

It is big waste in operation to introduce a long gap to completely let the ions to die out. Therefore partial ions may survive from the bunch train gap in realistic case. It is more important that multi-bunch train beam filling with short gaps can effective reduce the density of trapped ions comparing with single long bunch train case [9]. With this scheme, the density of trapped ions can be significantly reduced compared to a long single train filling pattern by a factor

$$f_{gap} \approx \frac{1}{N_{train}} \frac{1}{1 - e^{-\tau_{gap}/\tau_{ion}}}, \qquad (N_{train} << n_b). \tag{4}$$

where N_{train} is the number of bunch train, τ_{gap} is bunch train gap and τ_{ion} is order of ion oscillation period. Figure 2 shows the simulated build-up of ion density in PEPX [10]. The ion density can be reduced by a factor more than 100 with 183 bunch trains comparing with single bunch train filling.

The direct space charge force is used in the previous analysis [1, 8]. It is interesting that a wake force model is used in the analysis of the beam ion instability with general beam filling pattern. The wake of ions can be represented as [9]

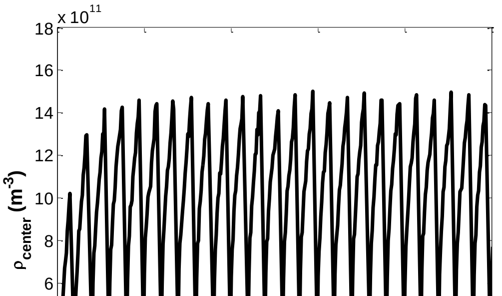

- **Figure 2:** Build-up of ion-cloud in PEPX. The pressure is 0.3nTorr (CO+). The beam consists of 183 bunch trains. The horizontal emittance is 81 *pm* and vertical emittance is 4.3 *pm*. The density near the beam is the ion density within $\sqrt{3}\sigma$.

$$W(z) = \hat{W}_y \, e^{-\frac{2\pi f_{i,y} z}{2Q_0 c}} \sin(\frac{2\pi f_{i,y} z}{c}) . \tag{5}$$

with

$$\hat{W}_y = N_i \left(\frac{r_p N}{A S_b} \right)^{1/2} \left[\frac{4}{3} \frac{1}{\sigma_y (\sigma_y + \sigma_x)} \right]^{3/2} , \tag{6}$$

$$f_{i,y} \approx \frac{c}{2\pi} \left(\frac{4 N r_p}{3 A S_b (\sigma_x + \sigma_y) \sigma_y} \right)^{1/2} , \tag{7}$$

where N_i is the number of ions, and Q_0 is the quality factor due to nonlinearity of the space charge force which is on the order of 10. The amplitude of the wake can be re-written as

$$\hat{W}_y = \frac{2\omega_i L}{c} \frac{S_b}{N} \rho_{i,eff} , \tag{8}$$

where L is the circumference of the ring and $\rho_{i,eff}$ is the effective ion density, which is defined as

$$\rho_{i,eff} = \frac{2\lambda_i}{3\sigma_y (\sigma_y + \sigma_x)} . \tag{9}$$

The exponential growth rate of beam ion instability with multi-bunch train beam filling is given by

$$\frac{1}{\tau} \approx \frac{r_e c \beta_y \bar{\rho}_{i,eff} Q}{\gamma} . \tag{10}$$

where $\bar{\rho}_{i,eff}$ is the average ion density seen by all bunches along the bunch train. The Q factor here includes both the nonlinear space charge effect and optics effect (variation of the beam size).

$$1/Q = 1/Q_0 + 1/Q_{optics} . \tag{11}$$

Eq. (10) can be extended to uniform filling pattern (constant ion density along the bunch train) and single bunch train filling patter case (ion density linearly increases along the bunch train) (Eq. 3). Therefore, it actually is the general case except the case of Eq (1), where there is a quasi-exponential growth, instead of exponential growth.

3.10.3 **Observations in SPEAR3**

SPEAR3 has a circumference of 234 m with a harmonic number of 372. SPEAR3 runs with six bunch train filling pattern in order to suppress the possible beam ion instability. Table 1 lists the main parameters of SPEAR3. Figure 3 shows the calculated ion frequency along the SPEAR3 ring with 200mA beam, which is useful to compare with the observed frequency. The vacuum of SPEAR3 ranges from 0.1 to 0.5 *nTorr*, which varies from section to section. The observations have been done in a period of one year [11].

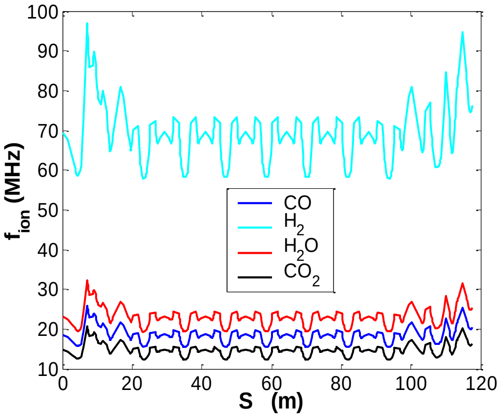

Figure 3: Calculated ion frequency in vertical plane along the ring for a beam current of 200mA.

Table 1 Typical Parameters of SPEAR3

Physics	***Unit***	
Horizontal Emittance	nm	10
Vertical Emittance	pm	14
Bunch Number		280
Harmonic Number		372
Beam Energy	*GeV*	3
Circumference	*M*	234
Bunch spacing	*ns*	2.1
RF frequency	*MHz*	476.315
Radiation Damping time	$\tau_x/\tau_y/\tau_z$ [*ms*]	4.0/5.3/3.2

3.10.3.1 *Dependence on Emittance and Vacuum Pressure*

Beam-ion instability was first observed in 200*mA* operation with a single bunch train filling pattern. Figure 4 shows the observed typical beam spectrum. The observed unstable modes of the lower vertical sidebands agree with the theoretical prediction of the beam ion instability and the frequencies of the unstable modes agree with theory. There is no horizontal instability. The observed bunch oscillation amplitude increases along the bunch train and saturates at the order of beam size as shown in Fig. 5. Coupled-bunch instabilities driven by the traditional impedances either do not saturate or saturate at much larger amplitudes. This indicates the observed instability is driven by the ions in the vacuum. Further tests have been carried out to confirm it. All skew quadrupole magnets were turned off to increase the vertical emittance. Figure 6 shows the measured vertical lower sidebands observed on the beam spectrum analyzer when the skew quadrupole magnets were on and off. When the skew quadrupole magnets were off, the maximum frequency of the observed sidebands reduced from 26.0 MHz to 13.0 MHz, and the maximum amplitude also dropped as predicted by the theory of beam ion instability. This indirectly confirms that the instability is driven by ions in the vacuum instead of the impedance inside the vacuum chamber because the traditional impedance doesn’t change with the beam emittance.

In order to further test that the vertical instability is driven by ions, the vacuum pressure was raised by partially turning off the vacuum pumps. Figure 7 shows the vertical sidebands at different average vacuum pressures along the ring with 300 mA total beam current. The beam fill pattern was a six bunch train, and there was no vertical beam instability at pressure 0.37 nTorr when all vacuum pumps were on. The instability appeared as the pressure increased, and it became stronger with a higher pressure. This directly confirms that the vertical instability observed in SPEAR3 is driven by ions in the vacuum chamber.

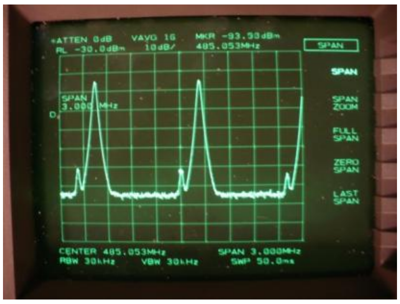

Figure 4: Beam spectrum at 200 mA with a single bunch train filling pattern. There are 280 bunches along the bunch train. The large peaks are the revolution harmonics and the low peaks are the vertical lower sidebands.

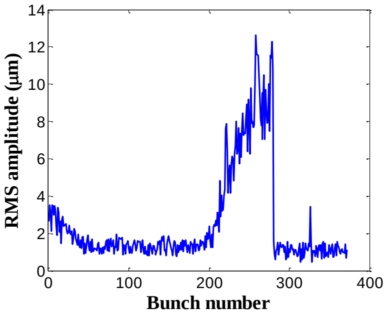

Figure 5: Measured beam's vertical oscillation amplitude with single bunch train filling pattern. Bunches 1-280 and 326 are filled with a total beam current of 200 mA.

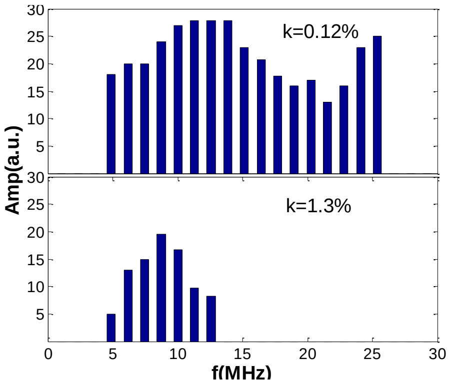

Figure 6: Observed vertical lower sidebands in a single bunch train filling pattern with 280 bunches and total beam current of 192 mA for different beam coupling: k=0.12% when skew quadrupole magnets are on (top) and k=1.3% when skew quadrupole magnets are off (bottom).

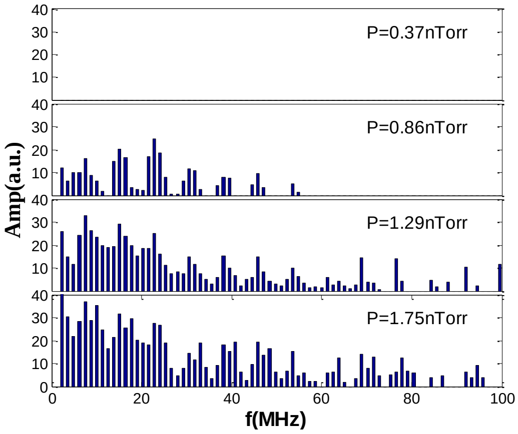

Figure 7: Observed vertical lower sidebands at different vacuum pressures. The beam consists of six bunch trains with total bunch number of 280. The beam current is 300 mA. There are no sidebands with the nominal pressure of 0.37nTorr. The vacuum pressure is increased by partially turning off the ion pumps.

3.10.3.2 *Dependence on Beam Current*

Beam current affects the instability in two ways: the frequencies of the unstable modes increase with the square root of the beam current and the instability growth rate increases linearly with beam current (with the assumption of a constant vacuum). Fig. 8 shows the vertical lower sidebands with various beam currents. The observation qualitatively agrees with the theory.

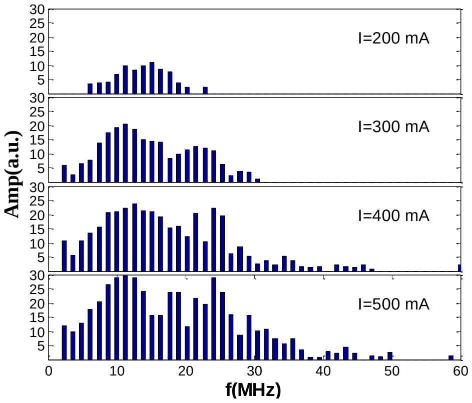

Figure 8: Observed vertical lower sidebands at different beam currents. The beam has single bunch train with 280 bunches.

3.10.3.3 *Dependence on Beam Filling Pattern*

The beam ion instability is sensitive to the beam filling pattern since in most cases more ions can survive from a shorter bunch train gap. Most light sources run with a single bunch filling pattern followed by a long gap to avoid multi-turn ion trapping and often to support a single isolated bunch for timing experiments. Figure 9 shows the vertical lower side band with different bunch train gaps. There is a stronger instability for a short train gap and a vertical beam size blow-up is also observed with short gap as shown in Fig. 10.

A multi-bunch train filling pattern can mitigate the instability in a low emittance ring by reducing the number of ions trapped by the beam. Figure 11 shows the vertical oscillation amplitude of the unstable modes (at sidebands) with one, four and six bunch trains. The beam current is 500 mA in all the cases. There is significant reduction with four bunch trains compared with a single bunch train. However, the reduction is small from four bunch trains to six bunch trains. The instability with six bunch trains was completely suppressed by increasing the vertical chromaticity from 2.0 to 2.6.

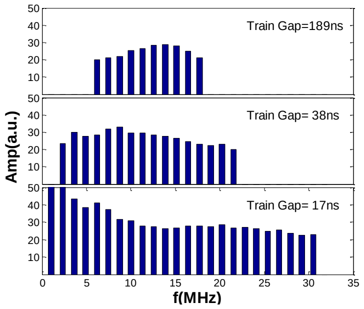

Figure 9: Measured vertical lower sidebands for different train gap length 189ns, 38ns and 17ns. The beam filling pattern is a single bunch train with total beam current 200mA.

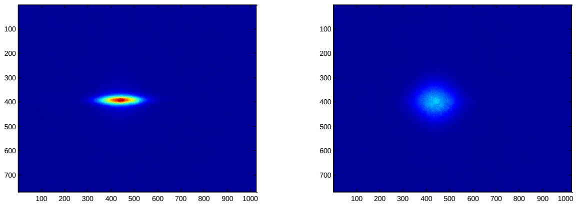

Figure 10: Beam profile with different bunch train gaps: 42 ns spacing (left) and no gap (right). The operational beam typically has a single bunch-train filling pattern.

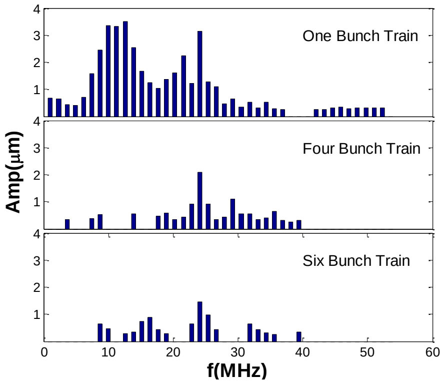

Figure 11: Oscillation amplitude of vertical lower sidebands for different beam filling patterns: one, four and six bunch trains. The total beam current is 500 mA with a total bunch number of 280 in all cases.

3.10.3.4 *Benchmark with Simulations*

Fig. 12 shows the simulated beam instability with different beam filling patterns. There is a fast instability in the linear regime and it is slowed down by the nonlinearity of space charge force when the amplitude is larger than the beam size. The instabilities with four and six bunch train are very similar. The simulations agree with the observation shown in Figure 11. The six bunch train filling pattern is the optimum one, which gives a growth time of 1.6 *ms* with a pressure of 0.5*nTorr*. The growth time will be 2.7 *ms* for a nominal pressure of 0.3*nTorr*. The growth time in the experiment is unknown. However, it is known that there is a weak instability with six bunch train beam filling pattern, which suggests a growth time slightly shorter than the radiation damping time of 5.3*ms*. The simulated growth time 2.7*ms* is close to that number. Note that the simulation is done with zero chromaticity and the real machine has a chromaticity of 2.0. It can be concluded that the simulation is within a factor of two of the observations. Figure 13 shows the detail of the instabilities with six bunch train filling pattern.

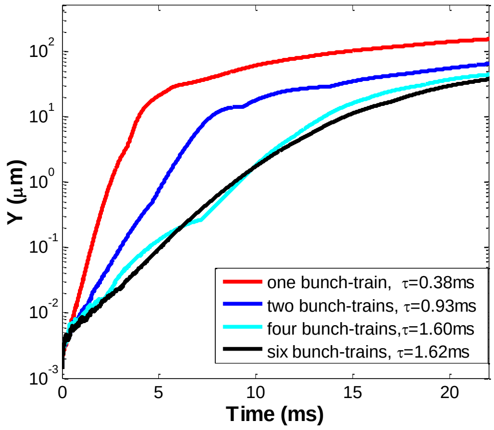

Figure 12: Simulated beam ion instability for different beam filling patterns. The total beam current is 500 mA with total bunch number of 280 in all cases. Zero chromaticity and total vacuum pressure of 0.5 nTorr with multi-gas species are used in the simulation.

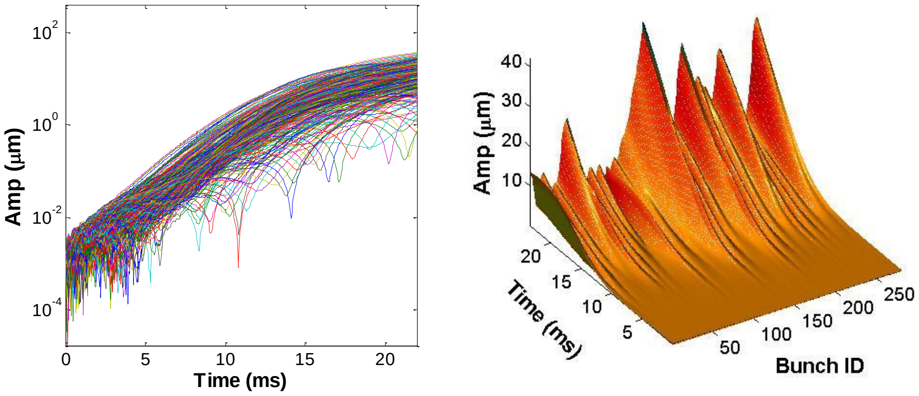

Figure 13: Build-up of beam ion instability with six bunch train filling pattern. the data in the two plots are the same. The vertical axis in the left plot is in logarithmic scale.

3.10.4 **References**

1. T. O. Raubenheimer and F. Zimmermann, “Fast beam-ion instability. I. Linear theory and simulations”, Phys. Rev. E 52, 5487 (1995).
2. J. Byrd, et al., “First Observations of a Fast Beam-Ion Instability”, Phys. Rev. Lett. 79, 79(1997).

3. J. Y. Huang, et al., “Direct Observation of the Fast Beam-Ion Instability”, Phys. Rev. Lett. 81, 4388 (1998).
4. M. Kwon, et al., “Experimental results on the fast beam-ion instability”, Phys. Rev. E 57, 6016 (1998).
5. H. S. Kang, et. al., in Proceeding of 2006 European Particle Accelerator Conference, Edinburgh, UK, 2771(2006)
6. R. Nagaoka, et al., in Proceedings of 2007 Particle Accelerator Conference, Albuquerque, USA, 2019(2007)
7. B. Jiang, et. al., Nucl. Instrum. Meth. A 614, 331(2010)
8. G. V. Stupakov, KEK Proceedings 96-6, 243 (1996)
9. L. Wang, Y. Cai, T. O. Raubenheimer and H. Fukuma, “Suppression of beam-ion instability in electron rings with multibunch train beam fillings”, Phys. Rev. ST Accel. Beams 14, 084401 (2011)
10. R. Hettel, et. al., in Proceedings of 2009 Particle Accelerator Conference, Vancouver, Canada, p2297(2009)
11. L. Wang, et. al., “Observation of beam ion instability in SPEAR3”, in Proceedings of 2011 International Particle Accelerator Conference, Kursaal, San Sebastian, Spain, MOPS090(2011)

3.11 Coherent Synchrotron Radiation: Theory and Simulations.

Alexander Novokhatski
SLAC National Accelerator Laboratory, 2575 Sand Hill Rd, Menlo Park, CA 94025
Mail to: novo@slac.stanford.edu

3.11.1 **Introduction**

The physics of coherent synchrotron radiation (CSR) emitted by ultra-relativistic electron bunches, known since the last century, has become increasingly important with the development of high peak current free electron lasers and shorter bunch lengths in storage rings. Coherent radiation can be described as a low frequency part of the familiar synchrotron radiation in bending magnets. As this part is independent of the electron energy, the fields of different electrons of a short bunch can be in phase and the total power of the radiation will be quadratic with the number of electrons. Naturally the frequency spectrum of the longitudinal electron distribution in a bunch is of the same importance as the overall electron bunch length. The interest in the utilization of high power radiation from the terahertz and far infrared region in the field of chemical, physical and biological processes has led synchrotron radiation facilities to pay more attention to the production of coherent radiation. Several laboratories have proposed the construction of a facility wholly dedicated to terahertz production using the coherent radiation in bending magnets initiated by the longitudinal instabilities in the ring. Existing synchrotron radiation facilities also consider such a possibility among their future plans.

There is a beautiful introduction to CSR in the “ICFA Beam Dynamics Newsletter” N 35 (Editor C. Biscari). In this paper we recall the basic properties of CSR from the theory [1-4] and what new effects, we can get from the precise simulations of the coherent radiation using numerical solutions of Maxwell’s equations [5]. In particular, transverse variation of the particle energy loss in a bunch, discovered in these simulations, explains the slice emittance growth in bending magnets of the bunch compressors and transverse de-coherence in undulators. CSR may play same the role as the effect of quantum fluctuations of synchrotron radiation in damping rings. It can limit the minimum achievable emittance in the synchrotron light sources for short bunches.

3.11.2 **Classical Synchrotron Radiation**

It is interesting to note that exactly 100 years ago G. A. Schott [1] published a formula for an intensity of radiation of a relativistic charged particle, which makes an instantaneously circular motion. The power radiated into the n th harmonic is described by

$$\frac{dI_n}{do}=\frac{e^2n^2}{2\pi c}\omega_0^2\left[J_n^2\left(\frac{nv}{c}\cos\theta\right)tg^2\theta+\frac{v^2}{c^2}J'^2_n\left(\frac{nv}{c}\cos\theta\right)\right] \tag{1}$$

where $do=\sin\theta d\theta d\varphi$, $\omega_0=2\pi f_0$ is a revolution frequency, v is a particle velocity, c is speed of light, e is an electron charge, J_n is a Bessel function of n-th order. Integration by solid angle gives [2]

$$I(n)=\frac{2e^2}{v}\omega_0^2\left[n\frac{v^2}{c^2}J'_{2n}\left(2n\frac{v}{c}\right)-n^2\left(1-\frac{v^2}{c^2}\right)\int_0^{v/c}J_{2n}(2n\xi)d\xi\right] \tag{2}$$

Finally for a continuous spectrum $dn=\dfrac{d\omega}{\omega_0}$ and consider only high values of n we can get an approximate formula [2]

$$I(\omega)=\frac{\sqrt{3}}{2\pi}\frac{\omega_0e^2}{c}\left(\frac{E}{mc^2}\right)F\left(\frac{\omega}{\omega_c}\right) \qquad F(\xi)=\xi\int_\xi^\infty K_{5/3}(\eta)d\eta \tag{3}$$

where $\omega_c=\dfrac{3}{2}\left(\dfrac{E}{mc^2}\right)^3$ is a critical harmonic frequency, E is the particle energy, m is the particle mass, $K_{5/3}(\eta)$ is a modified Bessel function. Plot of the function $F(\xi)$ is shown in Fig. 1. The function reaches a maximum value at 0.29 (approximately one third of the critical frequency). Approximate formulas [2] for small and large values of ξ are:

for $\xi<<1$

$$F(\xi)\approx 2^{2/3}\Gamma\left(\frac{2}{3}\right)\xi^{1/3}\approx 2.15\xi^{1/3} \tag{4}$$

for $\xi>>1$

$$F(\xi) \approx \sqrt{\frac{\pi}{2}}\, \xi^{1/2} \exp(-\xi) \left[1 + \frac{55}{72} \frac{1}{\xi} \right] \tag{5}$$

These approximate functions are also shown in Fig. 1.

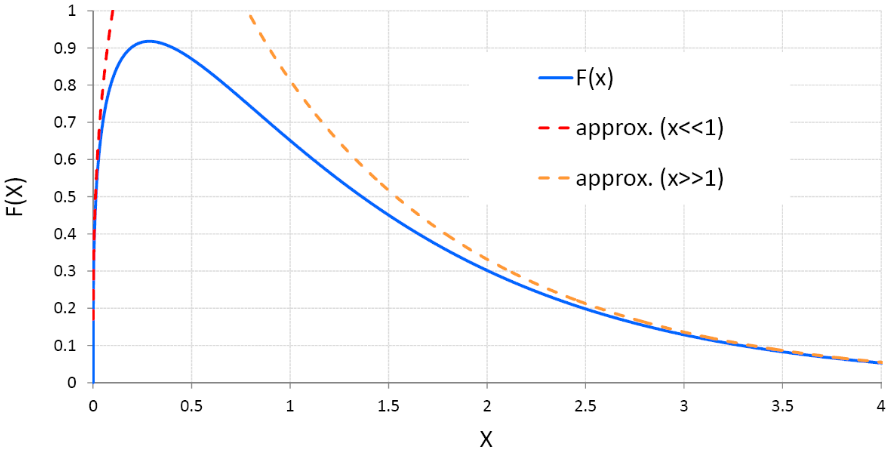

Figure 1: Function F(x) and its approximations

We can integrate the power loss spectrum over all frequencies to get the total power loss [3]

$$\frac{dE}{dt} = \int_0^\infty I(\omega)\, d\omega = \frac{2}{3} \omega_0^2 \frac{e^2}{c} \left(\frac{E}{mc^2} \right)^4 \tag{6}$$

We had the opportunity to observe experimentally this strong dependence of the energy during the SLAC B-factory operations. During the 2008 energy scan to study 2S, 3S and above 4S resonance, we need to change the energy of HER (High Energy Ring) from 8 GeV to 10 GeV. Simultaneously we measured the energy loss due to synchrotron radiation (incoherent radiation, linear with the beam current) and coherent radiation (quadratic with the beam current) of wake fields [6]. A plot of an energy loss per turn for incoherent radiation is shown at Fig. 2. A fit of the experimental data points with a power function gave an exact fourth order dependence.

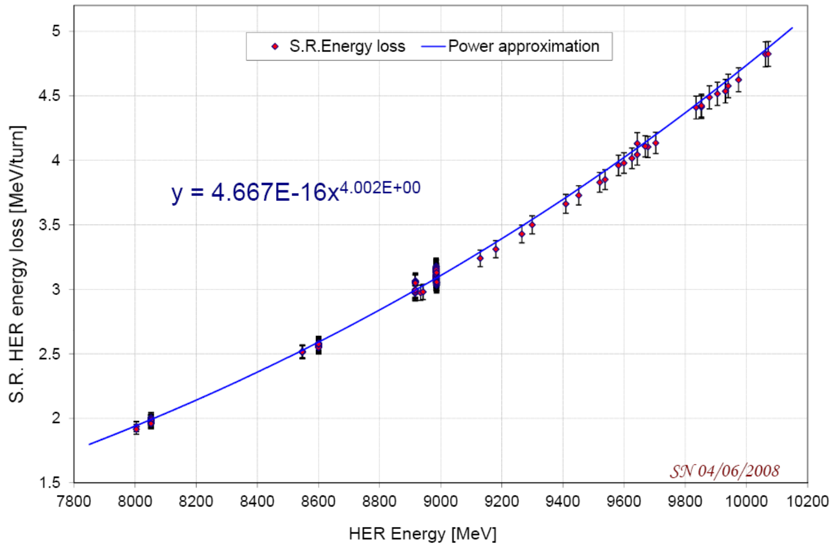

Figure 2: Measured synchrotron energy loss as a function of a beam energy.

Coherent Radiation

The presented formula (6) describes an energy loss of a single particle. To calculate the total loss of a bunch of particles, we need to know [3] the Fourier spectrum $j(\omega)$ of the bunch current $j(t)$

$$\frac{dE}{dt} = \int_0^\infty I(\omega)\left|j(\omega)\right|^2 d\omega \tag{7}$$

A single particle current is a δ-function in the time domain, so it has a constant value in the frequency domain $j(\omega)=1$. If we have many particles we may assume that the total current is a sum of single particles

$$j(t) = \sum_{k=1}^{N} \delta(t-t_k) \tag{8}$$

and Fourier spectrum is

$$j(\omega) = \int j(t)\exp(i\omega t)\,dt = \sum_{k=1}^{N}\exp(i\omega t_k) \tag{9}$$

whence

$$\left|j(\omega)\right|^2 = \sum_{k=1}^{N}\exp(i\omega t_k)\cdot\sum_{l=1}^{N}\exp(-i\omega t_l) = N + 2\sum_{k=1}^{N}\sum_{l=k+1}^{N}\cos\left(\omega\left(t_k - t_l\right)\right) \tag{10}$$

In accelerators the number of particles in a bunch is very high $N \sim 10^8 - 10^{12}$, so we can easily change a sum to an integral. If we have a function $\rho(\tau)$, which describes the particle distribution in a bunch, we can normalize this function to unity:

$$\int_{\tau_{\min}}^{\tau_{\max}} \rho(\tau)\,d\tau = 1$$

Now we change sums in the right side of (7) by integrals using this function

$$\sum_{k=1}^{N}\sum_{l=k+1}^{N}\cos\left(\omega\left(t_k - t_l\right)\right) \approx N^2 \int_{\tau_{\min}}^{\tau_{\max}} \rho\left(\tau_1\right)d\tau_1 \int_{\tau_1}^{\tau_{\max}} \cos\left(\omega\left(\tau_1 - \tau_2\right)\right)\rho\left(\tau_2\right)d\tau_2 \tag{11}$$

In this form (11) one can easily recognize a formula for the calculation of an eigenmode loss factor of a cavity, excited by a bunch passing through this cavity [7]. If we have a bunch with a Gaussian distribution and r.m.s. bunch length σ

$$\rho(t) = \frac{c}{\sqrt{2\pi}\sigma}\exp\left(-\frac{c^2t^2}{2\sigma^2}\right) \tag{12}$$

then after integrating by parts in (8) we get

$$I_b(\omega) = I(\omega)\left|j(\omega)\right|^2 = I(\omega)N\left[1 + N\exp\left(-\left(\frac{\omega\sigma}{c}\right)^2\right)\right] \tag{13}$$

The coherent part of the radiation can become noticeable in some region of a spectrum if

$$N\exp\left(-\left(\frac{\omega\sigma}{c}\right)^2\right) > 1 \quad \text{or} \quad \omega < \frac{c}{\sigma}\sqrt{\ln N} \quad \text{or} \quad f = \frac{\omega}{2\pi} < \frac{c}{2\pi\sigma}\sqrt{\ln N} \tag{14}$$

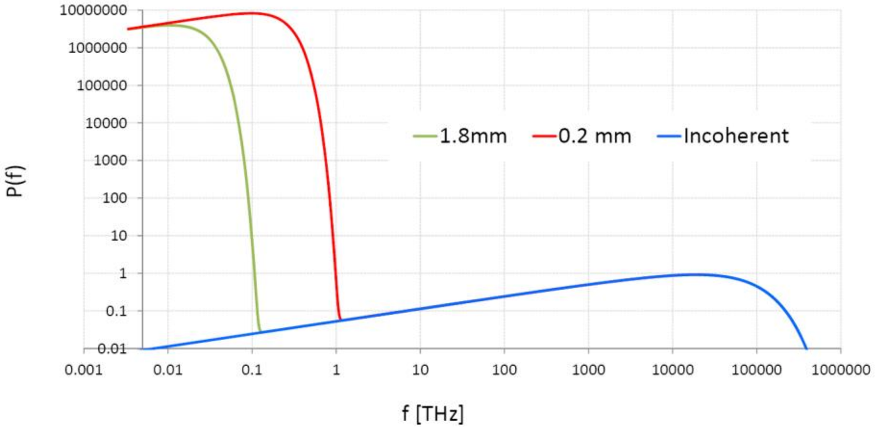

Figure 3: Power spectrum of the synchrotron radiation emitted by a 0.2 mm bunch (red line) and by a 1.8 mm bunch (green line) including incoherent radiation of a single particle (blue line).

For example the coherent part of a spectrum “touches” 1 THz when a bunch has $4{\cdot}10^8$ particles and its bunch length is of 0.2 mm. A critical frequency is usually much higher than a bunch frequency, for example for a particle energy is 1.3 GeV and revolution frequency is 2.71 MHz then critical frequency ${}^{\omega_c}\!/_{2\pi} = 6.7\cdot 10^4$ THz. A plot of the spectrum power of the synchrotron radiation for a bunch with presented parameters is shown in Fig. 3. The coherent spectrum power level is very high; however the total power can be small. Because the main spectrum is in the region of $\omega \approx \frac{c}{\sigma} \sim \omega_c$ we can use approximation (4)

$$I(\omega) = \frac{1}{\omega_0} I(n)$$
$$I(n) \approx \frac{3^{1/6}}{\pi}\Gamma\left(\frac{2}{3}\right)\frac{\omega_0^2 e^2}{c}\cdot\left(\frac{\omega}{\omega_0}\right)^{1/3} \tag{15}$$

to estimate the total coherent power

$$\frac{dE_{coh}}{dt} = N^2 \int_0^\infty I(\omega)\exp\left(-\left(\frac{\omega\sigma}{c}\right)^2\right) d\omega \approx \frac{3^{1/6}}{\pi}\Gamma^2\left(\frac{2}{3}\right)\frac{(Ne)^2}{\sigma^2} c\left(\frac{\omega_0}{c}\sigma\right)^{2/3} \tag{16}$$

To apply this formula (16) or formula (3) to an accelerator bending magnet [8] we simply hide a revolution frequency by making a change $\omega_0 = {}^{c}\!/_{R}$, and then the coherent power takes the form

$$\frac{dE_{coh}}{dt} \approx \frac{3^{1/6}}{\pi}\Gamma^2\left(\frac{2}{3}\right)\frac{(Ne)^2}{\sigma^2} c\left(\frac{\sigma}{R}\right)^{2/3} \tag{17}$$

This formula is very popular in the CSR study and was revised several times in modern literature [9-12]. The numerical coefficient is sometimes slightly different.

In real life bunches of electrons circulate inside a vacuum chamber of an accelerator. Usually a vacuum chamber has metal walls. This metal chamber can strongly effect the low frequency part of the radiation spectrum of a bunch. To get the analytical formulas to estimate this effect J. Schwinger used the model of two parallel metal infinite plates as an approximation of a beam chamber. According to [4] the power emitted into n th harmonic is completely different:

$$I_{\parallel}(n) = 4\pi \frac{n\omega_0}{h} \mathrm{Re}\left\{ \sum_{j=1,3,\ldots}^{\infty} \left[-H_n^{(1)} J_n + \frac{1}{2}\left(H_{n-1}^{(1)} J_{n-1} + H_{n+1}^{(1)} J_{n+1}\right)\right]\right\} \tag{17}$$

where *h* is distance between the plates, and the argument of all the Hankel functions is

$$\xi_{n,j} = \sqrt{n^2 - \left(j\frac{\pi c}{\omega_0 h}\right)^2} = \sqrt{n^2 - \left(j/\vartheta\right)^2} \tag{18}$$

Only modes for which, $\xi_{n,j}$ is real, or $j < n\vartheta \quad \vartheta = \frac{\omega_0}{c}\frac{h}{\pi}$ can contribute to the power. Finally a function $f_{\parallel}(n,\vartheta)$

$$f_{\parallel}(n,\vartheta) = \frac{3}{4}\frac{n}{\vartheta}\sum_{j=1,3,\ldots}^{j<n\vartheta}\left(\frac{j}{n\vartheta}\right)^4\left[K_{1/3}^2\left(\frac{j}{3\vartheta}\left(\frac{j}{n\vartheta}\right)^2\right) + K_{2/3}^2\left(\frac{j}{3\vartheta}\left(\frac{j}{n\vartheta}\right)^2\right)\right] \tag{19}$$

describes the coherent synchrotron radiation of a bunch between two metal plates [4]

$$I_{\parallel}(n) = \frac{\omega_0^2 e^2}{c}\cdot f_{\parallel}(n,\vartheta) \tag{20}$$

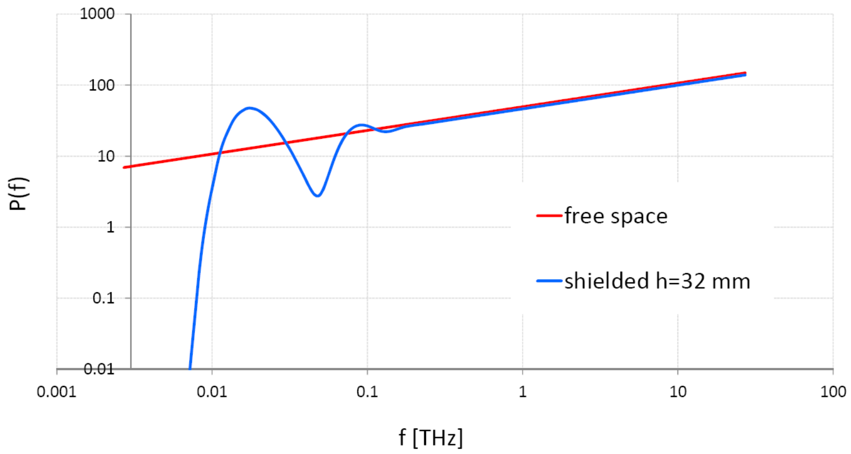

Figure 4: Comparison of the radiation power spectrum in free space and between two metal plates for the case of *R*=17.6 m, *h*=32 mm.

We have changed the numerical coefficient from 4/3 to 3/4 in formula (19) to match the radiation between two plates (20) and radiation in free space (15) at the harmonic numbers above the bunch frequency. The comparison of (20) and (15) is shown in Fig. 4. It can be seen that metal plates can not only cut the low frequency spectrum, but also increase the power at some frequencies. A fully electromagnetic simulation (which will be described in the next chapter) of the real chamber geometry shows a different result (Fig. 5).

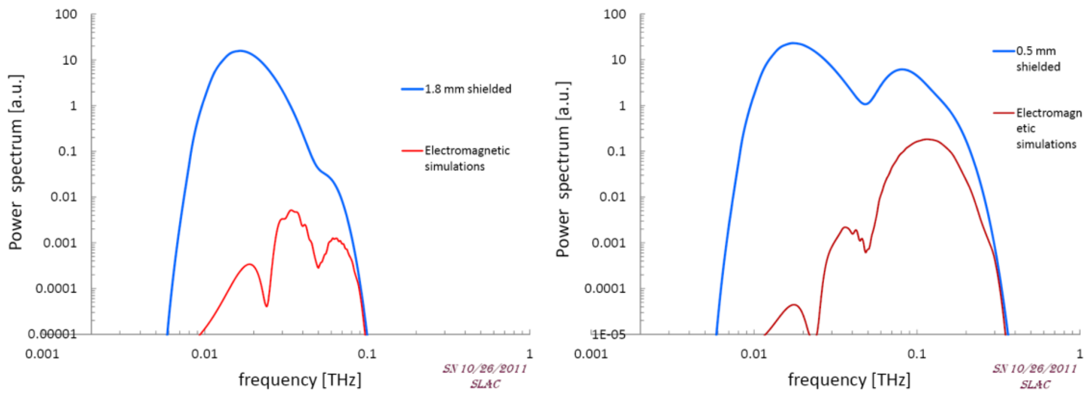

Figure 5: Comparison of the radiation of a 1.8 mm and 0.5 mm bunches between two metal plates (analytic solution, blue line) and the result of electromagnetic simulations of radiation in the taped beam chamber (red line).

Under the assumption that a bunch length l_b is comparable with the distance between plates, J. Schwinger [4] got the expression for the total coherent power emitted by a bunch with a uniform charge distribution

$$\frac{dE}{dt} \approx \frac{\sqrt{3}}{2}\frac{(Ne)^2}{l_b^2}c\cdot\left(\frac{\omega_0}{c}h\right) = \frac{\sqrt{3}}{2}\frac{(Ne)^2}{l_b^2}c\cdot\left(\frac{h}{R}\right) \tag{21}$$

3.11.3 **Electromagnetic CSR Simulation**

We may suggest that a direct solution of Maxwell’s equations together with Newton’s equations can describe the detailed structure of the CSR fields, the fields generated by an ultra-relativistic bunch of charged particles moving in a metal vacuum chamber inside a bending magnet. Electromagnetic components E, B must satisfy the equations

$$\begin{gathered}\frac{1}{c}\frac{\partial}{\partial t}\vec{E} = \nabla\times\vec{B} - \frac{4\pi}{c}\vec{j}_b \quad \nabla\bullet\vec{E} - 4\pi\rho_b \quad \vec{E}_{wall}\times\vec{n} = 0 \\ \frac{1}{c}\frac{\partial}{\partial t}\vec{B} = -\nabla\times\vec{E}_b \quad \nabla\bullet\vec{B} = 0 \quad \vec{B}_{wall}\bullet\vec{n} = 0\end{gathered} \tag{22}$$

A charge density and a charge current must satisfy a continuity equation

$$\nabla\bullet\vec{j}_b + \frac{1}{c}\frac{d}{dt}\rho_b = 0 \quad \rho_b = \sum_k \rho_k(\vec{x}) \quad \vec{j}_b = \sum_k \rho_k(\vec{x})\vec{v}_k \tag{23}$$

A Newton force includes electromagnetic components and a bending magnetic field

$$\frac{d}{dt}\vec{p}_k = e\vec{E} + \frac{\vec{v}_k}{c}\times e\left(\vec{B}+\vec{B}_{bend}\right) \quad \vec{p}_k = m\vec{v}_k \Big/ \sqrt{1-\frac{v_k^2}{c^2}} \tag{24}$$

Modeling ultrafast phenomena requires a special algorithm for solving the electromagnetic equations. This algorithm must be free of frequency dispersion which means that all propagating waves must have their natural phase velocity, completely independent of the simulation parameters like a mesh size or a time step. There are a lot of finite-difference schemes, which numerically solve Maxwell’s equations since the first one was published in 1966 [13]. Most of them are so-called ‘‘explicit’’ schemes, which means that the value of the field at the new time step is calculated only by the field values from the previous time step. Stability conditions for these schemes do not allow a time step to be greater than or equal to a space (mesh) step. This limitation brings an additional troublesome effect for wavelengths that are comparable to a mesh step. We state that this effect works like a frequency dispersion media, which is ‘‘hidden’’ in the finite-difference equation. The main strategy of our method is to use an implicit algorithm which does not have stability issues and employs a more efficient use of finite element mesh techniques. This method can produce self-consistent stable solutions for very short bunches. The scheme could have dispersion in the transverse direction. However, electromagnetic fields, which interact with a beam, propagate in the vacuum chamber at small angles, so the effect of dispersion in the transverse direction is less important than dispersion in the longitudinal direction. We also use a Fourier expansion in the vertical direction. To decrease the amount of needed memory we use a traveling mesh. This is very important for bunch compressor simulations at higher beam energies where the bunch length is a micron but the distance between bends is tens of meters. The mesh moves with the speed of light and we can definitely assume that the electromagnetic field in front of the bunch is zero. Because the time delay due to the bending magnet in the chicane is very small, we do not need more space for the bunch. A traveling mesh does not change the accuracy of the scheme or any conditions of stability. To simulate the real shape of a non-monochromatic bunch moving, for example, in a bending magnet we will use an ensemble of particles. We will track each particle and average the current (particle velocities) over the mesh. The charge density distribution will be integrated using the continuity equation for charge and current. This will help to smooth out errors of particle transitions from one cell to another. More details can be found in [5]. Other approaches for CSR calculations can be found in [14-16].

3.11.4 **CSR Field Dynamics**

3.11.4.1 ***Radiation in a Bend***

Let us first try to understand how a bunch field remakes itself when a bunch is rotated in a magnetic field. We have calculated the electromagnetic field of a three dimensional Gaussian bunch that is initially moving along the vacuum chamber very close to the speed of light. At some point the bunch enters a vertical magnetic field of a bend. What happens after can be seen at Fig. 6, where snapshots of the electric field line distributions are shown at different time moments. In these plots the white boxes with the red arrows show a bunch contour and a bunch velocity direction. Before entering a bend the bunch has only a transverse field, which can be seen as a set of vertical lines. A new field that is generated in a bend is a set of ovals, which increase in size with a time. We can outline two time periods of the field formation. The first period is when a bunch is still inside the region of its initial transverse field. The first two plots in Fig. 6 are related to this first period. The second period starts when the bunch is delayed so much that it is out of the region of the initial transverse field. The bunch is delayed because the velocity vector rotates and the longitudinal component becomes smaller and smaller than the speed of light, however field lines that are not very far away "don't know" about this change and continue to propagate at the speed of light. The last plot in Fig. 6 shows this situation. We may consider these fields to be the fields of the edge radiation in a bend.

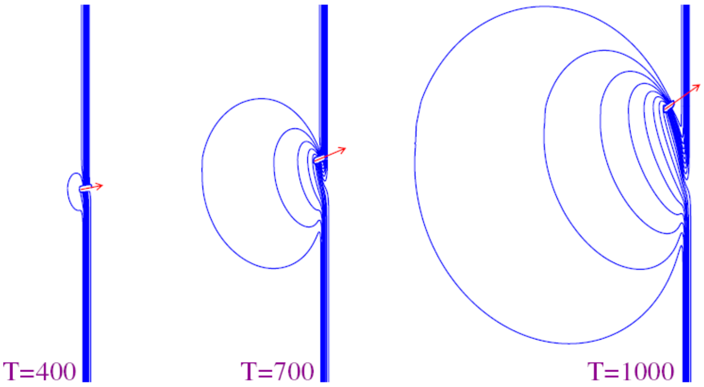

Figure 6: Snapshots of electric field lines of a bunch, which is moving in a magnetic field. White boxes show the bunch contour. Red arrows show the directions of the bunch velocity.

A more detailed picture of the field lines is shown in Fig. 7, where we also show the directions of the electric field lines by green arrows.

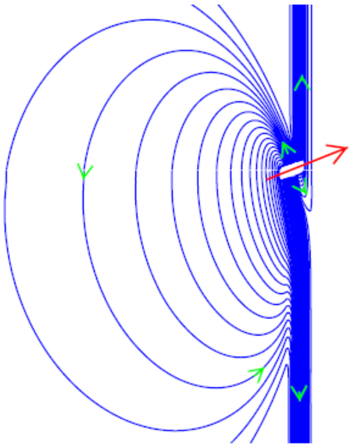

Figure 7: Detailed structure of the field pattern. Red arrow shows the direction of the bunch velocity. Green arrows show the field line direction. Upper field lines take the position of the lower lines and a part of the lower field lines take the position of the upper lines.

If one examines this picture he can see that the upper field lines take the position of the lower lines and a part of the lower field lines take the position of the upper lines. However at the far ends the transverse field lines continue traveling in the same initial direction. We can easily to explain such behavior if we present this field as a sum of two fields $\vec{E}=\vec{E}_{dp}+\vec{E}_{in}$. First field $\vec{E}_{dp}$ is the field of a dipole, which consists of two oppositely charged bunches. One bunch, which has a positive charge is the "real" one. This bunch is rotated in the magnetic field while the other bunch is a "virtual" one, which has an opposite charge and travels straight in the initial bunch direction. Second field $\vec{E}_{in}$ is the field of another "virtual", but positively charged bunch, which travels straight along the initial bunch direction. Naturally the virtual bunches together sum to zero. When we decompose the charges we decompose the fields and the very complicated structure of the radiation field becomes very simple. The decomposition of the field is shown in Fig. 8.

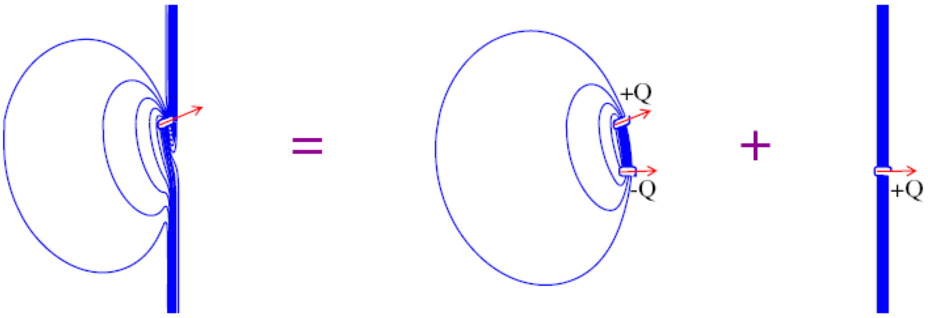

Figure 8: Decomposition of the field of a bunch moving in a magnetic field (left plot) into two fields: a field of a dipole (middle plot) and a field of a bunch moving straight in initial direction (right plot). Red arrows show directions of a bunch velocity

The interaction of the bunch with the dipole field $\vec{E}_{dp}$ continues for a longer time. Fig. 9 shows the absolute value of the electric field on the horizontal plane in the vertical center of the vacuum chamber in consecutive time steps. The white oval shows the real bunch contour. When a dipole is created an electric field appears between a real bunch and a virtual bunch. This field increases in value and reaches a maximum value when the bunches are completely separated and then it goes down as the bunches move apart leaving the fields only around the bunches. The bunch acquires an energy loss while interacting with the dipole field.

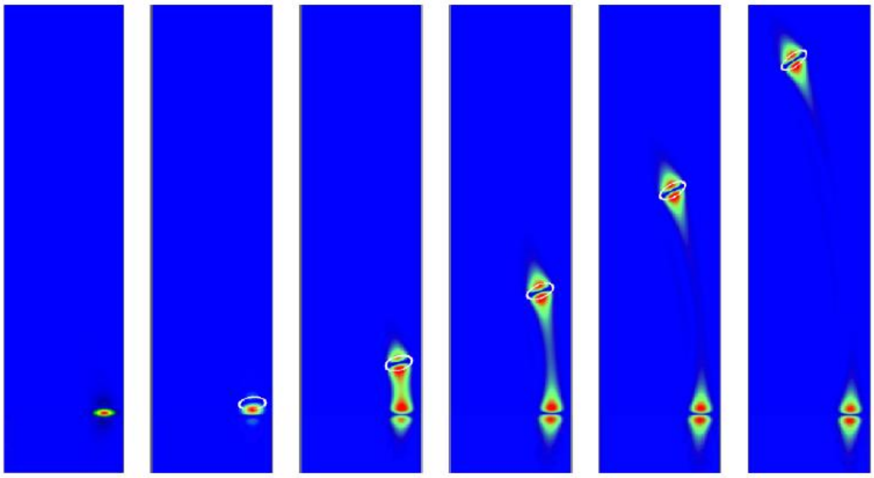

Figure 9: Absolute value of the electric field $\vec{E}_{dp}$ on the horizontal plane in the vertical center of the vacuum chamber in consecutive time steps. The red color corresponds to maximum value. The blue color corresponds to the minimum value of the field. The white oval shows the real bunch contour.

Continuing the study the radiation process we investigate a dense set of field lines in Fig. 7, a fine structure of the field in front of a bunch. This region is common with classical synchrotron radiation. We show a comparison in Fig. 10.

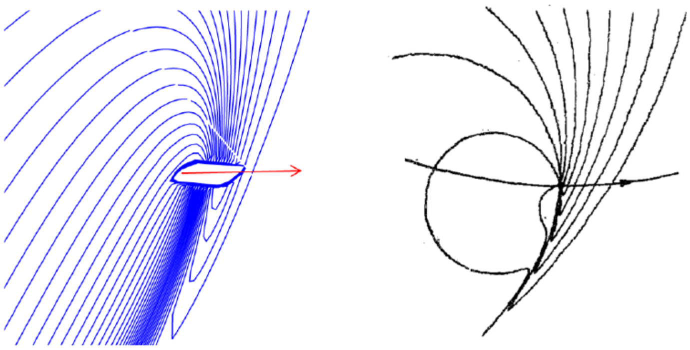

Figure 10: Fine structure of the field pattern in front of a bunch. The left plot shows field lines near a bunch. The right plot presents a picture from the reference [17].

The characteristic wavelength of the synchrotron radiation or an equivalent value of the bunch length for this relativistic factor is

$$\sigma_{s.r.} \approx \frac{R}{\gamma^3} \tag{25}$$

We chose reference [17], as it supplies a picture of the field lines of a particle with a relativistic factor $\gamma=6$. The equivalent value of the bunch length for this relativistic factor is very close to our bunch length. Fig. 10 shows this finite structure together with a plot from [17]. We can state that the region before a bunch is very close for both cases.

3.11.4.2 *Fields Acting inside a Bunch*

In order to study the fields acting on the particles inside the bunch we calculate the distribution of a collinear force $F_\bullet$ and a transverse force $F_\perp$ as projections to the bunch velocity

$$F_\bullet = \vec{J}_b \bullet \vec{E} \quad F_\perp = [\vec{J}_b \times \vec{E}]_x$$

We have found some very exciting fine structure of this force acting on the particle in the bunch. Fig. 11 shows a distribution of forces on the horizontal plane in the vertical center of the vacuum chamber at three time moments. The left three vertical plots in Fig. 11 show a bunch charge distribution. The starting plots are at the bottom at the time when a bunch just enters the magnetic field. The red arrows show the direction of the bunch velocity. The middle three vertical plots show a transverse force. Again, the red arrow shows the direction of the force. The transverse force is the well known space-charge force, which probably is compensated by a magnetic force in the ultra-relativistic case. The right three vertical plots show the collinear force, which is responsible for an energy gain or an energy loss. The red color corresponds to acceleration and energy gain and the blue color corresponds to deceleration or energy loss. The red arrows are collinear or anti collinear with a bunch velocity. We did not include these forces in the beam dynamics simulation in order to make the physical picture clear.

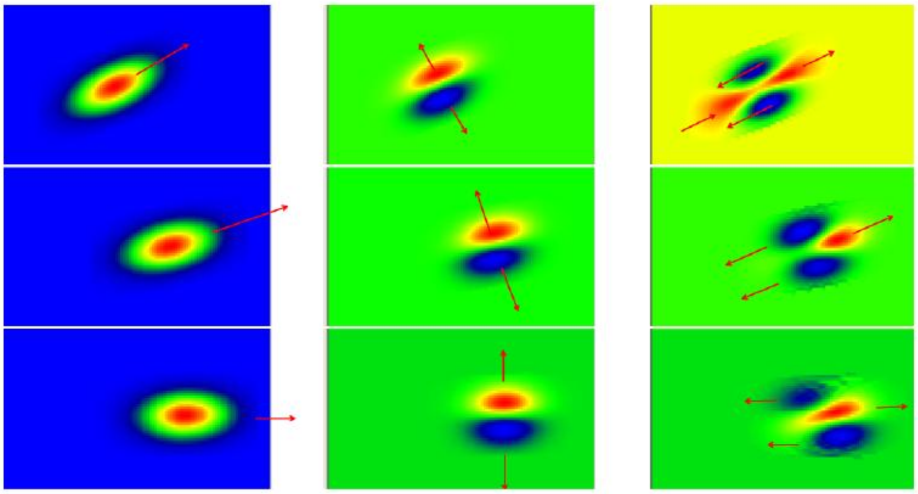

Figure 11: Bunch charge distribution, transverse forces and collinear forces on the horizontal plane in the vertical center of the vacuum chamber at three time moments. The starting plots are at the bottom at the time when a bunch just enters the magnetic field. The left three vertical plots show a bunch charge distribution. The red arrows show the direction of the bunch velocity. The middle three vertical plots show a transverse force. Again, the red arrows show the direction of the force. The right three vertical plots show the collinear force, which is responsible for an energy gain or energy loss.

We see here that the forces on the bunch are very complicated. The particles, which are in the center of the bunch, in front of the bunch and at the end are accelerated, whereas the particles at the boundaries are decelerating. This means that a bunch gets an additional energy spread in the transverse direction. The total effect is deceleration and the bunch loses energy. The asymmetry of the longitudinal fields can also be seen in Fig. 6-7, which shows the electric field line distributions. The bunch shape deformation due to the difference in the angular velocity along the radial position is usually small and can be seen only after some time; however the ultra-small beam emittance can be changed.

The integrated energy loss along the transverse direction as a function of the longitudinal coordinate is shown in Fig. 12 together with a bunch longitudinal distribution. One can see that the head of a bunch and tail are accelerated, when the rest of the bunch is decelerated. The shape of the energy loss distribution is compared with the analytical 1-D model [10] (green dashed line). We obtain a better agreement with the shape of the energy loss distribution for a larger bending radius and smaller bunch length. This comparison is shown at the right plot of Fig. 12. The transverse energy spread is smaller for a larger bending radius.

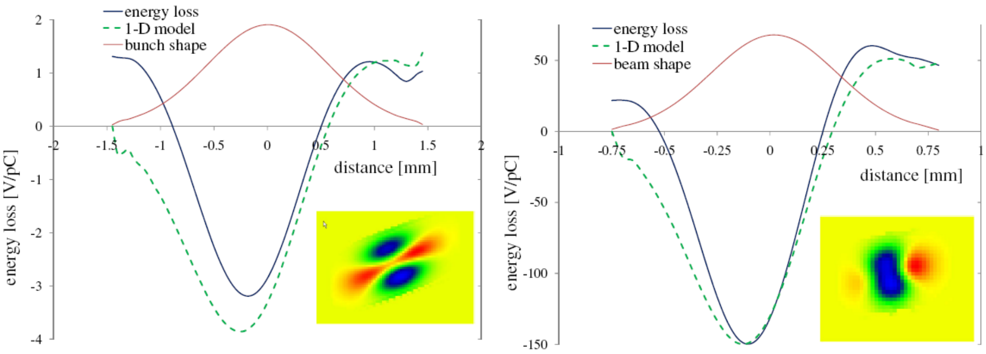

Figure12: Integrated energy loss along the transverse direction as a function of the longitudinal coordinate for two values of bending radius. The right plot shows the result for a bending radius 40 times larger and a bunch length that is two times smaller. The green dashed line is from the analytical 1-D model.

This complicated structure of the collinear field is very important. A bunch will get an additional transverse energy spread, which cannot be compensated. This energy spread in the magnetic field immediately generates emittance growth. This effect can limit the efficiency of the magnetic bunch compressors and as a result the efficiency of FELs.

3.11.4.3 *Coherent Edge Radiation*

As we mention above an ultra-relativistic bunch and CSR fields are moving together and interact for a long time. However one can see a field, which propagates straight ahead from the initial beam horizontal position. This field can be seen very well when the bunch gets a large horizontal displacement. Fig. 13 shows the distribution of the magnetic field on the horizontal plane in the vertical middle of the vacuum chamber. The large peak corresponds to the bunch field. The right picture is a magnified image of the left picture. Note the scales in the X and Z directions are different A red arrow shows the initial bunch X-position and the direction of the bunch velocity. A blue arrow shows the direction of the bunch velocity at this time.

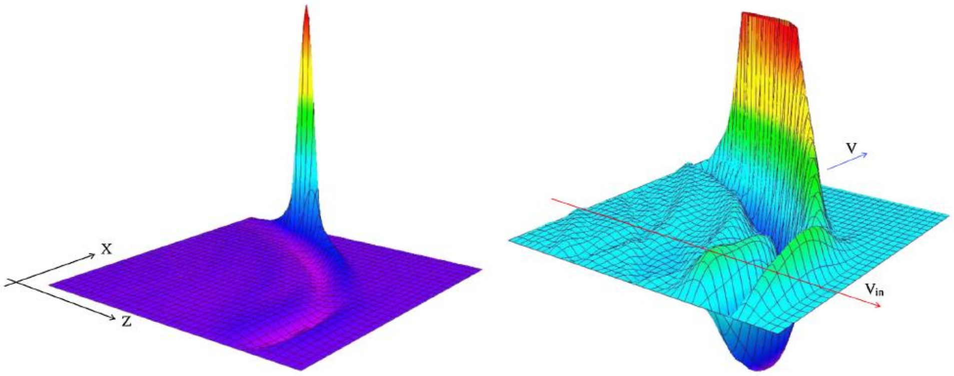

Figure13 : Coherent edge radiation. Distribution of the magnetic field on the horizontal plane in the vertical middle of the vacuum chamber. The large peak corresponds to the bunch field. The right picture is a magnified image of the left picture. Note the scales in the X and Z directions are different A red arrow shows the initial bunch X-position and the direction of the bunch velocity. A blue arrow shows the direction of the bunch velocity at this time.

Other Fig. 14 shows images of the coherent radiation in the form of transverse magnetic field distributions on the vertical planes of the vacuum chamber. The left and right sets of vertical plots correspond to different longitudinal positions. Each plot in a set shows a distribution at a different time. At first we see an image of edge radiation, then the image of synchrotron radiation and finally a bunch field image.

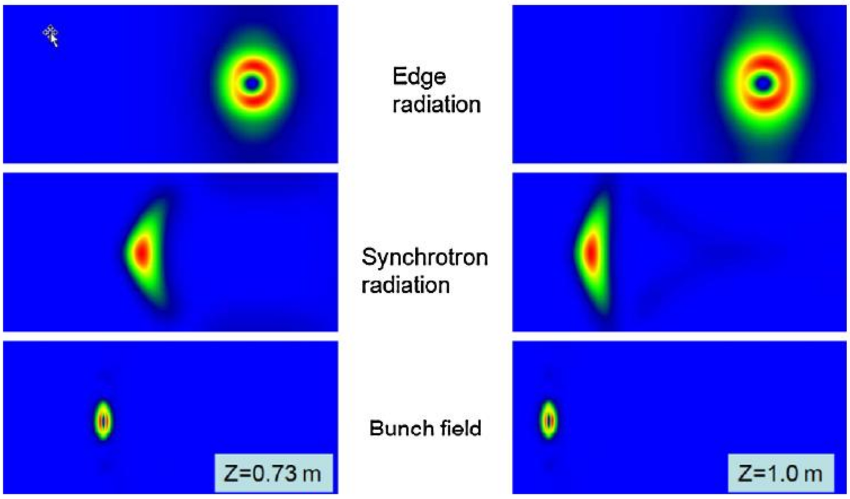

Figure 14: Images of radiation in the form of transverse magnetic field distributions. The left and right set of vertical plots corresponds to different longitudinal positions. Each plot in a set shows a distribution at a different time. The upper plot is an image of edge radiation, which appears first, the middle plot shows an image of the synchrotron radiation, which comes after and the last plot is a bunch field image.

The calculated images of the coherent edge radiation look very similar to the images, which we have seen on the YAG screen after the dump magnets, which bend the beam down at LCLS.

3.11.4.4 *Fields in the Beam Chamber of an Accelerator*

As we mentioned before, the metal walls of a vacuum chamber of an accelerator change the distribution of the radiation fields, but the self electromagnetic field of a bunch is also modified by the chamber geometry. This field is much stronger than the radiation fields. Fig. 15 shows the vertical electric field component inside the chamber when a bunch has left a magnet. The shape of a chamber follows a bunch trajectory. To see the radiation fields we need to magnify the amplitude by 1000 times.

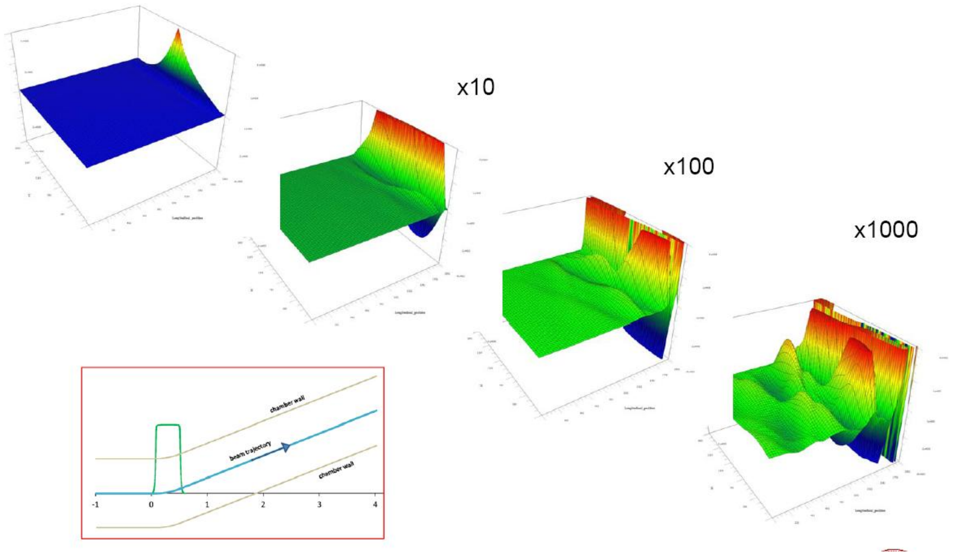

Figure 15: Magnified vertical component of the electric field of a bunch moving in the vacuum chamber after been bend by a magnet.

When a bunch changes position in a chamber, its electromagnetic field also changes and the bunch must react back: loosing and then gaining the kinetic energy. In some cases this effect can be a much stronger radiation loss. Let’s return back to Fig. 5, which shows the difference in spectrum of radiation for real vacuum chamber, which is usually used in the synchrotron light sources. The horizontal size of such a chamber allows a beam to move in a circle and the edge radiation to go straight to an optical window. This tapered chamber has a lot of RF eigenmodes, which may be responsible for the complicated behaviour of the spectrums.

3.11.5 **Conclusions**

We recall well-known formulas for synchrotron radiation and analyze the fine structure of the coherent synchrotron fields, excited by a short bunch in a bending magnet. We have found that there is much more interesting and detailed structure of the CSR fields, which have not been described by any previous study. A very important result is discovering the structure of the complicated collinear force. A bunch will get an additional energy spread in the transverse direction from the collinear force. This immediately leads to an emittance growth and decoherence that could limit FEL lasing for very short bunches. We will continue study this effect.

3.11.6 Acknowledgments

The author would like to thank Mike Sullivan and R. Clive Field for help and valuable comments, Franz-Josef Decker, Paul J. Emma and Yunhai Cai for support and interest in this work and physicists of the Beam Physics Department for useful discussions. This work was supported by Department of Energy Contract No. DE-AC0376SF00515

3.11.7 References

1. G. A. Schott, Electromagnetic Radiation, Cambridge (1912).
2. J. Schwinger, “On the Classical Radiation of Accelerated Electrons”, Phys. Rev. 75, Num 12, p. 1912 (1949).
3. L. I. Schiff, “Production of Particle Energies beyond 200 MeV”, Rev. of Sci. Instr. Vol. 7, Num. 1, p. 6 (1946)
4. J.S. Nodvick and D.S. Saxon, “Suppression of Coherent Radiation by Electrons in a Synchrotron”, Phys. Rev. 96 (1954)
5. A. Novokhatski, “"Field dynamics of coherent synchrotron radiation using a direct numerical solution of Maxwell's equations", Phys.Rev.ST Accel. Beams 14 (2011) 060707.
6. A. Novokhatski, M. Sullivan, “Loss Factor of the PEP-II Rings”, proceedings of the 11 th European Particle Accelerator Conference, Magazzini del Cotone, Genoa, Italy (2008), SLAC-PUB-13297
7. P. B. Wilson “Introduction to wake fields and wake potentials”, SLAC-PUB-4547, January 1989.
8. A. Chao, M. Tigner, “Accelerator Physics and Engineering”, World Scientific
9. P. Goldreich and D.A. Keeey, “Coherent Synchrotron Radiation”, Astrophysical Journal **170** (1971) 463
10. Ya. S. Derbenev et al., “Microbunch Radiative Tail-Head Interaction”, TESLA FEL-Report 1995-05 (1995)
11. J. B. Murphy, et al., “Longitudinal Wakefield for an Electron Moving on a Circular Orbit”, Part. Accel. 57, 9 (1997).
12. E. L. Saldin et al., “On the Coherent Radiation of an Electron bunch moving in an Arc of a Circle”, NIM, Sec. A, 417, 158 (1998).
13. K. S. Yee, IEEE Trans. Antennas Propag. 14, 302 (1966).
14. R. Li. Nucl. Instrum. Meth. Phys. Res. A, 429, 310, 1998.
15. G. Bassi et al., “Overview of CSR codes”, Nuc. Instrum. Methods Phys. Res. A, 557, pp. 189–204 (2006).
16. M. Borland, Phys. Rev. ST Accel. Beams 4, 070701 (2001).
17. S. G. Arutyunyan, Sov. Phys. Usp. 29, 1053-1057 (1986)

3.12 Nonlinear Momentum Compaction Factor and Generation of Coherent Synchrotron Radiation at the Metrology Light Source

J. Feikes, M. Ries, P. Schmid, G. Wüstefeld
Helmholtz-Zentrum Berlin (HZB), Albert-Einstein-Str. 15, 12489 Berlin, Germany

A. Hoehl, R. Klein, R. Müller, G. Ulm
Physikalisch-Technische Bundesanstalt (PTB), Abbestraße 2-12, 10587 Berlin, Germany

Corresponding authors:
Markus.Ries@helmholtz-berlin.de
Godehard.Wuestefeld@helmholtz-berlin.de

3.12.1 **Introduction**

Short electron bunches are of increasing interest for producing short X-ray pulses and coherent THz radiation (CSR). These short bunches can be achieved in electron storage rings by different methods, e.g. bunch slicing and crab cavities [1]. The low-α operation is another possibility to produce short bunches, typically of pico- and sub-pico-seconds length, and subject of this contribution. The Metrology Light Source (MLS) is the first storage ring optimized for low-α operation with the intention to produce intense CSR by short bunches. The low-α operation requires control of higher order, momentum dependent terms of α, leading to expanded possibilities of longitudinal beam dynamics. The low-α scheme and results are presented.

The MLS [2,3] of the PTB is dedicated to metrology utilizing radiation in the THz to the EUV spectral range. It was designed, built and is operated by the HZB [4]. To cover the tasks in the THz range, it is optimized to shorten bunches by using a flexible low-α optics [5]. The emitted THz radiation consists of pulses with 500 MHz repetition rate. An average power level of up to 60 mW can be produced. Bursting and stable "steady state" THz radiation can be generated.

The key parameter for shortening the bunch length is the "momentum compaction factor" α, a tunable, momentum dependent storage ring parameter which strongly affects the longitudinal bunch properties. The "zero current" bunch length scales within limits with $\sqrt{\alpha}$ [6]. Based on the experience obtained at BESSY II [7] on low-α optics operation, the MLS lattice was designed for a precise control of the momentum dependence of $\alpha=\alpha(\delta)$, to produce short bunches with good beam lifetime. The low-α operation is investigated at several other electron storage rings, in order to produce short X-ray pulses and CSR, for further references see [5].

The MLS is the first storage ring, which applies an advanced and dedicated method for reliable and easy tuning of the low-α optics, using sextupoles and octupoles to correct higher orders of α [5]. A similar octupole scheme was recently implemented at NewSUBARU [8]. With this method the electron beam can be stored at positive or negative values of α in different longitudinal bucket types, called rf- and α-buckets (see below).

The main parameters of the MLS are presented in Section 1.1.2. The low-α optics and examples of its capability, e.g. beam storing in α-buckets are presented in Section 1.1.3. The last part, Section 1.1.4, discusses CSR and its properties, to demonstrate that the main goals of THz production are achieved.

3.12.2 The Metrology Light Source

The MLS lattice consists of four double bend achromat cells. The main parameters are listed in Tab. 1. The "low-α optics" is a special machine setup, dedicated to control the bunch length. Several parameters can be varied, e.g. the beam energy, the α value or the rf-voltage. Depending on the machine settings, zero current bunch lengths of less than 1 ps (rms) in the low-α optics are expected. The lower value is still unknown; it depends on several limiting effects. The MLS is equipped with a novel higher order mode damped rf-cavity [9], with a large tuning range of the rf-voltage for further bunch length manipulations.

To operate the low-α mode, the beam is injected from a 105 MeV microtron into the storage ring and ramped to the specified energy. Then a sequence of different magnet optics settings is applied, to reduce α to the target value. An automated ramp procedure controls all these steps, from the injection to the desired energy and α value. This simplifies the low-α operation considerably. To avoid lifetime reductions or beam loss, these files are set up for a fixed transverse working point and small chromaticities.

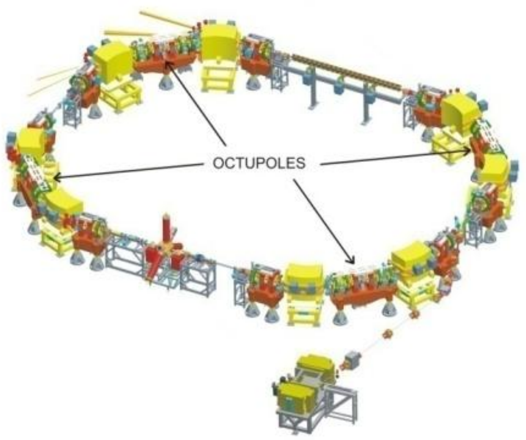

Figure 11: The MLS storage ring.

Parameter	***Value***	***Unit***
electron energy	105 … 630	MeV
storable current	$(1e^{-})$ ... 0.2	A
circumference	48	m
bending radius	1.528	m
rf-frequency f_{rf}	500	MHz
accelerating voltage V_{rf}	< 500	kV
ΔE / turn (630 MeV)	9.062	keV
nat. emittance (630 MeV)	100	nm rad
energy spread (630 MeV)	$4.4 \cdot 10^{-4}$	
α_0	-0.03 ... 0.07	

Table 1: The MLS machine parameters.

Alpha can be tuned to any value between -0.03 and 0.07. Presently currents of up to 180 mA with approximately 6 h lifetime can be stored in low-α optics at 630 MeV. Low-α optics are also available at lower energies. For the first time, low-α optics and THz generation are explored at such low energies, which offers the chance to obtain information on the minimum machine energy required for reliable THz generation.

3.12.3 The Low-α Optics

3.12.3.1 *α-Buckets*

In this section the low-α scheme is presented, with special attention to the nonlinear properties of α(δ) with respect to the relative momentum deviation δ and its control by sextupoles and octupoles. An effective Hamiltonian describing the longitudinal beam dynamics is applied to derive some properties of the low-α optics.

Alpha is defined by the relative change of the particle reference orbit length L_0 of the storage ring as a function of δ,

$$(L - L_0)/L_0 = \alpha\delta, \text{ where } \delta = (p - p_0)/p_0.$$

As electron storage rings operate in the highly relativistic limit, the particle velocity is approximated by the speed of light c. In the limit of α=0 the revolution times become independent of the momentum, this mode is also called "isochronous". To avoid additional orbit lengthening effects depending on the transverse particle oscillation amplitudes, the transverse chromaticities are set close to zero [10,11]. For the following discussion α(δ) is considered as a function of δ only and expanded into a power series, using the notation

$$\alpha = \alpha_0 + \alpha_1\delta + \alpha_2\delta^2 \dots$$

A close relation between the different α-terms and the multipoles required for its control [12] exists. The leading term α_0 depends on the linear dispersion function D (controlled by quadrupoles) within the dipoles of bending radius ρ,

$$\alpha_0 = \frac{1}{L_0}\oint \frac{D}{\rho} ds,$$

where s is the longitudinal orbit position. The term α_1 is defined by the longitudinal chromaticity, $\xi_s = (\partial f_s/\partial\delta)/f_{rev}$ at $\delta = 0$, where f_s is the synchrotron oscillation frequency and f_{rev} the revolution frequency. The two transverse and the longitudinal chromaticities are controlled by three sextupole families. Furthermore, the curvature of α at $\delta = 0$, defined by α_2, is adjustable by octupoles.

Longitudinal beam dynamics involving nonlinear α is presented in [5,12,13], for example. The dynamics, as discussed in the present note, can be derived from the Hamiltonian,

$$H = H_0 \cos(\phi) + 2\pi f_{rf}\left(\frac{\alpha_0}{2}\delta^2 + \frac{\alpha_1}{3}\delta^3 + \frac{\alpha_2}{4}\delta^4\right),$$

with $H_0 = f_{rev}eV_{rf}/E_0$, where E_0 is the particle energy, ϕ is the longitudinal phase position of the particle with respect to the rf-phase and V_{rf} the rf-voltage. Energy loss by synchrotron radiation is ignored. The additional α-terms lead to a more complicated dynamics, described by a Duffing oscillator if α_1=0. From this Hamiltonian fixed points FP(ϕ,δ) can be derived, see Tab. 2. For the more general case $\alpha_1 \neq 0$ see [14]. The δ-dependent fixed points are derived from the condition δα(δ)=0. If only α_0 is non-vanishing, these buckets are called rf-buckets, if the higher orders terms of $\alpha(\delta)=0$ become involved, we call it α-buckets, according to [13]. Depending on the order of α, the condition $\alpha(\delta)=0$ leads to a variety of new α-buckets. For our case, defined by α_0, α_1 and α_2, the fixed points lead to 4 bucket types, which we name A, B, C and D, see Fig. 2. Small amplitude oscillations around the fixed points and the zero current bunch length can be derived from the Hamiltonian [5], see Table 2.

Table 2: Stable fixed points FP (φ,δ), synchrotron frequency f_s and zero current bunch length σ for the different bucket types, for fixed V_{rf} phase. The bucket D does not have a potential minimum and is therefore not included in the table.

bucket	**FP** $(\boldsymbol{\phi},\boldsymbol{\delta})$	f_s	σ	α_0	α_2
A	(0,0)	f_{s0}	σ_0	>0	>0
$\mathrm{B}_{\alpha_1=0}$	$(0,\pm\sqrt{-\alpha_0/\alpha_2})$	$\sqrt{2}f_{s0}$	$\sqrt{2}\sigma_0$	<0	>0
C	$(\pi,0)$	f_{s0}	σ_0	<0	>0
$\mathrm{B}_{\alpha_1=0}$	$(\pi,\pm\sqrt{-\alpha_0/\alpha_2})$	$\sqrt{2}f_{s0}$	$\sqrt{2}\sigma_0$	>0	<0
C	(0,0)	f_{s0}	σ_0	>0	<0

The synchrotron oscillation frequency f_{s0} and the related bunch length σ_0 are the same as for the rf-bucket and are given by,

$$f_{s0}^2 = f_{rf}H_0\alpha_0/2\pi\ , \qquad \sigma_0^2 = (\delta_0^2c^2\alpha_0)/(2\pi f_{rf}H_0),$$

where δ_0 is the natural energy spread. As indicated in Tab. 2, buckets of the type A and C are better suited for short bunch production, the buckets B lead to $\sqrt{2}$ longer bunches.

For simplicity, in most of the following discussion we set $\alpha_1=0$. The low-α optics is then characterized by $\alpha=\alpha_0+\alpha_2\delta^2$. The bucket properties can be derived from the Hamiltonian. The A bucket is the most common operation mode at accelerators and includes the situation $\alpha(\delta)=\alpha_0$. This bucket type exists, if $\alpha_0/\alpha_2>0$, i.e. $\alpha(\delta)=\alpha_0+\alpha_2\delta^2=0$ has no real solution for δ, Fig. 2. There are real solutions, if α_0/α_2 becomes <0 and three new buckets B, C and D appear. The bucket acceptance depending on the rf-voltage is discussed in [5].

If α_0 crosses zero A changes smoothly from a single well potential into D, a double well potential, with the two buckets B in the center, see Fig. 2. The two B buckets are indicated by B_+ and B_-, each one with stable momentum fixed point different from zero displaced in energy. Beam stored in bucket A becomes now stored in the B buckets (double beam), at the same phase location. The additional bucket C appears centered around the former unstable fixed point of the A bucket. Beam can be stored in the bucket C, if it is injected there, and triple beam storage is possible [14].

The situation is different, if the new buckets are created by changing the sign of α_2, see Fig. 4. The bucket of type A changes smoothly to C, and the buckets B and D are displaced in longitudinal phase by π. Bucket C is a single well potential, the stored beam moves form A to C at the same phase location. Beam can be stored in buckets B, if it is injected there.

3.12.3.2 *Manipulating α-Buckets by Varying α_0*

In a first example of longitudinal beam optics manipulation, α_0 is decreased and crosses $\alpha_0=0$, where $\alpha_2>0$ is assumed. Before the $\alpha_0=0$ crossing, the sign of α_0/α_2 is positive, and the related fixed point for the B-bucket $(0, \pm\sqrt{-\alpha_0/\alpha_2})$ is complex. Passing $\alpha_0=0$, the fixed point becomes real and the bunch becomes stored in the B-buckets. By changing α_0, the bunch can be moved back and forth between buckets A and B without loosing electrons. An example of the stored beam in buckets A and B is given in Fig. 2. In the phase space plot, Fig. 2 left, the two B buckets are split in energy (vertical axis). The corresponding figure on the source point monitor, Fig. 2 right, shows a horizontal displacement because of dispersion at the location of the source point monitor. The bucket C is displaced by π in longitudinal phase space; it is not populated during this beam manipulation.

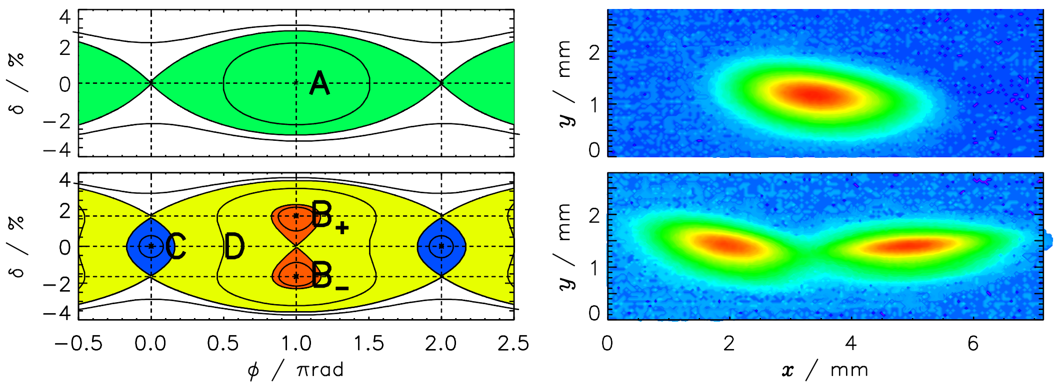

Figure 2: Longitudinal phase space plot with buckets A, B, C and D (left). Measurement of populated bunches in buckets A, B_+ and B_- by a source point imaging system in a dispersive section (right).

In Fig. 3 the chromatic orbits of the two beams stored in buckets B are shown. The orbit was measured in two steps, first by populating only B_+ buckets and afterwards B_- buckets. If both buckets are simultaneously populated, two separate photon beams are visible at the beam port, see Fig. 3. The beams are separated by 6 cm. Experiments with beams of slightly different energies can be performed [15]. The beam in the two B buckets is stored with several hours of lifetime. If $\alpha_1\neq0$, bunches in the two bucket types have different length. Simultaneously long and short bunches can be stored on separate chromatic orbits [14]. Up to a factor 2.7 of different bunch lengths were achieved.

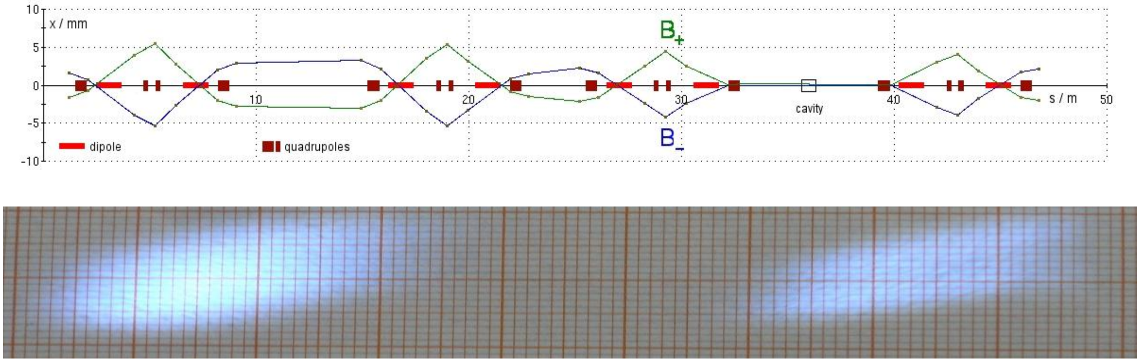

Figure 3: Simultaneous double beams of 170 mA at 10 h lifetime stored in the MLS. Upper part: chromatic orbits of the two beams, differing in momentum by about 2%. Lower part: synchrotron radiation spot at the beam port. The spot centers are separated by 6 cm.

Transferring current from bucket B_+ to B_- without loss is possible. This was demonstrated by an experiment, where the current in bucket B_- was kept constant within 2% over 10 h by controlling the current flow rate from bucket B_+ to B_- The current flow between the two buckets was controlled by slightly detuning the rf-frequency [16].

3.12.3.3 *Manipulating α-Buckets by Varying α_2*

In a second example α_0 is kept positive and α_2, the curvature of $\alpha(\delta)$, is changed. The value of α_2 decreases while increasing the octupole currents I_8 from -8A ($\alpha_2>0$) to +8A ($\alpha_2<0$). Bucket A changes into bucket C, if the sign of α_2 changes, see Fig. 4. The additional appearing buckets D, B_+ and B_- are displaced in phase by π and are therefore not populated. Additionally, the lifetime of the stored beam was measured. The machine setting was 250 MeV beam energy, 124 kV rf-voltage and 20 mA beam current. Fig. 4 shows the lifetime measurements (left) and simulated phase space plots (right) for the different buckets. The small insets in Fig. 4 (left) show the different curvature of $\alpha(\delta)$ in buckets A and C. This measurement was repeated for different settings of α_0, as indicated in the figure.

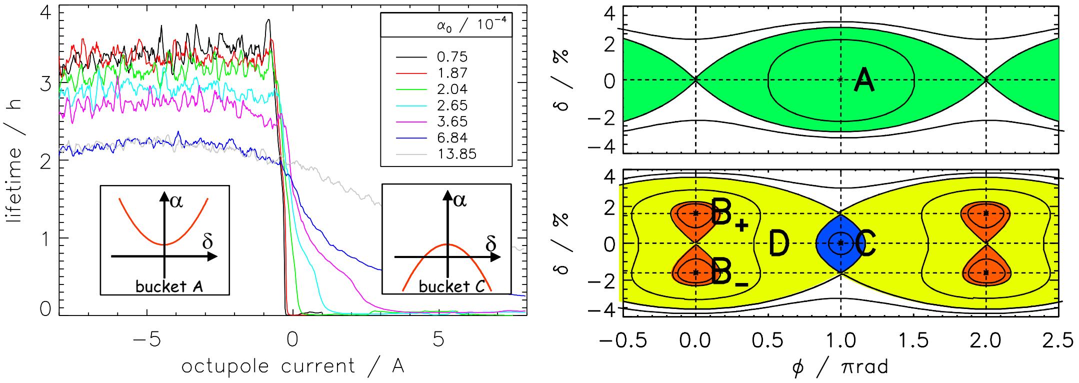

Figure 4: Lifetime effects for different octupole excitation currents I_8. Left: lifetime as a function of the current I_8 and different α_0 >0 settings. The small insets show the different curvatures of $\alpha(\delta)$ for the buckets A and C. The momentum acceptance of bucket C is limited by $\alpha(\delta)=0$. Right, upper part: for $\alpha_2>0$ beam is stored in the bucket A (green color). Right, lower part: for $\alpha_2<0$ beam is stored in the bucket C (blue color).

For positive octupole currents ($\alpha_2<0$), beam is stored in a C bucket. This bucket is limited in energy by two unstable fixed points δ_{FP}, derived from the condition $\alpha(\delta)=0$, resulting in $\delta_{FP}=\pm\sqrt{-\alpha_0/\alpha_2}$, which agree with the stable momentum fixed points of the B buckets. With increasing octupole strength, α_2 is further decreased leading to a vanishing momentum acceptance of bucket C and a pronounced loss of lifetime.

On the contrary, negative octupole currents cause a positive sign of α_2. Beam is stored in buckets of type A with a large momentum acceptance and a substantially improved lifetime. Already a small positive value of α_2 is sufficient to restore the lifetime even at very small α_0 values. The resulting lifetime shows a step function with respect to I_8. The low-α operation requires at least a small curvature of $\alpha(\delta)$ avoiding a crossing of $\alpha(\delta)=0$ for the particles in the momentum halo, see inset of Fig. 4. The value of $\alpha(\delta)$ of the momentum halo does not affect the bunch length. But it is mandatory for obtaining a good lifetime. The short bunch length is defined by the core of the bunch, which necessitates a small α.

The ability to control the leading coefficients of $\alpha(\delta)$ offers the possibility to study the properties and applications of the α-buckets. The appropriate sign of the curvature of α controlled by octupoles is the key tuning parameter to achieve very small values of α.

3.12.4 **Coherent Synchrotron Radiation at the MLS**

The main reason for generating short electron bunches is the production of coherent THz radiation. The properties of the CSR is measured and analyzed in time and frequency domain at a dedicated THz beam line of 64 mrad (horizontal) × 43 mrad (vertical) acceptance [17]. For the results shown in Fig. 5 the machine parameters were 630 MeV, $\alpha_0 = 1.3 \cdot 10^{-4}$ and $V_{rf} = 450$ kV yielding an estimated zero current bunch length of $\sigma_0 = 1.3$ ps.

The spectral characteristics of the CSR at the THz beam line were analyzed using a Vertex 80v Fourier transform spectrometer and a DTGS detector. The spectrum ranges from about 1 cm^{-1} to 50 cm^{-1}. A typical spectrum is shown in Fig. 5. The gain factor is defined, as the ratio between coherent and incoherent spectral power. The incoherent part, which is of low intensity, could be mixed with spurious contributions of coherent intensity. To correct the gain for these contributions and additional detector saturation effects, a liquid helium cooled Ge detector was used, in combination with polarizer grids and band-pass filters. The corrected gain leads to values of up to 10^5 at about 10 cm^{-1}.

The long wavelength limit of the spectrum is in close agreement with estimations from standard cutoff formulas for the vacuum chamber [18]. The small dipole bending radius ρ of the MLS is advantageous for the long wavelength range as the cutoff wavelength can be calculated by $\lambda_{\text{cutoff}} = 2h\sqrt{h/\rho}$ to 0.7 cm^{-1}, close to the value measured at the MLS. The full chamber height h is 42 mm.

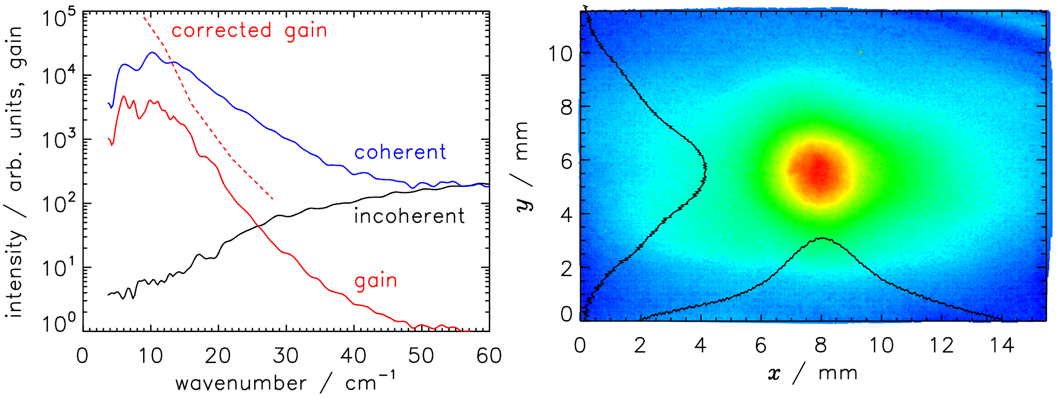

Figure 5: Left: Power spectrum of the CSR measured by a Vertex 80v FTIR spectrometer using a DTGS detector at 1 cm^{-1} resolution, at 630 MeV and 100 mA. The corrected gain was measured using band-pass filters and a Ge detector (red dashed line). Right: Spatial distribution of THz radiation measured by a THz camera.

The CSR can be emitted as stable (not shown), periodic or stochastic bursting in the time domain. The stable emission is only visible by a chopped THz beam, because the detectors used are not sensitive to constant signals and cannot resolve the bunch revolution time around the ring. Figure 6 shows the frequency spectrum in time domain of the two different types of THz signals, periodic and stochastic bursting. It was measured in 300 µA single bunch operation with $\alpha_0 = 5 \cdot 10^{-4}$ using an InSb detector of µsec time resolution. The bursting threshold depends on the peak current of the bunch. By increasing the rf-voltage, the bunch length decreases and the peak current increases. At a specific bunch length the current is above the bursting threshold [19], which is the point where the periodic bursting regime starts, see Fig. 6. The detector now sees a modulated THz signal, initially one, and then more specific frequencies. By further increasing the rf-voltage the bunch can be driven into the stochastic bursting regime. A systematic measurement of bursting thresholds for different MLS settings is given in [20], which agree well with theoretical predictions [21].

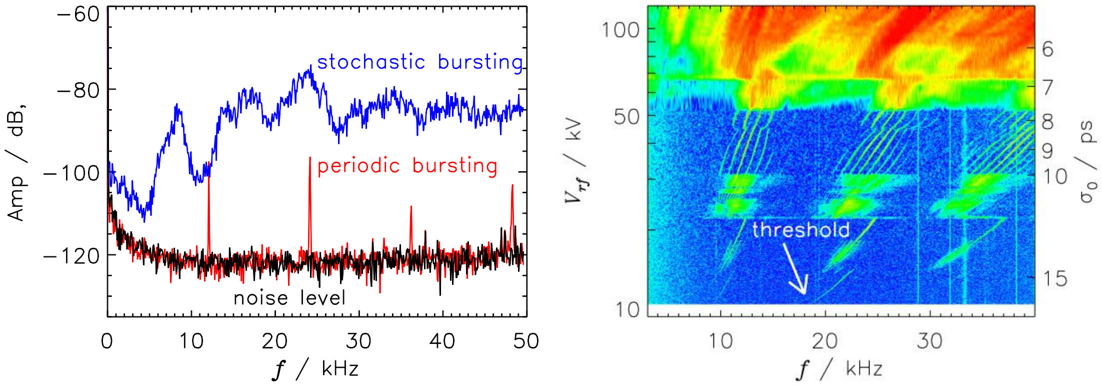

Figure 6: Temporal frequencies of CSR signals from a single bunch at the MLS. Left: The temporal frequency spectrum of the THz signal measured by an InSb detector. Three different regimes are identified: noise level (black), periodic bursting (red) and stochastic bursting (blue). Right: Waterfall plot of the temporal frequencies. The rf-voltage (left axis) is increased for shortening the bunch length (right axis) and for increasing the peak current. With increasing peak current the temporal emission characteristic changes from various periodic bursting patterns to stochastic bursting.

3.12.5 Summary

The MLS is the first storage ring optimized for generating CSR in the THz regime. Three sextupole families and one octupole family are required to adjust the first three expansion coefficients of the momentum compaction factor independently. Operation at positive or negative α in the whole electron energy range from 105 MeV to 630 MeV has been achieved. Additionally, the MLS offers the unique possibility to study the application of α-buckets. Stable, periodic and stochastic bursting CSR is available. A maximum average power of up to 60 mW could be demonstrated.

3.12.6 Acknowledgment

It is a pleasure to thank our HZB and PTB colleagues for the excellent support. We gratefully acknowledge fruitful discussions with A. Jankowiak and P. Kuske on these topics.

3.12.7 References

1. Zholents, “The Quest for Ultra-Short X-Ray Pulses”, Fermilab, (2011).
2. R. Klein et al., Phys. Rev. ST Accel. Beams 11, 110701 (2008).
3. B. Beckhoff et al., Phys. Status Solidi B 246, 1415 (2009).
4. D. Krämer et al., MLS Technical Design Report, BESSY, Germany (2003).
5. J. Feikes et al., Phys. Rev. STAB 14, 030705 (2011).
6. J. Feikes et al., ICFA Beam Dynamics Newsletter 35 (2004).
7. J. Feikes et al., Proc. of EPAC 2004, Lucerne, Switzerland, p. 1954 (2004).
8. Y. Shoji, Proc. of IPAC 2010, Kyoto, Japan, p. 289 (2010).
9. E. Weihreter, Proc. of EPAC 2008, Genoa, Italy, p. 2939 (2008).
10. Y. Shoji, Phys. Rev. ST Accel. Beams 8, 094001 (2005).
11. Y. Shoji, Phys. Rev. ST Accel. Beams 7, 090703 (2004).

12. K.-Y. Ng, Nucl. Instrum. Methods Phys. Res., Sect. A 404, p. 199 (1998).
13. D. Robin et al., Phys. Rev. E 38, p. 2149, (1993).
14. M. Ries et al., Proc. of IPAC 2011, San Sebastián, Spain, p. 945 (2011).
15. J. B. Murphy and S. L. Kramer, Phys. Rev. Lett. 84, p. 5516 (2000).
16. M. Ries et al., Low Emittance Rings Workshop 2011, Iraklion, Crete (2011)
17. R. Müller et al., J. Infrared Milli. Terahz. Waves **32**, 742-753 (2011).
18. R. L. Warnock, Report No. SLAC-PUB-5375 (1990).
19. G. Stupakov and S. Heifets, Phys. Rev. ST Accel. Beams 5, 054402 (2002).
20. J. Feikes et al., Proc. of IPAC 2010, Kyoto, Japan, p. 2508 (2010).
21. Y. Cai, Proc. of IPAC 2011, San Sebastián, Spain, p. 3774 (2011).

3.13 Experimental Aspects of CSR in the ANKA Storage Ring

A.-S. Müller, N. Hiller, A. Hofmann, E. Huttel, K. Il'in, V. Judin, B. Kehrer,
M. Klein, S. Marsching, C. Meuter, S. Naknaimueang, M.J. Nasse, A. Plech, P. Probst,
A. Scheuring, M. Schuh, M. Schwarz, M. Siegel, N. Smale, M. Streichert, KIT
F. Caspers, CERN
A. Semenov, H.-W. Hübers, DLR
E. Bründermann, Ruhr Universität Bochum
Mail to: Anke-Susanne.Mueller@kit.edu

3.13.1 **Introduction**

Since 2004 the ANKA storage ring regularly offers beam time for users of a special operation mode with short bunches that emit coherent synchrotron radiation (CSR) in the far infrared [1]. A research group dedicated to the study of CSR has been established at ANKA in 2007. The THz radiation is detected at the ANKA-IR1 beamline [2], where the synchrotron light is produced in the fringe field of a bending magnet. This edge radiation has the advantage of being more collimated than constant field radiation. Edge radiation allows the observation of frequencies down to 30 GHz through a modest vertical aperture of 15 mrad, which would not be possible with classical constant field emission due to the increasing beam divergence with decreasing frequency. In the course of a constant optimization process to better adapt to the needs of the user community, various studies with CSR have been performed to further the understanding of the underlying accelerator physics. In the following, an overview of the results, methods and techniques employed is given.

3.13.2 **The Low Alpha Optics of the ANKA Storage Ring**

Optics Functions and Parameter Range

The ANKA storage ring is operated in the energy range from 0.5 to 2.5 GeV. CSR is emitted for wavelengths longer than or equal to the bunch length. Since the natural bunch length increases with the beam energy according to $\sigma_s \propto (E_0)^{3/2}$ a low beam energy would be the obvious choice. However, longitudinal instabilities at lower energies (below 1.3 GeV in multi-bunch and below 1 GeV in single bunch operation) make a beam energy above 1.3 GeV the working point of choice.

The left hand plot of Fig. 1 shows RMS bunch lengths measured in single and multi-bunch operation as a function of the beam energy. For the single bunch data the synchrotron frequency was kept constant at (33.5 ± 0.1) kHz by increasing the RF voltage for higher energies accordingly. For the multi-bunch data the variation of the synchrotron frequency was higher (30.3 kHz to 37 kHz), therefore a scaling to the frequency of 33.5 kHz was applied for a better comparison. The effect of the instabilities at low beam energies is clearly visible. The single bunch measurement was performed for two different bunch currents (about 1.13 and 0.38 mA) to estimate the effect of the current dependent bunch lengthening. As expected this effect is more pronounced at lower beam energies. The multi-bunch measurement was performed in the same current range, for bunch currents around 0.85 mA. For users of short x-ray pulses, short bunch optics are also available at 1.6 and 1.8 GeV.

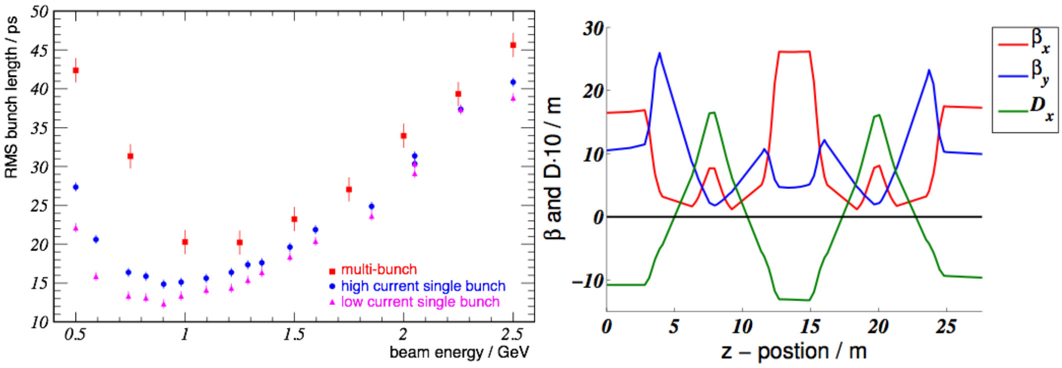

Figure 1: Left: Bunch length measured with a streak camera as a function of the beam energy for a constant synchrotron frequency. Whereas the bunch length at low beam energies is dominated by instabilities, in particular for the multi-bunch case, the increase with energy is the dominant effect for energies above 1.3 GeV. Right: Example of betatron functions and horizontal dispersion of the low-α_c optics for one of four sectors of the ANKA storage ring with an α_c of $4.6 \cdot 10^{-4}$. The optics functions were obtained from response matrix data and the LOCO program [3].

In order to provide coherent edge radiation to the experiments, the storage ring is filled at 0.5 GeV. The desired beam current is then ramped to the chosen end energy where the bunch length is gradually decreased by an optics change in a so-called "low-α_c squeeze", named for the respective momentum compaction factor characteristic of this optics. Measurements can be performed at any of the individual "squeeze states", allowing the adjustment of the bunch length to user demand.

The momentum compaction factor is defined as the relative increase of the electron's path length C along the closed orbit with a momentum deviation Δp with respect to the momentum of the reference particle p_0, $\Delta C/C = \alpha_c \, \Delta p/p_0$. Decreasing α_c will reduce the bunch length proportional with $(\alpha_c)^{1/2}$. A reduction of α_c from the regular value of $7.2 \cdot 10^{-3}$ to a value of $1.4 \cdot 10^{-4}$ was achieved but does not seem to be the ultimate limit. The right hand plot in Fig. 1 shows an examples of the optics function for one of four sectors of the ANKA storage rings for an α_c of $4.6 \cdot 10^{-4}$.

3.13.3 Detection of Coherent Synchrotron Radiation

The high-intensity CSR emitted from electron storage rings typically covers the frequency range up to about 1.5 THz, i.e. the detector system of choice is one optimized for this frequency range. In the emission of coherent radiation, the amplitudes of the electromagnetic fields add up linearly, resulting in a quadratic enhancement of the radiation's intensity. The total power radiated by a bunch consisting of N particles can be expressed as $P_{total} = N\, P_{incoh}\, (1 + N\, f_\lambda)$, where f_λ is a form factor describing the effect of the longitudinal charge distribution in the bunch. For a Gaussian charge distribution with RMS length σ_s the form factor is given by $f_\lambda = \exp(-(2\pi\sigma_s/\lambda)^2)$. This shows that the radiated intensity for a given wavelength will increase with decreasing bunch length.

Since the dynamics of the CSR emission is of interest, the detector system used should allow monitoring the turn-by-turn evolution of the THz signal. An ultra-fast detector can in addition resolve single bunches of a multi-bunch filling, thus making it possible to study not only single bunch effects with varying currents in a single shot but also possible influences on the THz emission from the filling pattern.

For the studies presented here, several detector systems were used. In addition to the more 'standard' and widely used silicon bolometer systems with time constants of the order of several 100 μs, faster systems based on superconducting materials, e.g., a Hot Electron Bolometer (HEB), were employed for studies in the far infrared range. For the longer wavelength range, a setup based on a Low Noise Block (LNB) was used. For measurements of the spectrum of the emitted CSR, we used a FTIR Bruker IFS 66V/s spectrometer as well as a Martin-Puplett type interferometer.

3.13.3.1 *Detector Systems Based on Superconducting Materials*

In many studies we used a detector system based on a superconducting NbN ultra-fast bolometer [4] with an intrinsic response time of ≈100 ps to resolve radiation from single bunches. The NbN bolometer is embedded into a planar log-spiral antenna which is integrated with an elliptical silicon lens. The detector covers the spectral range from 10 to 150 cm^{-1} (0.3 to 4.5 THz) mainly determined by the antenna [5]. The response to a few picoseconds long radiation pulse has the full width at half maximum of 165 ps that is defined by the readout electronics. A system noise equivalent power of 6×10^{-9} W $\mathrm{Hz}^{1/2}$ was optically measured for cw radiation at 0.8 THz.

Recently, a breakthrough with respect to response times was achieved with a system based on the high-temperature superconductor $YBa_2Cu_3O_{7-\delta}$ (YBCO). Due to a very fast electron energy relaxation time of the order of single picoseconds in YBCO, detectors made from this material are promising candidates for the ultra-fast detection of THz coherent synchrotron radiation (CSR).

We developed a THz detection system which monitors the CSR THz pulses directly in the time domain. The THz detector is made from an ultra-thin (15 nm) YBCO film on sapphire substrate with a critical temperature of superconducting transition of $T_C \approx 84$ K. These high critical temperatures allow us to operate the detector in a cryogen-free cooling system which is operated fully automatically. The synchrotron radiation enters the cryocooler through a polyethylene window. The detector signal is amplified with a room temperature amplifier (bandwidth of 65 GHz) and fed into an Agilent real-time oscilloscope with a bandwidth of 32 GHz. The bias is arranged via a room-temperature bias-tee.

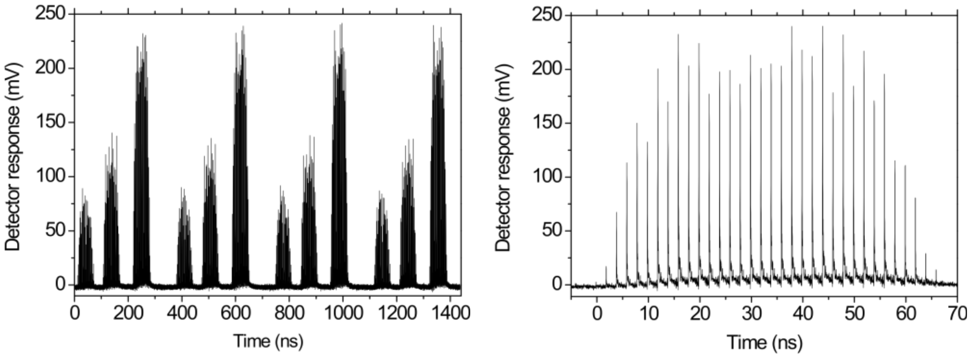

Figure 2: Left: Consecutive turns of the filling pattern of ANKA consisting of three trains filled with 33 bunches each monitored with the YBCO THz detector. Right: One train depicted in detail showing the 33 bunches with a repetition rate of 500 MHz (≙ 2 ns).

Fig. 2 (left) shows the YBCO detector response to the ANKA synchrotron radiation in the THz frequency range in the low-α_c mode (1.3 GeV). The filling pattern with three trains consisting of 33 bunches with a repetition rate of ≈2.7 MHz is clearly visible. Due to a very broad dynamic range of the YBCO THz detector of more than 30 dB [6] the detector response scales linearly with the input THz power, thus recording the increase of emitted THz power from the first to the third train (see Fig. 2, left) which is in good agreement with the measured bunch currents. Fig. 2 (right) shows one train in detail where the single bunches every 2 ns are monitored.

In Fig. 3 (left) the signal from a single THz bunch is depicted in detail. The pulse width (full width at half maximum) is determined to 23 ps, which represents the readout bandwidth limitation. Further optimization of the readout bandwidth as well as optical readout techniques, which allow for sub-picosecond temporal resolution, are under development.

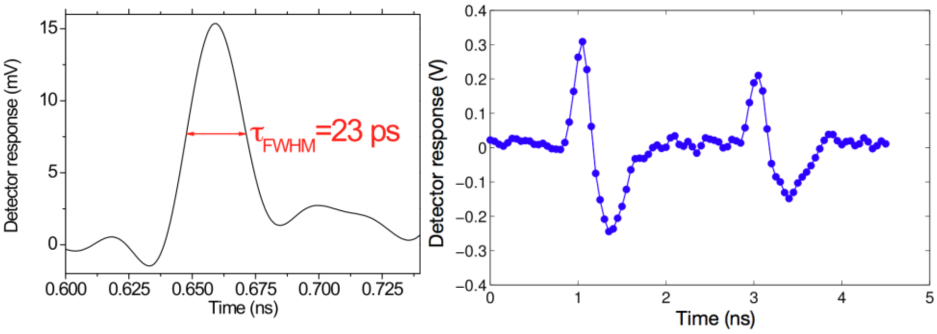

Figure 3: Left: One single bunch detected with the YBCO based system showing a pulse width at full width half maximum of only 23 ps which was the limit of the electronic readout bandwidth. Right: Two clearly separated consecutive bunches detected by a NbN based system with a slower time constant of about 165 ps.

3.13.3.2 *Detection in the Microwave Range: A LNB Based System*

The LNB is a commercially available device used for TV satellite receivers. It is a microwave mixer with an input frequency in the range of 10.7–12.75 GHz. There are two embedded local oscillators (LO), with frequencies of 9.75 GHz (low band) and 10.6 GHz (high band), allowing the observation of intermediate frequencies (IF) in two ranges: 950–2050 MHz and 1100–2150 MHz. The gain of the embedded amplifier is 50 dB. The noise factor of the detector is below 1 dB and it covers a dynamic range of about 20 dB. A Schottky diode and pre-amp allow the acquisition of the signal envelope [7].

Due to its high sensitivity, we could use the LNB even though the frequency range of the LNB lies below the CSR shielding cut-off of ANKA. Additional appeal of this setup is given by its simplicity and availability. Even though not all systematic effects of this detector setup have been explored up to now, its usefulness could already be shown in many experiments. On the left hand side of Fig. 4, for example, the response of the system to a single bunch pulse is shown. The fact that the distances of the peaks evident in the signal correspond to distances of structures with significant impedance contribution in the storage ring vacuum chamber hint at long range effects that can easily influence trailing bunches. The peak at about 140 ns, for example, corresponds to the distance IR1 – RF cavity in sector 4. The right hand plot of Fig. 4 shows the LNB signal measured around 11 GHz as a function of bunch length based on streak camera data. The obvious correlation clearly shows the potential for a method to determine the bunch length safely away from the frequency range affected by the bursting CSR.

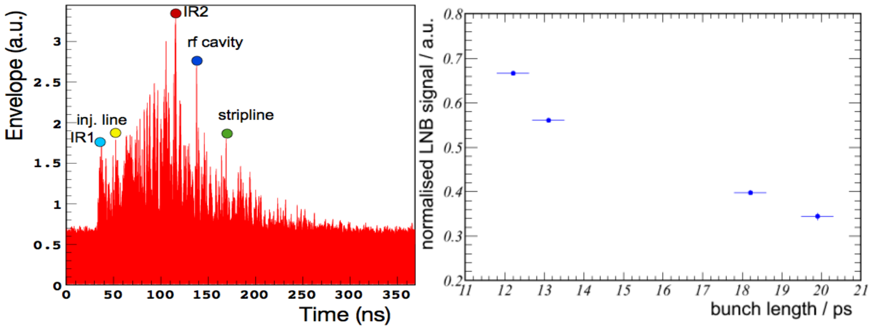

Figure 4: Left: LNB response to a single bunch pulse. The shape was determined in offline analysis summing 100 envelopes (roofs) of single signal traces taken with a 6 GHz oscilloscope. The oscilloscope was triggered using the revolution clock. The distances of the peaks evident in the signal correspond to distances of structures with significant impedance contribution in the storage ring vacuum chamber. Right: Correlation of LNB signal with the bunch length based on streak camera data.

3.13.4 **CSR Emission in the Bursting and Steady State Regime**

The mode of emission of the CSR depends mainly on the bunch charge. A well-documented and confirmed threshold describes this behavior (e.g., [8, 9]). The bunch dynamics around this threshold, in particular, provides interesting aspects to be investigated. In the following, we present results of studies of the temporal behavior and of measurements of the bunch and THz pulse shape done at the ANKA storage ring.

3.13.4.1 ***Time Evolution of the Emitted Coherent THz Radiation***

In order to investigate the temporal evolution of the emitted coherent THz radiation, we used a fast detector system based on a Hot Electron Bolometer. The signal was recorded with LECROY digital oscilloscopes (WR64Xi, WP7300 and WM8600A) with high sampling rates of 10-20 GS/s and bandwidths of 0.6, 3 or 6 GHz. The signal can either be recorded with maximum sampling rate for an excellent mapping of the filling pattern over a limited number of revolutions (typically about 4150) or with specifically reduced sampling for very long observation times (about 10^6 turns) but only for one bunch within the fill. New readout electronics under development at KIT will allow overcoming this limitation thus making it possible to record the time evolution of all bunches in a multi-bunch fill over long time spans simultaneously [10]. An FFT of the acquired time series yields the bursting spectrum with a frequency resolution of about 5 Hz. The advantage in comparison to standard spectrum analyzer measurements is the possibility to investigate the bursting in the time domain as well as in the frequency domain. Fig. 5 a) and b) show examples of the turn-by-turn THz signal for different single bunch currents above the bursting threshold measured with a NbN detector system. Fig. 5 c) presents a spectrogram of the turn-by-turn THz signal as a function of the single bunch current. The thresholds from steady state to bursting emission at around 0.35 mA and between different bursting modes at around 0.6 mA are clearly visible.

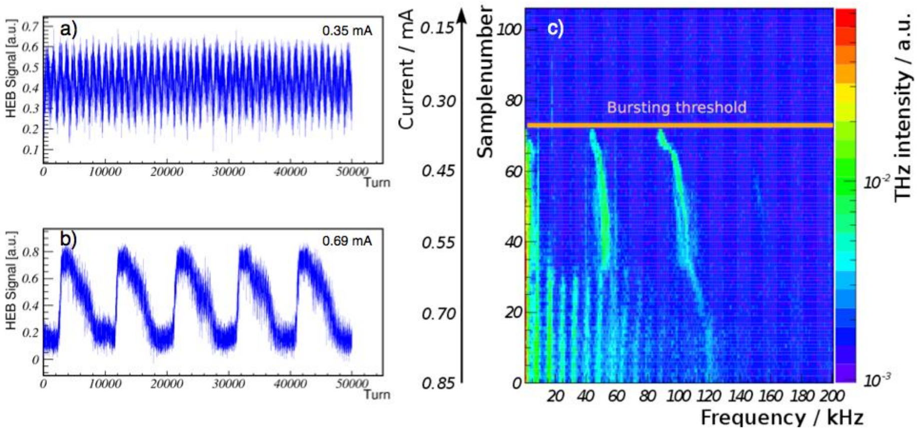

Figure 5: a) and b) Turn-by-turn THz signal for different single bunch currents above the bursting threshold measured with a NbN detector system. c) Spectrogram of the turn-by-turn THz signal as a function of the single bunch current. The thresholds from steady state to bursting emission at around 0.35 mA and between different bursting modes (examples for the time series in a) and b)) at around 0.6 mA are clearly visible.

3.13.4.2 *Measurements of Bunch Length and Shape*

The emission of bursting CSR does not only lead to different temporal structures as a function of the bunch current, it also leads to an effective lengthening of the bunch. Below the threshold for bursting emission, this is described by a solution of the Haïssinski equation using the appropriate wake field as input [11], above the bursting threshold the bunch length fluctuates yielding an effectively lengthened bunch [12]. For the ANKA storage ring, we measured the bunch lengthening with current with a Hamamatsu C5680 streak camera that is extended with a synchroscan plugin and a dual time base extender (double sweep unit) [13]. The left plot of Fig. 6 shows measurements for optics with different momentum compaction factors (denoted by the different values of the synchrotron frequency f_s) at a beam energy of 1.3 GeV and with an RF voltage of 150 kV in each of the four cavities. In addition, measurements of the bursting threshold determined from the THz signal are shown. The grey band is a fit to bursting threshold measurements, the dotted line is the threshold the streak camera data are approaching for high current values. Both measurements are compatible with a bunch length increase ∝ k $I^{3/7}$ [14]. However, the streak camera measurements seem to prefer a larger value of k. The right hand plot of Fig. 6 shows the effect of the bunch deformation for a high current bunch in comparison with a low current bunch as measured with the streak camera.

An alternative method to determine the bunch length form measurements in the microwave frequency range is based on the usage of the LNB detector system described above (see also [7]).

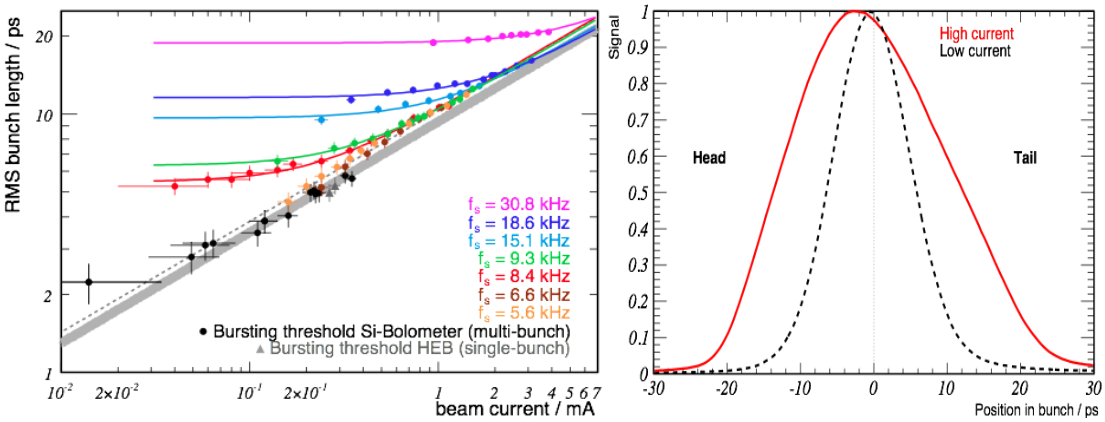

Figure 6: Left: Bunch length as a function of single bunch current. The color symbols represent streak camera measurements for different low-α_c optics, denoted by the value of the synchrotron frequency f_s. The black dots and grey triangles show independent measurements of the bursting threshold. Right: Examples of streak camera bunch profiles for high and low bunch currents showing the deformation and tilt toward the head of the distribution.

3.13.4.3 *The Terahertz Pulse in the Time Domain*

Additional insight can be gained from the temporal resolution of the electric field of the emitted THz radiation in the femto-second range. The pulse shape of the electric field of a coherent THz pulse, derived from first principles, is displayed on the left hand side of Fig. 7, showing the typical ‘single cycle’ behavior.

The fact that the coherent radiation is coupled in phase to the storage ring time structure makes it possible to measure the electrical field directly by an electro-optical sampling setup. A femtosecond oscillator (Ti:Sa, 30 fs, 805 nm, 500 MHz) is phase locked to the signal from a strip-line electrode in order to sense the THz-induced birefringence in the electro-optical crystal (ZnTe) [15, 16]. This allows to map the electrical field strength and thus directly the oscillation of the THz light. Averaged over many turns, the signal encompasses the carrier-envelope stable part of the light, but no individual bursts of THz radiation. At the same time waveguide modes are also resolved, as evidenced by the continuing oscillations (see Fig. 7 right).

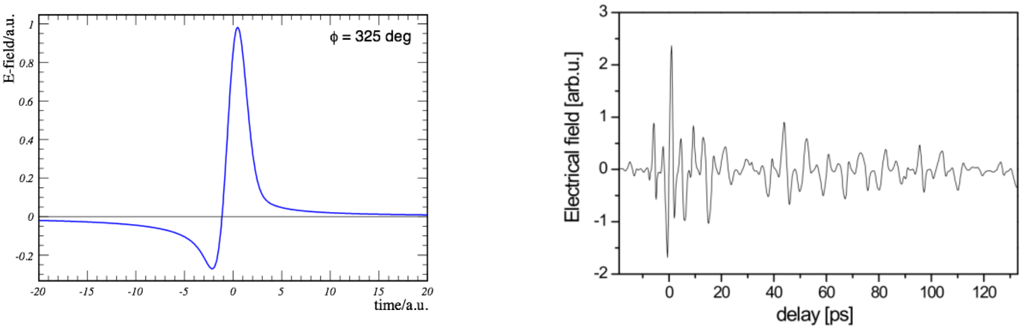

Figure 7: Left: Calculated shape of THz electric field showing the typical ‘single cycle’ shape [17]. Right: Measurement of the THz electric field in the ANKA IR 1 beam line based on the phase sensitive detection of THz radiation with electro-optical femto-second sampling [15, 16]. The zero delay is chosen arbitrarily at the highest signal amplitude.

3.13.5 **CSR and the Influence of the Ring Impedance**

Since the formation and bunch dynamics takes place within the confining system of the vacuum chamber, the impedance of the latter must play an important role in the understanding of the dynamics with CSR. We could show in systematic studies at the ANKA storage ring, that the observed behavior of the CSR indeed is influenced by the ring impedance. In the following we present studies about the effect of a scraper acting as ‘impedance knob’ and about the influence of one bunch to its adjacent bunch.

3.13.5.1 ***Effect of Controlled Impedance Changes on the CSR Emission***

In order to study the influence of the (geometric) impedance on the CSR emission in the THz range, we used a scraper as a kind of ‘impedance knob’. The wakefield of a scraper is caused by the discontinuities at the leading and trailing edges of the jaws and by the resistance of the metallic material. In our case the jaws can be considered as far apart and the kick therefore is due mostly to the jaw discontinuity: the geometric impedance dominates. The scraper effects have been studied before in detail [18] and its impact on the beam (e.g., closed orbit distortion) is well understood. The left hand side of Fig. 8 shows the THz signal in a multi-bunch fill as a function of beam current. Each upward step visible in the signal was caused by positioning a scraper blade closer to the beam, each downward step by moving the scraper away from the beam. The effect is observed irrespective of whether top or bottom jaw of the vertical scraper are used or both jaws are positioned symmetrically to the beam (in which case also the small orbit distortion of the order of ± 10 µm at peak value is cancelled out). A clearer view of the change in CSR dynamics is given in the right hand side of Fig. 8. where the THz signal is shown as a function of the single bunch current. Here the increase of the signal with a scraper close to the beam is evident. The bursting threshold (estimated from the crossing points of fits to the steady state and bursting regimes) appears shifted towards lower bunch currents (from 0.284 to 0.271 mA). In addition, the onset of bursting seems smeared out. Further studies with the above mentioned new readout electronics will focus on the temporal structure of the THz emission in this current range.

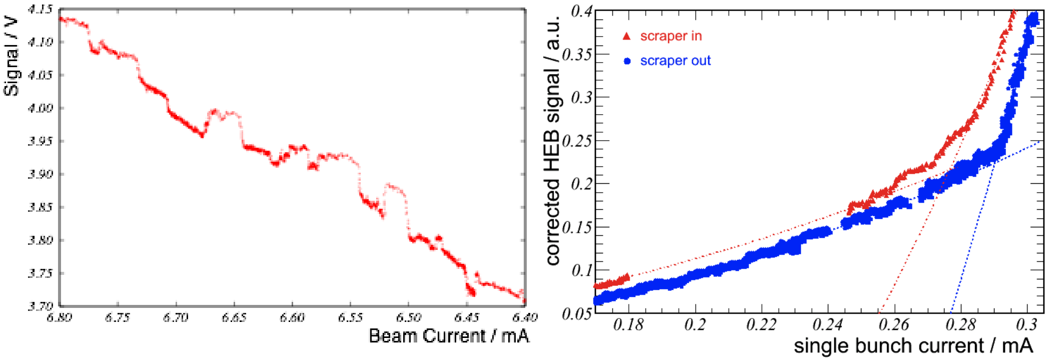

Figure 8: Left: THz signal detected with a Si bolometer as a function of beam current in a multi-bunch fill showing the effect of the scraper motion. Each upward step visible in the signal was caused by moving a scraper blade close to the beam, each downward step by moving the scraper away from the beam. Right: Time averaged amplitude of the THz signal measured with a NbN detector system as a function of the single bunch current with and without a scraper positioned close to the beam. The dashed lines represent fits to the steady state and bursting regimes, respectively. The crossing points can serve as an estimate for the bursting threshold.

3.13.5.2 *CSR in a Multi-Bunch Fill*

Earlier studies [18] have shown evidence of long range effects in the longitudinal wakefields, for example due to a scraper. Other indications of long range effects are shown in Figures 4 (left) and 7 (right) also without the presence of the scraper jaw. In that case an influence of a leading bunch on the emitted THz CSR of its successor should be present. In Fig. 9 we present evidence that this is indeed the case. The left hand side shows the THz signal for each bunch in a multi-bunch filling color coded in two categories: A) where the leading bunch has a current of at least 10% less than the witness bunch and B) where the leading bunch has a current of at least 10% above than the witness bunch. The dashed curve is a global fit to all data points below the bursting threshold. The bunches with a high current predecessor show a higher signal. In addition, the bursting threshold appears shifted to lower currents. Histograms of the difference of the witness bunch signal to the global fit clearly show the shift of the two distributions (see right hand side of Fig. 9). Another indication for a different bursting behavior of a multi-bunch fill is the increased high frequency content of the spectrum of the emitted CSR in comparison to a single bunch spectrum with comparable single bunch current (Fig. 10).

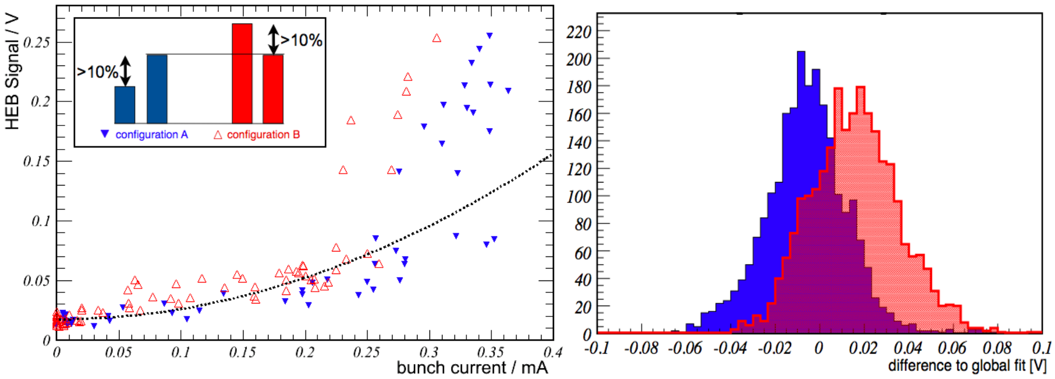

Figure 9: Left: THz signal from a NbN detector for the individual bunches of a multi-bunch filling pattern. The color coding represents the current ratio of the leading bunch to its successor. The dashed curve is a global fit to all data points below the bursting threshold. Right: Histograms of the difference of the witness bunch signal to the global fit for the two configurations for 52 consecutive measurements for a beam current of 20.5 mA and f_s=8 kHz. The shift of the mean value for the two distributions is clearly evident.

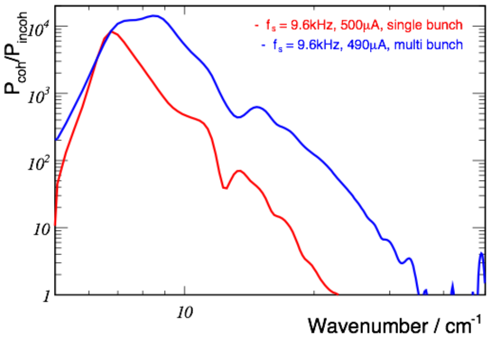

Figure 10: Ratio of coherent and incoherent spectrum for a multi-bunch and a single bunch fill with similar single bunch currents. The multi-bunch spectrum was normalized by the number of bunches in the fill.

3.13.6 **Summary**

Studies at the ANKA storage ring have been presented which demonstrate how CSR is a sensitive diagnostics tool for the dynamics of short bunches in electron storage rings, the understanding of which is important input for the design of future low emittance machines. The results were obtained by means of a large repertoire of experimental methods, such as a commercial off-the-shelf LNB, custom made fast superconducting detectors, a streak camera or, for the first time in rings, a setup for electro-optical sampling to study the physics of CSR. The bunch dynamics at the transition between steady state emission and the bursting regime is being explored in close collaboration between theory and experiment. Clear evidence has been presented that CSR is affected by the ring impedance and the filling pattern of the machine. Apart from their intrinsic interest in accelerator physics the findings presented above represent important milestones toward controlling CSR and the possibility to produce tailor-made radiation for user applications.

3.13.7 **Acknowledgements**

Sincere thanks go to all who have contributed to the various studies presented here. In particular we would like to thank Y.-L- Mathis and the ANKA IR team for their hospitality, G. Wüstefeld, J. Feikes, M. Ries and P. Kuske for many interesting discussions over the years, G. Rehm for great advice with the data acquisition and Y. Cai, B. Warnock, S. Novokhatski and B. Podobedov for inspiring input. Thanks go to Agilent for lending the real-time oscilloscope and to the ANKA technical team for their support.

Last but definitely not least, the authors would like thank the funding agencies that allowed us to work on the exciting topics: This work was funded in part by the German Federal Ministry of Education and Research (grants No. 05K2010 and 05K10VKC) and by the Initiative and Networking Fund of the Helmholtz Association (contract numbers VH-NG-320 and SO-NG-041).

3.13.8 **References**

1. A.-S. Müller et al., Far Infrared Coherent Synchrotron Edge Radiation at ANKA. page 2518, 2005. Particle Accelerator Conference (PAC 05), Knoxville, Tennessee, 16-20 May 2005.
2. Y.-L. Mathis, B. Gasharova, and D. A. Moss. Terahertz radiation at ANKA, the new synchrotron light source in Karlsruhe. J. Biol. Phys., 29:313–318, 2003.
3. J. Safranek. Experimental Determination of Storage Ring Optics Using Orbit Response Measurements. In Nuclear Instruments and Methods A388, pages 27–36. North-Holland Publishing Company, 1997.
4. Yu.P. Gousev, G.N. Gol’tsman, A.D. Semenov et al. Broadband ultrafast superconducting NbN detector for electromagnetic radiation. J. Appl. Phys., 75:3695, 1994.
5. A.D. Semenov, H. Richter, H.-W. Hübers et al. Terahertz performance of integrated lens antennas with a hot-electron bolometer. IEEE Transactions on Microwave Theory and Techniques, 55(239), 2007.
6. P. Probst et al., Applied Physics Letters 98, 043504 (2011).
7. V. Judin et. al., Observation of Microwave Radiation using low-cost Detectors at the ANKA Storage Ring, IPAC 2011
8. G. Stupakov and S. Heifets. Beam instability and microbunching due to coherent synchrotron radiation. Phys. Rev. ST Accel. Beams, 5(5):5–8, 2002.
9. Y. Cai, Linear theory of microwave instability in electron storage rings. Physical Review Special Topics Accelerators and Beams, 14(6):1–12, 2011.
10. M. Caselle, private communication
11. J. Haïssinski. Exact longitudinal equilibrium distribution of stored electrons in the presence of self-fields. Il Nuovo Cimento B (1971-1996), 18:72–82, 1973.
12. M. Klein,Optics Calculations and Simulations of Longitudinal Beam Dynamics for the Low-α-Mode at ANKA, PhD thesis, 2012.
13. N. Hiller et al., Status of Bunch Deformation and Lengthening Studies at the ANKA Storage Ring. 2011. 2nd International Particle Accelerator Conference IPAC2011 San Sebastian, Spain.
14. F. Sannibale, et al., A model describing stable coherent synchrotron radiation in storage rings. Phys. Rev. Lett., 93(9):094801, Aug 2004.
15. A. Plech et al., Electro-Optical sampling of Terahertz radiation emitted by short bunches in the ANKA synchrotron, PAC proceedings (2009).
16. S. Ibrahimkutty et al., Asynchronous sampling for Ultrafast experiments with low

momentum compaction at the ANKA ring, J. Synchr. Rad. 18 (2011) 539.
17. A.-S. Müller et al. Modeling the Shape of Coherent THz Pulses Emitted by Short Bunches in an Electron Storage Ring. 2008. EPAC'08, 11th European Particle Accelerator Conference, 23- 27 June 2008, Genoa, Italy.
18. A.-S. Müller et al. Investigation of scraper induced wakefields at ANKA. 2004. Prepared for 9th European Particle Accelerator Conference (EPAC 2004), Lucerne, Switzerland, 5-9 Jul 2004.

3.14 R&D for Ultimate Storage Rings

Robert Hettel, SLAC National Accelerator Laboratory
for the USR R&D Working Group [1]
Mail to: Hettel@slac.stanford.edu

3.14.1 **Introduction**

Synchrotron radiation from storage ring accelerators has been a dominant source of high brightness photons in a spectrum spanning infrared to hard X-ray for a multitude of scientific applications over the last several decades. Recently free electron lasers (FELs) have emerged as alternative sources of soft and hard X-rays, offering peak brightness many orders of magnitude higher than storage ring sources in ultrashort photon pulses having nearly complete transverse coherence and an energy bandwidth that will approach the transform limit as new seeding technology is invoked. Yet, in spite of these spectacular beam properties, ring-based sources will continue to play a vital role in X-ray science into the future since they offer beam properties that are complementary to FEL sources: they provide photons having low peak brightness with high average brightness and pulse repetition rate, photons that do not over-excite or damage samples the way those from FELs do [2]. Nevertheless there are emerging scientific applications and experimental methods that would greatly benefit from ring-based sources having much higher brightness and transverse coherence than present or near-future storage ring facilities. These include [3]

- nanometer imaging applications
- X-ray correlation spectroscopy
- diffraction microscopy, holography and ptychography
- "fast" science (picoseconds) with potential for "tickle and probe"

These science applications benefit from X-ray sources having average spectral brightness on the scale of 10^{22} photons/s/mm^2/mrad^2/0.1% BW or more (Figure 1), high coherent fraction and short-bunch (picosecond) capability. With future superconducting undulators, brightness on the scale of 10^{23} could be realized. The brightness and coherence properties can be provided by sources having 100 mA or more operating current and electron beam emittance near the diffraction limit for X-ray energies of interest. Given that the diffraction limited emittance for photon wavelength λ is $\lambda/4\pi$, electron emittance on the scale of 10 pm-rad is needed for 10-keV (1.2-Å) X-rays, a value that can be reached in the vertical plane by minimizing emittance coupling and vertical dispersion in today's storage ring light sources but that is far lower than the nm-rad horizontal emittances found in those sources.

At the moment there are two ring-based accelerator implementations that profess to offer the brightness and flux properties discussed above while serving many

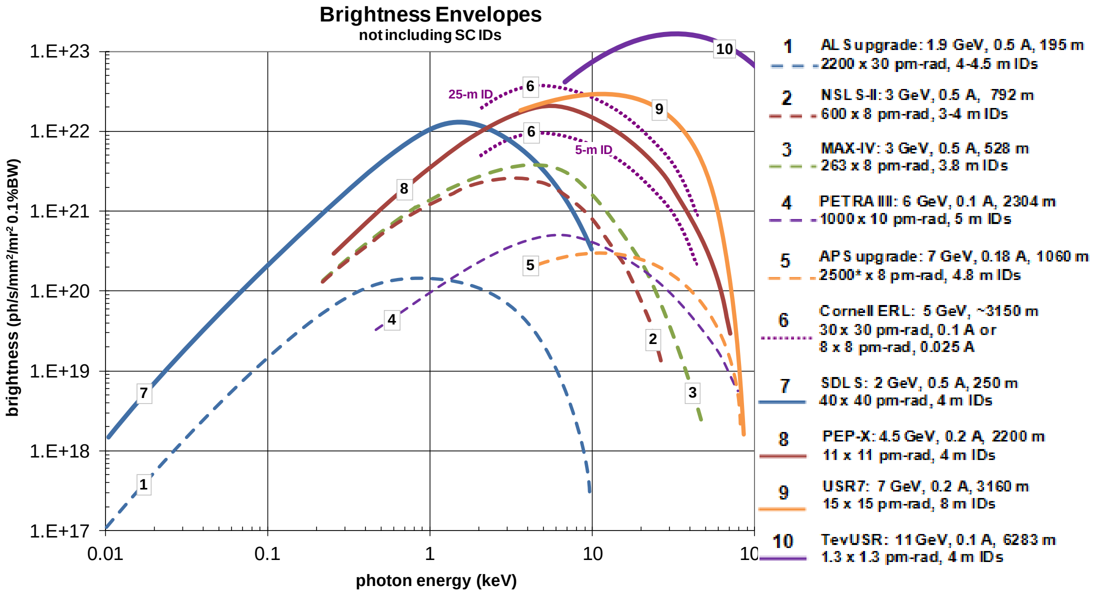

Figure 1. Approximate brightness envelopes for representative existing and near-future ring-based light sources (dashed curves), the proposed Cornell ERL (dotted curves), and possible future USRs (solid curves) using permanent magnet insertion devices (IDs). Superconducting IDs would increase performance for all facilities.

simultaneous X-ray experimental stations: the energy recovery linac (ERL) [4] and the so-called "ultimate" storage ring[1] (USR) [5,6,7,8]. Both technologies are capable of producing electron beams having emittances near the diffraction limit for keV X-rays. While ERLs promise distinct advantages for some photon beam parameters (e.g. reduced energy spread, short bunch production and the ability to tailor lattice optics for different insertion devices), they require significant R&D before a multi-GeV source for multi-keV X-rays could be implemented. In addition, very high brightness is available only to those few beamlines with very long (e.g., 25m or longer) undulators. USRs, on the other hand, can potentially provide diffraction-limited beams to many beam lines, with higher flux than ERLs based on a modest extrapolation of present-day technology. USRs also hold out the possibility of special modes of operation for short bunches and even lasing sources, while providing excellent operational reliability inherited from decades of experience with storage ring sources.

Horizontal electron emittance must be reduced by a factor of 100 or more from the lowest emittance values achieved in today's storage rings to reach the diffraction limit for multi-keV photons. Given that electron emittance ε_{e-} in a storage ring scales as

$$\varepsilon_{e-} \propto E_{e-}^2 \theta^3 F_{latt} \tag{1}$$

where E_{e-} is the electron energy, θ is the dipole bend angle and F_{latt} is a lattice cell type-dependent factor, emittance can be reduced by minimizing θ, increasing the number of dipoles and consequently the circumference C of the ring, with the result that ε_{e-} scales as C^{-3} for a given electron energy. Groups studying possible designs for ultimate rings, which would necessarily have large circumferences to reach diffraction limited

---

[1] The term "ultimate storage ring" might be presumptuous for describing diffraction-limited rings. Nevertheless we will use that term in this paper with the understanding that the definition of "ultimate" will most likely change in the future.

emittances for multi-keV X-rays, have as yet identified no technological show-stoppers for such an implementation. Nevertheless, the design of such very low emittance machines pushes the state of the art in lattice design, collective effects analysis, electron injection, beam stabilizing methods, and X-ray optics design. Furthermore the possibility for exploiting exotic modes of operation will require the development of new beam manipulation techniques and technology. Finally, ways to minimize the cost of high-performance accelerator magnet, vacuum chamber, rf, instrumentation and X-ray beam line components, together with conventional facilities like the experimental halls, need to be found for such large-scale facilities.

In the following we present an overview of the design goals and challenges for USRs and an outline of the elements of an R&D plan to support their design. A focused R&D program for USRs would reduce the risk and cost of a possible future project while delivering a design with optimized performance.

3.14.2 **USR Properties and Design Goals**

The primary goals for USR source design include reaching diffraction-limited electron emittance in both transverse planes for the X-ray wavelengths of interest to the source's user community, providing sufficient photon flux for user applications and providing X-ray optics and beam line systems that preserve the high-brightness beam qualities for the user. A secondary goal is to provide special operating modes if possible that would expand the envelope of X-ray experimentation. These modes might include short-bunch operation and X-ray lasing capabilities.

Specific properties of interest for USRs and any X-ray light source include

- spectral brightness and flux (average and peak)
- coherent fraction and coherent flux
- beam size, divergence and pulse length
- pulse repetition rate and pulse train structure
- energy spectrum and energy spread
- spatial, temporal and spectral stability
- photon polarization

Spectral brightness, coherent fraction and beam dimensions will reach unprecedented levels for storage ring sources having emittances approaching the X-ray diffraction limit (Figures 1 and 2). Table 1 lists parameters for USRs having peak performance in three photon spectral ranges: < ~ 2 keV, 2-20 keV, and >20 keV.

Besides having diffraction limited emittance, other features of USRs and their photon beams are worth noting, including:

- **"Round" beams:** Since vertical emittance can be adjusted to be close to or the same as horizontal emittance by generating vertical dispersion, operating near a coupling resonance, or other methods, vertical and horizontal beam size and divergence can be made to be similar with appropriate adjustment of betatron functions at photon source points, producing round or nearly round photon beams. These beams are far better matched into focusing optics than the flat beams produced by nm-emittance storage ring sources.
- **Short bunches:** The momentum compaction factor a for USRs tends to be a factor of ~20 lower than nm-emittance machines, producing electron bunch lengths on the order of 5-10 ps RMS, although lengthening of the bunches may

Table 1: Parameters for representative USRs targeting three photon spectral ranges.

Parameter	***< 2 keV(1)***	***2-20 keV(2)***	***>20 keV(3)***
electron energy (GeV)	2	4.5	11
circumference (m)	250	2200(4)	2π x 1000
beam current (I, mA)	500	200[4]	100
emittance ($\varepsilon_{x,y}$ @ I, pm-rad)	40/40	11/11	1.3/1.3[5]
max diffraction-limited $E_{X\text{-ray}}$ @ $\varepsilon_{x,y}$ [6] (keV)	2.5	9	76[5]
number of bunches	420	3300	8300
e- size @ ID (μm RMS)	6.0 / 8.5	7.4 / 3.3	2.5 / 1
e- divergence @ ID (μrad RMS)	6.6 / 4.7	1.5 / 3.3	0.5 / 1.3
e- bunch length (ps RMS)	6	10	10
e- energy spread (RMS)	0.9 x 10^{-3}	1.25 x 10^{-3}	1.43 x 10^{-3}
RF voltage (MV)	1	8.7	25
Damping wiggler length (m)	<10	90	188[5]
Lifetime @ I (h)	1.5	>2.4	4.5

(1) Very preliminary estimates for the SDLS [9].

(2) From PEP-X study [10].

(3) From preliminary study of Tevatron-sized USR [11].

(4) The existing PEP-X tunnel has six 120-m long straight sections, forming a hexagonal ring geometry, which do not contribute to emittance reduction other than providing space for damping wigglers and increasing the number of bunches that can be filled with a given charge to reach 200-mA operation. Studies indicate that a circular ring having ~1500-m circumference is sufficient to reach ~11 pm-rad emittance with ~130 mA.

[5] $\varepsilon_{x,y}$ = 2.8/2.8 pm, E_{phdiff} = 35 keV with L_{DW} = 0 m; $\varepsilon_{x,y}$ = 1/1 pm, E_{phdiff} = 99 keV with L_{DW} = 375 m.

[6] The diffraction limited photon energy corresponds to the case when photon and electron transverse phase spaces are matched, i.e. $\beta_x = \beta_y = L_{ID}/2\pi$, L_{ID} = ID length, a condition not met with the example USRs.

be needed in order to increase lifetime and reduce intrabeam scattering. The low-α lattice also enables the few- revolution transport of sub-ps electron bunches that might be injected from a linac source for very short-pulse experiments or to drive an FEL in the ring.

- **"Long" lifetime:** As electron bunch dimensions are reduced, the increased rate of electron-electron scattering within a bunch results in shorter lifetime because the large transverse momenta transferred to the longitudinal plane cause the electrons to fall outside the momentum aperture of the ring (Touschek effect). However, if the bunch dimensions are small enough then the available transverse momentum is insufficient, so fewer particles are lost from the momentum aperture, and Touschek lifetime increases to a few hours. This is seen in several USR designs and is expected to play a role for NSLS-II.
- **Damping wigglers:** Due to the low field strength of dipole magnets in large-circumference USRs, the electron energy loss per turn from the dipoles is very low, leading to long damping times (seconds) that exacerbate beam instabilities. These damping times can be greatly reduced by adding high-field wigglers which, if situated in straight sections having no dispersion, also reduce beam emittance by a factor of 2 or more. These damping wigglers can also serve as sources of hard X-rays. In the case of the 4.5-GeV PEP-X, 90 m of damping wigglers are required to reach 11-pm emittance. An 11-GeV, ~6-km USR may

not require damping wigglers but could still benefit from them.

- **On-axis injection:** As ring lattice emittance is reduced, so is the dynamic acceptance for injected particles. To reach the lowest emittance, dynamic acceptance may become too small to support off-axis injection, the mode that is typically used for accumulating beam in a given electron bucket with repeated injection shots. While it is desirable to preserve the capability for off-axis injection if possible, beam can be injected into a small dynamic acceptance on-axis if necessary. Accumulation is not possible with on-axis injection since electrons in the bucket are kicked out and replaced with the newly injected electron ("swap-out" injection [8]). On-axis injection and related technology would be needed for minimal emittance USRs.

In addition to the above, the low emittance, low momentum compaction, large circumference and possibility of very long straight sections in USRs open up the potential of implementing special modes of operation. These more speculative modes include:

- few-turn, sub-ps bunch mode
- 100-1000 turn mode, enabling very low emittance with reduced dynamic aperture, requiring injection of fresh electrons from a superconducting linac operating without energy recovery (e.g. ~1 mA @ few GeV)
- localized bunch compression systems with components located in long straight sections
- bunch tailoring with low alpha, non linear momentum compaction
- lasing in an FEL located in a switched bypass, where the post-lasing electron bunches are returned to the storage ring for damping
- partial lasing at soft X-ray wavelengths using the stored beam, requiring high peak current created by localized bunch manipulation

3.14.3 **Design Challenges and R&D Topics**

The principal challenges and areas of study associated with the design of USRs include [12,13] :

- **Scientific applications:** The projected capabilities of a USR are sufficiently advanced relative to present synchrotron sources that the full extent of photon research opportunities afforded by such high performance sources requires further examination and conceptual development. This is essential as these photon research opportunities are key factors influencing USR performance goals and associated design criteria.
- **Optimized ring parameters:** Once potential scientific applications are identified, requisite photon beam parameters, including brightness, flux, spectrum, coherent flux, coherent fraction, bunch length, etc., can be specified. Following this, studies are required to optimize storage ring parameters and capabilities, including circumference, electron energy and energy spread, emittance, insertion devices (IDs) and special operating modes, to meet science application goals and to maximize ring performance. An example of such an optimization is the trade-off between low emittance and the increase of energy

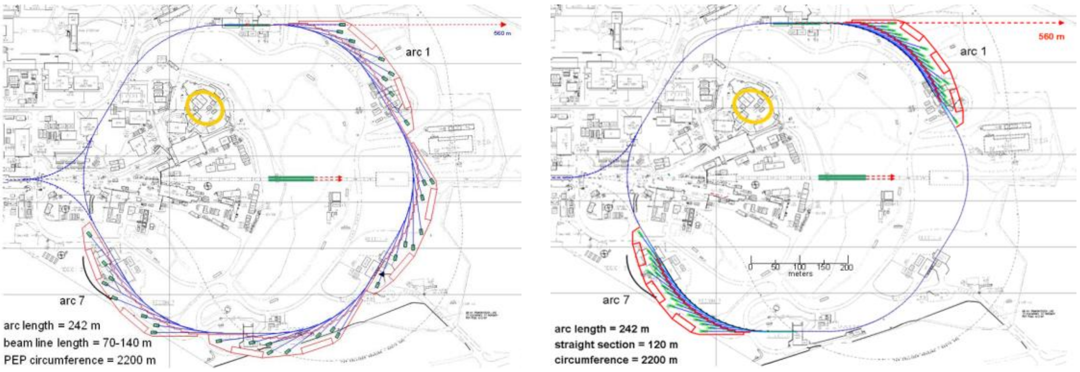

Figure 3: Distributed (left) vs. consolidated (right) beam line distribution for PEP-X. A lower emittance is attainable with the distributed configuration, while facility cost may be lower with the consolidated one.

spread incurred using damping wigglers to reach that emittance, which could result in a brightness reduction for higher undulator harmonics.

- **Lattice and geometry:** The choice of lattice cell types (e.g. multi-bend achromat, etc.), together with analyses of sensitivity to errors and associated beam dynamics (see below) are dependent on the emittance requirement, the number and lengths of straight sections for insertion devices and special components (e.g. long lasing IDs, bunch manipulation components, etc.), and the layout of photon beam lines and experimental halls. Lattice geometries that consolidate ID straight sections in sub-sections of the total ring circumference, instead of distributing them evenly around the ring, could lead to reduced construction costs for beam line experimental halls for large circumference USRs (Figure 3). The emittance for lattices having consolidated beam line straight sections might be larger than for those having an even distribution, so the cost-performance trade-off needs to be evaluated in light of scientific application requirements.
- **Dynamic and momentum acceptance:** The very strong focusing required for low emittance introduces large chromatic aberrations in the lattice that must be corrected using strong sextupoles. The sextupole field non-linearities introduce resonance driving terms that reduce dynamic and momentum acceptance, leading to very low lifetime and even the inability to inject beam into the machine. Detailed lattice studies are required to obtain sufficient acceptance.
- **Longitudinal emittance:** Reduction of electron energy spread would enhance the brightness of high harmonic radiation from undulators and potentially enable FEL operation. Lower longitudinal emittance would also enable shorter bunch operation. Ways to reduce longitudinal emittance should be studied.
- **Round beams:** Studies are required to determine the best way to produce oval or round beams other than relying purely on operating on a coupling resonance since that might impair injection or create difficulties in correcting the lattice.
- **Code development and benchmarking:** Computer codes are needed that provide integrated optimization of lattice and collective effects, that accurately represent the magnetic field interference in closely-spaced magnets, and that

accurately simulate beam impedances for short bunches. Codes should be benchmarked with experiments on existing machines, perhaps operated in unusual modes that mimic some aspects of a USR. One possibility is performing experiments on existing machines at low energy and in “extreme” lattices that require on-axis injection.

- **Collective effects and lifetime:** Studies are required to develop accurate models for intrabeam scattering (IBS), ring impedances, coherent synchrotron radiation impedances, and ion and electron cloud accumulation, as well as to understand their effects on beam dynamics, instabilities, and lifetime. Mitigation strategies will also need to be explored.
- **Injection:** On-axis injection schemes should be investigated. Such schemes may require kickers having very fast rise- and fall-times and very flat-top waveforms and possibly accumulator rings that can also serve as booster synchrotrons for injection. Again, some aspects of on-axis injection can be tested in existing machines, e.g., injection when operating near full coupling.
- **Injector type:** Different possibilities for the type of injector should be explored, including use of an accumulator ring, an ultra-low-emittance booster, or a full-energy linac. These should be compared for cost, feasibility, and reliability.
- **Special operating modes:** More detailed study is needed to evaluate the possibilities of the short bunch, tailored bunch, few-turn and lasing modes of operation mentioned in Section 2.
- **Accelerator systems and components:** The extremely low emittance and large circumference of USRs presents challenges for magnet and vacuum chamber design together with highly stable support systems, bunch lengthening and beam manipulation RF systems, advanced low level RF systems fast kickers and pulsers, precision electron orbit and photon beam trajectory feedback systems, multibunch feedback systems, and advanced beam diagnostics.
- **Photon beam line systems and components:** Preserving the brightness, coherence and stability of very low emittance photon beams presents challenges to X-ray mirrors, monochromators and other optical components, similar in many ways to those encountered at FEL facilities. Improved mirror polish/figures would reduce emittance and coherence degradation. Advances in micro-focusing optics, such as smaller zone plate line widths, would enhance microscope resolution. High average beam power and power density necessitates development of improved optical cooling and thermal designs for these components. Improved thermal designs and interlock strategies could reduce masking costs and provide more beam line layout flexibility. Enhanced beam stability systems incorporating advanced electron and photon beam position and beam shape/wavefront diagnostics into integrated servo systems that operate synergistically on both electron and photon optical systems. Optimization of experimental hall foundation and optical system supports for improved beam stability. Finally, developments in minimal optics and lens-less imaging methods would maximize performance in some cases.
- **Insertion devices:** Enhancements in permanent magnet and superconducting magnet technology would increase source brightness. Reducing undulator phase error would enhance performance for very high harmonics. High temperature

superconducting technology, novel magnetic structures for unique applications, devices that minimize unused power on optics and vertically oriented undulators would all contribute to USR performance. Note that the use of round beams and on-axis injection would support the use of insertion devices, such as helical undulators, with round beam apertures.

- **Value engineering:** Exploration of ways to maximize performance and minimize costs for large USR facilities is needed for all accelerator and beam line systems, as well as conventional facilities, which include the accelerator tunnel, beam line experimental halls, office buildings, temperature control systems and other utilities.

3.14.4 **USR R&D Program**

Many of the accelerator and photon beam line design challenges and studies outlined in Section 1.1.3 can be addressed in the near term with a modest R&D program conducted collaboratively by members of the light source accelerator and photon beam line communities in the US and internationally. Funding sources must be found to support these activities. These might include laboratory operations and/or R&D budgets as well as the funding agencies themselves.

Ideally the R&D program would be coordinated between contributors. Working groups could be set up to study various topics. To strengthen the endeavour, a coordinated R&D organization could be establishes, comprised of a coordinating council headed by a designated chairman serving on a rotating basis. This organization would engage international participants and produce progress reports as needed for oversight by participating laboratory managements. Such an organization could facilitate program funding especially if endorsed by funding agencies. At the moment such an organization does not exist, so study efforts are being supported on a small scale by individual laboratories that have some interest in USR development.

We note that the USR R&D program would benefit existing light source facilities and some general accelerator applications as well, as illustrated in Table 2. Accelerator physics studies related to USRs could be conducted on existing very low emittance light sources in the US and possibly those in other countries. For example, the 1-nm-rad, 6-GeV PETRA-III accelerator might be operated at 2 GeV to reach 100 pm-rad emittance, and the booster that shares the accelerator tunnel with the main storage ring for the Swiss Light Source might be used to test its function as an accumulator ring for on-axis injection. Vertical emittances on the pm-rad scale are already being realized at light sources in the US and elsewhere, enabling the possibility of special studies involving diffraction-limited emittances.

Table 2: Benefit of USR R&D to light sources and general accelerator applications.

Topic	***USR***	***Present ring light sources***	***All light sources (FELs, compact, etc)***	***General accel apps***
Stability in accelerator and beam lines	X	X	X	X
RF cavities (including harmonic)	X			X
RF power sources	X	X	X	X
Alignment	X	X	X	X
Combined function magnets	X		X	X
Impedance of vacuum chamber	X	X	X	X
Kickers for on-axis injection	X			X
Pulsed multipoles for off-axis injection	X	X		
High power absorbers	X	X	X	
X-ray optics cooling	X	X	X	
Mirror metrology	X	X	X	
Waverfront error detection/correction	X	X	X	
Minimal optics techniques (lensless, etc)	X	X	X	
Photon beam monitors and transducers	X	X	X	
Superconducting IDs (low and high Tc)	X	X	X	X
Low phase error IDs for high harmonics	X	X	X	
IDs that minimize unused power on optics	X	X	X	
Novel IDs for unique applications	X	X	X	X
Vertical undulators	X		X	

3.14.5 **References**

1. The USR Working Group in the US has the following initial members:
   ANL/APS: M. Borland, L. Emery, R. Gerig, D. Haeffner, A. Xiao
   BNL/NSLS: F. Willeke
   LBNL/ALS: D. Robin, C. Steier
   SLAC/SSRL: Y. Cai, A. Chao, R. Hettel, X. Huang, C.-C. Kao, T. Rabedeau, J. Safranek, J. Schmerge

   The Working Group is expected to grow in the future and will include international participants.
2. ANL, BNL, LBNL, SLACNAL, Science and Technology of Future Light Sources - A White Paper, SLAC R-917, 2008.
3. "Workshop on Science at the Hard X-ray Diffraction Limit", XDL 2011, Cornell, June 2011.
4. J.A. Crittenden et al., Proc. Particle Accelerator Conference 2009, Vancouver, 2009.
5. A. Ropert et al., Proc. European Particle Accelerator Conference 2000, Vienna, 2000.
6. K. Tsumaki, N. Kumagai, Nucl. Instr. Meth. A 565 (2006) 394.
7. R. Hettel et al., Proc. Particle Accelerator Conference 2009, Vancouver, 2009.
8. M. Borland, AIP Conf Proc 1234, 2009.
9. C. Steier, internal technical note, LBNL, January 2012.
10. Y. Cai et al., SLAC-PUB-14785, 2011.
11. M. Borland, to be published in Proc. of Intl. Particle Accelerator Conference 2012, New Orleans, 2012.
12. M. Bai et al., *Nucl. Instr. and Meth. A* (2010), doi:10.1016/j.nima.2010.01.045.
13. Meeting notes from the APS/SLAC/LBNL USR working group, November 2011.

4 Activity Reports

4.1 High Energy Physics Collider Table (1984-2011)

Weiren Chou (Fermilab) for the ICFA Beam Dynamics Panel
Mail to: chou@fnal.gov

In September 2011, we received a request from Stefan Michalowski, Executive Secretary of the *Organization for Economic Cooperation and Development* (OECD) *Global Science Forum* (GSF), for input on changes over the past 20-25 years in the numbers and locations of energy-frontier HEP accelerators. In his letter he said:

"*The OECD Global Science Forum (GSF) is a committee whose members are senior science policy officials of the OECD's member and observer countries. My job at OECD is to ensure the timely and efficient execution of the GSF work programme. In recent years, the Forum has published reports on the prospects for international collaboration in a number of scientific fields, including high-energy physics, astronomy and astrophysics, nuclear physics and astroparticle physics. In addition, the GSF has tackled generic issues associated with establishing, funding, and operating large research facilities such as accelerators. These reports (which can be found on the Forum's web site,* www.oecd.org/sti/gsf*) are the results of extensive international consultations that have involved officials of funding agencies and representatives of the organized scientific community (notably, the various working groups of IUPAP, such as ICFA). I will add, parenthetically, that the GSF played an essential role in the establishment of IUPAP/ICUIL, a group that you have, I believe, collaborated with recently.*

"One of the GSF's current activities is a case study of how one particular research infrastructure – CERN – generates impacts that go beyond its primary mission of advancing fundamental knowledge. In connection with this project, I wish to prepare a graph (or other visual representation) that shows the evolution, during the past 20-25 years, in the numbers and locations of energy-frontier HEP accelerators. As a former particle physicist myself, I have a general idea of how things have changed since I was a postdoc at SLAC from 1977 to 1982, but I am seeking more precise data and a deeper understanding of what has occurred in the field. I would also be willing to discuss a more complex/sophisticated depiction of current trends, possibly including intensity-frontier and cosmic-frontier projects. At the recommendation of ICFA secretary Roy Rubinstein (on copy), I am turning for help to you in your capacity as Chair of ICFA's Bean Dynamics Panel.

"As we discussed yesterday, I would be very grateful if you could consult with your colleagues on this matter, and if you could help me in my quest for both accurate data and good ideas."

We discussed this request at our panel meeting in September 2011 in San Sebastian, Spain during IPAC2011 and decided to compile an HEP collider table to send to GSF. This table is the collaborative efforts of panel members as well as many colleagues around the world. We tried to be as accurate as possible. However, if readers find errors, please let us know and we'll correct.

HEP Colliders (1984-2011) (Revision April 18, 2012)

Location	Accelerator	Type	Energy	Operations Period	Impact	Note
SSCL	SSC	p-p	20 x 20 TeV	N/A	Cancellation a blow to the world HEP program, especially in the US	Construction began in 1989 but was canceled by the US Congress in 1993
CERN	LHC	p-p	7 x 7 TeV	2009-present	Highest energy collider, first to use 2-in-1 SC magnet technology, limits on Higgs mass, search for physics beyond SM, Quark-gluon plasma physics	Inauguration in October 2008, re-commissioning in late 2009, currently operating at 4 x 4 TeV
		Pb-Pb	574 x 574 TeV (2.76 x 2.76 TeV per nucleon)			
	LEP	e+e-	104.5 x 104.5 GeV	1989-2000	Precise measurement of Z and W bosons, determination of the number of light neutrino families to be 3, exclusion of Higgs mass below 114 GeV	Highest energy lepton collider
	SPS	p-pbar	315 x 315 GeV	1981-1984	Discovery of W and Z bosons, first to use stochastic cooling technology	Now as both LHC injector (450 GeV) and fixed-target machine (400 GeV)
	ISR	p-p	31.4 x 31.4 GeV	1971-1984	First hadron collider and first p-pbar collider	Also ran in p-d, d-d, p-alpha, alpha-alpha modes
Fermilab	Tevatron	p-pbar	980 x 980 GeV	1983-2011	Discovery of Top quark and Tau neutrino, first large accelerator using SC magnet technology	Ran as both a fixed-target machine and a collider
KEK	KEKB	e+e-	8 (e-) x 3.5 (e+) GeV	1998-2010	CP violation in the decay of B-meson, confirmation of the CKM mattrix	Highest luminosity collider
	TRISTAN	e+e-	32 x 32 GeV	1986-1995	First large accelerator using SC RF technology	

SLAC	PEP-II	e+e-	9 (e-) x 3.1 (e+) GeV	1999-2008	CP violation in B-Bbar system, confirmation of the CKM mattrix	
	SLC	e+e-	46.2 x 46.2 Gev	1988-1998	Precise measurement of Z boson, including most precise indirect constraint on Higgs mass	First (and only) e+e- linear collider, 80% polarized e-
DESY	HERA	e-p	27.5 x 920 GeV	1992-2007	Test of QCD, proton structure function	Polarized e- and e+
	PETRA	e+e-	23.4 x 23.4 GeV	1978-1986	Discovery of Gluon	Ligth source since 2009
	DORIS	e+e-	5.6 x 5.6 GeV	1974-1992	Decays of J/Psi and Ypsilon resonances, B physics	e+/e- collision with hydrogen target in 2012
Cornell	CESR	e+e-	1.8 x 1.8 GeV to 5.5 x 5.5 GeV	1979-2008	Measurement of |Vub|, observation of "penguin" and $b \to s\gamma$ decays, CKM matrix constraining the unitarity triangle	Currently operating in two modes: light source and damping ring test accelerator
BNL	RHIC	p-p, Au-Au	250 x 250 GeV	2000-present	Quark-gluon plasma discovery, nuclear phase diagram, source of proton spin	
INFN	DAFNE	e+e-	0.51 x 0.51 GeV	1999-present	High precision K physics, crab-waist operation for future Super-B	
IHEP/China	BEPC & BEPC-II	e+e-	1.5 x 1.5 GeV to 2.5 x 2.5 GeV	1988-2005, 2008-present	Charm-τ physics	
BINP	VEPP-200	e+e-	0.2 x 0.2 GeV to 1 X 1 GeV	2010-present	Hadron production measurement; p-pbar and n-npar near threshold	
	VEPP-4M	e+e-	1.5 x 1.5 GeV to 5 x 5 GeV	1984 -present	τ and Psi mass measurement, 2-gamma physics	

5 Workshop and Conference Reports

5.1 51st ICFA Advanced Beam Dynamics Workshop on Future Light Sources (FLS2012)

Swapan Chattopadhyay, Cockcroft-Walton Institute, U.K.
George Neil and Gwyn Williams, Jlab, U.S.A.
Email to: neil@jlab.org

FLS2012, was held March 5-9, 2012 at Thomas Jefferson National Accelerator Facility in Newport News Virginia. This continuing series of ICFA-sponsored workshops dating back to 199X addresses the science and technology required for development of future light sources. This workshop was attended by 150 scientists from 11 countries and consisted of a number of plenary presentations, submitted oral talks and working sessions for discussion of key ideas and issues. The program was assembled from an international program committee led by Stephen Benson. It can be found on the conference website www.jlab.org/conferences/FLS2012. The workshop featured an energetic interchange of ideas befitting a field growing in activity and importance as this one, and was notable for the progress that was reported since the last meeting in this series. A highlight of the workshop was a presentation by Herman Winick on the 20 year genesis of the LCLS. It was a sobering reminder to ignore rejections from funding agencies when the fundamental ideas are sound and strongly connected to requirements defined by a user community. The proposals for LCLS were rejected by DOE at least 4 times in the early years before a broad set of user activities finally were identified to justify the activity.

Other plenary talks covered applications and user needs in soft and hard x rays including XDL2011, Science at the Hard X-ray Diffraction Limit, Controlling Electron Spins on the Nanoscale, and X-ray Lasers for Structural and Dynamic Biology. This led to presentations on the associated technologies of Optics and Beamlines, ERLs, Ultimate Storage Rings, Amplifier R&D, Coherent hard X-rays, Photoinjectors, Insertion Devices, Diagnostic Needs, Laser-Plasma Accelerator-based FELs, and Intense Super-radiant X-rays from a Compact Source.

Working groups met each day in parallel sessions to discuss technology for FELs, Compact Sources, ERLs, Storage Rings, Undulators and Wigglers, Timing and Diagnostics, and Injectors. In addition a number of joint sessions were held to cross-fertilize ideas or expand the awareness of technological requirements derived from other areas.

Topics of apparent growing interest included ultimate storage rings, soft and hard x-ray oscillators, seeded high power FELs, compact sources, and guns, including cathodes. For example, Compton scattering, high frequency linacs, or use of superconducing, rf, or photonic wigglers offer hope of university sized hard x-ray sources. Several new light source proposals were discussed including MARIE at Los Alamos though other proposals have been turned down, delayed, or are inactive.

The highlights of the FEL working group included efforts on soft x-ray FELs, hard x-ray FELs FEL theory, and test facility design and concepts. Several talks dealt with x ray oscillators for photon production for users and soft x ray oscillators for both users and as a seed for FEL hard x ray amplifiers, utilizing advanced techniques such as

EEHG for up-conversion. (NLCTA and SSRF have demonstrated 7th harmonic.) It was noted that hard x-ray users are now starting to demand performance requirements in repetition rate, coherence, and line width previously only cited by soft x-ray users. Common themes being addressed in proposals and facilities now include high rep rate, longitudinal coherence, and low cost. Emittance exchange was a hot topic. A new facility called LUNE5X was proposed in France at SOLEIL consisting of a conventional linac and a laser wakefield accelerator to study seeding approaches and undulator technology. Groups at Daresbury discussed the proposed CLARA machine and SLAC the proposed NLCTA experiment.

The highlights of the Compact Sources working group included: laser wakefield accelerators, inverse Compton systems, srf accelerators, compact rings, compact undulators, and the science enabled by compact sources. Several promising avenues appear to be able to get systems down to university scale to broaden the reach of light source use.

The highlights of the ERL working group included discussions of system trades with FEL devices and the perceived advantages and disadvantages of each approach. Technologies for ERLs led the group to have several joint sessions with the Storage Ring group, the Injector Group, the the FEL group and the Sources and Diagnostics. This group had perhaps a more limited scope because of the recent ERL Workshop dedicated to such technology.

The Storage Ring working group reviewed the most recent progress with low emittance ring design and optimization. The goal of an ultimate storage ring remained a desire, while in the near term upcoming ring plans and methods for improving performance of existing rings offers pleanty of work. The required R&D was enumerated and the differences with ERLs delineated. Ultrashort bunches and the progress toward a short bunch lattice for THz sources led to major interchanges.

The highlights of the Undulator and Wiggler working group were the discussions on the progress of both cryogenic and superconducting undulators. Another key topic was the development of practical elliptically polarized systems with variable ellipticity. Issues with in-vacuum undulators, wakefield control and radiation damage limits consumed a major portion of the discussion time, though time was allowed for a joint session with both the Compact Source group and the Storage ring group to compare notes on requirements and issues.

The highlights of the Timing and Diagnostics working group continued what has been a topic of study by several groups for the last few years, namely maintaining tight timing between the laser bunches and rf control and other lasers. The problem begins with the detection of the short bunches of electrons that is required to obtain the resolution required to optimize the system. Optical techniques seem to be stuck around 100 fs resolution in most cases. Additional issues appear when one is interested in CW non-destructive monitoring of the beam, though several possible techniques are under investigation. High dynamic range is also an issue to resolve in order to handle the halo issue in CW machines.

The highlights of the Injector working group remains the area in future light source development with the most leverage (and present risk) in machine design. Significant progress was reported from proponents of DC guns including KEK, JAEA, JLab, and especially the Cornell group who have now demonstrated 50 mA average currents for significant run times with useful emittances in their test injector. Progress in CW rf guns at DESY, AsTeC and LBNL gives hope for that approach to also be successful.

SRF guns are also making progress with HZDR, ELBE, and Niowave/U. Wisconsin all reporting progress. Development of designer cathode materials was identified as a desirable goal with much activity already in process at many labs.

There was much too much discussed to be covered in this short report; we encourage interested readers to view the working group summaries and papers presented on JACOW: www.jacow.org when the conference proceedings are published by Editors Fay Hannon and Chris Tennant. In the meantime, many slides from the workshop are available on the workshop website cited above.

The workshop was fun, exciting, and energetic thanks to the participation of so many great contributors. We hope the participants brought home a good set of ideas to carry forward. We thank Staff Services of Jefferson Laboratory for their efforts to make the workshop a success and we are very appreciative of financial support from SURA/JSA.

6 Forthcoming Beam Dynamics Events

6.1 52nd ICFA Advanced Beam Dynamics Workshop on High Intensity High Brightness Hadron Beams (HB2012)

This is the second announcement for the 52nd ICFA Advanced Beam Dynamics Workshop on High-Intensity and High-Brightness Hadron Beams which will be held in Beijing, China from September 17-21, 2012. The workshop will be hosted by Institute of High Energy Physics (IHEP), Chinese Academy of Sciences.

This workshop is a continuation of the successful biennial HB workshop series started about ten years ago (2002 at Fermilab, 2004 at GSI, 2006 at KEK, 2008 at ORNL and 2010 at PSI). HB workshop series is a platform for presenting and discussing new progresses, status and future developments of high intensity and high brightness hadron beams, including beam physics, linear and circular hadron machines, technical systems and accelerator projects (under construction or in design) around the world.

HB2012 website: http://hb2012.ihep.ac.cn

Key Dates

Website accepts abstracts:	March 7, 2012
Registration opens:	March 7, 2012
Abstract submission deadline:	June 17, 2012
Final program is ready	July 7, 2012
Early registration deadline:	July 17, 2012
Online registration deadline:	August 17, 2012
Hotel reduced rate deadline:	August 17, 2012
Paper submission deadline:	September 15, 2012
Workshop:	September 17-21
IHEP tour	September 21

Workshop Agenda

The workshop will run five days (September 17-21, 2012) with a welcome reception on Sunday evening, September 16th from 6-8:00 pm. The workshop main topics will be driven by the participants but are expected to cover:

- Beam dynamics in high-intensity circular machines
- Beam dynamics in high-intensity linacs
- Accelerator system design, injection, extraction, beam-material interaction
- Commissioning, operations and performance
- Beam diagnostics and instrumentation for high-intensity beams

Workshop Venue

The workshop will be held at the Park Plaza Beijing West located in Haidian District, Beijing, China. The hotel is ideally situated at the end of Chang’an Avenue in west Beijing. And it’s within close proximity to numerous major enterprises and important venues, including Wukesong Arena.

Workshop Registration

All workshop attendees are urged to register early using the following registration link:

https://spms.kek.jp/pls/hb2012/registration.page?ID=18

The total workshop registration fee is $500 USD for regular attendees for early registration before July 17, 2012, beyond that the fee will be increased to $600 USD.

The total workshop registration fee includes:

- Workshop kit
- Welcome reception
- Coffee breaks
- Lunch meals
- Workshop banquet
- Visit/travel to IHEP

Letter of Invitation and Visa Application Form

After your successful registration, an invitation letter issued by IHEP will be sent to your email within a week. But if you need a visa application form issued by Chinese Academy of Sciences, please send the following information to Mr. Tiejun Deng, dengtj@ihep.ac.cn.

- Full name
- Passport number
- Nationality
- Name a city where you want to apply your visa
- Fax number
- Mailing address

E-mail Facilities

Several computers will be available at the workshop venue for participants to send and receive e-mails. Guestrooms of the Park Plaza Beijing West hotel have complimentary high-speed broadband internet access. Meeting rooms of the hotel have free wireless high-speed internet access.

Registration Desk

The registration desk will be open from 2-7 p.m. on Sunday evening, September 16 at the workshop venue, Park Plaza Beijing West.

Accommodations

The workshop hotel is the workshop venue, Park Plaza Beijing West. A block of rooms has been reserved for the period September 15-23 at a special rate of 600 RMB (1 or 2 beds with 1 free breakfast) or 660 RMB (1 or 2 beds with 2 free breakfasts) per night. Room reservations should be made before August 17 in order to guarantee rooms at these rates.

When you register for HB2012, you can fill in hotel reservation information. The secretariat of HB2012 will help you to contact with the hotel to book your stay. Within a month, the hotel will send you a confirmation email. But if you do not receive the email after your successful registration, please contact with the head of the secretariat, Jingshi ZHAO at zhaojs@ihep.ac.cn.

Park Plaza Beijing West

Address:	No. 17 Xicui Rd, Haidian District, Beijing, 100036, China
Reservations:	400 678 0687 (China Toll-free Reservations) +1 (800) 777 1700 (US/Canada Toll-free)
Telephone:	+ 86 10 6813 0088
Fax:	+ 86 10 6813 3399
Email:	beijingwest@parkplaza.com
Web site:	http://www.parkplaza.com/beijing-hotel-cn-100036/chnbjng

Transportation

Beijing is served by one major airport: Beijing Capital International Airport. Details on the airport can be found at the link http://en.bcia.com.cn/. Transportation from the airport to **Park Plaza Beijing West** is as follows:

- By taxi: You can get a taxi right outside the arrival terminals. It is about 40 km from the airport to the workshop hotel. The fare is about 147RMB (22 USD).
- By Subway: You can take Beijing Subway from the Airport Station to Dongzhimen Station, from which transfer to Line 2. Then make another change from Line 2 to Line 1 at Jianguomen Station. Take the direction to Pingguoyuan and stop off at Wanshoulu Station or Wukesong Station. Then it takes about 15 minutes’ walk to the north.
- Airport shuttle bus: You also can take airport shuttle bus from the airport to the Gongzhufen bus station. The fare is 16RMB (2.4USD). Then you can take a taxi to the workshop hotel. The fare is about 25RMB (3.5 USD). You can go to the HB2012 website to check an electric figure showing the hotel name and the address in Chinese, so you can print it and bring it with you when taking taxi in Beijing.

Proceedings

The conference proceedings will be published through the Joint Accelerator Conference Website (JACoW). The conference proceedings will be archived by JACoW and available worldwide through the JACoW servers.

Abstract and Manuscript Submission

The HB2012 website is now open for abstract submission. Please check the workshop website. The deadline for abstract submission is June 17, 2012.

Oral Presentations

For oral presentations, a Windows-based laptop will be provided onto which speakers can download their PowerPoint presentations. There will be no slide projector or overhead projector.

Posters

Poster boards will be available. The usable poster board size is 114 × 231 cm (45” × 91”). Posters can be installed at anytime before the poster session and should be removed at the end of the session.

Fellowships

A limited number of grants will be awarded to young scientists and students who have demonstrated outstanding work in their field of research. Grants will cover the workshop fee and the local expenses. Travel expenses are not catered for by the grant.

Applicants should include a brief cover letter, including details of their proposed contribution, together with the name and email address of one referee who is able to qualify the candidate's suitability.

Applications should be submitted by email only to: lizhihui@ihep.ac.cn

The closing date for submission of applications is **15 July 2012**.

International Organizing Committee (IOC)

Caterina Biscari	Italy
Alex Chao	SLAC, USA
Jia-er Chen	Peking University, China
Yong Ho Chin	KEK, Japan
Weiren Chou	FNAL, USA
Ronald Davidson	PPPL, USA
John Galambos	ORNL, USA
Roland Garoby	CERN, Switzerland
Ingo Hofmann	GSI, Germany
Stephen Holmes	FNAL, USA
Andrew Hutton	JLAB, USA
Sergey Ivanov	IHEP, Russia
Ji-Ho Jang	KAERI, Korea
In Soo Ko	PAL, Korea
Jean-Michel Lagniel	CEA-Saclay, France
Yoshi Mori	Kyoto University, Japan
Christopher Prior	RAL, UK
Ji Qiang	LBNL, USA
Thomas Roser	BNL, USA
Amit Roy	IUAC, India
Lawrence Rybarcyk	LANL, USA
Mike Seidel	PSI, Switzerland
Jingyu Tang (Co-Chair)	IHEP, China
Maury Tigner	Cornell University, USA
Jiuqing Wang (Co-Chair),	China
Jie Wei	MSU, USA
Bill Weng	BNL, USA
Yoshishige Yamazaki	MSU, USA

Local Organizing Committee (LOC)

Jiuqing Wang (Co-Chair)	IHEP, China
Jingyu Tang (Co-Chair)	IHEP, China

Li Ma	IHEP, China
Weimin Pan	IHEP, China
Chuang Zhang	IHEP, China
Shinian Fu	IHEP, China
Tongzhou Xu	IHEP, China
Yanwei Chen	IHEP, China
Gang Chen	IHEP, China
Zhihui Li (scientific secretary)	IHEP, China
Jingshi Zhao (head of secretariat)	IHEP, China
Ning Zhao (JACoW editor)	IHEP, China

Contact Information

Jiuqing Wang (co-chair)	wangjq@ihep.ac.cn
Jingyu Tang (co-chair)	tangjy@ihep.ac.cn
Zhihui Li (scientific secretary)	lizhihui@ihep.ac.cn
Jingshi Zhao (head of secretariat)	zhaojs@ihep.ac.cn
Ning Zhao (JACoW editor)	zhaoning@ihep.ac.cn

6.2 ICFA Beam Dynamics Mini-Workshop on Deflecting/Carb Cavity Applications in Accelerators

We would like to welcome you to the 3rd ICFA Advanced Beam Dynamics Mini-Workshop on Deflecting/Crabbing Cavity Applications in Accelerators that will be held in Lanzhou, China, from July 18-20, 2012. This mini-workshop is hosted by Tsinghua University and will be held at the Institute of Modern Physics (IMP), Chinese Academy of Science in Lanzhou, China. The purpose of this workshop is to bring together researchers in various accelerator communities to discuss advances in the deflecting/crabbing RF cavity for accelerator applications including generation of short x-ray pulses in synchrotron light sources, luminosity upgrade in high energy colliders, beam manipulations, emittance exchange, and diagnostics.

The workshop web site is:

https://conferences.lbl.gov/conferenceDisplay.py?confId=18 , It includes program information, abstract submission, registration, travel, and local transportation information.

International Organizing Committee

John Byrd (LBNL, USA)
Huaibi Chen (Chair, Tsinghua University, China, Chair)
Wei Gai (ANL, USA)
Derun Li (LBNL, USA)
Peter McIntosh (Daresbury, UK)
Alireza Nassiri (ANL, USA, Co-Chair)
Robert Rimmer (JLab, USA)
Andrei Seryi (JAI, UK)
Hongwei Zhao (IMP, China)
Frank Zimmermann (CERN, Switzerland)

Scientific Program Committee

Graeme Burt (Lancaster University, UK)
Rama Calaga (CERN, Switzerland)
Alessandro Gallo (INFN/LNF, Italy)
Jie Gao (IHEP, China)
Kenji Hosoyama (KEK, Japan)
Derun Li (LBNL, USA, Chair)
Jianfei Liu (SINAP, China)
Alireza Nassiri (ANL, USA)

Local Organizing Committee

Yuan He (IMP, China, Chair)
Wenhui Haung (Tsinghua University, Co-Chair)
Wenzhong Tang (IMP, China)
Yawei Yang (Tsinghua University, ANL)
Xiaohua Yuan (IMP, China)

Contacts:

International Organizing Committee Chair: Ali Nassiri (nassiri@aps.anl.gov)
Program Committee Chair: Derun Li (dli@lbl.gov)
Local Committee Co-Chairs: Yuan He and Wenhui Huang (hey.yuan@yahoo.com and huangwh@mail.tsinghua.edu.cn)

6.3 International Computational Accelerator Physics Conference (ICAP 2012)

The 2012 International Computational Accelerator Physics Conference will be held August 19 - 24, 2012 in Rostock-Warnemunde (Germany) at the coast of the Baltic Sea.

The conference venue will be the ~~Yachthafenresidenz Hohe Dune~~ (http://www.hohe-duene.de) located just besides the yachting harbour of Warnemunde.

ICAP is focused on advances in Computational Accelerator Physics and Numerical Field Calculation, and their application to existing and future machines. ICAP 2012 will provide a unique forum for experts and novices to share their experience and to exchange information and ideas in the above mentioned fields.

The ICAP 2012 Scientific Program Committee encourages those actively engaged in the field of Computational Accelerator Physics and Numerical Field Calculation to participate and contribute to the scientific program by submitting abstracts for poster or oral presentations. Opening of abstract submission will be announced soon. Further information concerning all aspects of the conference can be found on the conference website

http://www.icap12.uni-rostock.de

The registration of the 11th International Computational Accelerator Physics Conference is open and I would like to invite you to register as soon as possible. So please do not wait until the deadline. You will find all necessary information at Registration on our web site.

The same is true for accommodation: we have reserved 100 Hotel rooms in the Yachthafenresidenz Hohe Dune for participants of ICAP 2012. These rooms can be booked until May 28, 2012 using the keyword ~~ICAP 2012~~. For room rates see the table on the web page. A fax form for booking rooms at the Yachthafenresidenz and information on other accommodation is also available on the web page.

You may download the conference flyer and poster from our website.

Contact

Ursula van Rienen
Scientific Program Committee Chair
Universitat Rostock
Institut fur Allgemeine Elektrotechnik
Albert Einstein Str. 2
18059 Rostock
GERMANY
Phone +49(0)381 498-7070
Fax +49(0)381 498-7081
ursula.van-rienen@uni-rostock.de
http://www.iae.uni-rostock.de

6.4 15th Biennial Beam Instrumentation Workshop (BIW2012)

This is a second announcement of the 15th biennial Beam Instrumentation Workshop (BIW2012), to be held in Newport News, Virginia, April 15-19 2012. This workshop is dedicated to exploring the physics and engineering challenges of beam diagnostics and measurement techniques for charged particle accelerators. BIW12 is being hosted by the Thomas Jefferson National Accelerator Facility. The meeting program includes tutorials on selected topics, invited and contributed talks, as well as plenary and poster sessions and vendor exhibits. The recipient of the 2012 Faraday Cup Award, sponsored by Bergoz Instrumentation, Inc., will also be announced.

The conference website is http://www.jlab.org/conferences/biw12 , and includes program information, abstract submission, and registration links. Though abstract submission ended Feb 25 2012, late abstracts will be considered. Early workshop registration continues through March 15 2012.

We hope that you enjoy the workshop, and find it intellectually stimulating. If there is anything we can do to make your conference experience and stay more enjoyable, just ask us at BIW12_admin@jlab.org . We look forward to seeing you in April in Newport News.

BIW 2012 Workshop Chair: Kevin Jordan

6.5 34th International Free-Electron Laser Conference (FEL2012)

The 34th International Free-Electron Laser Conference will take place from Sunday August 26 to Friday August 31, 2012 in Nara, Japan. The organizer of the conference, SPring-8 and Kyoto University, invites you to participate in this conference.

FEL2012 will focus on the scientific, technological, and user aspects of free-electron lasers. The Scientific Program of the conference will consist of invited talks and contributed presentations in the form of oral presentations or as a poster.

http://fel2012.spring8.or.jp/

FEL Conference

The scientific part of the 34th International Free-Electron Laser Conference will take place from Monday August 27 to Friday August 31, 2012. The detail conference topics will be announced soon. Lab tour for SACLA will be held in afternoon Friday August 31, 2012.

Conference Location and Site

Nara Prefectural New Public Hall was constructed in 1987 in commemoration of the 100th anniversary of the establishment of Nara Prefecture. It is located in the center of Nara National Park, which is famous for its beauty and 1,200 tame deer.

Nara was the capital of Japan from 710 to 784, so, it has many historical shrines and temples containing national treasures. Famous tourist spots such as Kofukuji Temple, Todaiji Temple, Kasuga Shrine are within walking distance from the hall.

The hall has an impressive Noh theatre, which can be easily converted into a multi-purpose auditorium, conference rooms with simultaneous interpretation equipments for up to four languages, a reception hall and a spacious garden.

101 Kasugano-cho, Nara-shi, 630-8212, Nara, Japan
URL: http://www.shinkokaido.jp/english/index.html

Important Dates

March 16 (Friday) ------- Start abstract submission and registration.
May 1 (Tuesday) --------- Abstract submission deadline.
May 1 (Tuesday) --------- Deadline request for student support.
May 31 (Thursday) ------- Deadline nominations FEL prize.
July 13 (Friday) -------- End of early registration.
August 22 (Wednesday) --- Deadline for paper submission.
August 22 (Wednesday) --- Deadline for online registration.
August 26 (Sunday) ------ Conference reception.
August 29 (Wednesday) --- Conference banquet.
August 31 (Friday) ------ Conference tour.
August 31 (Friday) ------ End of the conference.

FEL Prize

The members of the FEL Prize Committee invite you to make a nomination for the 2012 FEL prize and for the 2012 Young Scientist FEL award, which will be awarded at the FEL 2012 conference.

The FEL prize is given to a person who has contributed significantly to the advancement of the field of Free-Electron Laser. In addition, it gives the international FEL community the opportunity to recognize one of its members for her or his outstanding achievements.

The Young Scientist FEL award is intended to honor an important contribution to FEL science and technology by a person who is less than 35 years of age. A date of birth or current age is necessary information. The nomination letter for this prize must have attachment with selected paper(s) published by the nominee.

Nominations should detail the outstanding achievement for which the nominated person should be recognized. A brief proposed citation should be part of the nomination letter. It is recommended that contributions are accompanied by support letters, (no more than 3 letter) substantiating the significant contributions to the science of FEL relevant to the nomination.

Nominations and supporting letters for both prizes should be sent or e-mailed to the Chair of the FEL Prize Committee:

Eisuke J. Minehara
FEL Nomination Committee Chair
eminehara@werc.or.jp

Deadline for nominations and supporting letter: May 31, 2011

Conference Fee

55,000 JPY: registration until 13 July 2011
60,000 JPY: registration after 13 July 2011
30,000 JPY: student registration (until 13 July 2011)
+ 3,000 JPY: Excursion charge
10,000 JPY Companion ticket (Reception, Conference dinner, pre-registration, Excursion)

Information about payment procedures will be informed as soon as possible.

Student support

A limited number of student grants are available to support student participation in FEL 2012. These grants will cover the cost of the registration fee. To be considered for financial support a letter of recommendation from the student's advisor must be received no later than May 1, 2012.

The letter should be mailed or emailed to

Hideaki OHGAKI
Institute of Advanced Energy, Kyoto University
Gokasho, Uji, Kyoto 6110011, Japan
email: ohgaki@iae.kyoto-u.ac.jp

Information

Local Organizing Secretariat

Toshiteru Kii
Institute of Advanced Energy, Kyoto University

Gokasho, Uji, 6110011, Kyoto, Japan
Fax: +81 774 383426
Email : info.fel2012@spring8.or.jp
Web : http://fel2012.spring8.or.jp/

7 Announcements of the Beam Dynamics Panel

7.1 ICFA Beam Dynamics Newsletter

7.1.1 Aim of the Newsletter

The ICFA Beam Dynamics Newsletter is intended as a channel for describing unsolved problems and highlighting important ongoing works, and not as a substitute for journal articles and conference proceedings that usually describe completed work. It is published by the ICFA Beam Dynamics Panel, one of whose missions is to encourage international collaboration in beam dynamics.

Normally it is published every April, August and December. The deadlines are 15 March, 15 July and 15 November, respectively.

7.1.2 Categories of Articles

The categories of articles in the newsletter are the following:

1. Announcements from the panel.
2. Reports of beam dynamics activity of a group.
3. Reports on workshops, meetings and other events related to beam dynamics.
4. Announcements of future beam dynamics-related international workshops and meetings.
5. Those who want to use newsletter to announce their workshops are welcome to do so. Articles should typically fit within half a page and include descriptions of the subject, date, place, Web site and other contact information.
6. Review of beam dynamics problems: This is a place to bring attention to unsolved problems and should not be used to report completed work. Clear and short highlights on the problem are encouraged.
7. Letters to the editor: a forum open to everyone. Anybody can express his/her opinion on the beam dynamics and related activities, by sending it to one of the editors. The editors reserve the right to reject contributions they judge to be inappropriate, although they have rarely had cause to do so.

The editors may request an article following a recommendation by panel members. However anyone who wishes to submit an article is strongly encouraged to contact any Beam Dynamics Panel member before starting to write.

7.1.3 How to Prepare a Manuscript

Before starting to write, authors should download the template in Microsoft Word format from the Beam Dynamics Panel web site:

http://www-bd.fnal.gov/icfabd/news.html

It will be much easier to guarantee acceptance of the article if the template is used and the instructions included in it are respected. The template and instructions are expected to evolve with time so please make sure always to use the latest versions.

The final Microsoft Word file should be sent to one of the editors, preferably the issue editor, by email.

The editors regret that LaTeX files can no longer be accepted: a majority of contributors now prefer Word and we simply do not have the resources to make the conversions that would be needed. Contributions received in LaTeX will now be returned to the authors for re-formatting.

In cases where an article is composed entirely of straightforward prose (no equations, figures, tables, special symbols, etc.) contributions received in the form of plain text files may be accepted at the discretion of the issue editor.

Each article should include the title, authors' names, affiliations and e-mail addresses.

7.1.4 Distribution

A complete archive of issues of this newsletter from 1995 to the latest issue is available at

http://icfa-usa.jlab.org/archive/newsletter.shtml.

This is now intended as the primary method of distribution of the newsletter.

Readers are encouraged to sign-up for electronic mailing list to ensure that they will hear immediately when a new issue is published.

The Panel's Web site provides access to the Newsletters, information about future and past workshops, and other information useful to accelerator physicists. There are links to pages of information of local interest for each of the three ICFA areas.

Printed copies of the ICFA Beam Dynamics Newsletters are also distributed (generally some time after the Web edition appears) through the following distributors:

Weiren Chou	chou@fnal.gov	North and South Americas
Rainer Wanzenberg	rainer.wanzenberg@desy.de	Europe++ and Africa
Toshiyuki Okugi	toshiyuki.okugi@kek.jp	Asia** and Pacific

++ Including former Soviet Union.

** For Mainland China, Jiu-Qing Wang (wangjq@mail.ihep.ac.cn) takes care of the distribution with Ms. Su Ping, Secretariat of PASC, P.O. Box 918, Beijing 100039, China.

To keep costs down (remember that the Panel has no budget of its own) readers are encouraged to use the Web as much as possible. In particular, if you receive a paper copy that you no longer require, please inform the appropriate distributor.

7.1.5 Regular Correspondents

The Beam Dynamics Newsletter particularly encourages contributions from smaller institutions and countries where the accelerator physics community is small. Since it is impossible for the editors and panel members to survey all beam dynamics activity worldwide, we have some Regular Correspondents. They are expected to find interesting activities and appropriate persons to report them and/or report them by themselves. We hope that we will have a "compact and complete" list covering all over the world eventually. The present Regular Correspondents are as follows:

Liu Lin	Liu@ns.lnls.br	LNLS Brazil
Sameen Ahmed Khan	Rohelakan@yahoo.com	SCOT, Oman
Jacob Rodnizki	Jacob.Rodnizki@gmail.com	Soreq NRC, Israel
Rohan Dowd	Rohan.Dowd@synchrotron.org.au	Australian Synchrotron

We are calling for more volunteers as Regular Correspondents.

7.2 ICFA Beam Dynamics Panel Members

Name	**eMail**	**Institution**
Rick Baartman	baartman@lin12.triumf.ca	TRIUMF, 4004 Wesbrook Mall, Vancouver, BC, V6T 2A3, Canada
Marica Biagini	marica.biagini@lnf.infn.it	LNF-INFN, Via E. Fermi 40, C.P. 13, Frascati, Italy
John Byrd	jmbyrd@lbl.gov	Center for Beam Physics, LBL, 1 Cyclotron Road, Berkeley, CA 94720-8211, U.S.A.
Yunhai Cai	yunhai@slac.stanford.edu	SLAC, 2575 Sand Hill Road, MS 26 Menlo Park, CA 94025, U.S.A.
Swapan Chattopadhyay	swapan@cockroft.ac.uk	The Cockcroft Institute, Daresbury, Warrington WA4 4AD, U.K.
Weiren Chou (Chair)	chou@fnal.gov	Fermilab, MS 220, P.O. Box 500, Batavia, IL 60510, U.S.A.
Wolfram Fischer	wfischer@bnl.gov	Brookhaven National Laboratory, Bldg. 911B, Upton, NY 11973, U.S.A.
Yoshihiro Funakoshi	yoshihiro.funakoshi@kek.jp	KEK, 1-1 Oho, Tsukuba-shi, Ibaraki-ken, 305-0801, Japan
Jie Gao	gaoj@ihep.ac.cn	Institute for High Energy Physics, P.O. Box 918, Beijing 100039, China
Ajay Ghodke	ghodke@cat.ernet.in	RRCAT, ADL Bldg. Indore, Madhya Pradesh, 452 013, India
Ingo Hofmann	i.hofmann@gsi.de	High Current Beam Physics, GSI Darmstadt, Planckstr. 1, 64291 Darmstadt, Germany
Sergei Ivanov	sergey.ivanov@ihep.ru	Institute for High Energy Physics, Protvino, Moscow Region, 142281 Russia
In Soo Ko	isko@postech.ac.kr	Pohang Accelerator Lab, San 31, Hyoja-Dong, Pohang 790-784, South Korea
Elias Metral	elias.metral@cern.ch	CERN, CH-1211, Geneva 23, Switzerland
Yoshiharu Mori	mori@rri.kyoto-u.ac.jp	Research Reactor Inst., Kyoto Univ. Kumatori, Osaka, 590-0494, Japan
George Neil	neil@jlab.org	TJNAF, 12000 Jefferson Ave., Suite 21, Newport News, VA 23606, U.S.A.
Toshiyuki Okugi	toshiyuki.okugi@kek.jp	KEK, 1-1 Oho, Tsukuba-shi, Ibaraki-ken, 305-0801, Japan
Mark Palmer	mark.palmer@cornell.edu	Wilson Laboratory, Cornell University, Ithaca, NY 14853-8001, USA
Chris Prior	c.r.prior@stfc.ac.uk	ASTeC Intense Beams Group, STFC RAL, Chilton, Didcot, Oxon OX11 0QX, U.K.
Yuri Shatunov	Yu.M.Shatunov@inp.nsk.su	Acad. Lavrentiev, Prospect 11, 630090 Novosibirsk, Russia
Jiu-Qing Wang	wangjq@ihep.ac.cn	Institute for High Energy Physics, P.O. Box 918, 9-1, Beijing 100039, China
Rainer Wanzenberg	rainer.wanzenberg@desy.de	DESY, Notkestrasse 85, 22603 Hamburg, Germany

The views expressed in this newsletter do not necessarily coincide with those of the editors.
The individual authors are responsible for their text.